

Copyright
by
Larisa Vladimirovna Branets
2005

The Dissertation Committee for Larisa Vladimirovna Branets
certifies that this is the approved version of the following dissertation:

**A Variational Grid Optimization Method Based on a Local
Cell Quality Metric**

Committee:

Graham F. Carey, Supervisor

Luis A. Caffarelli

Clint N. Dawson

Thomas J.R. Hughes

Mary F. Wheeler

**A Variational Grid Optimization Method Based on a Local
Cell Quality Metric**

by

Larisa Vladimirovna Branets, B.S., M.S.

DISSERTATION

Presented to the Faculty of the Graduate School of
the University of Texas at Austin
in Partial Fulfillment
of the Requirements
for the Degree of

DOCTOR OF PHILOSOPHY

The University of Texas at Austin,
August 2005

Acknowledgments

I wish to express my sincere gratitude to my supervisor Dr. Graham F. Carey for his guidance and advice, and to all my committee members for their valuable suggestions and references. I want to thank my family for their love, care and support, and I am grateful to everybody who helped to make this work possible.

This work was supported by Los Alamos and Sandia National Laboratories.

A Variational Grid Optimization Method Based on a Local Cell Quality Metric

Publication No. _____

Larisa Vladimirovna Branets, Ph.D.
The University of Texas at Austin, 2005

Supervisor: Graham F. Carey

Computational grid optimization, correction, improvement and remeshing techniques have become increasingly important as the application problem and domain complexity increases. It is well recognized that distorted elements may degrade accuracy of finite element and finite volume simulations or cause them to fail. Hence, automatically generated grids containing millions of cells, created to fit a domain with complex geometry and adapt to features of different scales, often require correction before they can be effectively used for a numerical simulation. In this work a new variational grid smoothing formulation is developed and an extensive study of its mathematical properties, applicability and limitations is performed. The approach is based on a local cell quality metric, which is introduced as a function of the Jacobian matrix of the fundamental map from the reference cell. The mathematical properties of the local quality measure are analyzed and new theoretical results are proved. The grid improvement strategy is formulated as an optimization problem and a modified Newton scheme is used in the optimization algorithm which is implemented in a new software package. The effectiveness of the algorithm is tested on several representative

grids and for different transport application problems.

The resulting methodology is applicable to general unstructured hybrid meshes in 2 and 3 dimensions. It overcomes several difficulties encountered by other smoothing algorithms, such as effects of changing valence (number of cells sharing the same node). The formulation includes extensions to unfolding, adaptive redistribution, treatment of tangentially “sliding” boundary nodes and hanging nodes, as well as elements with curved edges or surfaces, commonly used to provide better fit of domain boundaries or interfaces.

The above techniques are applied to a set of mathematically representative problems including problems of geometric design as well as transport processes with the aim of studying the effect of the smoothing approach on the solvability and accuracy. Both 2D and 3D test problems are considered, including a moving mesh Lagrangian formulation for a fluid interface problem, non-Newtonian blood flow in curved branched pipes and a brain mapping/deformation problem. The associated numerical simulations are made on both serial and parallel PC cluster systems.

Table of Contents

Acknowledgments	iv
Abstract	v
List of Figures	ix
List of Tables	xiii
Chapter 1 Mesh improvement techniques	1
1.1 Introduction: mesh needs and research goals	1
1.1.1 Contributions	2
1.1.2 Overview	4
1.2 Smoothing techniques	5
1.3 Quality measures	10
Chapter 2 Variational formulation of the smoothing problem	16
2.1 Mapping and variational statement	16
2.1.1 Derivation from 2D Winslow smoother	16
2.1.2 Properties of the functional	18
2.1.3 Analogy with 3D hyperelasticity	21
2.2 Interior and exterior penalty treatments	27
2.2.1 Euler-Lagrange equations for penalty formulation (2.19) in 2D.	30
2.3 Discretization	31
Chapter 3 Local quality measure	34
3.1 Linear simplex elements	35
3.1.1 2D triangular element	35

3.1.2	3D tetrahedral element	40
3.2	Maximum principle	44
3.3	Tensor product linear elements	52
3.3.1	2D quadrilateral element	53
3.3.2	3D hexahedral element	55
3.3.3	Prisms	56
3.4	Quadratic simplices	58
3.4.1	2D triangular quadratic element	58
3.4.2	3D tetrahedral quadratic element	63
3.5	Biquadratic elements	65
3.5.1	Quadratic quadrilateral with one curved edge.	67
Chapter 4 Solution algorithm and numerical implementation		74
4.1	Treatment of constraints	81
4.2	Parallel implementation	83
Chapter 5 Numerical examples		85
5.1	Smoothing and unfolding of meshes in nonconvex domains	85
5.1.1	Large-scale tetrahedral mesh for basin modeling	89
5.1.2	Hexahedral mesh of a brain	92
5.2	Valence treatment	96
5.2.1	Algorithm performance on meshes with points of changing valence.	96
5.2.2	Properties of the smoothing functional on meshes with changing valence	102
5.2.3	Bounds on angles	110
5.2.4	Algorithm with varying θ	112
5.3	Meshes with curvilinear elements	114
5.4	Effect of mesh distortion on the problem solvability	119
5.4.1	Condition number study	119
5.4.2	Solution error induced by local curvilinear mesh distortion.	127

Chapter 6	Adaptivity and mapping control	131
6.1	Preserving cell size distribution during smoothing	132
6.2	Mapping control and domain shape recovery	135
6.2.1	Introducing mapping control in the metric and smoothing formulations	135
6.2.2	Domain shape recovery	136
6.3	Introducing adaptivity in the smoothing formulation	141
6.4	Combining adaptive refinement (h-) and redistribution (r-) strategies	147
6.5	Error analysis	152
Chapter 7	Transport applications	160
7.1	Moving interface problems: application to Lagrangian computations in fluid dynamics	160
7.1.1	Rayleigh-Taylor instability problem.	161
7.2	Blood flow in arterial branches	169
Chapter 8	Concluding remarks	183
	Bibliography	185
	Vita	192

List of Figures

2.1	Natural boundary conditions in 2D.	21
2.2	Degenerate and folded elements.	27
2.3	Functions $\chi_{0,1}(x)$ and $\chi_{0,1}^{-1}(x)$	29
2.4	Objective function for grid untangling $E_{\theta,\varepsilon}$, $\theta = 0.5$, $\varepsilon = 0.1$, $v = 1$	30
3.1	The linear map of the regular reference triangle onto an arbitrary triangle.	36
3.2	Level sets of $Q_{\theta}(x, y)$ on triangle with vertices $(0, 0)$, $(0, 1)$, (x, y)	37
3.3	The linear map of the regular reference tetrahedron onto an arbitrary tetrahedron.	41
3.4	Bilinear map and local numbering of vertices.	53
3.5	Level sets on quadrilateral element with vertices $(0, 0)$, $(0, 1)$, $(1, 0)$, (x, y)	54
3.6	Trilinear map.	55
3.7	Types of basis triples for computation of bounds for E_{θ} and $\det S$ on trilinear element.	56
3.8	Types of basis triples in sufficient nondegeneracy condition for trilinear element.	56
3.9	The map for the prismatic element.	57
3.10	The quadratic map \mathbf{r} of the regular reference triangle onto an arbitrary triangle.	59
3.11	Degenerate quadratic triangles with a) one, b) two and c) three curved edges (degeneracy at red vertices).	60
3.12	Degenerate quadratic triangles (degeneracy at red points).	61
3.13	Level sets as functions of position for lower mid-edge node in quadratic triangle with all other nodes fixed on the regular shape.	62
3.14	The quadratic map of the regular reference tetrahedron onto an arbitrary tetrahedron.	63
3.15	Quadratic map for quadrilaterals.	65
3.16	Quadrilateral with one curved edge.	67
3.17	“Admissible” positions for node 2 (inside the red contour) of a biquadratic element with other nodes fixed on the ideal shape.	68
3.18	“Admissible” positions for node 2 (inside the green contour) deduced from the 8-node serendipity element.	69
3.19	Level sets as functions of position of the node 2 of a biquadratic element.	70
3.20	“Restricted” biquadratic map.	71
3.21	Admissible positions for node 2 (inside the contour) of a quadrilateral with one curved edge.	72
5.1	Triangular grid in nonconvex domain. Initial mesh (left) and smoothed mesh (right).	86

5.2	Initial grid (left), smoothed grid with fixed boundary nodes (middle) and smoothed grid with “sliding” boundary nodes (right) for the complex domain having two “cavities”.	87
5.3	Unfolding. Initial mesh (left), smoothed mesh, $\theta = 0.8$ (middle) and smoothed mesh, $\theta = 0.2$ (right).	88
5.4	Unfolding. $(Q_\theta)_{\min}$ and J_{\min} vs number of iterations.	88
5.5	Interior of the basin mesh, 56,211 cells, initial (top) and smoothed (bottom).	90
5.6	Fragment of the basin mesh, initial (left) and smoothed (right).	91
5.7	Interior of the basin mesh, cell distortion before and after smoothing.	91
5.8	Hexahedral mesh of a brain, 15,036 cells.	92
5.9	Hexahedral mesh of a brain: colored distorted elements and detected “gaps”.	94
5.10	Hexahedral mesh of a brain: cut-outs before (left) and after smoothing (right).	95
5.11	Hexahedral mesh of a brain: one element before (left) and after smoothing (right).	96
5.12	Triangular grids. Initial meshes (left), smoothed meshes, $\theta = 0.8$ (middle) and smoothed meshes $\theta = 0.2$ (right).	97
5.13	Quadrilateral grid smoothing. From left to right: initial grid, grid after 3 iterations of the smoother with $\theta = 0.8$, $\theta = 0.2$	98
5.14	Smoothing. $(Q_\theta)_{\min}$, J_{\min} and \mathcal{I}_h vs number of iterations.	98
5.15	Initial 3D grid.	99
5.16	Grid slice after smoothing with $\theta = 0.8$ (left) and $\theta = 0.2$ (right).	99
5.17	Cut-away showing 1/8 of a sphere for initial hybrid 3D grid.	100
5.18	Cut-away showing 1/8 of a sphere for hybrid 3D grid smoothed with $\theta = 0.2$ (top) and $\theta = 0.8$ (bottom).	101
5.19	Patch of triangles.	103
5.20	Patch of quadrilaterals.	103
5.21	Optimal position δ as a function of valence and θ . On top: $v = 2$, on bottom: $v = 0.5$	104
5.22	Interior node of valence $val = 6$	105
5.23	Level sets of β on a patch of valence 3 (top) and 5 (bottom).	106
5.24	From top to bottom, left to right: whole smoothed grid, smoothed grid with free nodes on the boundaries of deleted patches, smoothed grid with patch boundaries fixed from initial grid, smoothed grids with vertex angle χ equal to 120, 80 and 90 degrees.	108
5.25	Zoom on the initial regular grids with one node removed.	108
5.26	Zoom on the smoothed grids: on top $\theta = 0.2$, on bottom $\theta = 0.8$	109
5.27	Sensitivity of angle bounds for triangles.	112
5.28	From top to bottom: grid smoothed with $\theta = 0.2$, varying θ , and $\theta = 0.8$	113
5.29	Grids of curved triangles: a) initial, b) smoothed with $\theta = 0.8$, and c) smoothed with $\theta = 0.2$	115
5.30	Folded grid of curved triangles.	116
5.31	Evolution of grid of curvilinear triangles during unfolding.	116
5.32	$(Q_\theta)_{\min}$ and J_{\min} vs number of iterations. Upper figures: smoothing; lower figures: unfolding of the 2D curvilinear mesh.	117

5.33	From left to right: a) curvilinear tetrahedral mesh inside a cylinder, b) smoothing result with fixed cylindrical boundary and c) with free boundary.	118
5.34	Test hexahedral grids with progressively decreasing angle between the lower tubes.	122
5.35	Condition numbers and their estimates for 3D test grids.	123
5.36	Dependence of $\kappa(K)$ on quadrilateral cell's distortion.	124
5.37	Grid with large $\kappa(K)$	125
5.38	Grid with small $\kappa(K)$	125
5.39	$\kappa(K)$ and its estimate on quadrilateral cell.	126
5.40	Solution error dependence on the local mesh deformation; L_2 and H^1 errors (top), and L_∞ error (bottom).	128
5.41	L_∞ solution error dependence on the local mesh deformation; mesh with 8-node "serendipity" elements.	129
6.1	Subregion showing initial grid (top), smoothed with $\theta = 0.2$ grid (bottom left) and smoothed with $\theta = 0.8$ grid (bottom right).	133
6.2	Fragments of initial grid (left), smoothed with $\theta = 0.2$ grid (middle) and smoothed with $\theta = 0.8$ grid (right).	134
6.3	Target element definition.	135
6.4	Target shape recovery of 2D quadrilateral mesh.	137
6.5	3D domains: reference (top), target (bottom, left) and initial (bottom, right) shapes.	139
6.6	Shape recovery in 3D.	140
6.7	Adaptive mesh redistribution: smooth mesh on the surface $(x, y, u(x, y))$ projected onto the computational domain (x, y)	142
6.8	Adaptation to a) point source, b) steep front and c) sine function.	144
6.9	Directional adaptation to local exponential source (on top) and sine function (on bottom).	146
6.10	Interpolation error vs number of d.o.f. for different strategies.	148
6.11	Resulting meshes (left) and their corner zoom for L_2 (middle) and H^1 error cases for different strategies, from top to bottom: adaptive refinement, adaptive redistribution, adaptive refinement following redistribution, uniform refinement following redistribution.	150
6.12	Comparison of the L_2 errors for solutions on uniform and adaptive meshes for $\theta = 0.8$ (top) and $\theta = 0.1$ (bottom).	156
6.13	Comparison of the H^1 errors for solutions on uniform and adaptive meshes for $\theta = 0.8$ (top) and $\theta = 0.1$ (bottom).	157
6.14	Plots of L_2 error vs estimate for solution on adaptive meshes for $\theta = 0.8$ (top) and $\theta = 0.1$ (bottom).	158
6.15	Plots of H^1 error vs estimate for solution on adaptive meshes for $\theta = 0.8$ (top) and $\theta = 0.1$ (bottom).	159

7.1	Conservative remap between the old (black) and the new (green) meshes; density fluxes are calculated over swept regions.	163
7.2	Solution to RT instability problem at $t=3.43$, no remap.	165
7.3	Solution to RT instability problem at $t=5.32$, interpolation remap.	166
7.4	Solution to RT instability problem at $t=5.58$, conservative remap.	167
7.5	Grid corrections: before (left) and after smoothing (right); arrows indicate the interface.	168
7.6	Domains and boundary conditions for the blood flow simulation: without constrictions (top) and with constrictions (bottom).	170
7.7	Two views of brain arteries.	171
7.8	Flow at $Re = 20$, $\mu_0/\mu_\infty = 1$: a) boundary stress, b) pressure and c) velocity magnitude.	173
7.9	Flow at $Re = 20$, $\mu_0/\mu_\infty = 0.1$: a) boundary stress, b) pressure and c) velocity magnitude.	174
7.10	Flow at $Re = 20$, $\mu_0/\mu_\infty = 0.03$: a) boundary stress, b) pressure and c) velocity magnitude.	175
7.11	Flow at $Re = 20$, $\mu_0/\mu_\infty = 0.01$: a) boundary stress, b) pressure and c) velocity magnitude.	176
7.12	Boundary stress for flow in constricted pipes at $Re = 20$, a) $\mu_0/\mu_\infty = 1$, b) $\mu_0/\mu_\infty = 0.03$ and c) $\mu_0/\mu_\infty = 0.01$	177
7.13	Flow in constricted pipes at $Re = 20$, $\mu_0/\mu_\infty = 0.01$: a) boundary stress, b) pressure and c) velocity magnitude.	178
7.14	Pumping flow at $Re = 20$, $\mu_0/\mu_\infty = 0.01$: velocity magnitude at different times.	180
7.15	Flow in straight pipes at $Re = 20$, $\mu_0/\mu_\infty = 0.01$: 1) boundary stress, 2) pressure and 3) velocity magnitude.	182

List of Tables

3.1	Comparison of triangle distortion measures.	38
3.2	Comparison of tetrahedron distortion measures.	43
6.1	Comparison of different adaptive strategies: minimum cell areas.	151

Chapter 1

Mesh improvement techniques

1.1 Introduction: mesh needs and research goals

Generating quality meshes that permit reliable accurate simulations remains a major technical and theoretical problem. The need to solve more complex applications for multi-material domains with irregular geometry and varying spatial scales exacerbates the difficulty. For example, large scale simulations now involve meshes with millions of cells and feature sizes that vary by orders of magnitude. As mesh generation becomes more automated, generated meshes are often unreliable and may contain unusable or geometrically distorted elements, so improving the mesh has become a time consuming but pressing task. This adversely impacts our ability to do efficient simulation and design because of the complexity of geometry, material interfaces and feature multiscale. Direct approaches of the state of the art grid generators, such as CUBIT, which are currently used in industry and national labs, often generate meshes with poorly shaped elements, such as simplices that are slivers and quadrilaterals with reentrant corners as well as tangled meshes. Consequently, it may take man-months to construct a suitable mesh for an important large scale problem. In simulations where moving boundaries arise, the situation can be much worse since the mesh deteriorates as cells deform degrading accuracy, conditioning, and computational effectiveness (more iterations and shorter timesteps). Periodic remeshing and frequent grid smoothing are needed, as well as other corrective actions. Also of particular interest because of widespread use of quadratic bases and the need to match curved boundaries, are parametrically mapped elements. Despite their practical value in fitting the domain geometry, the effect of distortion due to the quadratic map from the reference element to an element

with curved boundaries has not been sufficiently analyzed in the literature. There remain many unresolved mathematical questions related to mesh generation, mesh optimization and remeshing. These include questions related to completion of a mesh from a given surface point, properties of unstructured meshes, mesh quality with respect to angle bounds, mesh metric bounds, algorithm convergence, and so on.

A variety of mesh improvement techniques, such as topological and quality-based operators (node insertion/removal, edge/face swap, local refinement or element deletion) or smoothing (modifying node placement so as to improve a mesh without modifying the mesh connectivity), have been developed to improve the quality of automatically generated meshes. Previous work in the smoothing area include Laplacian smoothing, optimization-based smoothing, and physics-based smoothing. Adaptive mesh redistribution is also a closely related area. For general treatments of these two issues see, for instance [1, 2, 3, 4].

In the present work we focus on mesh smoothing, optimization and adaptation by node redistribution and we examine this issue mathematically from the standpoint of local cell quality. A novel scalar cell quality indicator is introduced and used to construct a global functional for mesh optimization, smoothing and correction. This metric is related to the underlying mathematical behavior associated with maps from the reference cell and therefore to fundamental interpolation ideas in finite element (FE) approximation. It is shown to generalize readily to high dimensions and to have several desirable features. The effect of cell/element distortion on the solution accuracy and incorporation in mathematical and numerical analysis is also of interest and has been investigated during the course of the study.

1.1.1 Contributions

The primary contributions of this work are:

1. The mathematical properties of the functional and the local quality measure are analyzed. In particular:
 - Existence of the solution is proved for the smoothing formulation;

- A Maximum Principle is proved for the local quality metric.
2. The effect of local changes in mesh topology is investigated; mathematical analysis and numerical investigations of issues related to varying nodal valence in the mesh are performed.
 3. An optimization algorithm for 2D and 3D meshes is developed that includes
 - unfolding;
 - smoothing;
 - adaptive redistribution;
 - treatment of hanging nodes;
 - treatment of moving boundaries;
 - treatment of curved boundaries.
 4. A set of mathematically representative examples, which are challenging for other smoothing algorithms, is developed in order to test the techniques (verification). Robustness and efficiency of the optimization algorithm is tested on several large-scale application meshes in 2 and 3 dimensions, including a tetrahedral mesh for basin modeling and a hexahedral mesh for brain deformation problem.
 5. The role of our smoothing technique in obtaining accurate solutions is investigated for several transport applications. An algorithm for a moving mesh Lagrangian formulation for a fluid interface problem is developed and implemented, and application tests for this problem and for non-Newtonian blood flow in curved branched pipes are run and results analyzed.
 6. The impact of mesh distortion on the application problem solvability is investigated:
 - Estimates for the conditioning of matrices are derived in terms of the mesh quality;
 - Dependence of the error in the solution on the mesh quality is examined both numerically and analytically.

7. The adaptive redistribution strategy is compared to refinement, and the combination of the two strategies is also examined.

Some of the results obtained during the course of this work have been published or are in press [5, 6, 7, 8] and some were presented at international conferences.

1.1.2 Overview

The outline of the thesis is as follows: we first provide an overview of related literature on mesh smoothing techniques and mesh quality. In Chapter 2, we present a mathematical formulation of a variational smoothing algorithm and introduce a local cell quality metric. The properties of the functional are examined and the existence of minimizers is proved. Chapter 3 is devoted to the complete analysis of the quality metric. The comparison analysis with other quality measures on linear simplex elements is carried out. A Maximum Principle for the quality metric is proved, providing a way to estimate the quality of tensor-product and curvilinear (quadratic) elements, as well as determine their nondegeneracy. In Chapter 4, we describe solution techniques and state the numerical smoothing algorithm. The reduced Hessian matrix used in the damped Newton solution algorithm, is proved to be symmetric positive definite, thus allowing the use of fast and efficient iterative solvers for numerical linear system. Convergence of the modified damped Newton scheme is established theoretically and confirmed numerically. A treatment for “sliding” boundary nodes and hanging nodes is developed. In Chapter 5 we present and discuss numerical studies, including smoothing strategies and identifying problem areas for 3D large-scale meshes; study of the valence effects on the smoother; theoretical investigations of the dependence of matrix condition numbers and bounds on element angles on the distortion metric. In Chapter 6 we describe the extensions of the smoothing formulation to adaptive redistribution and mapping control. Applications presented here include domain shape recovery, comparison between adaptive redistribution and refinement, and theoretical and numerical analysis of the interpolation error in terms of the distortion metric. In Chapter 7 we present and discuss transport applications, including the effect of smoothing on the solution to a moving interface fluid flow problem set in a pure Lagrangian frame, and for a non-Newtonian flow

in two curved branching pipe geometries. We conclude the thesis in Chapter 8, where we summarize the results and point to directions of further research.

1.2 Smoothing techniques

Due to their simplicity, the oldest and most widely used algorithms for mesh smoothing are the Laplacian-type smoothers [9, 10], which rely on the properties of conformal maps and harmonic functions to ensure a good mesh, but have many limitations, e.g. they may fail for non-convex regions. Most of these algorithms are derived from the Laplacian structured grid generation techniques [9, 11, 12, 1, 13, 14]. More recent approaches to mesh smoothing are optimization-based [15, 16, 17, 18, 2]. In these techniques the nodes in the grid are moved so as to maximize (minimize) a given objective function that describes in some sense a quality (distortion) metric. This quality metric must be a function of the mesh node coordinates and, usually, it is maximized by local point relaxation strategies (i.e. locally over a patch of cells and then globally through all patches in the mesh). Several authors developed algorithms for smoothing that are based on solving simple physical “analog” problems, such as using a system of springs between nodes [3], a system of interacting bubbles [19], or a set of lines drawn on a rubber-like material, stretched to fit the physical domain [20]. Some smoothing techniques combine all of the above ideas or adjust them to a particular class of smoothing problems [21] - [35].

Throughout the present work we will use the following notation: latin letters x, y, \dots represent the coordinates in physical domain Ω , greek letters ξ, η, \dots stand for coordinates in reference domain $\hat{\Omega}$, S is the Jacobian matrix of the map from the reference domain to the physical domain, $J = \det S$ is the Jacobian determinant and $G = S^T S$ is the metric tensor of this map.

One of the earliest studies of optimization strategies is due to Winslow [9]. Here, a method for numerical construction of topologically regular, nonuniform 2D triangle meshes is derived by formulating a potential problem, with two families of the mesh lines playing the role of equipotentials. The triangle mesh is mapped into a regular equilateral triangle array composed of three sets of straight lines intersecting each other at 60° , of which any

two sets are sufficient to define the mesh. These two sets are associated with functions $\xi(x, y)$, $\eta(x, y)$, which satisfy the Laplace equations

$$\nabla^2\xi = 0, \quad \nabla^2\eta = 0. \quad (1.1)$$

Solving (1.1), the intersecting “equipotentials” $\xi = \text{const}$ and $\eta = \text{const}$, together with the third set drawn through the intersection points, form the desired triangle mesh. Equations (1.1) were solved numerically by inverting them and writing them in terms of $x(\xi, \eta)$ and $y(\xi, \eta)$, using finite-difference approximation. Based on this method, Godunov [11] devised an algorithm for mesh generation for initial boundary value problems, in which changes in the boundary data induce changes in the mesh. Thompson [12] used Winslow’s method to develop an automatic numerical grid generator for a general multi-connected region containing any number of arbitrarily shaped bodies.

Brackbill and Saltzman [10] extend these ideas to adaptively vary the zone sizes and enforce orthogonality of grid lines in the resulting mesh. They propose the idea that a mesh generator can be formulated to optimize a composite objective function consisting of several measurable properties of the mesh, e.g. the global smoothness of the mapping may be measured by

$$I_s = \int_{\Omega} ((\nabla\xi)^2 + (\nabla\eta)^2) dV, \quad (1.2)$$

the orthogonality by

$$I_o = \int_{\Omega} (\nabla\xi \cdot \nabla\eta)^2 dV \text{ or } I'_o = \int_{\Omega} (\nabla\xi \cdot \nabla\eta)^2 J^3 dV$$

and the weighted volume variation by

$$I_v = \int_{\Omega} wJ dV.$$

To formulate a suitable minimization problem, the objective function for I'_o or I_v is combined with I_s as a weighted multi-objective function $I = I_s + \lambda_v I_v + \lambda'_o I'_o$ to be minimized with $\lambda_v \geq 0, \lambda'_o \geq 0$. This idea of multi-objective functions was further extended in [15], where the precise form of weights for functionals of smoothness, orthogonality and adaptivity was established according to their orders of grid scaling. An optimization multiple-pass

procedure was considered, where first a smooth and near-orthogonal grid was obtained from an initial invalid grid, and then, in subsequent solution passes, this grid was redistributed to accommodate the approximability measure for the solution, while maintaining the smoothness and near-orthogonality of the grid. For an adaptation functional, local error estimates based on an *a posteriori* error analysis were employed, with the objective being to adjust the grid so that the local error is equidistributed. The Polak-Ribiere optimization algorithm was used for minimization of the objective function.

In [1] it was shown that a grid with mesh lines graded by applying a subsequent transformation to a grid generated as the solution to the Laplace system could have been generated directly by mapping the Poisson system

$$\nabla^2 \xi^i = P^i$$

for coordinate functions $\xi^i, i = 1, \dots, n$, dimension n , from the physical to the reference domain. Here appropriate “control functions” P^i are specified and the mapped equation is coupled and nonlinear. A similar approach can be applied to

$$\nabla \cdot (w \nabla \xi^i) = 0$$

where the weight function w acts as a diffusivity to grade the mesh preferentially. These control functions may be used to implement attraction of the grid lines to points and lines in space, as well as for adaptivity. For the latter purpose the weights were proposed to be taken as functions of derivatives of an adaptive function. A brief description of variational grid generation techniques with several choices for objective functions, presented in terms of metric tensor coefficients is also given in [1]. This idea is extended in [14] and control functions are introduced to control cell size.

Mesh redistribution techniques for the evolution problem were considered in [36]. Here, the variational problem was posed with respect to both solution and coordinate transformation. For the objective functional, the weighted sum of the mean-square residual functional and the smoothing functional was taken. A penalty term was included in the smoothing part of the functional in order to constrain the motion of the nodes when the mesh attempts to fold.

A variational grid generation method introduced in [20] relies on the use of the invariants of the left Cauchy-Green tensor $S^T S$ of the reference cell deformation into a current cell:

$$I_1 = \text{tr}(S^T S), I_2 = \frac{1}{2} ((\text{tr}(S^T S))^2 - \text{tr}(S^T S)^2), I_3 = \det(S^T S).$$

Functionals are defined in terms of these invariants and grids are obtained by minimization of these energy-like functionals. This also provides a clear mechanical interpretation of the grid generation method: the underlying mechanical model for this method is the rubber membrane model. That is, consider a hexahedron of rubber-like material with a regular cubic pattern drawn on it, which is stretched to adjust its boundary to the boundary of the physical domain Ω . Then the transformation of the original cubic pattern provides the mesh in Ω . Since axioms that characterize the properties of valid deformation measures have been established, this approach is consistent with a choice of deformation measure as the energy function from elasticity theory

$$\sigma = C_1(I_1 - I_3 - 2) + C_2(I_2 - 2I_3 - 1) + K(J - 1)^2,$$

where C_1, C_2, K are constants. Again, the functional controls smoothness and orthogonality, as well as the size of the element. An alternative weight function for adaptation can be introduced based on control of the gradient of the solution and enters instead of constant K in the above expression. This method was implemented in [37] with various interpolation methods to correct space localization of the adaptation.

The effect of a Laplacian smoother on Delaunay triangulations was explored in [38]. The algorithm for constraining Laplacian smoothing to maintain a Delaunay triangulation was shown to measurably improve Laplacian smoothing.

In [16] an approach is presented to produce acceptable quality meshes from a topologically valid initial mesh by solving a constrained optimization problem. The variables for an iterative optimization procedure (the Fletcher-Reeves conjugate direction algorithm) are the nodal coordinates of the finite element mesh. Appropriate bounds (area positiveness) are imposed to prevent an unacceptable mesh.

Canann [17] presents a mesh smoothing technique that uses optimization principles (conjugate-gradient method) to minimize Oddy’s distortion metric [39] throughout a mesh, instead of concentrating efforts directly on nodal operations. Oddy’s distortion metric for an element is derived using the normalized (dimensionless) Jacobian matrix

$$S' = \frac{S}{(\det S)^{1/n}}, \quad \text{dimension } n$$

in order to remove the effect of element size. From the analogy between element distortion and strain, Green’s strain is used, and only one term from Green’s strain, which is a direct function of the Jacobian, is used to compute distortion metric

$$D = \frac{\text{tr}(G^T G)}{(\det G)^{2/n}} - \frac{1}{n} \left(\frac{\text{tr}(S^T S)}{(\det S)^{2/n}} \right)^2.$$

This metric provides a continuous scalar evaluation of an element’s distortion, and is sensitive to combined stretching and shearing of the element.

Two optimization smoothing algorithms for finite element triangulations are developed in [18]. The first algorithm is based on element geometry and is constructed to maximize the minimum value of shape regularity quality $q(t)$ [40] over a triangulation. The second algorithm is based on local interpolation errors and with the use of *a posteriori* error estimates leads to adaptive improvement of finite element triangulations. The algorithm for computing a triangulation is a common iterative Jacobi or Gauss-Seidel-like method in which one sweeps through the vertices, locally optimizing the position of a single vertex while holding all others fixed. *A posteriori* error estimates require the solution of a local Neumann problem in each element. A theoretical analysis of the Hessian properties on a cell is performed as part of the study in [40].

Another approach to structured grid generation based on the Winslow method is described in [13]. Instead of approximating The Euler-Lagrange equations (1.1), the authors approximate the functional (1.2) and solve the minimization problem using numerical optimization techniques. They show that the discretized functional approaches infinity as any cell degenerates, and thus, its minimization ensures all grid cells be convex quadrilaterals. A generalization to the case of adaptive grids based on harmonic maps between surfaces is also considered in this paper.

A formulation of the optimization method for grid smoothing in [41] gives several measures of mesh quality for tetrahedral meshes such as dihedral angles, solid angles, and element aspect ratios. Combinations of these can be used within the optimization method framework. The algorithm seeks to maximize the minimum value of the mesh quality measure, and requires function and gradient evaluations dependent on a local free vertex position. An analog of the steepest descent method is used in the algorithm.

Clearly, one can extend mesh optimization to include adaptivity to the physics of the application problem as well as to the geometry. Such adaptive mesh redistribution techniques are of significant interest in the mesh optimization community [42] - [45].

1.3 Quality measures

Quality measures are extensively referred to in many studies of mesh generation, remeshing and smoothing techniques. The notion of geometric quality of the mesh arises in early studies of finite element discretization error. Zlamal [46] proved related estimates for the discretization error in the solution of a second order BVP. The solution was approximated by polynomials of third and fourth degree on triangular elements. Estimates included expressions involving derivatives, cell diameter and a factor $1/\sin\theta$, where θ is the smallest angle of all triangles of the given mesh.

The notion of a mapping with bounded distortion is introduced in [47] and it is proved that each such mapping gives a minimum value to some Dirichlet-type functional. Mapping $f : U \rightarrow R^n$, $f \in W_n^1(U)$ is said to be a mapping with bounded distortion when

$$\left(\sum_{k=1}^n \sum_{i=1}^n \left(\frac{\partial f_k}{\partial x_i}(x) \right)^2 \right)^{n/2} \leq n^{n/2} K^n J(x, f),$$

holds a.e. $x \in U$, where $1 \leq K < \infty$ is some constant and $J(x, f)$ is the Jacobian determinant of the mapping f . Thus, the distortion coefficient is defined accordingly as

$$q = \frac{\sqrt{\sum_{k=1}^n \sum_{i=1}^n \left(\frac{\partial f_k}{\partial x_i}(x) \right)^2}}{\sqrt{n}(J(x, f))^{1/n}}.$$

Babuska and Aziz [48] have shown that the minimum-angle condition in a planar triangulation (i.e. in an acceptable triangulation no angle should be small) is too restrictive

and can be replaced by a condition that limits the maximum allowable angle. An essential condition is that no angle of a triangular element be close to π , i.e. degenerate obtuse.

In [49] an algebraic decomposition of the Jacobian matrix is given which relates physical and computational variables. This invertible decomposition parametrizes the mesh by cell orientation, cell orthogonality, cell volume, and cell aspect ratio. The contribution of the mesh to the truncation error for the discretized Laplacian, approximated with finite differences, is investigated.

In [1] a study of the truncation error in finite difference approximations of derivatives of a function, given on a curvilinear coordinate system (physical quadrilateral grid) is performed. In the 2D case, the truncation error depends upon grid uniformity and orthogonality.

In [50] the terminology “slivers” was introduced for tetrahedra with small ratio of inscribed sphere radius to circumscribed sphere radius. An equivalent nondimensional measure

$$\frac{\text{Volume}^4}{(\sum_{f=1}^4 \text{Area of a face}_f^2)^3}$$

was used in [21] for computational efficiency.

Definitions of shape parameters for quadrilaterals, that include aspect ratio, skewness, taper and warpage (a total of 4 shape parameters for a flat quadrilateral) are given in [51]. It is shown that these shape parameters can be expressed in terms of simple polynomial coefficients with a clear physical meaning, and can be evaluated from the Jacobian matrix. The quadrilateral procedure is extended in [52] to the hexahedron and it is shown that the hexahedron has 15 shape parameters.

An adaptive strategy for finite element solution of 3D viscous flow problems, based on an advancing front mesh generator, is presented in [53]. The problem of mesh validity is considered. In particular, the dependence of error bounds of the finite element solution on the shape of tetrahedral elements is examined. Analytical bounds for the Stokes problem solution in [54] include a factor $\sigma = h/\rho$ defined as the regularity of the element, where h is the largest edge length and ρ is the diameter of the inscribed sphere. The authors carried out a sensitivity analysis to study the variations of σ for deformation of a tetrahedron away

from equiangular shape. Since σ is costly to compute, an estimate α called the aspect ratio, is suggested instead:

$$\alpha = \frac{\sqrt{2}\bar{h}^3}{12V},$$

where \bar{h} is average edge length.

In [55] a variational algorithm that controls the lengths of grid lines, cell areas, and the orthogonality of grid lines is used for generating boundary-conforming grids on surfaces. Additional geometric control is provided using weights. Numerical geometric quality measures are used to judge the success of the algorithm. Geometric properties of the grids, such as discrete length, area and orthogonality measures are evaluated using averages and deviations, via a statistical approach.

A brief overview of tetrahedron quality measures is given in [56], which also provides a comparison of the fidelity of these measures to a set of distortion sensitivity tests, as well as a comparison of the computational expense of such measures. The measures that were judged best able to characterize all distortions of all tests are:

$$\frac{\text{circumscribing sphere radius}}{\text{inscribed sphere radius}}, \quad \frac{\text{maximum edge length}}{\text{inscribed sphere radius}}, \quad \frac{V^4}{(\sum_{i=1}^4 \text{area of a face}_i^2)^3},$$

$$\frac{(1/6 \sum_{i=1}^6 l_i)^3}{V}, \quad \frac{\sqrt{1/6 \sum_{i=1}^6 l_i^2}^3}{V},$$

where V is the volume of the tetrahedron and $l_i, i = 1, \dots, 6$ are its edges lengths. The two latter measures were most computationally effective.

An algorithm for the generation of a high-quality well-graded quadrilateral element mesh from a triangular element mesh is presented in [57] and makes use of the following “distortion coefficients”:

$$\alpha(ABC) = 2\sqrt{3} \frac{\|CA \times CB\|}{\|CA\|^2 + \|AB\|^2 + \|BC\|^2} \text{ for triangle } ABC, \text{ and}$$

$$\beta = \frac{\alpha_3\alpha_4}{\alpha_1\alpha_2} \text{ for the quadrilateral,} \tag{1.3}$$

where $\alpha_1 \geq \alpha_2 \geq \alpha_3 \geq \alpha_4$ are values of so called “distortion coefficients” of the subtriangles, produced by cutting the quadrilateral along its two diagonals. Quality of the triangular

(quadrilateral) mesh is defined to be the geometrical mean of the α (β) values of all cells in the mesh.

A tetrahedron shape measure

$$\eta(T) = \frac{12(3V)^{2/3}}{\sum_{i=1}^6 l_i^2} = \frac{3\sqrt[3]{\lambda_1\lambda_2\lambda_3}}{\lambda_1 + \lambda_2 + \lambda_3} = \frac{3\sqrt[3]{\det(S^T S)}}{\text{tr}(S^T S)} \quad (1.4)$$

is given in [58], where λ_i denote eigenvalues of the metric tensor $S^T S$ for the transformation between tetrahedron T and regular reference tetrahedron \hat{T} . The geometric explanation of η is that it characterizes the shape of the inscribed ellipsoid.

Three tetrahedron shape measures - the minimum solid angle θ_{\min} (or $\sigma_{\min} = \sin(\theta_{\min}/2)$), the radius ratio $\rho = 3r_{in}/r_{circ}$, and the mean ratio $\eta = 12(3V)^{2/3}/\sum_{i=1}^6 l_i^2$, are discussed in [59]. For different shape measures μ, ν , a relationship of the form $c_0\mu^{e_0} \leq \nu \leq c_1\mu^{e_1}$ is obtained, where c_0, c_1, e_0 and e_1 are positive constants. This implies that if one measure approaches zero for a poorly-shaped tetrahedron, so does the other ($\mu \rightarrow 0 \Rightarrow \nu \rightarrow 0$ and $\nu \rightarrow 0 \Rightarrow \mu \rightarrow 0$). Combined with the property that each measure attains a maximum value only for the regular tetrahedron, this means that the shape measures are “equivalent” in that larger values of the measures represent good quality tetrahedra (close to a regular tetrahedron) and smaller values represent poor quality tetrahedra (close to degenerate). For the tetrahedron shape measures σ_{\min}, ρ and η , the following equivalency relationships hold:

$$\begin{aligned} \eta^3 &\leq \rho \leq (2/\sqrt[4]{6})\eta^{3/4}; \\ \eta^{3/2}/16 &\leq \sigma_{\min} \leq \sqrt[4]{8}\eta^{3/4}; \\ \sqrt{3}/24\rho^2 &\leq \sigma_{\min} \leq (2/\sqrt[4]{3})\rho^{1/2}. \end{aligned} \quad (1.5)$$

In [40, 18] the shape regularity quality of a triangle t is given by

$$q(t) = \frac{4\sqrt{3}|t|}{|l_1|^2 + |l_2|^2 + |l_3|^2}.$$

The study of its geometrical properties shows that $q(t)$ has circular level sets, when considered a function of the location of one vertex of t with the other two vertices fixed. Moreover, it is independent of the size of t and the formula used for computing the area $|t|$ signal reorientation of a triangle by changing sign, which can be used to avoid mesh folding.

Another algorithm for the construction of solution-adapted triangular 2D meshes within an optimization framework is considered in [26]. Here an approximation of the second spatial derivative of the solution u is used to get a metric in the computational domain of the form:

$$|D^2u(t, t)| = \left| \sum_{i,j} t_i t_j \frac{\partial^2 u}{\partial x_i \partial x_j} \right|.$$

A mesh quality objective function based on this metric

$$Q_K = 20.78 V_K / P_K^2 F\left(\frac{h_K}{h}\right),$$

is proposed and optimized, where V_K, P_K are area and perimeter of the element K , $h_K = P_K/3$ and h is the desired mesh size. The quality measure Q_K is a product of “shape” quality and a function of mesh size F that satisfies $0 \leq F(x) \leq 1$ and $F(x) = 1 \Leftrightarrow x = 1$. The suggested choice of F which has no other extrema is

$$F(x) = (m(x)^\beta [2 - m(x)^\beta]), m(x) = \min\{x, 1/x\}.$$

A different approach to unite shape and size quality metrics is presented in [33, 34].

Characteristics of grid lines, faces of 3D grids and grid cells are presented in terms of invariants of the metric tensor and their relations in [4]. Various grid characteristics, such as skewness, stretching, torsion, warping, cell aspect ratio, cell volume, characteristics of nonorthogonality, departure from conformality, cell deformation, and grid density, are formulated through quantities which measure the features of the coordinate curves, surfaces and transformations. Geometric interpretations of metric-tensor invariants are given for both 2D and 3D grids. Reference [60] contains an overview of several element quality metrics. Several aspects of geometric mesh quality metrics are examined in [61]. This includes discussion of the mathematical definition of mesh quality metrics, their properties, a capability for analyzing and classifying various metrics (including a way to show how metrics are related and means of identifying redundant metrics). The approach is based on element Jacobian matrices and an algebraic framework that uses the matrix norm, trace, and determinant.

Despite their practical value in fitting geometry, except for a few specialized studies such as those in [62, 35], there has been relatively little work on analyzing the effect of

distortion due to the quadratic map from the reference element to the element with curved boundaries. Prior studies on curvilinear elements focus on the issue of the map invertibility [63], or only the nonvanishing of the Jacobian [64, 65]. These studies include elaborate numerical schemes to determine if the Jacobian vanishes for the 6-node triangle [66] and 8-node quadrilateral elements [67]. Their extensions for 3D or more complex elements are only partially successful. The nonvanishing of the mapping Jacobian is proved [63] to be sufficient for the invertibility of the quadratic 6-node triangle. However, for other, more complex, quadratic elements a similar result has not been proven yet. In [62] several distortion parameters for an 8-node quadrilateral with curved boundaries are derived using the theory of geodesics. The authors in [35] extend the angle-based quality metric, originally defined for linear triangles and quadrilaterals in [57], for use in the optimization of meshes consisting of quadratic triangles and quadrilaterals. They also extended the formulation to unfolding by adding a barrier part to their quality functional.

In the next chapter we present a mathematical approach for analyzing mesh deformation that leads to a new cell quality metric suitable for mesh optimization.

Chapter 2

Variational formulation of the smoothing problem

In this chapter we present a novel variational smoothing formulation and demonstrate how an analogy can be drawn between it and the Laplace-based smoothing techniques in 2D and hyperelasticity problems in 3D. We first discuss the class of mappings, their properties and variational statement. Of particular importance is a mesh distortion metric, which arises from the variational problem formulation. We examine the distortion functional properties, including its Euler-Lagrange equations, natural boundary conditions, and existence of minimizers. We also introduce functional extensions for tangled meshes and present the discretization framework.

2.1 Mapping and variational statement

2.1.1 Derivation from 2D Winslow smoother

In the literature review of Chapter 1, Section 1.2 we introduced the Winslow smoother [9] as a well-known strategy. Here, the ideas of harmonic functions and maps lead to the associated Dirichlet integral

$$\mathcal{I} = \int_{\Omega} [(\nabla\xi)^2 + (\nabla\eta)^2] dx dy. \quad (2.1)$$

The pair of Laplace problems (1.1) follows as the associated pair of Euler-Lagrange equations. Mapping the variational problem to the reference domain $(\xi, \eta) \in \hat{\Omega}$ we have

$$\mathcal{I} = \int_{\hat{\Omega}} \frac{x_{\xi}^2 + x_{\eta}^2 + y_{\xi}^2 + y_{\eta}^2}{x_{\xi}y_{\eta} - x_{\eta}y_{\xi}} d\xi d\eta \quad (2.2)$$

for $x(\xi, \eta)$ and $y(\xi, \eta)$. This can be expressed compactly as

$$\mathcal{I} = \int_{\hat{\Omega}} \frac{\text{tr}(S^T S)}{\det S} d\xi d\eta \quad (2.3)$$

where tr denotes the trace (recall Section 1.2 for the notations). Following the ideas of optimization-based smoothing and of quality metrics as functions of the metric tensor or Jacobian matrix, it is natural to relate the integrand of (2.3) to a quality measure. We define the corresponding local distortion measure as

$$\beta(S) = \frac{\frac{1}{2}\text{tr}(S^T S)}{\det S}, \quad (2.4)$$

which we have scaled so that its range is $[1, \infty)$. Thus, when the map between the reference and physical frames is identity ($S = I$), the value of distortion measure is one $\beta(I) = 1$, and when the map approaches degeneracy $\det S \rightarrow 0$, $\beta \rightarrow +\infty$. We define the local mesh quality as $Q_0 = \beta^{-1}$.

In fact, this distortion measure generalizes to any dimension directly [34] as

$$\beta(S) = \frac{(\frac{1}{n}\text{tr}(S^T S))^{n/2}}{\det S}. \quad (2.5)$$

The map and distortion metric here are for general reference and physical domains, but we are particularly interested in the map from a reference cell $\hat{\Omega}_c$ onto an arbitrary cell in the physical domain. In the course of this work, we will thoroughly investigate the properties of the distortion measure (2.5). As we will see below, β is a “fair” shape control measure in the sense that it detects all types of degenerate elements and does not depend upon the size of the element. (Note that this distortion metric is insufficient, since it will not control size.)

Since in most applications it is desirable to exercise control on element size as well as shape, we introduce a “dilation” or size control metric and combine both metrics into a composite measure. In the literature review of Chapter 1, we indicated several approaches invented to unite element shape and size control, and we will follow one of them. Let v be a target element size measure (related to area in 2D and volume in 3D) defined *a priori*. For example, in the case of a “desired” uniform grid, v is taken to be the average cell area

$$v = \frac{\int_{\hat{\Omega}} \det S d\vec{\xi}}{\int_{\hat{\Omega}} d\vec{\xi}}.$$

Then the ratios $\det S/v$ and $v/\det S$ indicate the departure of $\det S$ from v . If a specified grading in size is desired, then v may be specified (as we will see later in Chapter 6). Since $\det S$ can be above or below v , we use the symmetric dilation measure

$$\mu(S) = \frac{1}{2} \left(\frac{v}{\det S} + \frac{\det S}{v} \right), \quad (2.6)$$

which has its origin in the Zhoukowsky conformal map $z + 1/z$. Then the dilation measure achieves its minimum $\mu = 1$ when $v = \det S$ and $\mu \rightarrow \infty$ as $\det S \rightarrow \infty$ or 0 .

Following the ideas of multi-objective functions, we now define an additive distortion-dilation measure

$$E_\theta = (1 - \theta)\beta(S) + \theta\mu(S), \quad (2.7)$$

where coefficient $0 \leq \theta < 1$ can be adjusted to emphasize the respective distortion and dilation terms either *a priori* or via feedback.

Remark: Note, that in this section we are considering the mesh smoothing problem only. That is, the initial mesh is valid and has positive Jacobians everywhere, so metrics (2.5), (2.6) and (2.7) are well defined. The extensions of the metric definitions to more general cases (zero or negative Jacobians) is described later in Section 2.2.

Now the variational grid smoothing formulation can be stated as follows: minimize the functional

$$\mathcal{I} = \int_{\hat{\Omega}} E_\theta(S) d\vec{\xi}, \quad (2.8)$$

subject to specified boundary (or other) constraints. In this general formulation, the reference domain is a union of all N_c reference elements (one for each cell in the mesh) $\hat{\Omega} = \bigcup_c \hat{\Omega}_c$ and (2.8) is understood as

$$\mathcal{I} = \sum_{c=1}^{N_c} \int_{\hat{\Omega}_c} E_\theta(S) d\vec{\xi}.$$

2.1.2 Properties of the functional

For clarity of exposition, let us return to the 2D case and write the functional (2.8) in the following way

$$\mathcal{I} = (1 - \theta)\mathcal{I}_\beta + \theta\mathcal{I}_\mu, \text{ where } \mathcal{I}_\beta = \int_{\hat{\Omega}} \beta(S) d\xi d\eta, \quad \mathcal{I}_\mu = \int_{\hat{\Omega}} \mu(S) d\xi d\eta. \quad (2.9)$$

We already know that functional \mathcal{I}_β is elliptic, since its Euler-Lagrange equations are the Laplace equations (1.1). Below we will obtain the Euler-Lagrange equations and natural boundary conditions for our composite variational problem. By mapping the problem to the physical domain we have

$$\begin{aligned}
\mathcal{I}_\beta(\xi, \eta) &= \int_{\hat{\Omega}} \beta d\xi d\eta = \frac{1}{2} \int_{\Omega} ((\nabla \xi)^2 + (\nabla \eta)^2) dx dy; \\
\mathcal{I}_\mu(\xi, \eta) &= \int_{\hat{\Omega}} \mu d\xi d\eta = \int_{\Omega} \mu J^{-1} dx dy = \frac{1}{2} \int_{\Omega} \left(\frac{1}{v} + v J^{-2} \right) dx dy \\
&= \frac{\text{meas } \Omega}{2v} + \frac{v}{2} \int_{\Omega} (\xi_x \eta_y - \xi_y \eta_x)^2 dx dy.
\end{aligned} \tag{2.10}$$

The variations of the functionals are

$$\begin{aligned}
\delta \mathcal{I}_\beta &= \int_{\Omega} (\nabla \xi \cdot \nabla \delta \xi + \nabla \eta \cdot \nabla \delta \eta) dx dy \\
&= \int_{\partial \Omega} \left(\frac{\partial \xi}{\partial \mathbf{n}} \delta \xi + \frac{\partial \eta}{\partial \mathbf{n}} \delta \eta \right) ds - \int_{\Omega} (\Delta \xi \delta \xi + \Delta \eta \delta \eta) dx dy; \\
\delta \mathcal{I}_\mu &= v \int_{\Omega} J^{-1} (\delta \xi_x \eta_y - \delta \xi_y \eta_x + \xi_x \delta \eta_y - \xi_y \delta \eta_x) dx dy \\
&= v \int_{\partial \Omega} \left(J^{-1} \begin{pmatrix} \eta_y \\ -\eta_x \end{pmatrix} \cdot \mathbf{n} \delta \xi + J^{-1} \begin{pmatrix} -\xi_y \\ \xi_x \end{pmatrix} \cdot \mathbf{n} \delta \eta \right) ds \\
&\quad + v \int_{\Omega} (((J^{-1} \eta_x)_y - (J^{-1} \eta_y)_x) \delta \xi + ((J^{-1} \xi_y)_x - (J^{-1} \xi_x)_y) \delta \eta) dx dy.
\end{aligned}$$

Since we are going to use different values of θ in the smoothing algorithm, it is useful to understand the effect of the dilation functional. The corresponding Euler-Lagrange equations (from the dilation functional only, $\theta = 1$) in the physical domain Ω are

$$\begin{aligned}
J_y^{-1} \eta_x &= J_x^{-1} \eta_y \\
J_y^{-1} \xi_x &= J_x^{-1} \xi_y,
\end{aligned} \tag{2.11}$$

or, equivalently, since $J^{-1} \neq 0 \Rightarrow \xi_x \eta_y \neq \xi_y \eta_x$,

$$(J^{-1})_x = (J^{-1})_y = 0 \text{ in } \Omega \Rightarrow J = \text{const in } \hat{\Omega}. \tag{2.12}$$

From the definition of the dilation measure (2.6) we have $J = v$ on Ω . If we assign different values of v for different cells in the grid, we can repeat the derivation and get $J|_c = v_c$ for

each cell c in the grid. Note, that the dilation part of the functional alone ($\theta = 1$) cannot be used for the mesh smoothing, since it has no elliptic properties and will not guarantee the solution existence of the variational problem (which is considered later in this chapter).

The Euler-Lagrange equations for the full functional (2.8) in physical domain Ω follow easily from the variational statement as

$$\begin{aligned} -(1 - \theta)\Delta\xi + v\theta(J_y^{-1}\eta_x - J_x^{-1}\eta_y) &= 0 \\ -(1 - \theta)\Delta\eta + v\theta(J_y^{-1}\xi_x - J_x^{-1}\xi_y) &= 0. \end{aligned}$$

In order to obtain the natural boundary conditions let us represent the domain boundary as a collection of parts, each of which is given by either $\xi = \text{const}$ or $\eta = \text{const}$ coordinate lines:

$$\partial\Omega = \left(\Gamma^\xi = \bigcup_i \Gamma_i^\xi \right) \cup \left(\Gamma^\eta = \bigcup_j \Gamma_j^\eta \right), \text{ where } \Gamma_i^\xi : \xi = \text{const}_i, \quad \Gamma_j^\eta : \eta = \text{const}_j,$$

and any two parts may share only their end-points. Then $\delta\xi = 0$ on Γ^ξ and $\delta\eta = 0$ on Γ^η so the natural boundary conditions are

$$\begin{aligned} \begin{pmatrix} \theta \frac{v}{j} \eta_y + (1 - \theta) \xi_x \\ -\theta \frac{v}{j} \eta_x + (1 - \theta) \xi_y \end{pmatrix} \cdot \mathbf{n} &= 0 \quad \text{on } \Gamma^\eta; \\ \begin{pmatrix} -\theta \frac{v}{j} \xi_y + (1 - \theta) \eta_x \\ \theta \frac{v}{j} \xi_x + (1 - \theta) \eta_y \end{pmatrix} \cdot \mathbf{n} &= 0 \quad \text{on } \Gamma^\xi. \end{aligned}$$

Let us analyze these conditions on a representative part of the boundary, Γ_0^ξ . For the natural boundary conditions coming from the shape control part of the functional (with $\theta = 0$) we get $\nabla\eta \cdot \mathbf{n} = 0$, which means that grid lines given by level curves $\eta = \text{const}$ tend to align orthogonally to the boundary (see Figure 2.1, a)). For the conditions coming from the size control part (with $\theta = 1$) we obtain $\nabla\xi \parallel \mathbf{n}$, i.e. grid lines $\xi = \text{const}$ tend to align parallel to the boundary (see Figure 2.1, b)). Thus, natural boundary conditions impose orthogonality of the grid lines near/to the boundary.

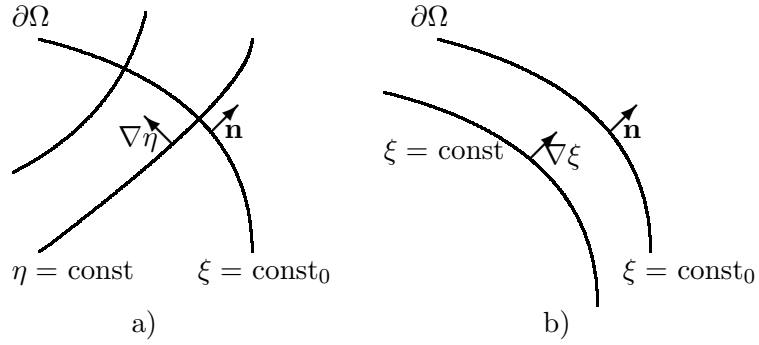


Figure 2.1: Natural boundary conditions in 2D.

2.1.3 Analogy with 3D hyperelasticity

A useful way of approaching the variational smoothing formulation (2.8) is by drawing the analogy between our smoothing problem in 3D and a problem of equilibrium for hyperelastic material. We can then draw on several theoretical results from the theory of hyperelastic deformation to infer related properties of our 3D generalization of the metric. More specifically, in our case the local measure E_θ represents a stored energy function for hyperelastic material $W : \hat{\Omega} \times \mathbb{M}_+^3 \rightarrow \mathbb{R}$ and the distortion functional $\mathcal{I} = \int_{\hat{\Omega}} E_\theta(S) d\vec{\xi}$ is the total energy of the material. The admissible deformations $\mathbf{x} : \hat{\Omega} \rightarrow \mathbb{R}^3$ satisfy the constraints $\det \nabla \mathbf{x} = \det S > 0$ in $\hat{\Omega}$ and $\mathbf{x} = \mathbf{x}_0$ on the boundary. In our formulation, thus, we have no applied body or surface forces. The solution sought is the admissible deformation minimizing the total energy. Thus, using the theory developed for hyperelastic materials in [68], we will demonstrate how certain theoretical results apply to our case.

Existence of the minimizers.

We are interested mainly in two types of boundary conditions for the problem:

- boundary conditions of place: $\mathbf{x}(\vec{\xi}) = \mathbf{x}_0(\vec{\xi})$ on part of the boundary Γ_0 , which correspond to specifying the location of mesh boundary nodes;
- unilateral boundary conditions of place: $\mathbf{x}(\Gamma_2) \subset C$, where C is some given closed subset of \mathbb{R}^3 , which models contact without friction and corresponds to movement of

mesh nodes along the given boundary.

Existence results for the hyperelasticity problem with both types of boundary conditions above are proved in [68] based on John Ball's theory [69]. We now reformulate this result considering that our stored energy function does not explicitly depend on $\text{Cof}S = (\det S)S^{-T}$, and we do not need to impose any conditions on $\text{Cof}S$.

Lemma 1 *For existence of the solution in the set*

$$\begin{aligned} \Phi &= \{ \mathbf{x} \in \mathbf{W}^{1,p}(\hat{\Omega}); \det \nabla \mathbf{x} \in L^r(\hat{\Omega}), \\ &\quad \mathbf{x} = \mathbf{x}_0 \text{ a.e. on } \Gamma_0, \\ &\quad \mathbf{x} \in C \text{ a.e. on } \Gamma_2, \\ &\quad \det \nabla \mathbf{x} > 0 \text{ a.e. in } \hat{\Omega} \} \end{aligned} \tag{2.13}$$

(provided it is nonempty and $\inf_{\mathbf{x} \in \Phi} \mathcal{I}(\mathbf{x}) < +\infty$) the stored energy function W must satisfy three assumptions:

1. *Polyconvexity: for almost all $\vec{\xi} \in \hat{\Omega}$, there exists a convex function $\mathbb{W}(\vec{\xi}, \cdot) : \mathbb{M}^3 \times (0, +\infty) \rightarrow \mathbb{R}$ such that*

$$\mathbb{W}(\vec{\xi}, S, \det S) = W(\vec{\xi}, S) \text{ for all } S \in \mathbb{M}_+^3;$$

the function $\mathbb{W}(\cdot, F, \delta) : \hat{\Omega} \rightarrow \mathbb{R}$ is measurable for all $(F, \delta) \in \mathbb{M}^3 \times (0, +\infty)$.

2. *Behavior as $\det S \rightarrow 0^+$: for almost all $\vec{\xi} \in \hat{\Omega}$,*

$$\lim_{\det S \rightarrow 0^+} W(\vec{\xi}, S) = +\infty.$$

3. *Coerciveness: there exist constants a_1, a_2, p, r such that*

$$a_1 > 0, p \geq 2, r > 1, a_2 \in \mathbb{R},$$

$$W(\vec{\xi}, S) \geq a_1(\|S\|^p + (\det S)^r) + a_2$$

$$\text{for almost all } \vec{\xi} \in \hat{\Omega} \text{ and for all } S \in \mathbb{M}_+^3. \tag{2.14}$$

Proof:

We follow here step by step the existence proof (for the problem with boundary conditions of place only) in [68] but applied now to our case (no dependence on $\text{Cof}S$).

(1) *All integrals are well defined.* A consequence of the first assumption: For almost all $\vec{\xi} \in \hat{\Omega}$, the function $\mathbb{W}(\vec{\xi}, \cdot) : \mathbb{M}^3 \times (0, +\infty) \rightarrow \mathbb{R}$ is continuous (it is convex and real-valued on an open subspace of a finite-dimensional space); for all $(F, \delta) \in \mathbb{M}^3 \times (0, +\infty)$, the function $\mathbb{W}(\cdot, F, \delta) : \hat{\Omega} \rightarrow \mathbb{R}$ is measurable, and $\mathbb{M}^3 \times (0, +\infty)$ is a Borel set. Therefore the function $\mathbb{W} : \hat{\Omega} \times \mathbb{M}^3 \times (0, +\infty) \rightarrow \mathbb{R}$ is a Caratheodory function, and consequently the function

$$\vec{\xi} \in \hat{\Omega} \rightarrow \mathbb{W}(\vec{\xi}, \nabla \mathbf{x}(\vec{\xi}), \det \nabla \mathbf{x}(\vec{\xi})) \in \mathbb{R}$$

is measurable for each $\mathbf{x} \in \Phi$ ($\det \nabla \mathbf{x}(\vec{\xi}) \in (0, +\infty)$ for almost all $\vec{\xi} \in \hat{\Omega}$). Since the function W is in addition bounded below (by the coerciveness inequality), we conclude that the integral

$$\int_{\hat{\Omega}} W(\vec{\xi}, \nabla \mathbf{x}) d\vec{\xi} = \int_{\hat{\Omega}} \mathbb{W}(\vec{\xi}, \nabla \mathbf{x}, \det \nabla \mathbf{x}) d\vec{\xi}$$

is a well defined extended real number in the interval $[a_2 \text{vol} \hat{\Omega}, +\infty]$ for each $\mathbf{x} \in \Phi$.

(2) We find the following *lower bound* for $\mathcal{I}(\mathbf{x})$, $\mathbf{x} \in \Phi$ using coerciveness of function W , the Poincare inequality and the boundary condition $\mathbf{x} = \mathbf{x}_0$ on Γ : there exist constants $c > 0$ and $d > 0$ such that

$$\mathcal{I}(\mathbf{x}) \geq c\{ \|\mathbf{x}\|_{1,p,\hat{\Omega}}^p + |\det \nabla \mathbf{x}|_{0,r,\hat{\Omega}}^r \} + d \text{ for all } \mathbf{x} \in \Phi.$$

(3) Let (ϕ^k) be an *infimizing sequence* for the functional \mathcal{I} , i.e. a sequence that satisfies

$$\phi^k \in \Phi \forall k, \text{ and } \lim_{k \rightarrow \infty} \mathcal{I}(\phi^k) = \inf_{\mathbf{x} \in \Phi} \mathcal{I}(\mathbf{x}).$$

By assumption, $\inf_{\mathbf{x} \in \Phi} \mathcal{I}(\mathbf{x}) < +\infty$, and thus by (2) the sequence $(\phi^k, \det \nabla \phi^k)$ is bounded in the reflexive Banach space $\mathbf{W}^{1,p}(\hat{\Omega}) \times L^r(\hat{\Omega})$, where $p \geq 2, r \geq 1$. Hence there exists a subsequence $(\phi^l, \det \nabla \phi^l)$ that converges weakly to an element (ϕ, δ) in the space $\mathbf{W}^{1,p}(\hat{\Omega}) \times L^r(\hat{\Omega})$. By the properties of mappings $\phi \in \mathbf{W}^{1,p}(\hat{\Omega}) \rightarrow \text{Cof} \nabla \phi \in \mathbf{L}^{p/2}(\hat{\Omega})$ and

$\phi \in \mathbf{W}^{1,p}(\hat{\Omega}) \rightarrow \det \nabla \phi$, proved in [68], we have

$$\left\{ \begin{array}{l} \phi^l \rightharpoonup \phi \text{ in } \mathbf{W}^{1,p}(\hat{\Omega}), p \geq 2, \\ \text{Cof} \nabla \phi^l \rightharpoonup H \text{ in } \mathbf{L}^q(\hat{\Omega}), \frac{1}{p} + \frac{1}{q} \leq 1, \\ \det \nabla \phi^l \rightharpoonup \delta \text{ in } L^r(\hat{\Omega}), r \geq 1 \end{array} \right\} \Rightarrow \left\{ \begin{array}{l} H = \text{Cof} \nabla \phi \\ \delta = \det \nabla \phi \end{array} \right.$$

(4) *Show that $\phi \in \Phi$, i.e. establish that $\det \nabla \phi > 0$ almost everywhere in $\hat{\Omega}$ and that $\phi = \mathbf{x}_0$ on Γ . This part uses Mazur's theorem and is exactly the same as in the original proof.*

(5) *Show that*

$$\int_{\hat{\Omega}} W(\vec{\xi}, \nabla \phi(\vec{\xi})) d\vec{\xi} \leq \liminf_{l \rightarrow \infty} \int_{\hat{\Omega}} W(\vec{\xi}, \nabla \phi^l(\vec{\xi})) d\vec{\xi}.$$

Let us consider a subsequence (ϕ^m) of (ϕ^l) such that the sequence $(\int_{\hat{\Omega}} W(\vec{\xi}, \nabla \phi^m(\vec{\xi})) d\vec{\xi})$ converges. Using the result of step (3) and Mazur's theorem, we conclude that for each m , there exist integers $j(m) \geq m$ and numbers μ_t^m , $m \leq t \leq j(m)$, such that

$$\mu_t^m \geq 0, \sum_{t=m}^{j(m)} \mu_t^m = 1,$$

$$D^m = \sum_{t=m}^{j(m)} \mu_t^m (\nabla \phi^t, \det \nabla \phi^t) \xrightarrow{m \rightarrow \infty} (\nabla \phi, \det \nabla \phi)$$

in $\mathbf{L}^p(\hat{\Omega}) \times L^r(\hat{\Omega})$.

Hence there exists a subsequence (D^n) of (D^m) such that

$$\sum_{t=n}^{j(n)} \mu_t^n (\nabla \phi^t(\vec{\xi}), \det \nabla \phi^t(\vec{\xi})) \xrightarrow{n \rightarrow \infty} (\nabla \phi(\vec{\xi}), \det \nabla \phi(\vec{\xi}))$$

for almost all $\vec{\xi} \in \hat{\Omega}$.

Since the function $\mathbb{W}(\vec{\xi}, \cdot)$ is continuous on the set $\mathbb{M}^3 \times (0, +\infty)$ for almost all $\vec{\xi} \in \hat{\Omega}$ as a consequence of the first assumption, and since from step (4) $\det \nabla \phi(\vec{\xi}) > 0$ for almost all $\vec{\xi} \in \hat{\Omega}$, we have

$$\begin{aligned} W(\vec{\xi}, \nabla \phi(\vec{\xi})) &= \mathbb{W}(\vec{\xi}, (\nabla \phi(\vec{\xi}), \det \nabla \phi(\vec{\xi}))) \\ &= \lim_{n \rightarrow \infty} \mathbb{W} \left(\vec{\xi}, \sum_{t=n}^{j(n)} \mu_t^n (\nabla \phi^t(\vec{\xi}), \det \nabla \phi^t(\vec{\xi})) \right) \end{aligned}$$

for almost all $\vec{\xi} \in \hat{\Omega}$. Using this relation, Fatou's lemma, and the assumed convexity of the function $\mathbb{W}(\vec{\xi}, \cdot)$ for almost all $\vec{\xi} \in \hat{\Omega}$, we obtain

$$\begin{aligned} \int_{\hat{\Omega}} W(\vec{\xi}, \nabla \phi(\vec{\xi})) d\vec{\xi} &\leq \liminf_{n \rightarrow \infty} \int_{\hat{\Omega}} \mathbb{W} \left(\vec{\xi}, \sum_{t=n}^{j(n)} \mu_t^n (\nabla \phi^t(\vec{\xi}), \det \nabla \phi^t(\vec{\xi})) \right) d\vec{\xi} \\ &\leq \liminf_{n \rightarrow \infty} \sum_{t=n}^{j(n)} \mu_t^n \int_{\hat{\Omega}} W(\vec{\xi}, \nabla \phi^t(\vec{\xi})) d\vec{\xi} \\ &= \lim_{n \rightarrow \infty} \int_{\hat{\Omega}} W(\vec{\xi}, \nabla \phi^n(\vec{\xi})) d\vec{\xi} = \lim_{m \rightarrow \infty} \int_{\hat{\Omega}} W(\vec{\xi}, \nabla \phi^m(\vec{\xi})) d\vec{\xi}. \end{aligned}$$

(6) The function ϕ is thus a solution to the minimization problem since $\phi \in \Phi$ by step (4), and since

$$\mathcal{I}(\phi) \leq \liminf_{l \rightarrow \infty} \mathcal{I}(\phi^l) = \inf_{\mathbf{x} \in \Phi} \mathcal{I}(\mathbf{x}) \Rightarrow \mathcal{I}(\phi) = \inf_{\mathbf{x} \in \Phi} \mathcal{I}(\mathbf{x}). \blacksquare$$

Proof of existence of minimizers for a total distortion functional:

In our case, the second assumption of the Lemma is obviously true. The coerciveness is easy to establish, using the fact that the Jacobian determinant is bounded from above by the volume of physical domain $\det S < V$,

$$\begin{aligned} W(\vec{\xi}, S) = E_\theta(S) &= (1 - \theta) \frac{\frac{1}{3^{3/2}} \|S\|^3}{\det S} + \theta/2 \left(\frac{v + (\det S)^2/v}{\det S} \right) \geq \\ &\geq \frac{1 - \theta}{3^{3/2} V} \|S\|^3 + \frac{\theta}{2vV} (\det S)^2 + \frac{\theta v}{2V}. \end{aligned}$$

Thus, we establish $a_1 = \min \left(\frac{1 - \theta}{3^{3/2} V}, \frac{\theta}{2vV} \right)$, $a_2 = \frac{\theta v}{2V}$, $p = 3 \geq 2$ and $r = 2 \geq 1$.

It remains to show the polyconvexity of E_θ . The size control part μ is a convex function of $\det S$, and we will show that the shape control part β is a convex function of two variables $(S, \det S)$ (we denote $\hat{\beta}(S, \det S) = \beta(S)$) by proving that its second derivative is positive definite:

$$\hat{\beta}''(F, \det F)(S, \cdot) = \begin{pmatrix} \frac{(\frac{1}{3} \text{tr} F^T F)^{1/2} \text{tr} S^T S + \frac{1}{3} (\text{tr} F^T S)^2 (\frac{1}{3} \text{tr} F^T F)^{-1/2}}{\det F} & - \frac{(\frac{1}{3} \text{tr} F^T F) \text{tr} F^T S}{(\det F)^2} \\ - \frac{(\frac{1}{3} \text{tr} F^T F) \text{tr} F^T S}{(\det F)^2} & \frac{2(\frac{1}{3} \text{tr} F^T F)^2}{(\det F)^3} \end{pmatrix} \quad (2.15)$$

for all $F, S \in \mathbb{M}_+^3$. The quadratic form defined by this second derivative is equal to

$$(xy)\hat{\beta}(xy)^T = \frac{2(y\frac{1}{3}\frac{\text{tr}F^T F}{\det F} - \frac{x}{2}\text{tr}F^T S)^2 + \frac{x^2}{6}(2\text{tr}F^T F\text{tr}S^T S - (\text{tr}F^T S)^2)}{(\frac{1}{3}\text{tr}F^T F)^{1/2}\det F}$$

and is positive for any $x, y \in \mathbb{R}$ since

$$\text{tr}F^T S \leq (\text{tr}F^T F)^{1/2}(\text{tr}S^T S)^{1/2}$$

by the Cauchy-Schwarz inequality. \blacksquare

Transition to 2D

The hyperelastic material problem is naturally defined in three dimensions. However, we can formulate certain constraints on this 3D problem that allow us to transform it to a form suitable for our 2D smoothing formulation. Note, that the size control part of the functional \mathcal{I}_μ is the same in any dimension, so we are only concerned about the transition of the shape control part \mathcal{I}_β .

Appealing once again to elasticity theory, the columns of the deformation gradient $S = \nabla \mathbf{x}$ form the basis in the tangent vector space. Hence, it is natural in our work to consider the Jacobian matrix as a basis and its columns as the associated vectors. We will employ this idea later in Chapter 3 for the discussion of local metric properties. At this moment, however, our goal is to reduce the 3D formulation to 2 dimensions only. To do this we have to eliminate the dependence on the third coordinate, and put some restriction on the redundant third basis vector:

$$S = \begin{pmatrix} & & 0 \\ S_2 & & \\ & 0 & \\ 0 & 0 & g_3 \end{pmatrix}, \quad \det S = g_3 \det S_2,$$

where S_2 is the 2×2 Jacobian matrix for a 2D map with columns (basis vectors in 2D) \mathbf{g}_1 and \mathbf{g}_2 . If we now set

$$g_3^2 = \frac{1}{2}\text{tr}(S_2^T S_2) = \frac{1}{2}(\mathbf{g}_1^2 + \mathbf{g}_2^2)$$

substituting in (2.5) we obtain

$$\beta_{3D}(S) = \frac{\left(\frac{1}{3}\text{tr}(S^T S)\right)^{3/2}}{\det S} = \frac{\left(\frac{1}{3}\text{tr}(S_2^T S_2) + \frac{g_3^2}{3}\right)^{3/2}}{g_3 \det S_2} = \frac{\frac{1}{2}\text{tr}(S_2^T S_2)}{\det S_2} = \beta_{2D}(S_2).$$

That is, the desired 2D restriction is achieved.

2.2 Interior and exterior penalty treatments

In the previous section we considered the mesh smoothing formulation for a given valid grid and, thus, defined all metrics for mappings with positive Jacobians only. Note, that formally we can extend the previous definitions for all mappings as follows by modifying E_θ so that

$$E_\theta(S) = +\infty, \text{ when } \det S \leq 0. \quad (2.16)$$

For example, on the degenerate and folded elements in Figure 2.2, the distortion metric is infinite $E_\theta = +\infty$.

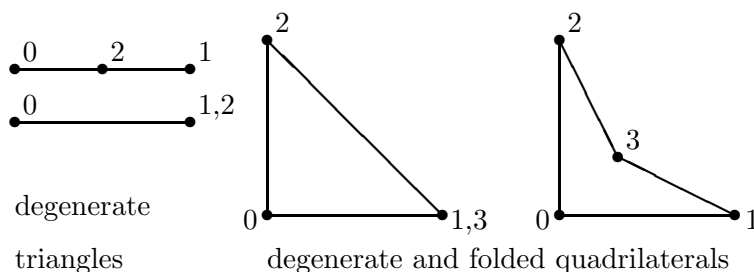


Figure 2.2: Degenerate and folded elements.

The total distortion functional \mathcal{I} takes the form of an internal or barrier penalty functional. That is, the functional penalizes a mesh with Jacobians close to zero, and does not accept any mesh with $\det S \leq 0$. This is an important property, which ensures that a result of smoothing (2.8) cannot contain any folded or degenerate elements.

However, in most practical applications requiring smoothing and correction of the mesh, the initial mesh can be folded or can contain nonconvex cells. The previous functional and minimization procedure cannot be applied directly to folded meshes, since the barrier

prevents correction of the folded mesh. In order to address the problem of invalid initial grids, the functional (2.8) can be modified to the form of an exterior penalty function [15, 70]. That is, the modified functional will penalize any folded mesh with negative Jacobians, while still accepting it.

The barrier in the original functional (2.8) is due to the presence of $\det S$ in the denominator of the integrand. An exterior penalty formulation can be developed by replacing this factor $\det S$ by a function $\chi_\varepsilon(\det S)$, such that $\chi_\varepsilon(x) \rightarrow x$ when $x > 0$, $\chi_\varepsilon(x) \rightarrow 0$ when $x \leq 0$, so the new integrand will be a finite approximation of the original infinite barrier. In the present work, we use the rational function [70]

$$\chi_\varepsilon(x) = \frac{x}{2} + \frac{1}{2}\sqrt{\varepsilon^2 + x^2} \quad (2.17)$$

since it has the properties

$$\begin{aligned} \chi_\varepsilon(x) &\approx x && \text{when } x \gg \varepsilon \\ \chi_\varepsilon(x) &\approx \frac{\varepsilon^2}{4x} && \text{when } x \rightarrow -\infty \\ \alpha &= \frac{\chi'_\varepsilon(x)x}{\chi_\varepsilon(x)} : |\alpha| \leq 1, \quad 0 \leq \frac{\chi''_\varepsilon(x)x^2}{\chi_\varepsilon(x)} \leq 1 - \alpha. \end{aligned} \quad (2.18)$$

The plot of this function and its reciprocal for $\varepsilon = 0.1$ is shown in Figure 2.3. We can see that for the positive values of argument x the function approximates x very well, and its reciprocal grows smoothly but fast with the decrease in $x < 0$.

Remark: A different approach, where an exponential penalty term is added to the objective function in order to give it a monotonically decreasing property with a single minimum, is considered for surface meshes in [35].

The formulation of the grid unfolding problem now becomes: minimize the functional

$$\mathcal{I}_\varepsilon = \int_{\hat{\Omega}} E_{\theta,\varepsilon}(S) d\vec{\xi}, \quad \text{where } E_{\theta,\varepsilon}(S) = \frac{\phi_\theta(S)}{\chi_\varepsilon(\det S)}, \quad (2.19)$$

where

$$\phi_\theta(S) = (1 - \theta) \left(\frac{1}{n} \text{tr}(S^T S) \right)^{n/2} + \frac{\theta}{2} (v + (\det S)^2/v), \quad (2.20)$$

subject to boundary or other constraints. This modification allows the minimization procedure to start from a folded grid, and since the value of the functional \mathcal{I}_ε is significantly

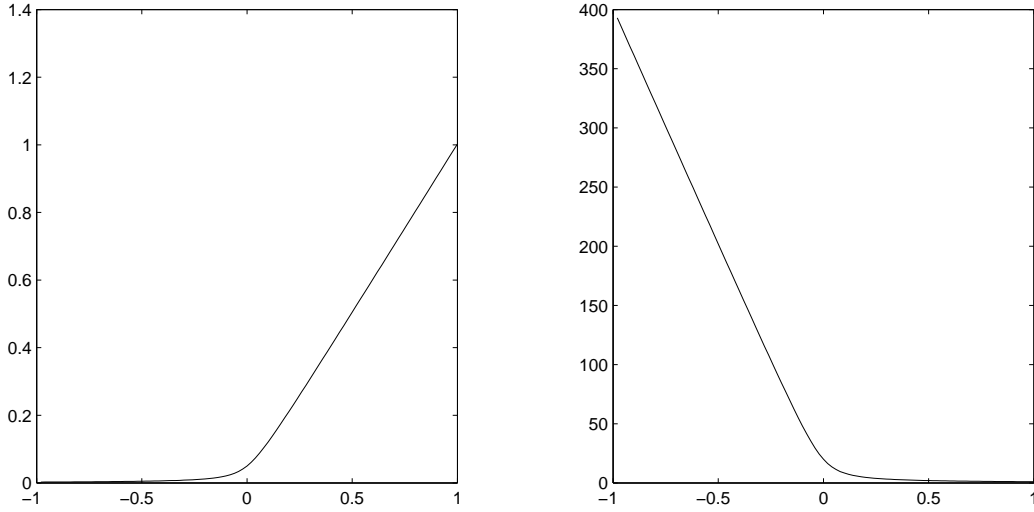


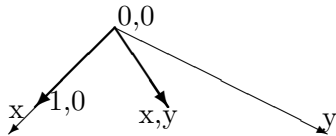
Figure 2.3: Functions $\chi_{0,1}(x)$ and $\chi_{0,1}^{-1}(x)$.

increased when folded cells are present in the grid, the final grid will not contain nonconvex cells (assuming there exists such a mesh solution for the given connectivity and boundary conditions).

The plot of values for the modified objective function $E_{\theta,\varepsilon}(S)$ in 2D with

$$S = \begin{pmatrix} 1 & x \\ 0 & y \end{pmatrix}$$

shown in Figure 2.4 demonstrates that function is monotone and convex. The simple form of the Jacobian matrix used for the plot corresponds, for example, to a corner basis of a quadrilateral cell with bilinear map, or to a linear triangle map with a right reference triangle (see Figure of the basis below). Thus, $y < 0$ corresponds to a reentrant corner of a quadrilateral cell, or to a triangle with negative area. We can observe that when $y < 0$ the modified objective function $E_{\theta,\varepsilon}$ takes a large value.



Note that once the grid is untangled the exterior penalty can be removed and the

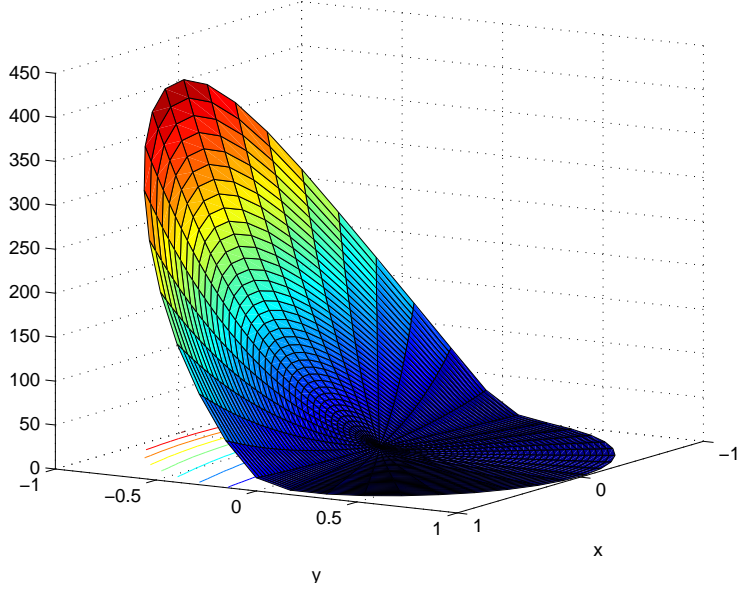


Figure 2.4: Objective function for grid untangling $E_{\theta,\varepsilon}$, $\theta = 0.5$, $\varepsilon = 0.1$, $v = 1$.

scheme is allowed to revert to the previous form with interior barrier penalty behavior. The natural barrier prevents “refolding”.

2.2.1 Euler-Lagrange equations for penalty formulation (2.19) in 2D.

We will concentrate our attention on the shape control part of the functionals, since only this part is responsible for the unfolding. As we already established, for the 2D variational problem

$$\min \mathcal{I}_\beta = \frac{1}{2} \int_{\hat{\Omega}} \frac{\text{tr}(S^T S)}{\det S} = \frac{1}{2} \int_{\Omega} ((\nabla \xi)^2 + (\nabla \eta)^2) dx dy$$

the corresponding Euler-Lagrange equations are

$$\Delta \xi = 0, \quad \Delta \eta = 0.$$

For the penalty formulation (2.19) of the same problem

$$\min \mathcal{I}_{\beta,\varepsilon} = \frac{1}{2} \int_{\hat{\Omega}} \frac{\text{tr} S^T S}{\chi_\varepsilon(\det S)} d\xi d\eta = \frac{1}{2} \int_{\Omega} D((\nabla \xi)^2 + (\nabla \eta)^2) dx dy$$

where $D = \det S / \chi_\varepsilon(\det S)$, the Euler-Lagrange equations become

$$\nabla \cdot (D \nabla \xi) = 0, \quad \nabla \cdot (D \nabla \eta) = 0. \quad (2.21)$$

(Note that for the change of variables under the integral we assume $\det S \neq 0$).

The diffusivity coefficient D influences mesh grading and has the following properties (with our choice of χ_ε):

- (1) $D \approx 1$ when $\det S \gg \varepsilon$,
- (2) $D \approx -4/\varepsilon^2$ when $\det S \rightarrow -\infty$ and
- (3) $D \rightarrow 0$ when $\det S \rightarrow 0$.

In [14] it was shown that a solution to diffusion problem (2.21) satisfies

$$D \det S = \text{const.} \quad (2.22)$$

Thus, in our case the situation (1) corresponds to the equidistributed grid, situation (2) - to mesh clustering, and situation (3) - to dilation of the mesh cells. This means that when we start the untangling procedure on a folded cell, it first shrinks to one point (situation (2)) and then dilates (situations (3) and (1)). The final size of the cell is determined by the size control part of the metric. This behavior is indeed observed in numerical tests in both 2D and 3D cases, as will be illustrated later in Chapter 5.

2.3 Discretization

In order to obtain a convenient discretized problem formulation from (2.8), let us introduce the vector of all grid node coordinates of a candidate mesh

$$\mathbf{R}^T = (\mathbf{X}_1^T, \dots, \mathbf{X}_n^T), \quad \mathbf{X}_i \in \mathbb{R}^N,$$

where N is the total number of grid nodes. From this vector we can extract, for each cell c in the mesh, the vector of coordinates of its $N_{c,v}$ vertices

$$\mathbf{X}_{c,i} = \mathcal{R}_c \mathbf{X}_i, \quad \mathcal{R}_c \in \mathbb{R}^{N_{c,v} \times N}.$$

The discretized form of the minimization problem (2.8) is then: find the solution to

$$\mathbf{R} = \arg \min_{\mathbf{R}} \mathcal{I}_h, \quad \mathcal{I}_h = \sum_{c=1}^{N_c} \sum_{q(c)=1}^{N_q} \sigma_{q(c)} E_\theta(S|_{q(c)}), \quad (2.23)$$

where contributions to the functional from each cell c are approximated using a numerical integration rule. Let the N_q discrete contributions to this integration rule from one cell be defined by indices $\{q(c)\}$. The rows of Jacobian matrix $S|_{q(c)}$ are computed as

$$S^T = (\mathbf{a}_1, \dots, \mathbf{a}_n), \quad \mathbf{a}_i|_{q(c)} = \mathcal{Q}_{q(c)} \mathcal{R}_c \mathbf{X}_i. \quad (2.24)$$

A set of matrices $\mathcal{Q}_{q(c)}$ and weights $\sigma_{q(c)}$ determine a numerical integration rule on a cell. The discretized functional for the untangling formulation (2.19) then becomes

$$\mathcal{I}_{h,\varepsilon} = \sum_{c=1}^{N_c} \sum_{q(c)=1}^{N_q} \sigma_{q(c)} \frac{\phi_\theta(S|_{q(c)})}{\chi_\varepsilon(\det S|_{q(c)})}. \quad (2.25)$$

We will discuss the discretization of boundary node constraints in Chapter 4.

The computational complexity for evaluating the discretized functional can be estimated as follows:

- a) computation of one Jacobian matrix $S|_{q(c)}$ requires computing n matrix-vector products of $n \times N_{c,v}$ matrix and $N_{c,v} \times 1$ vector (or $n^2 N_{c,v}$ multiplications and $n^2(N_{c,v} - 1)$ additions);
- b) computation of distortion metric $E_\theta(S|_{q(c)})$ requires a constant number of operations: 3 ($n = 2$) or 14 ($n = 3$) for $\det S|_{q(c)}$ and 16 ($n = 2$) or 30 ($n = 3$) for $E_\theta(S|_{q(c)})$;
- c) $N_q N_c$ multiplications and $N_q N_c - 1$ additions for estimating \mathcal{I}_h .

Thus, the total number of operations is of the order of $2n^2 N_c N_q N_{c,v}$.

Remarks:

1. The formulation can be applied to any unstructured grid including those containing different types of cells, using appropriate integration rules (see 4. below);
2. Unstructured grids will have varying nodal valence and this effect will also be investigated in the numerical work of Section 5.2;
3. The general formulation is written in n dimensions and, thus, is applied here for both 2D and 3D;
4. The rule for integration should be chosen consistent with the penalty form of the original functional, i.e. it has to enforce the barrier property of the discrete functional

so that the set of admissible shapes will not get larger for the discretized problem and we will not obtain invalid cells in the smoothed mesh.

Chapter 3

Local quality measure

In many recent optimization-based mesh improvement strategies the main component is a quality metric. (See references in Section 1.2). The properties of the metric impact the algorithm performance, and the rules for numerical approximation should be consistent with those desired properties. For example, it is important for numerical approximation of the metric to be able to detect all the elements forbidden by the associated quality metric.

Due to the constantly increasing interest in optimization-based mesh smoothing techniques, there is a growing literature on element quality metrics. The most extensively analyzed in terms of their quality are the common linear simplex elements: the 3-noded triangle and 4-noded tetrahedron. On these elements we perform a comparison analysis between our metric and other popular quality measures. There are fewer results for tensor-product and quadratically mapped elements, which, despite their practical value, are difficult to analyze, especially in 3D. A key goal of this chapter is to present an extensive study of the quality metric defined in Chapter 2 for several practical elements, as well as develop a consistent and efficient rule for computing its numerical analog (integral over the cell). In some instances our metric coincides with a quality measure known from the literature, and we will then only briefly mention its properties as established in the cited works. All other results are new and were obtained by the author.

For example, the function $\beta(S)$, reformulated in terms of invariants of the metric tensor of coordinate transformation $G = S^T S$, was considered in [4]. It was shown that $\beta(S)$ controls the cell angles and cell aspect ratio in the 2D case and has similar properties in 3D. The estimates for the angle α between two cell edges and cell aspect ratio F (ratio

of the lengths of the edges) for 2D quadrilateral cells are

$$\sin^2 \alpha \geq (1/\beta)^2, \quad 2 \leq F + 1/F \leq 4\beta^2 - 2.$$

Thus $\beta \rightarrow 1$ enforces $\alpha \rightarrow \pi/2$ and $F \rightarrow 1$; i.e. a square cell. The modified distortion measure E_θ retains these properties of $\beta(S)$. It is an indicator for quasi-isometry of the mapping [33, 34] - an analog of mapping conformality characterization, in the sense that

$$\gamma^2 I \leq S^T S \leq \Gamma^2 I,$$

where γ and Γ can be estimated from E_θ .

In the following sections, we examine the properties of the local distortion metric $E_\theta(S)$ or corresponding local quality measure $Q_\theta(S) = E_\theta^{-1}(S)$ ($Q_0(S) = \beta^{-1}(S)$) on basic 2D and 3D isoparametric elements given by linear and quadratic maps (which are most widely used in grid generation and for FE analysis).

3.1 Linear simplex elements

3.1.1 2D triangular element

Taking the reference element to be the equilateral triangle with sides of length 1 and vertices $\mathbf{m}_1, \mathbf{m}_2, \mathbf{m}_3$, the linear map onto an arbitrary triangular element with area A , edges of lengths l_1, l_2, l_3 , and vertices $\mathbf{v}_1, \mathbf{v}_2, \mathbf{v}_3$ (see Figure 3.1) can be expressed in terms of barycentric coordinates as

$$\begin{pmatrix} 1 \\ x \\ y \end{pmatrix} = \begin{pmatrix} 1 & 1 & 1 \\ \mathbf{v}_1 & \mathbf{v}_2 & \mathbf{v}_3 \end{pmatrix} \begin{pmatrix} 1 & 1 & 1 \\ \mathbf{m}_1 & \mathbf{m}_2 & \mathbf{m}_3 \end{pmatrix}^{-1} \begin{pmatrix} 1 \\ \xi \\ \eta \end{pmatrix} \quad (3.1)$$

Thus, the constant Jacobian matrix can be computed from the relation

$$\begin{pmatrix} x \\ y \end{pmatrix} = \mathbf{v}_1 + \xi(\mathbf{v}_2 - \mathbf{v}_1) + \eta \left(\frac{2\mathbf{v}_3 - \mathbf{v}_1 - \mathbf{v}_2}{\sqrt{3}} \right),$$

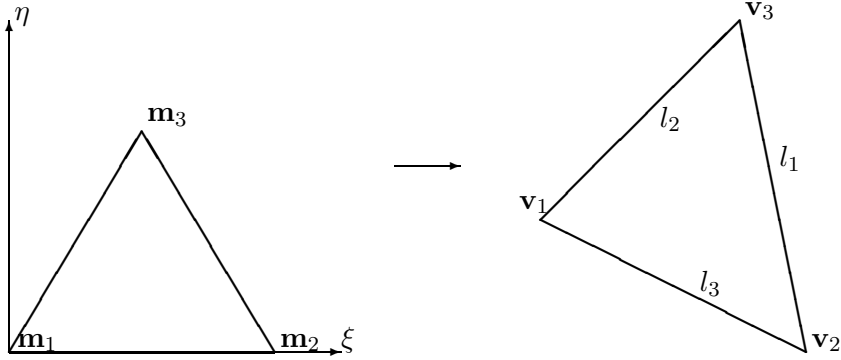


Figure 3.1: The linear map of the regular reference triangle onto an arbitrary triangle.

and we get

$$\det S = \frac{4}{\sqrt{3}}A, \quad \text{tr}(S^T S) = \frac{2}{3}(l_1^2 + l_2^2 + l_3^2).$$

The value of the distortion measure is

$$\beta = \frac{l_1^2 + l_2^2 + l_3^2}{4\sqrt{3}A}$$

so the quality measure Q_0 is

$$Q_0 = \frac{4\sqrt{3}A}{l_1^2 + l_2^2 + l_3^2}.$$

We see that the metric reduces here to a well known example [40, 57] of a “fair” geometric measure in the sense that it is equal to 0 on any type of degenerate triangle. It is also normalized (takes values from the interval $[0, 1]$).

The corresponding additive measure from (2.7) is

$$E_\theta = (1 - \theta) \frac{l_1^2 + l_2^2 + l_3^2}{4\sqrt{3}A} + \frac{\theta}{2} \left(\frac{\sqrt{3}}{4A} + \frac{4A}{\sqrt{3}} \right).$$

The level sets of the corresponding quality measure $Q_\theta = E_\theta^{-1}$ for a triangle with a fixed edge $(0, 0) - (0, 1)$ as a function of the coordinates (x, y) of the opposite vertex are shown in Figure 3.2 for different values of parameter θ . Each level set curve is given by the equation $Q_\theta(x, y) = \text{const}$. As θ increases, the quality measure becomes less restrictive in the sense that it admits more points in the regions $Q_\theta > \text{const}$, as can be seen by comparing the

“interior” areas for a given level curve in each graph of Figure 3.2. However, it remains a “fair” measure.

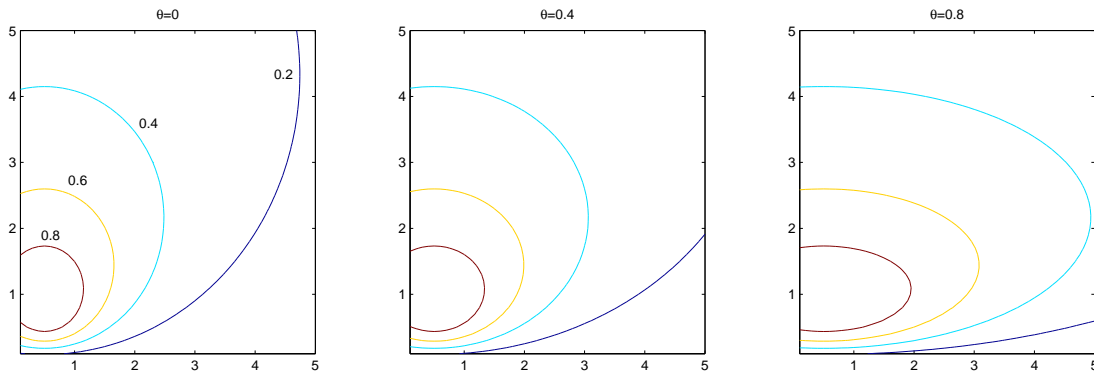


Figure 3.2: Level sets of $Q_\theta(x, y)$ on triangle with vertices $(0, 0), (0, 1), (x, y)$.

Comparison with other triangle shape distortion measures. Following the notion of quality measure equivalency introduced in [59], we now prove relationships of the form

$$c_0\beta^{e_0} \leq \alpha \leq c_1\beta^{e_1}, \text{ where } c_0, c_1, e_0, e_1 > 0,$$

where α is a distortion measure with values from $[1, \infty)$. These inequalities imply that both measures α and β go to infinity simultaneously $\alpha \rightarrow \infty \iff \beta \rightarrow \infty$, i.e. both measures detect the same types of degenerate elements. If the bound is tight, i.e. constant c_i is optimal (denoted by \leq^t), for example $\alpha \leq^t \beta$ then $\beta \rightarrow 1 \implies \alpha \rightarrow 1$. Thus, such quality measures are interchangeable if used in the mesh optimization methods.

Let us consider a triangle with area A , side lengths $l_1 \geq l_2 \geq l_3$, inradius r , circumradius R , shortest altitude h and smallest angle Θ . Then using our distortion measure for the triangle above,

$$\beta = \frac{\sum_{i=1}^3 l_i^2}{4\sqrt{3}A}$$

we can establish equivalency estimates of the form given with the metrics indicated in the left column of the Table 3.1. The derivations for the inequalities in Table 3.1 with respect to each of the 7 comparison measures are listed below:

Distortion metric	Equivalency estimates
$\alpha_1 = \frac{(\sum_{i=1}^3 l_i)^2}{12\sqrt{3}A},$ Watabayshi and Galt [71]	$\frac{1}{3}\beta \leq \alpha_1 \leq^t \beta$
$\alpha_2 = \frac{R}{2r},$ Cavendish, Field, Frey [50]	$\frac{\sqrt{3}}{6}\beta \leq \alpha_2 \leq^t \beta^2$
$\alpha_3 = \frac{l_1}{\sqrt{3}r}$	$\frac{2}{3}\beta \leq \alpha_3 \leq 3\beta$
$\alpha_4 = \frac{\sqrt{3}l_1}{2h},$ Suhara and Fukudo [72]	$\beta \leq^t \alpha_4 \leq 2\beta$
$\alpha_5 = \frac{\sqrt{\sum_{i=1}^3 l_i^2}}{2h}$	$\frac{\sqrt{3}}{3}\beta \leq \alpha_5 \leq \frac{3}{2}\beta$
$\alpha_6 = \frac{l_1}{l_3},$ not “fair” measure	$\alpha_6 \leq \frac{4\sqrt{3}}{3}\beta$
$\alpha_7 = \frac{\sqrt{3}}{2\sin\Theta},$ smallest angle	$\frac{1}{6}\beta \leq \alpha_7 \leq \frac{3}{2}\beta$

Table 3.1: Comparison of triangle distortion measures.

1. From the estimates

$$\sum_{i=1}^3 l_i^2 \leq \left(\sum_{i=1}^3 l_i\right)^2 \leq 3 \sum_{i=1}^3 l_i^2$$

we get

$$\beta/3 \leq \alpha_1 \leq \beta,$$

where the upper bound is tight.

2. For the radii, we have $r = 2A/\sum_{i=1}^3 l_i$ and $R = l_1 l_2 l_3 / 4A$. Since $l_1 l_2 l_3 \leq (\sum_{i=1}^3 l_i / 3)^3$ we get a tight estimate

$$\alpha_2 = \frac{l_1 l_2 l_3 (\sum_{i=1}^3 l_i)}{16A^2} \leq \frac{(\sum_{i=1}^3 l_i)^4}{16 \cdot 3^3 A^2} = \alpha_1^2 \leq \beta^2.$$

On the other hand, $R \geq l_i/2$ for $i = 1, 2, 3$, thus $R > (\sum_{i=1}^3 l_i)/6$ and

$$\alpha_2 \geq \frac{(\sum_{i=1}^3 l_i)^2}{24A} = \frac{\sqrt{3}}{2} \alpha_1 \geq \frac{\sqrt{3}}{6} \beta.$$

3. Using triangle inequality $l_1 < l_2 + l_3$ we get $l_1 < (\sum_{i=1}^3 l_i)/2$ and

$$\alpha_3 = \frac{l_1 (\sum_{i=1}^3 l_i)}{2\sqrt{3}A} \leq \frac{(\sum_{i=1}^3 l_i)^2}{4\sqrt{3}A} = 3\alpha_1 \leq 3\beta.$$

Also $l_1 \geq (\sum_{i=1}^3 l_i)/3$ and

$$\alpha_3 \geq 2\alpha_1 \geq 2/3\beta.$$

4. From $A = 1/2 l_1 h$ it follows that $\alpha_4 = \sqrt{3} l_1^2 / 4A$. Estimates $\sum_{i=1}^3 l_i^2 \leq 3l_1^2 \leq 2l_1^2 + (l_2 + l_3)^2 \leq 2 \sum_{i=1}^3 l_i^2$ lead to

$$\beta \leq \alpha_4 \leq 2\beta.$$

5. From 4., $\alpha_5 = l_1 \sqrt{\sum_{i=1}^3 l_i^2} / 4A$ and

$$\sqrt{\alpha_1 \beta} = \frac{(\sum_{i=1}^3 l_i) \sqrt{\sum_{i=1}^3 l_i^2}}{12A} < \alpha_5 < \frac{(\sum_{i=1}^3 l_i) \sqrt{\sum_{i=1}^3 l_i^2}}{8A} = 3/2 \sqrt{\alpha_1 \beta}.$$

Thus

$$\sqrt{3}/3\beta \leq \alpha_5 \leq 3/2\beta.$$

6. Since $l_3 \geq h$ we get

$$\alpha_6 \leq \frac{l_1}{h} = 2/\sqrt{3}\alpha_4 \leq 4\sqrt{3}/3\beta.$$

The lower bound inequality does not hold, since α_6 is not a “fair” measure. For example, let us consider a set of nearly degenerate triangles with one vertex approaching the middle of the opposite edge $\mathbf{v}_3 \rightarrow \frac{1}{2}(\mathbf{v}_1 + \mathbf{v}_2)$, where $\mathbf{v}_1 = (0, 0)$, $\mathbf{v}_2 = (1, 0)$. For these triangles $\alpha_6 \rightarrow 2$, $\beta \rightarrow +\infty$, and β cannot be used to bound α_6 from below. As we see, the existence of such a one sided relationship means that the distortion measure α_6 is not capable of detecting all cases of degeneracy, but those degeneracies that it does identify will be also detected by the measure β .

7. From $\sin \Theta = l_3/2R = 2A/l_1l_2$ and $2l_2 \geq l_2 + l_3 > l_1 \geq \frac{\sum_{i=1}^3 l_i}{3}$ it follows that

$$1/6\beta \leq \frac{3l_1^2}{2(\sum_{i=1}^3 l_i)^2} < \frac{3l_1l_2\beta}{\sum_{i=1}^3 l_i^2} = \alpha_7 = \frac{\sqrt{3}l_1l_2}{4A} \leq \frac{\sqrt{3}(l_1^2 + l_2^2)}{8A} \leq 3/2\beta.$$

The integration rule (recall representations (2.23), (2.24)) for triangular element is given by

$$\mathcal{Q} = \begin{pmatrix} -1 & 1 & 0 \\ -\frac{1}{\sqrt{3}} & -\frac{1}{\sqrt{3}} & \frac{2}{\sqrt{3}} \end{pmatrix}, \quad N_q = 1, \quad \sigma = 1.$$

Since the map is affine, the 1-point quadrature is exact and the numerical distortion metric is the same as the continuous metric.

3.1.2 3D tetrahedral element

We now extend these ideas to the tetrahedral element. For the mapping of the regular tetrahedral reference element with edges of length 1 and vertices $\mathbf{m}_1, \mathbf{m}_2, \mathbf{m}_3, \mathbf{m}_4$ onto an arbitrary tetrahedron with vertices $\mathbf{v}_1, \mathbf{v}_2, \mathbf{v}_3, \mathbf{v}_4$, volume V and edge lengths l_1, \dots, l_6 ,

(see Figure 3.3) we have

$$\begin{pmatrix} 1 \\ x \\ y \\ z \end{pmatrix} = \begin{pmatrix} 1 & 1 & 1 & 1 \\ \mathbf{v}_1 & \mathbf{v}_2 & \mathbf{v}_3 & \mathbf{v}_4 \end{pmatrix} \begin{pmatrix} 1 & 1 & 1 & 1 \\ \mathbf{m}_1 & \mathbf{m}_2 & \mathbf{m}_3 & \mathbf{m}_4 \end{pmatrix}^{-1} \begin{pmatrix} 1 \\ \xi_1 \\ \xi_2 \\ \xi_3 \end{pmatrix}. \quad (3.2)$$

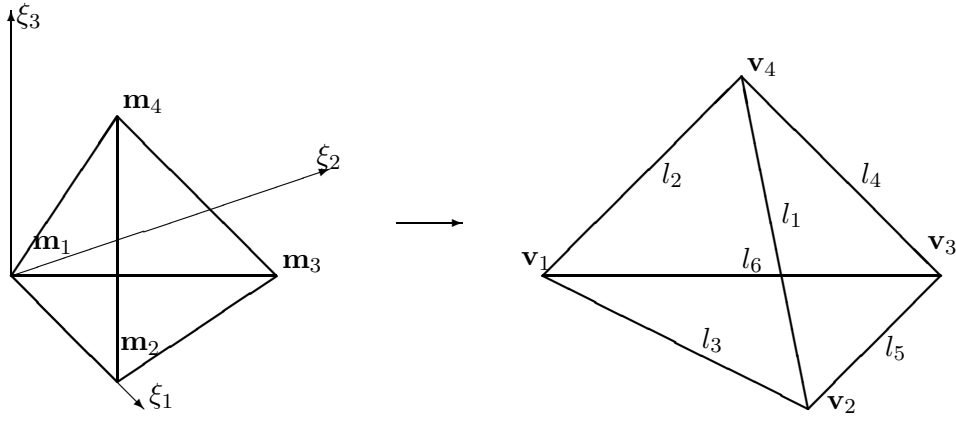


Figure 3.3: The linear map of the regular reference tetrahedron onto an arbitrary tetrahedron.

Thus

$$\begin{pmatrix} x \\ y \\ z \end{pmatrix} = \mathbf{v}_1 + \xi_1(\mathbf{v}_2 - \mathbf{v}_1) + \xi_2 \left(\frac{2\mathbf{v}_3 - \mathbf{v}_1 - \mathbf{v}_2}{\sqrt{3}} \right) + \xi_3 \left(\frac{3\mathbf{v}_4 - \mathbf{v}_1 - \mathbf{v}_2 - \mathbf{v}_3}{\sqrt{6}} \right)$$

and

$$\det S = 6\sqrt{2}V, \quad \text{tr}(S^T S) = \frac{1}{2} \sum_{i=1}^6 l_i^2.$$

For the corresponding quality measure and additive distortion-dilation measure respectively

we now get

$$Q_0 = \frac{72\sqrt{3}V}{\left(\sum_{i=1}^6 l_i^2\right)^{3/2}},$$

$$E_\theta = (1 - \theta) \frac{\left(\sum_{i=1}^6 l_i^2\right)^{3/2}}{72\sqrt{3}V} + \frac{\theta}{2} \left(\frac{1}{6\sqrt{2}V} + 6\sqrt{2}V \right),$$

with $Q_\theta = E_\theta^{-1}$. These are also “fair” measures in the sense given above. A related tetrahedron shape measure

$$\eta = \frac{12(3V)^{2/3}}{\sum_{i=1}^6 l_i^2} = (Q_0)^{2/3}$$

was derived in [58] from the singular values of transformation S . Geometrically η reflects the shape of the inscribed ellipsoid.

Comparison with other tetrahedron distortion measures. Let us consider a tetrahedron with volume V , face areas $S_i, i = 1, \dots, 4$, edge lengths $l_1 \geq \dots \geq l_6$, inradius r , circumradius R , and smallest solid angle Θ . Then using the distortion measure

$$\beta = \frac{\left(\sum_{i=1}^6 l_i^2\right)^{3/2}}{72\sqrt{3}V}$$

we can establish the estimates in Table 3.2. (In [59], the comparison analysis between measures $\eta = \beta^{-3/2}$, $\rho = \frac{r}{R}$ and Θ resulted in the estimates (1.5).) The derivations for the inequalities in Table 3.2 follow the same general idea as that seen previously for the triangle. For the 3 comparisons in Table 3.2 we have, in row order:

1. Follows from

$$\sum_{i=1}^6 l_i^2 \leq \left(\sum_{i=1}^6 l_i\right)^2 \leq 6 \sum_{i=1}^6 l_i^2.$$

2. The area of a triangle does not exceed the area of the equilateral triangle with the same perimeter, so

$$S_i \leq \sqrt{3}/36 P_i^2 = \sqrt{3}/4 ((l_{i1} + l_{i2} + l_{i3}/3)^2 \leq \sqrt{3}/12 (l_{i1}^2 + l_{i2}^2 + l_{i3}^2),$$

and

$$\sum_{i=1}^4 S_i^2 \leq (\sqrt{3}/12)^2 \sum_{i=1}^4 (l_{i1}^2 + l_{i2}^2 + l_{i3}^2)^2 \leq 1/12 \left(\sum_{i=1}^6 l_i^2\right)^2,$$

Distortion metric	Equivalency estimates
$\alpha = \frac{(\sum_{i=1}^6 l_i)^3}{6^4 \sqrt{2} V}$ <p>Dannelongue and Tanguy [53]</p>	$\frac{\sqrt{6}}{36} \beta \leq \alpha \leq \beta$
$\nu = \frac{(\sum_{i=1}^4 S_i^2)^3}{3^7 V^4},$ <p>Cougny, Shephard and Georges [21]</p>	$\frac{3\sqrt{3}}{16\sqrt{2}} \beta \leq \nu \leq 64\beta^4$
$\phi = \frac{l_1}{2\sqrt{6}r},$ <p>Baker [73]</p>	$\frac{\sqrt{3}}{4\sqrt{8}} \sqrt{\beta} \leq \phi \leq \frac{\sqrt{15}}{2} \beta$

Table 3.2: Comparison of tetrahedron distortion measures.

implies that

$$\nu \leq \frac{(1/12(\sum_{i=1}^6 l_i^2)^2)^3}{3^7 V^4} = 64\beta^4.$$

Using the estimate from [59]

$$\sum_{i=1}^4 S_i \geq 3\sqrt[4]{3}\sqrt{V}l_1$$

and $l_1^2 \geq 1/6 \sum_{i=1}^6 l_i^2$, we get

$$\sqrt{\sum_{i=1}^4 S_i^2} \geq 1/2 \sum_{i=1}^4 S_i \geq 3\sqrt[4]{3}/4\sqrt{V}l_1,$$

$$\sum_{i=1}^4 S_i^2 \geq \frac{9\sqrt{3}}{4} V \sqrt{1/6 \sum_{i=1}^6 l_i^2}$$

and, finally,

$$\nu \geq \frac{3\sqrt{3}}{16\sqrt{2}} \beta.$$

In [56] it was shown that the distortion measure ν is significantly sensitive to element distortions. In particular, it is able to characterize all types of poorly shaped tetrahedra, such as a “needle” element, “flat” element, “sliver” element, etc. The existence

of a two sided relationship between ν and β means that the measure β is also sensitive to all tetrahedral element distortions mentioned above.

3. The formula for the inradius is

$$r = \frac{3V}{\sum_{i=1}^4 S_i}, \text{ and from 2. } \sum_{i=1}^4 S_i \leq \sqrt{3}/6 \sum_{i=1}^6 l_i^2.$$

From triangle inequalities $l_1 < l_2 + l_3$, $l_1 < l_4 + l_5$ and $l_2 < l_4 + l_6$ we get $3l_1^2 < 5 \sum_{i=2}^6 l_i^2$ and thus $l_1 < \sqrt{5/8 \sum_{i=1}^6 l_i^2}$. Hence,

$$\phi = \frac{l_1(\sum_{i=1}^4 S_i)}{6\sqrt{6}V} \leq \sqrt{15}/2\beta.$$

On the other hand

$$\phi = \frac{l_1(\sum_{i=1}^4 S_i)}{6\sqrt{6}V} \geq \frac{3\sqrt[4]{3}l_1^{3/2}}{6\sqrt{6}V} \geq \frac{\sqrt[4]{3}}{\sqrt[4]{8}}\sqrt{\beta}.$$

The integration rule below for the tetrahedron is again exact:

$$\mathcal{Q} = \begin{pmatrix} -1 & 1 & 0 & 0 \\ -\frac{1}{\sqrt{3}} & -\frac{1}{\sqrt{3}} & \frac{2}{\sqrt{3}} & 0 \\ -\frac{1}{\sqrt{6}} & -\frac{1}{\sqrt{6}} & -\frac{1}{\sqrt{6}} & \frac{3}{\sqrt{6}} \end{pmatrix}, \quad N_q = 1, \quad \sigma = 1.$$

3.2 Maximum principle

In this section we formulate and prove a maximum principle for the metric $E_\theta(S)$, which helps in analyzing its behavior on elements with nonconstant Jacobian matrices.

In order to formulate the maximum principle property for the local additive measure E_θ we consider each $n \times n$ matrix as a collection of its columns

$$S = (S(\cdot, 1), S(\cdot, 2), \dots, S(\cdot, n)).$$

The general algebraic property of the additive measure is stated in the following Theorem.

Theorem 1 *Let an $n \times n$ matrix S have the following representation*

$$S = \sum_{j=1}^m S_j \Lambda_j, \quad \sum_{j=1}^m \Lambda_j = I, \quad \Lambda_j \geq 0, \quad (3.3)$$

where Λ_j are diagonal matrices. This can be equivalently written columnwise as

$$S(\cdot, i) = \sum_{j=1}^m S_j(\cdot, i) \lambda_{ij}, \quad \sum_{j=1}^m \lambda_{ij} = 1, \quad \lambda_{ij} \geq 0, \quad \forall i = 1, \dots, n.$$

Let us also introduce a multi-index $\alpha = (\alpha_1, \dots, \alpha_n)$ with $\alpha_i = 1, \dots, m$, and define “combinational matrices”

$$\tilde{S}_\alpha = (S_{\alpha_1}(\cdot, 1), S_{\alpha_2}(\cdot, 2), \dots, S_{\alpha_n}(\cdot, n)). \quad (3.4)$$

Then there exist coefficient functions $a_\alpha(\lambda_{ij}) : a_\alpha \geq 0, \sum_{\alpha=1}^{m^n} a_\alpha = 1$, such that

$$\det S = \sum_{\alpha=1}^{m^n} a_\alpha \det \tilde{S}_\alpha \geq \min_{\alpha} \det \tilde{S}_\alpha. \quad (3.5)$$

Moreover, for the additive metric E_θ , we have

$$E_\theta(S) \leq \max_{\alpha} E_\theta(\tilde{S}_\alpha), \quad (3.6)$$

and if $\min_{\alpha} \det \tilde{S}_\alpha > 0$ then there exist coefficient functions $b_\alpha(S) : b_\alpha \geq 0, \sum_{\alpha=1}^{m^n} b_\alpha = 1$, such that

$$E_\theta(S) \leq \sum_{\alpha=1}^{m^n} b_\alpha E_\theta(\tilde{S}_\alpha) \leq \max_{\alpha} E_\theta(\tilde{S}_\alpha). \quad (3.7)$$

Proof:

Note, that if the determinant of at least one “combinational matrix” is not positive $\det \tilde{S}_\alpha \leq 0$, then the Theorem statement

$$E_\theta(S) \leq \max_{\alpha} E_\theta(\tilde{S}_\alpha) = \infty$$

is trivial. So, we only need to consider the case $\min_{\alpha} \det \tilde{S}_\alpha > 0$. First we will state and prove two auxiliary lemmas, and then finish the proof of the Theorem.

Lemma 2 Let an $n \times n$ matrix S have the following representation

$$S = (1 - \xi)S_1 + \xi S_2, \quad 0 \leq \xi \leq 1 \quad (3.8)$$

and let $\det \tilde{S}_\alpha > 0$ for all the “combinational matrices”

$$\tilde{S}_\alpha = (S_{\alpha_1}(\cdot, 1), S_{\alpha_2}(\cdot, 2), \dots, S_{\alpha_n}(\cdot, n)),$$

where multi-index $\alpha = (\alpha_1, \dots, \alpha_n)$ with $\alpha_i = 1, 2$.

Then there exist coefficient functions $a_\alpha(\xi) : a_\alpha \geq 0, \sum_{\alpha=1}^{2^n} a_\alpha = 1$, such that

$$\det S = \sum_{\alpha=1}^{2^n} a_\alpha \det \tilde{S}_\alpha \geq \min_{\alpha} \det \tilde{S}_\alpha > 0; \quad (3.9)$$

and coefficient functions $b_\alpha(S) = \frac{a_\alpha \det \tilde{S}_\alpha}{\det S} \geq 0, \sum_{\alpha=1}^{2^n} b_\alpha = 1$, such that

$$\beta(S) \leq \sum_{\alpha=1}^{2^n} b_\alpha \beta(\tilde{S}_\alpha) \leq \max_{\alpha} \beta(\tilde{S}_\alpha). \quad (3.10)$$

Proof:

In order to prove the inequalities (3.10), (3.9) we will use the bisection argument.

1. Let us consider the case of $\xi = 1/2$. Then

$$\begin{aligned} \operatorname{tr}(S^T S) &= \operatorname{tr} \left(\left(\frac{1}{2}S_1 + \frac{1}{2}S_2 \right)^T \left(\frac{1}{2}S_1 + \frac{1}{2}S_2 \right) \right) \leq \frac{1}{2} \operatorname{tr}(S_1^T S_1) + \frac{1}{2} \operatorname{tr}(S_2^T S_2) = \\ &= \frac{1}{2^n} \sum_{\alpha} \operatorname{tr} (S_{\alpha_1}^T S_{\alpha_1}(\cdot, 1), S_{\alpha_2}^T S_{\alpha_2}(\cdot, 2), \dots, S_{\alpha_n}^T S_{\alpha_n}(\cdot, n)) = \\ &= \frac{1}{2^n} \sum_{\alpha} \operatorname{tr}(\tilde{S}_\alpha^T \tilde{S}_\alpha). \end{aligned}$$

Using the additivity of the determinant function with respect to the columns of a matrix, we get

$$\det S = \det \left(\frac{1}{2}S_1 + \frac{1}{2}S_2 \right) = \frac{1}{2^n} \sum_{\alpha} \det \tilde{S}_\alpha, \quad a_\alpha \left(\frac{1}{2} \right) = \frac{1}{2^n}, \quad \det S \geq \min_{\alpha} \det \tilde{S}_\alpha.$$

Let us consider the following inequality

$$\left(\frac{1}{n2^n} \sum_{\alpha} \operatorname{tr}(\tilde{S}_\alpha^T \tilde{S}_\alpha) \right)^{n/2} \leq \frac{1}{2^n} \sum_{\alpha} \left(\frac{1}{n} \operatorname{tr}(\tilde{S}_\alpha^T \tilde{S}_\alpha) \right)^{n/2}. \quad (3.11)$$

After introduction of the following notations: $q = n/2$, $N = 2^n$, $x_\alpha = \frac{1}{n} \text{tr}(\tilde{S}_\alpha^T \tilde{S}_\alpha)$ the above inequality (3.11) takes a form of the Holder inequality

$$\sum_{\alpha=1}^N |x_\alpha y_\alpha| \leq \left(\sum_{\alpha=1}^N y_\alpha^p \right)^{1/p} \left(\sum_{\alpha=1}^N x_\alpha^q \right)^{1/q},$$

where $y_\alpha = 1 \forall \alpha$, $1/p + 1/q = 1$. Thus, we get

$$\beta(S) \det S = \left(\frac{1}{n} \text{tr}(S^T S) \right)^{n/2} \leq \frac{1}{2^n} \sum_{\alpha} \left(\frac{1}{n} \text{tr}(\tilde{S}_\alpha^T \tilde{S}_\alpha) \right)^{n/2} = \frac{1}{2^n} \sum_{\alpha} \beta(\tilde{S}_\alpha) \det \tilde{S}_\alpha,$$

and, finally

$$\beta(S) \leq \sum_{\alpha} b_\alpha \beta(\tilde{S}_\alpha), \quad b_\alpha = \frac{\det \tilde{S}_\alpha}{\sum_{\alpha} \det \tilde{S}_\alpha} = \frac{\det \tilde{S}_\alpha}{2^n \det S}.$$

2. Let us now take any $\xi \in [0, 1]$.

a) Let us bisect the interval $[0, 1]$; then at the middle point $\xi_1 = 1/2$ we get a matrix $S_3 = S(\xi_1) = \frac{1}{2}(S_1 + S_2)$. Let us denote by $[l_1, r_1]$ the half of the interval containing ξ : $\xi \in [l_1, r_1]$ and assume, without loss of generality, that this interval is $[l_1, r_1] = [0, 1/2]$.

Then, using item 1. of this proof, we get

$$\begin{aligned} \beta(S|_{\frac{1}{4}}) \det S|_{\frac{1}{4}} &= \beta\left(\frac{1}{2}S_1 + \frac{1}{2}S_3\right) \det\left(\frac{1}{2}S_1 + \frac{1}{2}S_3\right) \leq \frac{1}{2^n} \sum_{\chi, \chi_i=1 \text{ or } 3} \beta(\tilde{S}_\chi) \det \tilde{S}_\chi \\ &= \frac{1}{2^n} \sum_{\chi, \chi_i=1 \text{ or } 2} \beta\left(\frac{1}{2}S_1 + \frac{1}{2}\tilde{S}_\chi\right) \det\left(\frac{1}{2}S_1 + \frac{1}{2}\tilde{S}_\chi\right) = \\ &\leq \frac{1}{2^n} \sum_{\chi} \frac{1}{2^n} \sum_{\zeta, \zeta_i=1 \text{ or } \chi_i} \beta(\tilde{S}_\zeta) \det \tilde{S}_\zeta = \sum_{\alpha} a_\alpha \beta(\tilde{S}_\alpha) \det \tilde{S}_\alpha, \end{aligned}$$

where \tilde{S}_α is determined from two multi-indices χ and ζ and consists of the columns of matrices S_1 and S_2 , and

$$\det S|_{\frac{1}{4}} = \frac{1}{2^n} \sum_{\chi} \frac{1}{2^n} \sum_{\zeta, \zeta_i=1 \text{ or } \chi_i} \det(S_{\zeta_1}(\cdot, 1), \dots, S_{\zeta_n}(\cdot, n)) = \sum_{\alpha} a_\alpha \left(\frac{1}{4}\right) \det \tilde{S}_\alpha.$$

Thus,

$$\beta(S|_{\frac{1}{4}}) \leq \sum_{\alpha} b_\alpha \beta(\tilde{S}_\alpha), \quad b_\alpha = \frac{a_\alpha \det \tilde{S}_\alpha}{\sum_{\alpha} a_\alpha \det \tilde{S}_\alpha}.$$

b) Let us bisect the interval $[l_1, r_1]$ and continue the reasoning in item a). Continuing the bisection, we will obtain two sequences of points $\{l_i\}_1^\infty$ and $\{r_i\}_1^\infty$, such that

$l_i \rightarrow \xi$ from the left and $r_i \rightarrow \xi$ from the right as $i \rightarrow \infty$. Using the additivity of the determinant function with respect to the columns of a matrix, we compute the coefficients

$$a_\alpha(\xi) = \xi^{(\# \text{ of } \alpha_j=1, j=1, \dots, n)} (1 - \xi)^{(\# \text{ of } \alpha_j=2, j=1, \dots, n)}$$

in the formula for $\det S = J(\xi)$ at a point ξ :

$$J(\xi) = \det(\xi S_1 + (1 - \xi) S_2) = \sum_{\alpha} a_\alpha(\xi) \det \tilde{S}_\alpha.$$

Due to the continuity of the determinant we get

$$\lim_{i \rightarrow \infty} J(l_i) = \lim_{i \rightarrow \infty} \sum_{\alpha} a_\alpha(l_i) \det \tilde{S}_\alpha = \sum_{\alpha} a_\alpha(\xi) \det \tilde{S}_\alpha, \quad \lim_{i \rightarrow \infty} a_\alpha(l_i) = a_\alpha(\xi).$$

Since the function $\beta(\xi)$ is continuous and $\beta(l_i) \leq \sum_{\alpha} (a_\alpha(l_i) \det \tilde{S}_\alpha / J(l_i)) \beta(\tilde{S}_\alpha) \forall i$, we have

$$\begin{aligned} \lim_{i \rightarrow \infty} \beta(l_i) &\leq \sum_{\alpha} \beta(\tilde{S}_\alpha) \lim_{i \rightarrow \infty} (a_\alpha(l_i) \det \tilde{S}_\alpha / J(l_i)) = \\ &= \sum_{\alpha} \beta(\tilde{S}_\alpha) (a_\alpha(\xi) \det \tilde{S}_\alpha / J(\xi)). \quad \blacksquare \end{aligned}$$

Lemma 3 *Let an $n \times n$ matrix S have the following representation*

$$S = \sum_{j=1}^m S_j \Lambda_j, \quad \sum_{j=1}^m \Lambda_j = I, \quad \Lambda_j \geq 0, \quad (3.12)$$

where Λ_j are diagonal matrices, which can be equivalently written columnwise as

$$S(\cdot, i) = \sum_{j=1}^m S_j(\cdot, i) \lambda_{ij}, \quad \sum_{j=1}^m \lambda_{ij} = 1, \quad \lambda_{ij} \geq 0, \quad \forall i = 1, \dots, n.$$

Let $\det \tilde{S}_\alpha > 0$ for all the “combinational matrices”

$$\tilde{S}_\alpha = (S_{\alpha_1}(\cdot, 1), S_{\alpha_2}(\cdot, 2), \dots, S_{\alpha_n}(\cdot, n)), \quad (3.13)$$

where multi-index $\alpha = (\alpha_1, \dots, \alpha_n)$ with $\alpha_i = 1, \dots, m$.

Then there exist coefficient functions $a_\alpha(\lambda_{ij}) : a_\alpha \geq 0, \sum_{\alpha=1}^{m^n} a_\alpha = 1$, such that

$$\det S = \sum_{\alpha=1}^{m^n} a_\alpha \det \tilde{S}_\alpha \geq \min_{\alpha} \det \tilde{S}_\alpha > 0; \quad (3.14)$$

and coefficient functions $b_\alpha(S) = \frac{a_\alpha \det \tilde{S}_\alpha}{\det S} \geq 0$, $\sum_{\alpha=1}^{m^n} b_\alpha = 1$, such that

$$\beta(S) \leq \sum_{\alpha=1}^{m^n} b_\alpha \beta(\tilde{S}_\alpha) \leq \max_{\alpha} \beta(\tilde{S}_\alpha). \quad (3.15)$$

Proof:

1. Let us prove the statement for the case $\Lambda_j = \lambda_j I$, $j = 1, \dots, m$ by induction:

- a) For $m = 2$ the statement is proved in Lemma 2;
- b) Let the statement of Lemma 3 be true for $m = k$;
- c) Let us prove it for $m = k + 1$. Then

$$S = \sum_{j=1}^{k+1} \lambda_j S_j = (1 - \lambda_{k+1}) \sum_{j=1}^k f_j S_j + \lambda_{k+1} S_{k+1},$$

where coefficients $f_j = \lambda_j / \sum_{t=1}^k \lambda_t$. Introducing the notation $S_Q = \sum_{j=1}^k f_j S_j$, the inequalities (3.15), (3.14) hold for matrix S_Q by induction argument b). Each “combinational matrix” produced from columns of two matrices S_Q and S_{k+1} can be written as

$$\tilde{S}_{\chi, \chi_i=Q \text{ or } k+1} = \sum_{j=1}^k f_j \tilde{S}_{\alpha, \alpha_i=j \text{ or } k+1},$$

where matrices \tilde{S}_α are the “combinational matrices” in (3.13) produced from all S_j , $1 \leq j \leq m$. Thus, from the induction argument b) we have

$$\beta(\tilde{S}_{\chi, \chi_i=Q \text{ or } k+1}) = \beta \left(\sum_{j=1}^k f_j \tilde{S}_{\alpha, \alpha_i=j \text{ or } k+1} \right) \leq \sum_{\nu} \frac{a_\nu \det \tilde{S}_\nu \beta(\tilde{S}_\nu)}{\det \tilde{S}_{\chi, \chi_i=Q \text{ or } k+1}}$$

and $\det \tilde{S}_{\chi, \chi_i=Q \text{ or } k+1} \geq \min_{\nu} \det \tilde{S}_\nu$. Finally, we demonstrated that matrices S_Q and S_{k+1} satisfy the conditions of Lemma 2 and thus for $\forall \lambda$, $0 \leq \lambda \leq 1$ the inequality

$$\begin{aligned} \beta(S) \det S &\leq \sum_{\chi} a_\chi \beta(\tilde{S}_{\chi, \chi_i=Q \text{ or } k+1}) \det(\tilde{S}_{\chi, \chi_i=Q \text{ or } k+1}) \leq \\ &\leq \sum_{\chi} a_\chi \sum_{\nu} a_\nu \det \tilde{S}_\nu \beta(\tilde{S}_\nu) = \sum_{\nu'} a_{\nu'} \det \tilde{S}_{\nu'} \beta(\tilde{S}_{\nu'}), \\ \det S &= \sum_{\chi} a_\chi \det \tilde{S}_{\chi, \chi_i=Q \text{ or } k+1} = \sum_{\chi} a_\chi \sum_{\nu} a_\nu \det \tilde{S}_\nu = \sum_{\nu'} a_{\nu'} \det \tilde{S}_{\nu'}. \end{aligned}$$

2. The case $m = 2$ can be reduced to the case of item 1. above after rewriting the linear combination of two matrices $S = S_1(I - \Lambda) + S_2\Lambda$, $\Lambda = \text{diag}(\lambda_i)$ in terms of their “combinational matrices”

$$S = \sum_{\alpha_1, \dots, \alpha_n=1}^2 (1 - \lambda_1)^{2-\alpha_1} \lambda_1^{\alpha_1-1} \dots (1 - \lambda_n)^{2-\alpha_n} \lambda_n^{\alpha_n-1} \tilde{S}_\alpha.$$

3. The case of $m > 2$ is proved by induction in a manner similar to item 1. ■

From the Lemma 3 we have

$$\det S = \sum_{\alpha=1}^{m^n} a_\alpha \det \tilde{S}_\alpha \geq \min_{\alpha} \det \tilde{S}_\alpha > 0;$$

where $a_\alpha(\lambda_{ij}) : a_\alpha \geq 0$, $\sum_{\alpha=1}^{m^n} a_\alpha = 1$, and

$$\beta(S) \leq \sum_{\alpha=1}^{m^n} b_\alpha \beta(\tilde{S}_\alpha) \leq \max_{\alpha} \beta(\tilde{S}_\alpha),$$

where $b_\alpha(S) = \frac{a_\alpha \det \tilde{S}_\alpha}{\det S} \geq 0$, $\sum_{\alpha=1}^{m^n} b_\alpha = 1$. It remains to show that inequality

$$\mu(S) \leq \sum_{\alpha} b_\alpha \mu(\tilde{S}_\alpha)$$

holds for the function $\mu(S) = \frac{1}{2} (\det S/v + v/\det S)$. This inequality is equivalent to

$$1 + \frac{(\det S)^2}{v^2} \leq \frac{\det S}{v} \sum_{\alpha} \frac{a_\alpha \det \tilde{S}_\alpha}{\det S} \left(\frac{\det \tilde{S}_\alpha}{v} + \frac{v}{\det \tilde{S}_\alpha} \right) = \sum_{\alpha} a_\alpha \left(1 + \frac{(\det \tilde{S}_\alpha)^2}{v^2} \right)$$

or $\left(\sum_{\alpha} a_\alpha \det \tilde{S}_\alpha \right)^2 \leq \sum_{\alpha} a_\alpha (\det \tilde{S}_\alpha)^2$. The last inequality takes form of the Cauchy inequality

$$(\mathbf{x}^T \mathbf{y})^2 \leq (\mathbf{x}^T \mathbf{x})(\mathbf{y}^T \mathbf{y})$$

after introduction of the notations $x_\alpha = \sqrt{a_\alpha}$, $y_\alpha = \sqrt{a_\alpha} \det \tilde{S}_\alpha$, $\forall \alpha = 1, \dots, m^n$.

Thus,

$$E_\theta(S) = (1 - \theta)\beta(S) + \theta\mu(S) \leq \sum_{\alpha=1}^{m^n} b_\alpha E_\theta(\tilde{S}_\alpha) \leq \max_{\alpha} E_\theta(\tilde{S}_\alpha)$$

for any $0 \leq \theta < 1$. ■

In application to finite-element grids defined by mappings, this property implies that if the Jacobian matrix of a map can be presented in the form (3.3), as in the case of tensor product linear elements or simplex quadratic elements as considered below, then the following important results follow

1. The value of additive metric E_θ at any point in the cell is bounded from above (and thus controlled) by the finite linear combination of its values on “combinational matrices”, which are easy to compute. Thus, we obtain a practical rule for computing the element quality indicator.
2. The formula for computation of the Jacobian determinant in (3.5) readily supplies a sufficient condition for such local map nondegeneracy:

$$\det \tilde{S}_\alpha > 0 \quad \forall \alpha \Rightarrow \det S > 0. \quad (3.16)$$

3. After uniform refinement of a grid, the upper bound on E_θ will remain unchanged (provided the constants v are computed properly for each grid).
4. The “consistent” rule (in the sense defined earlier) for integration of the distortion measure over such an element is:

$$\int_{\hat{\Omega}_c} E_\theta(S) d\vec{\xi} \approx \sum_{\alpha} \sigma_{\alpha} E_\theta(\tilde{S}_{\alpha}), \quad (3.17)$$

with constant weights $\sigma_{\alpha} > 0$, $\sum_{\alpha} \sigma_{\alpha} = 1$. In the algorithm, implementation this rule would require computation of all $|\alpha|$ “combinational matrices” on each element and evaluation of the distortion measure E_θ on them. The weights can be set, for example, to provide exact computation of the area of the reference element $\int_{\hat{\Omega}_c} \det S d\vec{\xi}$ using this rule. If all “combinational matrices” \tilde{S}_{α} are used in the integral approximation (i.e. all weights are nonzero) then, as a consequence of (3.6), the value of the discrete functional will control (bound) the value of the original functional (2.8)

$$\begin{aligned} \mathcal{I} &= \sum_c \int_{\hat{\Omega}_c} E_\theta(S) d\vec{\xi} \leq \sum_c \sum_{\alpha} \left(\int_{\hat{\Omega}_c} b_{\alpha}(S) d\vec{\xi} \right) E_\theta(\tilde{S}_{\alpha}) \leq \\ &\leq \frac{1}{\min \sigma_{\alpha}} \sum_c \sum_{\alpha} \sigma_{\alpha} E_\theta(\tilde{S}_{\alpha}) = \frac{\mathcal{I}_h}{\min \sigma_{\alpha}}. \end{aligned}$$

We will examine this bound later in this chapter on several types of elements. In the case of meshes with piecewise constant Jacobian determinant ($\det S = \text{const}$ on each cell) $\mathcal{I} = \mathcal{I}_h$.

3.3 Tensor product linear elements

The case of the mapped tensor product linear cell in n dimensions is more complex than the case of simplices, since the Jacobian matrix, and hence the additive measure E_θ , are not constant on the cell. Nevertheless, by employing the maximum principle, we can always compute an upper bound for the additive measure (lower bound for quality measure). “Combinational matrices” for this bound are a full set of constant matrices arising from a representation of the Jacobian matrix on the tensor product cell. We will consider this in general and then illustrate it in the 2D and 3D cases.

The map of a unit hypercube $0 \leq \xi_1, \dots, \xi_n \leq 1$ onto the tensor product linear cell with vertices \mathbf{r}_ν , where multi-index $\nu = (\nu_1, \dots, \nu_n)$, $\nu_i = 0, 1$ defines a binary node numbering, can be written as

$$\mathbf{r} = \sum_{\nu} (1 - \xi_1)^{(1-\nu_1)} \xi_1^{\nu_1} \dots (1 - \xi_n)^{(1-\nu_n)} \xi_n^{\nu_n} \mathbf{r}_\nu \quad (3.18)$$

and columns of its Jacobian matrix are

$$S(\cdot, i) = \sum_{\nu} (1 - \xi_1)^{(1-\nu_1)} \xi_1^{\nu_1} \dots (1 - \xi_{i-1})^{(1-\nu_{i-1})} \xi_{i-1}^{\nu_{i-1}} (-1)^{1-\nu_i} \quad (3.19)$$

$$(1 - \xi_{i+1})^{(1-\nu_{i+1})} \xi_{i+1}^{\nu_{i+1}} \dots (1 - \xi_n)^{(1-\nu_n)} \xi_n^{\nu_n} \mathbf{r}_\nu.$$

Clearly, this representation of the Jacobian matrix is equivalent to the form (3.3), where the sum contains $m = 2^{n-1}$ terms. Each such term in the i^{th} column representation is a difference between position vectors of two cell vertices

$$\mathbf{r}(\nu_1, \dots, \nu_{i-1}, 1, \nu_{i+1}, \dots, \nu_n) - \mathbf{r}(\nu_1, \dots, \nu_{i-1}, 0, \nu_{i+1}, \dots, \nu_n)$$

and can be sought as an i^{th} basis vector, corresponding to the edge basis vector on the reference element. Thus, the upper bound for additive measure requires calculation of E_θ

on all $m^n = 2^{n(n-1)}$ bases that can be composed from the set of edge basis vectors. The computational complexity for evaluating this bound includes m Jacobian matrix evaluations and m^n evaluations of the distortion measure, which gives 120 operations for $n = 2$ and 2460 operations for $n = 3$ (68 and 1436 operations correspondingly for evaluation of the Jacobian determinants only for the mapping nondegeneracy conditions).

3.3.1 2D quadrilateral element

For the bilinear cell (see Figure 3.4), the “combinational matrices” correspond to all vertex bases of the quadrilateral cell. Thus, from (3.16) we obtain a sufficient condition for the bilinear map nondegeneracy - Jacobians positive at all four vertices - which is well known [74] to be both a necessary and sufficient condition for invertibility of a bilinear cell. For the metric we get

$$E_\theta \leq \sum_{j,k=0}^1 b_{jk} E_\theta(\tilde{S}_{jk}) \leq \max_{j,k} E_\theta(\tilde{S}_{jk}).$$

From the binary indices introduced above we can define the local numbering of cell vertices conveniently as follows (see also Figure 3.4):

$$\mathbf{r}_{j,k} = \mathbf{r}(2k + j).$$

Employing this numbering and recalling (3.18), the rule for metric integration over a

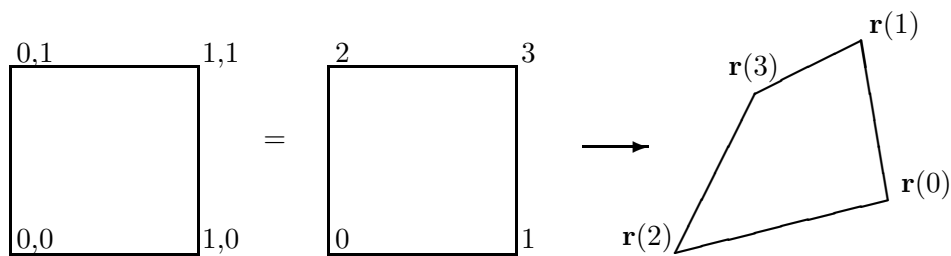


Figure 3.4: Bilinear map and local numbering of vertices.

bilinear element is defined by

$$\mathcal{Q}_0 = \begin{pmatrix} -1 & 1 & 0 & 0 \\ -1 & 0 & 1 & 0 \end{pmatrix}, \quad \mathcal{Q}_1 = \begin{pmatrix} -1 & 1 & 0 & 0 \\ 0 & -1 & 0 & 1 \end{pmatrix},$$

$$\mathcal{Q}_2 = \begin{pmatrix} 0 & 0 & -1 & 1 \\ -1 & 0 & 1 & 0 \end{pmatrix}, \quad \mathcal{Q}_3 = \begin{pmatrix} 0 & 0 & -1 & 1 \\ 0 & -1 & 0 & 1 \end{pmatrix},$$

$$N_q = 4, \quad \sigma = 1/4.$$

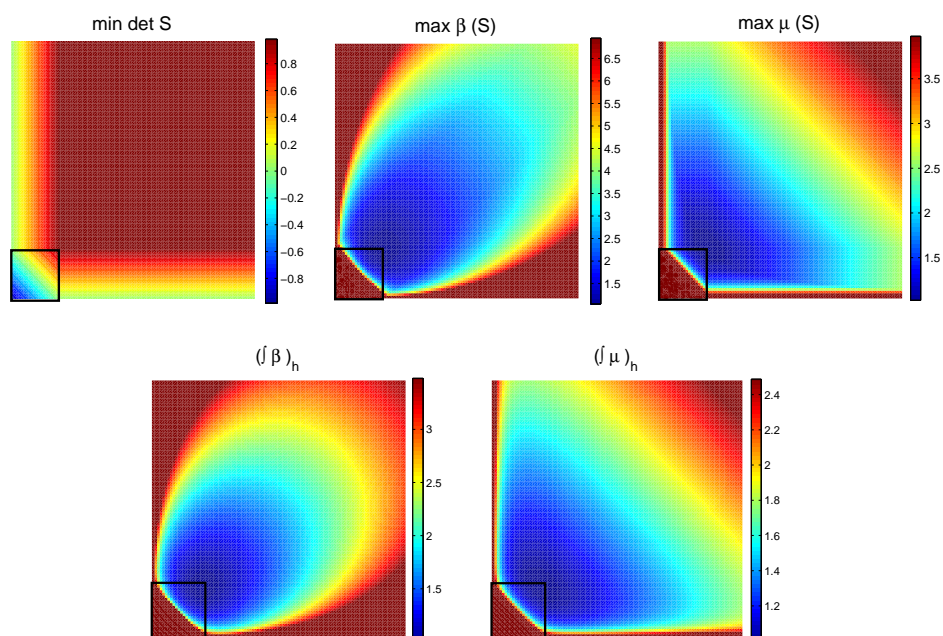


Figure 3.5: Level sets on quadrilateral element with vertices $(0, 0), (0, 1), (1, 0), (x, y)$.

Figure 3.5 illustrates properties of the metric E_θ and its approximation on the bilinear element. The color map in the Figure represents level sets for the minimum value of the Jacobian determinant, maximum values of shape distortion β and dilation metric μ , as well as numerical approximations of respective parts of the cell total “energy” (recall the

elasticity analogy) $(\int \beta(S))_h = \sum_{\alpha} \sigma_{\alpha} \beta(\tilde{S}_{\alpha})$ and $(\int \mu(S))_h = \sum_{\alpha} \sigma_{\alpha} \mu(\tilde{S}_{\alpha})$, as functions of the position (x, y) of node 3 for deviation from a regular square element. From this Figure we can see that, up to a scaling constant, level sets of the approximation to the total cell distortion nearly coincide with those of the metric maximum. The boundaries of level sets for numerical distortion are smoother than those for the maximum values, thus the numerical approximation is a little more restrictive in terms of acceptable element shapes.

3.3.2 3D hexahedral element

For a trilinear cell (Figure 3.6), the representation of the Jacobian matrix can be computed from trilinear images of the edge basis triples in reference space. All 64 basis triples can be

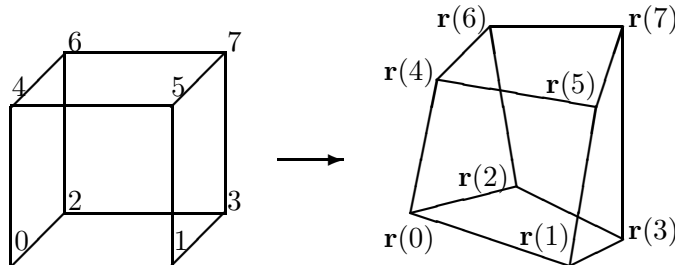


Figure 3.6: Trilinear map.

obtained from the four distinct vector triples shown in Figure 3.7 by rotation and reflection (after reflection the orientation should be changed to preserve the initial “right” basis triple orientation).

Nondegeneracy of the trilinear map (recall (3.16)) is guaranteed (sufficiency) by checking positivity of 27 expressions containing combinations of Jacobians of all 64 edge bases. These conditions include positive Jacobians at all eight vertices of the cell, positive sum of Jacobians of all bases of type IV, and positive combinations of Jacobians of bases of types II and III, which are schematically illustrated in Figure 3.8. The general problem of determining the set of conditions that are both necessary and sufficient for the trilinear map nondegeneracy remains an open question.

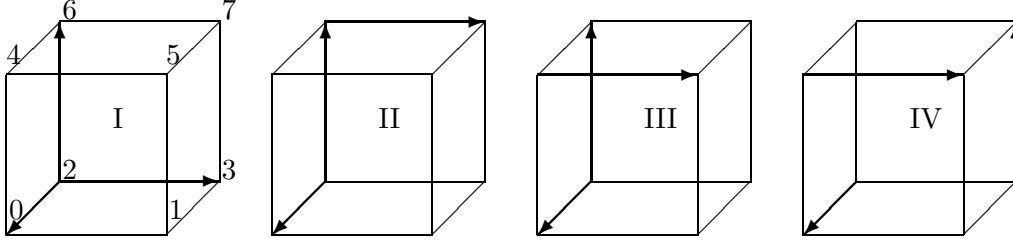


Figure 3.7: Types of basis triples for computation of bounds for E_θ and $\det S$ on trilinear element.

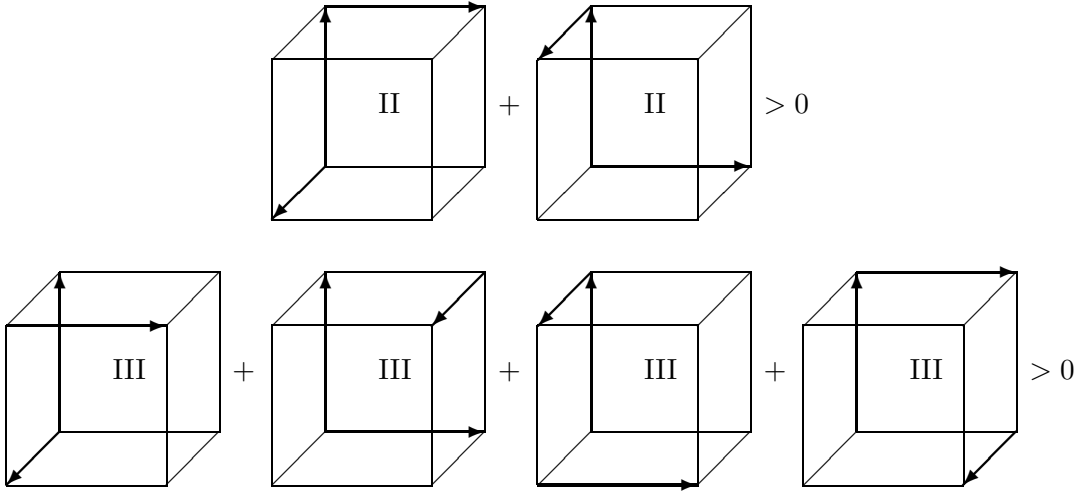


Figure 3.8: Types of basis triples in sufficient nondegeneracy condition for trilinear element.

The integration rule for the metric on a trilinear cell is defined here by

$$N_q = 64, \sigma_I = \frac{1}{27}, \sigma_{II} = \frac{1}{(2) \cdot (27)}, \sigma_{III} = \frac{1}{(4) \cdot (27)}, \sigma_{IV} = \frac{1}{(8) \cdot (27)},$$

where weights correspond to basis types shown in Figure 3.7 and matrices $\{Q_{q(c)}\}$ are easy to compute.

3.3.3 Prisms

Let us consider a prismatic cell in 3D defined by the tensor product map of a 2D triangular basis and linear map in the third direction. If we take the reference prism element to

be defined by a regular triangle as its base with vertical height 1, then the map onto an arbitrary prism with vertices $\mathbf{v}_1, \dots, \mathbf{v}_6$ is (see Figure 3.9)

$$\begin{aligned} \mathbf{r}(\vec{\xi}) &= (1 - \xi_3) \left(\mathbf{v}_1 + \xi_1(\mathbf{v}_2 - \mathbf{v}_1) + \xi_2 \left(\frac{2\mathbf{v}_3 - \mathbf{v}_1 - \mathbf{v}_2}{\sqrt{3}} \right) \right) \\ &+ \xi_3 \left(\mathbf{v}_4 + \xi_1(\mathbf{v}_5 - \mathbf{v}_4) + \xi_2 \left(\frac{2\mathbf{v}_6 - \mathbf{v}_4 - \mathbf{v}_5}{\sqrt{3}} \right) \right). \end{aligned} \quad (3.20)$$

The columns of the Jacobian matrix for this map can be written in the form (3.3) as

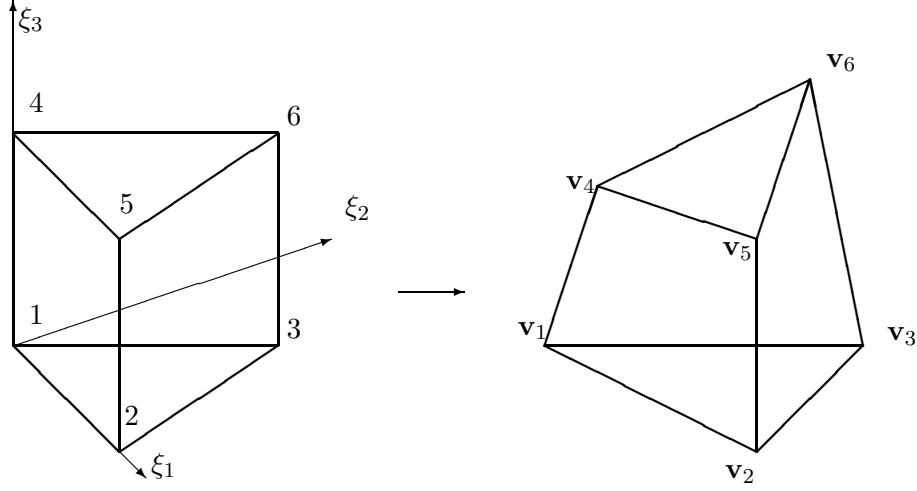


Figure 3.9: The map for the prismatic element.

$$\begin{aligned} S(\cdot, 1) &= (1 - \xi_3)(\mathbf{v}_2 - \mathbf{v}_1) + \xi_3(\mathbf{v}_5 - \mathbf{v}_4), \\ S(\cdot, 2) &= (1 - \xi_3) \left(\frac{2\mathbf{v}_3 - \mathbf{v}_1 - \mathbf{v}_2}{\sqrt{3}} \right) + \xi_3 \left(\frac{2\mathbf{v}_6 - \mathbf{v}_4 - \mathbf{v}_5}{\sqrt{3}} \right), \\ S(\cdot, 3) &= \left(1 - \xi_1 - \frac{\xi_2}{\sqrt{3}} \right) (\mathbf{v}_4 - \mathbf{v}_1) + \left(\xi_1 - \frac{\xi_2}{\sqrt{3}} \right) (\mathbf{v}_5 - \mathbf{v}_2) + \frac{2\xi_2}{\sqrt{3}} (\mathbf{v}_6 - \mathbf{v}_3), \end{aligned} \quad (3.21)$$

and we obtain two candidates for each of the two first columns for the “combinational matrices” from 2D bases on both top and bottom triangular faces and three candidates for the third column corresponding to three third edge basis vectors. Thus, the total number of “combinational matrices” in the maximum principle estimate for the prismatic element is equal to 12, and the formula for the Jacobian determinant yields the following 9 sufficient nondegeneracy conditions:

$$\det \left(\mathbf{v}_2 - \mathbf{v}_1, \frac{2\mathbf{v}_6 - \mathbf{v}_4 - \mathbf{v}_5}{\sqrt{3}}, \mathbf{v}_{k+4} - \mathbf{v}_{k+1} \right) +$$

$$\begin{aligned}
& + \det \left(\mathbf{v}_5 - \mathbf{v}_4, \frac{2\mathbf{v}_3 - \mathbf{v}_1 - \mathbf{v}_2}{\sqrt{3}}, \mathbf{v}_{k+4} - \mathbf{v}_{k+1} \right) > 0, \\
\det \left(\mathbf{v}_{3j+2} - \mathbf{v}_{3j+1}, \frac{2\mathbf{v}_{3j+3} - \mathbf{v}_{3j+1} - \mathbf{v}_{3j+2}}{\sqrt{3}}, \mathbf{v}_{k+4} - \mathbf{v}_{k+1} \right) > 0, \quad j = 0, 1, \quad k = 0, 1, 2.
\end{aligned}$$

(399 operations are required for evaluating the Jacobian determinants in the above conditions, and 591 for the maximum principle bound.)

The matrices $\{\mathcal{Q}_{q(c)}\}$ for the integration rule for the distortion metric over the prismatic element can be readily obtained from (3.21) and $N_q = 12$, $\sigma_q = 1/12 \quad \forall q$.

3.4 Quadratic simplices

3.4.1 2D triangular quadratic element

Let us take the reference element to be the same regular triangle with sides of unit length, which we used for the definition of a linear triangular element map. The quadratic map onto an arbitrary curved triangular element with vertex and edge control coordinates $\mathbf{v}_1, \mathbf{v}_2, \mathbf{v}_3, \mathbf{v}_4, \mathbf{v}_5, \mathbf{v}_6$ (see Figure 3.10) can be expressed as

$$\begin{aligned}
\mathbf{r}(\xi, \eta) &= \left(1 - 3\xi - \sqrt{3}\eta + \frac{4}{\sqrt{3}}\xi\eta + 2\xi^2 + \frac{2}{3}\eta^2 \right) \mathbf{v}_1 + \\
&+ \left(-\xi + \frac{1}{\sqrt{3}}\eta - \frac{4}{\sqrt{3}}\xi\eta + 2\xi^2 + \frac{2}{3}\eta^2 \right) \mathbf{v}_2 + \\
&+ \left(-\frac{2}{\sqrt{3}}\eta + \frac{8}{3}\eta^2 \right) \mathbf{v}_3 + \left(\frac{8}{\sqrt{3}}\xi\eta - \frac{8}{3}\eta^2 \right) \mathbf{v}_4 + \\
&+ \left(\frac{8}{\sqrt{3}}\eta - \frac{8}{\sqrt{3}}\xi\eta - \frac{8}{3}\eta^2 \right) \mathbf{v}_5 + \left(4\xi - \frac{4}{\sqrt{3}}\eta - 4\xi^2 + \frac{4}{3}\eta^2 \right) \mathbf{v}_6.
\end{aligned} \tag{3.22}$$

The Jacobian matrix of the map (3.22) may be expressed in the form (3.3) employed earlier for the maximum principle as

$$S = \lambda_1 S_1 + \lambda_2 S_2 + \lambda_3 S_3, \tag{3.23}$$

where

$$\begin{aligned}
\lambda_1 &= \left(1 - \xi - \frac{\eta}{\sqrt{3}} \right), \quad S_1 = \left(4\mathbf{v}_6 - 3\mathbf{v}_1 - \mathbf{v}_2, \frac{1}{\sqrt{3}}(-3\mathbf{v}_1 + \mathbf{v}_2 - 2\mathbf{v}_3 + 8\mathbf{v}_5 - 4\mathbf{v}_6) \right); \\
\lambda_2 &= \left(\xi - \frac{\eta}{\sqrt{3}} \right), \quad S_2 = \left(\mathbf{v}_1 + 3\mathbf{v}_2 - 4\mathbf{v}_6, \frac{1}{\sqrt{3}}(\mathbf{v}_1 - 3\mathbf{v}_2 - 2\mathbf{v}_3 + 8\mathbf{v}_4 - 4\mathbf{v}_6) \right); \tag{3.24}
\end{aligned}$$

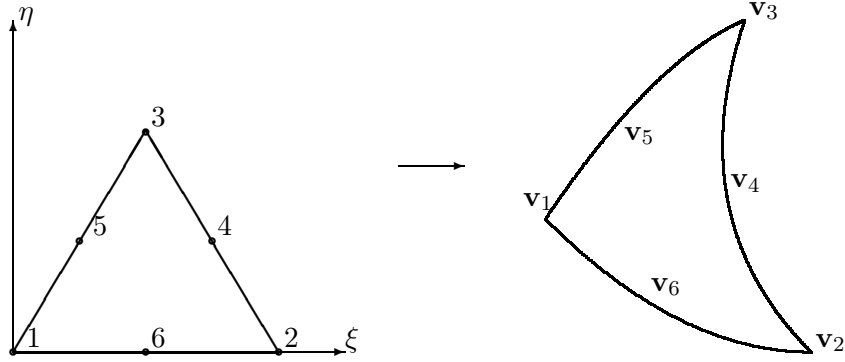


Figure 3.10: The quadratic map \mathbf{r} of the regular reference triangle onto an arbitrary triangle.

$$\lambda_3 = \frac{2}{\sqrt{3}}\eta, \quad S_3 = (\mathbf{v}_1 - \mathbf{v}_2 + 4\mathbf{v}_4 - 4\mathbf{v}_5, \frac{1}{\sqrt{3}}(\mathbf{v}_1 + \mathbf{v}_2 + 6\mathbf{v}_3 - 4\mathbf{v}_4 - 4\mathbf{v}_5)).$$

As before, the columns $S_i(\cdot, 1)$ and $S_i(\cdot, 2)$ of these matrices can also be considered as 2D basis vectors at the cell vertices and used to form 9 different bases or “combinational matrices” $\tilde{S}_\alpha = (S_i(\cdot, 1), S_j(\cdot, 2))$, $i, j = 1, 2, 3$, $\alpha = 1, \dots, 9$. The Jacobian determinant of the map then is written

$$\det S = \sum_{i,j=1}^3 \lambda_i \lambda_j \det (S_i(\cdot, 1), S_j(\cdot, 2)) = \sum_{\alpha} a_{\alpha}(\xi, \eta) \det \tilde{S}_{\alpha}, \quad (3.25)$$

where functions of local coordinates $a_{\alpha}(\xi, \eta) \geq 0$ are positive inside the triangular element and can be zero only on its boundary, and $\sum_{\alpha} a_{\alpha}(\xi, \eta) = 1$. In fact, there are only 6 different functions $a_{\alpha}(\xi, \eta)$ in (3.25) and we can regroup the terms in this sum to verify that the following 6 conditions

$$\det S_1 > 0, \quad \det S_2 > 0, \quad \det S_3 > 0, \quad (3.26)$$

$$\det(S_1(\cdot, 1), S_2(\cdot, 2)) + \det(S_2(\cdot, 1), S_1(\cdot, 2)) > 0,$$

$$\det(S_1(\cdot, 1), S_3(\cdot, 2)) + \det(S_3(\cdot, 1), S_1(\cdot, 2)) > 0,$$

$$\det(S_2(\cdot, 1), S_3(\cdot, 2)) + \det(S_3(\cdot, 1), S_2(\cdot, 2)) > 0$$

guarantee nondegeneracy of the map (3.22). (Computation of all the Jacobian determinants in the above nondegeneracy condition requires 159 additions/multiplications).

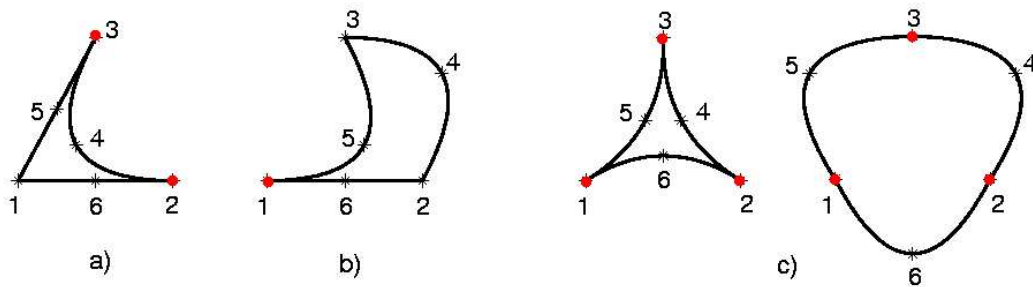


Figure 3.11: Degenerate quadratic triangles with a) one, b) two and c) three curved edges (degeneracy at red vertices).

Figures 3.11 and 3.12 illustrate some representative examples of degenerate shapes, which are all forbidden by the metric E_θ and the nondegeneracy conditions above. Figure 3.11 shows some degenerate shapes where control nodes on curved edges have been located to produce zero Jacobian at one or more of the vertices 1,2,3 which lie on the ideal equilateral triangular shape. This picture gives us the general idea of the edge curvatures that can be achieved in the quadratically mapped triangle without degenerating the map. Of particular practical interest are, of course, examples a) of the single curved edge and b) of two curved edges in the element, since such curved elements are likely to arise when one or two edges coincide with an interface or exterior boundary. Note, that one edge can curve outwards without any restrictions, if the element remains symmetric, but its inward deformation is limited insofar as the Jacobian condition is concerned. Figure 3.12 a) presents a degenerate quadratic triangle with nodes $\mathbf{v}_1 = \mathbf{v}_2 = (0, 0)$, $\mathbf{v}_3 = (1, 0)$, $\mathbf{v}_4 = (1/2, -\sqrt{3}/4)$, $\mathbf{v}_5 = (1/2, \sqrt{3}/4)$, $\mathbf{v}_6 = (1/2, 0)$, where $\det S$ is positive at all vertices 1,2,3, but zero at a mid-edge node 6. In Figure 3.12 b) $\det S > 0$ at all 6 nodes, but is equal to zero at one point $\xi = 2/3, \eta = 0$ on the boundary of the element given by $\mathbf{v}_1 = (0, 0)$, $\mathbf{v}_2 = (1/2, 0)$, $\mathbf{v}_3 = (1, 0)$, $\mathbf{v}_4 = (3/4, -\sqrt{3}/8)$, $\mathbf{v}_5 = (1/2, \sqrt{3}/4)$, $\mathbf{v}_6 = (5/8, 0)$. Finally, in Figure 3.12 c) the Jacobian determinant is positive everywhere on the boundary, but zero at the marked interior point $\xi = 1/2, \eta = 1/\sqrt{3}$ of the triangle $\mathbf{v}_1 = (0, 0)$, $\mathbf{v}_2 = (1, 0)$, $\mathbf{v}_3 = (1/2, \sqrt{3}/2)$, $\mathbf{v}_4 = (9/16, 3\sqrt{3}/4)$, $\mathbf{v}_5 = (7/16, 3\sqrt{3}/4)$, $\mathbf{v}_6 = (1/2, -\sqrt{3}/4)$.

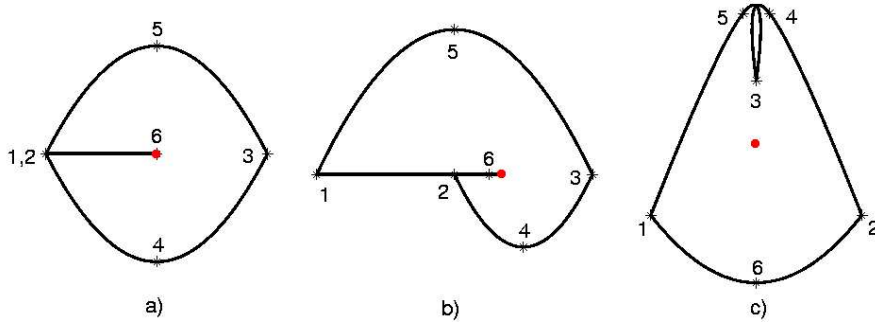


Figure 3.12: Degenerate quadratic triangles (degeneracy at red points).

Returning to (3.25), the matrices enter in the maximum principle bound as before:

$$E_\theta(S) \leq \max_\alpha E_\theta(\tilde{S}_\alpha)$$

and the integration rule over quadratic triangle with weights corresponding to the vertex bases $\sigma_1 = 1/6$, and for other combinational matrices $\sigma_2 = 1/12$, has $N_q = 9$ contributions. (Computation of the bound requires 276 operations).

Figure 3.13 illustrates some of the properties of the metric E_θ on the curvilinear element. The color maps in the Figure represent level sets of minimum value of Jacobian determinant, maximum values of shape distortion β and dilation metric μ , as well as numerical approximations of parts of the cell total “energy” $(\int \beta(S))_h = \sum_\alpha \sigma_\alpha \beta(\tilde{S}_\alpha)$ and $(\int \mu(S))_h = \sum_\alpha \sigma_\alpha \mu(\tilde{S}_\alpha)$, as functions of the position of one mid-edge node 6 in a regular-shaped triangle (Figure 3.10). This Figure shows that deformation of the edge inwards is restricted in the same small triangular region by all the functions (region of negative $\det S$ and infinite metrics above the straight edge configuration). The regions of small shape and size distortion are, of course, bounded and much more restrictive than a nondegeneracy condition. Comparing the maximum distortion with the numerical approximation of total cell distortion, we can see that (up to a scaling constant), as expected, the approximation rule based on the maximum principle result is even more restrictive in terms of acceptable shapes.

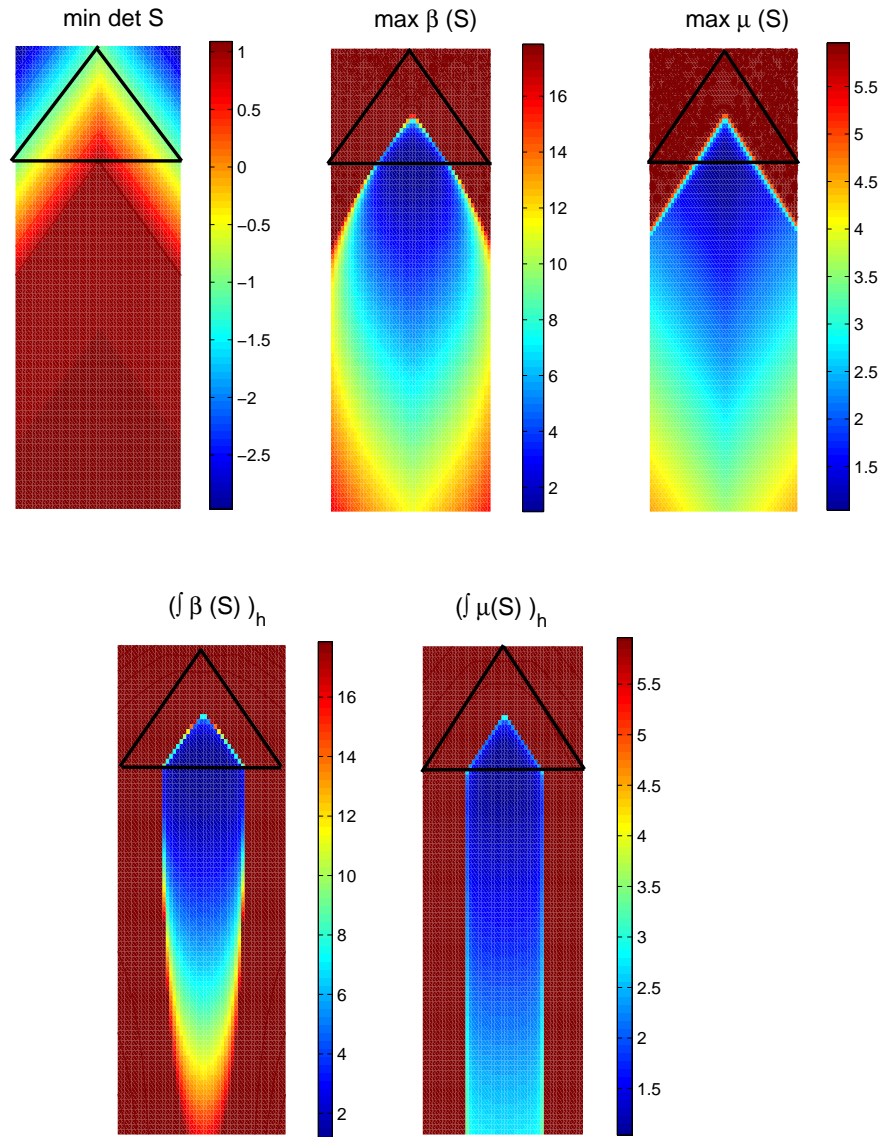


Figure 3.13: Level sets as functions of position for lower mid-edge node in quadratic triangle with all other nodes fixed on the regular shape.

3.4.2 3D tetrahedral quadratic element

As in the case of linear simplices, the 2D results of the previous section can be extended directly to the 3D quadratic tetrahedron. The Jacobian matrix in this case also has linear dependence upon local coordinates of the reference cell and the maximum principle applies. Taking the reference element to be the regular tetrahedron with edges of unit length, the

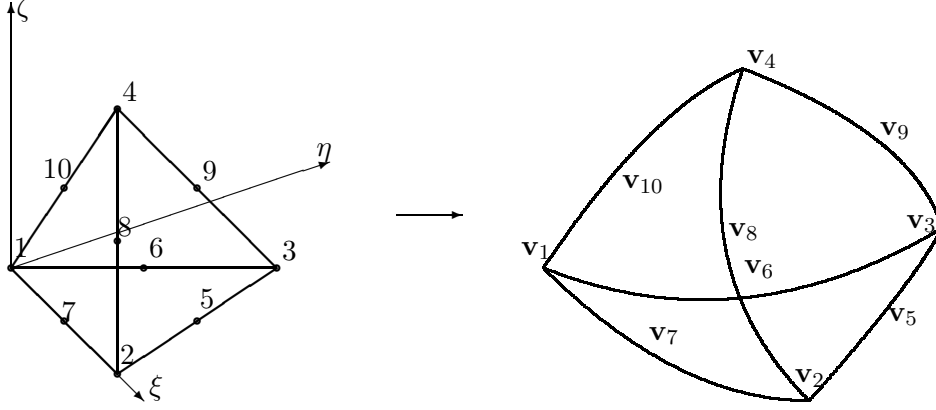


Figure 3.14: The quadratic map of the regular reference tetrahedron onto an arbitrary tetrahedron.

quadratic map onto a tetrahedron with curved edges and faces with vertex and edge control node coordinates $\mathbf{v}_1, \dots, \mathbf{v}_{10}$ as in Figure 3.14 has a Jacobian matrix of the form

$$S = \left(1 - \xi - \frac{\eta}{\sqrt{3}} - \frac{\zeta}{\sqrt{6}}\right) S_1 + \left(\xi - \frac{\eta}{\sqrt{3}} - \frac{\zeta}{\sqrt{6}}\right) S_2 + \left(\frac{2\eta}{\sqrt{3}} - \frac{\zeta}{\sqrt{6}}\right) S_3 + \sqrt{\frac{3}{2}}\zeta S_4, \quad (3.27)$$

where each matrix S_i corresponds to a basis (or 3×3 Jacobian matrix) at vertex \mathbf{v}_i

$$\begin{aligned} S_1(\cdot, 1) &= 4\mathbf{v}_7 - 3\mathbf{v}_1 - \mathbf{v}_2, \quad S_1(\cdot, 2) = \frac{-3\mathbf{v}_1 + \mathbf{v}_2 - 2\mathbf{v}_3 + 8\mathbf{v}_6 - 4\mathbf{v}_7}{\sqrt{3}}, \\ S_1(\cdot, 3) &= \frac{-3\mathbf{v}_1 + \mathbf{v}_2 + \mathbf{v}_3 - 3\mathbf{v}_4 - 4\mathbf{v}_6 - 4\mathbf{v}_7 + 12\mathbf{v}_{10}}{\sqrt{6}}; \\ S_2(\cdot, 1) &= \mathbf{v}_1 + 3\mathbf{v}_2 - 4\mathbf{v}_7, \quad S_2(\cdot, 2) = \frac{\mathbf{v}_1 - 3\mathbf{v}_2 - 2\mathbf{v}_3 + 8\mathbf{v}_5 - 4\mathbf{v}_7}{\sqrt{3}}, \\ S_2(\cdot, 3) &= \frac{\mathbf{v}_1 - 3\mathbf{v}_2 + \mathbf{v}_3 - 3\mathbf{v}_4 - 4\mathbf{v}_5 - 4\mathbf{v}_7 + 12\mathbf{v}_8}{\sqrt{6}}; \\ S_3(\cdot, 1) &= \mathbf{v}_1 - \mathbf{v}_2 + 4\mathbf{v}_5 - 4\mathbf{v}_6, \quad S_3(\cdot, 2) = \frac{\mathbf{v}_1 + \mathbf{v}_2 + 6\mathbf{v}_3 - 4\mathbf{v}_5 - 4\mathbf{v}_6}{\sqrt{3}}, \end{aligned}$$

$$\begin{aligned}
S_3(\cdot, 3) &= \frac{\mathbf{v}_1 + \mathbf{v}_2 - 3\mathbf{v}_3 - 3\mathbf{v}_4 - 4\mathbf{v}_5 - 4\mathbf{v}_6 + 12\mathbf{v}_9}{\sqrt{6}}; \\
S_4(\cdot, 1) = \mathbf{v}_1 - \mathbf{v}_2 + 4\mathbf{v}_8 - 4\mathbf{v}_{10}, \quad S_4(\cdot, 2) &= \frac{\mathbf{v}_1 + \mathbf{v}_2 - 2\mathbf{v}_3 - 4\mathbf{v}_8 + 8\mathbf{v}_9 - 4\mathbf{v}_{10}}{\sqrt{3}}, \\
S_4(\cdot, 3) &= \frac{\mathbf{v}_1 + \mathbf{v}_2 + \mathbf{v}_3 + 9\mathbf{v}_4 - 4(\mathbf{v}_8 + \mathbf{v}_9 + \mathbf{v}_{10})}{\sqrt{6}}.
\end{aligned}$$

All the coefficients in this representation (3.27) of the Jacobian matrix are nonnegative and less than or equal to 1, and their sum is 1. The upper bound on a distortion measure $E_\theta(S)$ for the quadratic tetrahedral element contains contributions from $4^3 = 64$ bases, which can be obtained by forming all possible basis triples $\tilde{S}_\alpha = (S_i(\cdot, 1), S_j(\cdot, 2), S_k(\cdot, 3))$, $i, j, k = 1, \dots, 4$ from the four vertex bases in (3.27).

Nondegeneracy of the quadratic tetrahedron can be guaranteed by checking only 20 conditions:

$$\begin{aligned}
&\det S_i > 0, \quad i = 1, \dots, 4; \\
&\det(S_i(\cdot, 1), S_j(\cdot, 2), S_j(\cdot, 3)) + \det(S_j(\cdot, 1), S_i(\cdot, 2), S_j(\cdot, 3)) + \\
&\det(S_j(\cdot, 1), S_j(\cdot, 2), S_i(\cdot, 3)) > 0, \quad 0 \leq i \neq j \leq 4; \\
&\det(S_i(\cdot, 1), S_j(\cdot, 2), S_k(\cdot, 3)) + \det(S_j(\cdot, 1), S_i(\cdot, 2), S_k(\cdot, 3)) + \\
&\det(S_i(\cdot, 1), S_k(\cdot, 2), S_j(\cdot, 3)) + \det(S_k(\cdot, 1), S_j(\cdot, 2), S_i(\cdot, 3)) + \\
&\det(S_j(\cdot, 1), S_k(\cdot, 2), S_i(\cdot, 3)) + \det(S_k(\cdot, 1), S_i(\cdot, 2), S_j(\cdot, 3)) > 0, \\
&0 \leq i \neq j \neq k \leq 4.
\end{aligned} \tag{3.28}$$

(Computation of the above Jacobian determinants requires 1580 additions/multiplications, and evaluation of the bound in the maximum principle takes 2604 operations, which is comparable to the computational complexity we obtained earlier for a 3D tensor-product element). Note that, similar to the case of the trilinear map, it is not clear what set of conditions will be both necessary and sufficient for nondegeneracy of the map (3.27).

The integration rule has $N_q = 64$ contributions with weights corresponding to a vertex basis $\sigma_1 = 1/20$, a combination from two vertex bases $\sigma_2 = 1/120$, a combination of

three different vertex bases $\sigma_3 = 1/240$.

Not surprisingly, there is a greater variety of limiting curvatures and shapes for degenerate curved tetrahedra than triangles but we may still draw an analogy between several cases, e.g. the cases of all three inward curved edges in a triangle and all six edges of a tetrahedron curved inwards (towards the center of the element). The case of most practical interest corresponding to one face of a tetrahedron fitting the curved boundary surface is represented by three curved edges forming this face. The inward curvatures of these edges are limited in the same sense as for the 2D case.

3.5 Biquadratic elements

The map of a unit square $0 \leq \xi, \eta \leq 1$ onto the curvilinear quadrilateral cell with nodes $\mathbf{r}_1, \dots, \mathbf{r}_9$ (see Figure 3.15) can be written as

$$\begin{aligned} \mathbf{r} = & (1 - 2\xi)(1 - \xi)(1 - 2\eta)(1 - \eta)\mathbf{r}_1 + & (3.29) \\ & + 4\xi(1 - \xi)(1 - 2\eta)(1 - \eta)\mathbf{r}_2 + \xi(2\xi - 1)(1 - 2\eta)(1 - \eta)\mathbf{r}_3 + \\ & + 4(1 - 2\xi)(1 - \xi)\eta(1 - \eta)\mathbf{r}_4 + 16\xi(1 - \xi)\eta(1 - \eta)\mathbf{r}_5 + 4\xi(2\xi - 1)\eta(1 - \eta)\mathbf{r}_6 + \\ & + (1 - 2\xi)(1 - \xi)\eta(2\eta - 1)\mathbf{r}_7 + 4\xi(1 - \xi)\eta(2\eta - 1)\mathbf{r}_8 + \xi(2\xi - 1)\eta(2\eta - 1)\mathbf{r}_9. \end{aligned}$$

The columns of the Jacobian matrix for this map can be written in the form

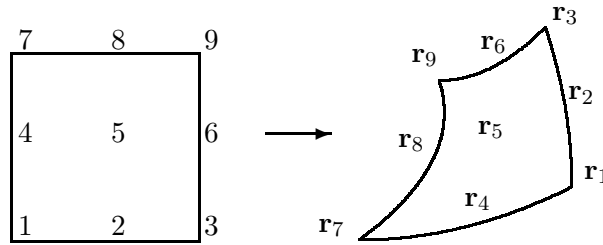


Figure 3.15: Quadratic map for quadrilaterals.

$$\begin{aligned} S(\cdot, 1) = & \{(1 - \xi)(-3\mathbf{r}_1 + 4\mathbf{r}_2 - \mathbf{r}_3) + \xi(\mathbf{r}_1 - 4\mathbf{r}_2 + 3\mathbf{r}_3)\}(1 - 2\eta)(1 - \eta) + \\ & + \{(1 - \xi)(-3\mathbf{r}_4 + 4\mathbf{r}_5 - \mathbf{r}_6) + \xi(\mathbf{r}_4 - 4\mathbf{r}_5 + 3\mathbf{r}_6)\}4\eta(1 - \eta) + \end{aligned}$$

$$\begin{aligned}
& + \{(1 - \xi)(-3\mathbf{r}_7 + 4\mathbf{r}_8 - \mathbf{r}_9) + \xi(\mathbf{r}_7 - 4\mathbf{r}_8 + 3\mathbf{r}_9)\} \eta(2\eta - 1); \\
S(\cdot, 2) & = \{(1 - \eta)(-3\mathbf{r}_1 + 4\mathbf{r}_4 - \mathbf{r}_7) + \eta(\mathbf{r}_1 - 4\mathbf{r}_4 + 3\mathbf{r}_7)\} (1 - 2\xi)(1 - \xi) + \\
& + \{(1 - \eta)(-3\mathbf{r}_2 + 4\mathbf{r}_5 - \mathbf{r}_8) + \eta(\mathbf{r}_2 - 4\mathbf{r}_5 + 3\mathbf{r}_8)\} 4\xi(1 - \xi) + \\
& + \{(1 - \eta)(-3\mathbf{r}_3 + 4\mathbf{r}_6 - \mathbf{r}_9) + \eta(\mathbf{r}_3 - 4\mathbf{r}_6 + 3\mathbf{r}_9)\} \xi(2\xi - 1).
\end{aligned}$$

The coefficients in this representation are all less or equal to 1, their sum is one, but, unlike the preceding case of quadratic simplices or linear elements, they can be negative. Thus, we cannot apply the maximum principle proof to this case, although we still have

$$\text{tr}(S^T S) = \sum_{\alpha} a_{\alpha} \text{tr}(\tilde{S}_{\alpha}^T \tilde{S}_{\alpha}) \text{ and } \det S = \sum_{\alpha} a_{\alpha} \det \tilde{S}_{\alpha}, \quad \sum_{\alpha} a_{\alpha} = 1,$$

but now $-1 \leq a_{\alpha} \leq 1$. In order to be able to bound the coefficients in

$$\beta(S) \leq \sum_{\alpha} \frac{a_{\alpha} \det \tilde{S}_{\alpha}}{\det S} \beta(\tilde{S}_{\alpha})$$

we first need to formulate the nondegeneracy conditions (for $\det S > 0$) for the mapping. This is a challenging problem in itself and apparently has not been addressed previously in the literature.

As we have already seen, the bilinear element is nondegenerate if and only if the Jacobian determinants at all its four vertices are positive [74], or in other words, there is no reentrant corner having interior angle greater than or equal to π . Equivalently, the two pairs of triangles, formed by splitting the quadrilateral by its two diagonals, are nondegenerate. A similar approach using subdivision by diagonals to two pairs of triangles with quadratically curved edges would be easy to apply for the curvilinear quadrilateral as well (e.g. [35]), but, as we will show below, it is not valid in this case. In particular, the Jacobian matrix of the biquadratic element cannot be conveniently presented as a linear combination of matrices corresponding to pairs of quadratic triangles, generated by splitting the cell by diagonals, as in the case of the bilinear cell.

However, in more restrictive settings that are of greater practical interest, such as the case where only one edge is quadratically curved, it is possible to carry out the analysis. We will now consider this situation in detail.

3.5.1 Quadratic quadrilateral with one curved edge.

Let us consider a biquadratic element with all nodes fixed on the ideal unit square shape, except for mid-edge node 2. The displacement of node 2 from its ideal position is denoted by a vector $\mathbf{x} = a\mathbf{g}_1 + b\mathbf{g}_2$, where $\mathbf{g}_1, \mathbf{g}_2$ are two unit basis vectors in 2D (see Figure 3.16). Thus, the Jacobian matrix for this element at any point (ξ, η) inside the cell reduces to

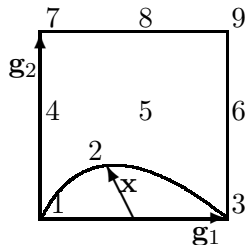


Figure 3.16: Quadrilateral with one curved edge.

$$S = (\mathbf{g}_1 + 4(1 - 2\xi)(1 - 2\eta)(1 - \eta)\mathbf{x}, \mathbf{g}_2 + 4\xi(1 - \xi)(4\eta - 3)\mathbf{x}). \quad (3.30)$$

We require that the determinant be positive for all $0 \leq \xi, \eta \leq 1$. That is,

$$\det S = 1 + 4(1 - 2\xi)(1 - 2\eta)(1 - \eta)a + 4\xi(1 - \xi)(4\eta - 3)b > 0. \quad (3.31)$$

This condition is equivalent to

$$-\frac{1}{4} < a < \frac{1}{4}, \quad -1 < b < \frac{1}{6}(1 + \sqrt{1 - 16a^2}) \quad (3.32)$$

and implies that node 2 may lie within the bounded subregion shown in Figure 3.17. The upper bound on b in (3.32) can be derived from quadratic inequality (3.31) with $\eta = 0$.

This can be compared with the nondegeneracy condition for the two quadratic triangles defined by vertices 1, 2, 3, 5, 7, 4 and 1, 2, 3, 6, 9, 5 of Figure 3.16 which is

$$-\frac{1}{4} < a < \frac{1}{4}, \quad b < \frac{1}{4} + a, \quad b < \frac{1}{4} - a. \quad (3.33)$$

This comparison implies that node 2 is now more restricted in its inward movement, but it can now move any distance downwards without making the triangular elements invalid.

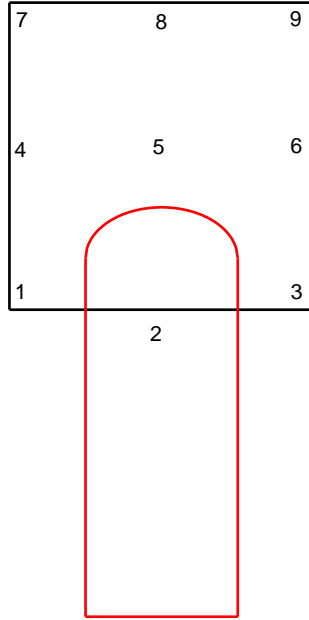


Figure 3.17: “Admissible” positions for node 2 (inside the red contour) of a biquadratic element with other nodes fixed on the ideal shape.

(Note, that although the elements are valid, accuracy may be an issue if $|b|$ is large.) This clearly indicates that checking nondegeneracy of the two pairs of triangles composing the given biquadratic element is not equivalent and might not be enough to guarantee nondegeneracy of the biquadratic map. In particular, in our case the lower bound on b (on downward movement of node 2) in (3.32) is caused by the connection between nodes 2 and 8, which is not “captured” in any of the composing triangles.

We can also compare the nondegeneracy conditions (3.32) for the 9-node biquadratic element with one curved edge against the nondegeneracy conditions for the 8-node serendipity element with one curved edge. The map for an 8-node serendipity element can be obtained from a biquadratic map (3.29) by constraining the position of the mid-cell node 5

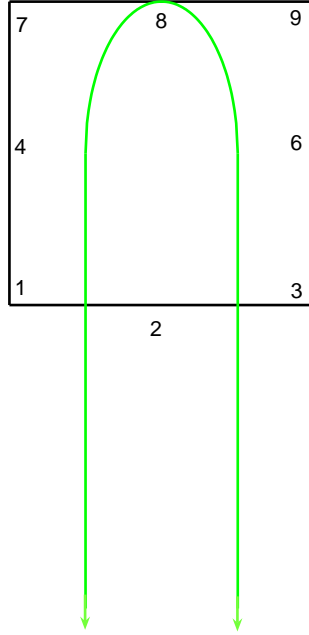


Figure 3.18: “Admissible” positions for node 2 (inside the green contour) deduced from the 8-node serendipity element.

as

$$\mathbf{r}_5 = \frac{\mathbf{r}_2 + \mathbf{r}_4 + \mathbf{r}_6 + \mathbf{r}_8}{2} - \frac{\mathbf{r}_1 + \mathbf{r}_3 + \mathbf{r}_7 + \mathbf{r}_9}{4}.$$

The Jacobian matrix for such an element reduces to (compare to (3.30))

$$S = (\mathbf{g}_1 + 4(1 - 2\xi)(1 - \eta)\mathbf{x}, \mathbf{g}_2 - 4\xi(1 - \xi)\mathbf{x})$$

and the nondegeneracy condition

$$\det S = 1 + 4(1 - 2\xi)(1 - \eta)a - 4\xi(1 - \xi)b > 0$$

is equivalent to

$$-\frac{1}{4} < a < \frac{1}{4}, \quad b < \frac{1}{2}(1 + \sqrt{1 - 16a^2}), \quad (3.34)$$

which is illustrated in Figure 3.18. Not surprisingly, in this sense the serendipity element can tolerate much greater distortions than a biquadratic element.

The level set color maps for minimum Jacobian determinant and maximum of shape and size metrics on the quadratic quadrilateral with one curved edge as functions of position of mid-edge node 2 are illustrated in Figure 3.19.

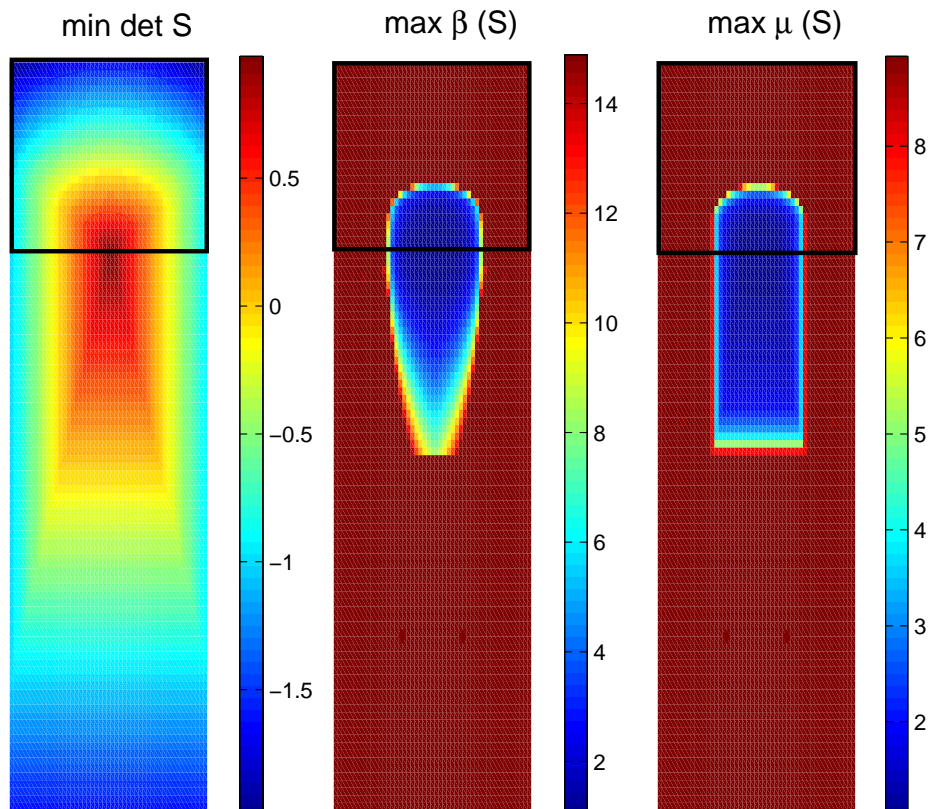


Figure 3.19: Level sets as functions of position of the node 2 of a biquadratic element.

The preceding case can be generalized from the square to the arbitrary quadrilateral in Figure 3.20. The displacement of node 2 from its ideal position on the bilinear element (middle of the edge 1-3) is denoted by \mathbf{x} (see Figure 3.20). The basis vectors at a point

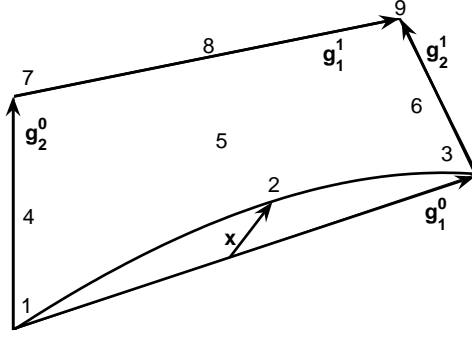


Figure 3.20: “Restricted” biquadratic map.

(ξ, η) inside the bilinear cell may be expressed in terms of the edge vectors shown as

$$\mathbf{g}_1^{lin} = \mathbf{g}_1^0(1 - \eta) + \mathbf{g}_1^1\eta, \quad \mathbf{g}_2^{lin} = \mathbf{g}_2^0(1 - \xi) + \mathbf{g}_2^1\xi.$$

The Jacobian matrix of the “restricted” biquadratic map described above can be written compactly as

$$S = (\mathbf{g}_1^{lin} + 4(1 - 2\xi)(1 - 2\eta)(1 - \eta)\mathbf{x}, \mathbf{g}_2^{lin} + 4\xi(1 - \xi)(4\eta - 3)\mathbf{x}) \quad (3.35)$$

and its determinant is

$$\det S = \det S^{lin}(1 + 4(1 - 2\xi)(1 - 2\eta)(1 - \eta)\tilde{a} + 4\xi(1 - \xi)(4\eta - 3)\tilde{b}), \quad (3.36)$$

where

$$\tilde{a} = \frac{\det(\mathbf{x}, \mathbf{g}_2^{lin})}{\det S^{lin}}, \quad \tilde{b} = \frac{\det(\mathbf{g}_1^{lin}, \mathbf{x})}{\det S^{lin}}, \quad \text{and } S^{lin} = (\mathbf{g}_1^{lin}, \mathbf{g}_2^{lin}).$$

The nondegeneracy conditions for this map are the same as (3.32), only now \tilde{a} and \tilde{b} are functions of local coordinates. The more strict inequalities, which guarantee nondegeneracy of the “restricted” biquadratic map everywhere inside the cell, are

$$\begin{aligned} |\det(\mathbf{x}, \mathbf{g}_2^0)| &< \frac{1}{4} \min\{\det S_1, \det S_7\}, \\ |\det(\mathbf{x}, \mathbf{g}_2^1)| &< \frac{1}{4} \min\{\det S_3, \det S_9\}, \\ -\min\{\det S_1, \det S_3\} &< \det(\mathbf{g}_1^0, \mathbf{x}) < \frac{1}{6} \min\{\det S_1, \det S_3\}, \\ -\min\{\det S_7, \det S_9\} &< \det(\mathbf{g}_1^1, \mathbf{x}) < \frac{1}{6} \min\{\det S_7, \det S_9\}, \end{aligned} \quad (3.37)$$

where $\det S_i$ denotes the Jacobian determinant at one of the vertices $i = 1, 3, 7, 9$ of the bilinear cell. Figure 3.21 shows the corresponding admissible region for node 2 of the quadrilateral from Figure 3.20.

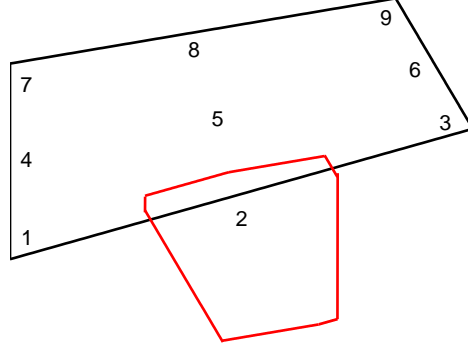


Figure 3.21: Admissible positions for node 2 (inside the contour) of a quadrilateral with one curved edge.

In the case of a nondegenerate biquadratic map we can always find a finite upper bound for the distortion measure. For example, in order to obtain the upper bound on measure E_θ of the “restricted” biquadratic map considered above, we use the following estimates on coefficient functions from (3.36)

$$A = |4(1 - 2\xi)(1 - 2\eta)(1 - \eta)\tilde{a}| < 1, \quad B = |4\xi(1 - \xi)(4\eta - 3)\tilde{b}| < 3,$$

$$C = |4(1 - 2\xi)(1 - 2\eta)(1 - \eta)\tilde{b}| < 4, \quad D = |4\xi(1 - \xi)(4\eta - 3)\tilde{a}| < 3/4.$$

Then

$$\begin{aligned} \text{tr}(S^T S) &= (\mathbf{g}_1^{lin})^2 (1 + 4(1 - 2\xi)(1 - 2\eta)(1 - \eta)\tilde{a}) + 4(1 - 2\xi)(1 - 2\eta)(1 - \eta)\tilde{b}\mathbf{g}_2^{lin})^2 + \\ &+ (\mathbf{g}_2^{lin})^2 (1 + 4\xi(1 - \xi)(4\eta - 3)\tilde{b}) + 4\xi(1 - \xi)(4\eta - 3)\tilde{a}\mathbf{g}_1^{lin})^2 \\ &\leq (\mathbf{g}_1^{lin})^2 ((1 + A)^2 + D^2) + (\mathbf{g}_2^{lin})^2 (C^2 + (1 + B)^2) + \\ &+ 2(\mathbf{g}_1^{lin} \cdot \mathbf{g}_2^{lin})((1 + A)C + (1 + B)D) \\ &< 249/16(\mathbf{g}_1^{lin})^2 + 43(\mathbf{g}_2^{lin})^2 \leq 43\text{tr}((S^{lin})^T S^{lin}). \end{aligned} \tag{3.38}$$

From this result it is easy to verify that

$$\beta(S) < 43 \frac{\det S^{lin}}{\det S} \beta(S^{lin})$$

and

$$\mu(S) \leq (1 + A + B)^2 \frac{\det S^{lin}}{\det S} \mu(S^{lin}),$$

so

$$E_\theta(S) < 43 \frac{\det S^{lin}}{\det S} E_\theta(S^{lin}).$$

However, these estimates do not have the same practical value as the maximum principle. They are not constructive in the sense that they do not help to establish the mapping properties, such as nondegeneracy and element quality. They indicate, nevertheless, that if the initial mesh of quadrilaterals with a curved edge is valid, then the variational smoothing formulation can be applied.

The numerical integration rule for the biquadratic element, by analogy, contains $N_q = 36$ contributions (from all bases in the representation of $\det S$). However, establishing the validity of an initial mesh of biquadratic elements, as well as formulating an unfolding algorithm for such a mesh, remains an open question.

Chapter 4

Solution algorithm and numerical implementation

This chapter is devoted to the description of the numerical solution technique used for the variational smoothing formulation. The gradient of the smoothing functional (2.8), and the untangling functional (2.19), are nonlinear, so an iterative optimization algorithm, such as Newton's method or another gradient descent method, should be applied to the associated nonlinear algebraic problem. In the present work, the modified damped Newton's method is used. The modified Hessian of the distortion functional is proved to give a positive definite linear system. This method is easy to modify into a Lagrange multiplier method, which can be used for constrained minimization problems. The necessity to impose constraints arises, for instance, when the boundary nodes are allowed to tangentially "slide" along the boundary or when the mesh contains hanging nodes. The algorithm extensions for the treatment of such constraints, as well as a strategy for its parallel implementation, are also formulated.

In order to account for a Dirichlet-type boundary condition (fixed mesh boundary nodes) we seek the coordinate vector \mathbf{R} in the following form $\mathbf{R} = (I - B)\mathbf{R}_b + B\mathbf{R}_{in}$, where $B \in \mathbb{R}^{N \times N}$ is the diagonal matrix with the entries $b(i, i) = 1$ if i^{th} node is internal (its coordinates may be changed) and $b(i, i) = 0$ if i^{th} node is a fixed boundary node. Then \mathbf{R}_b is a given vector satisfying the coordinate boundary conditions and \mathbf{R}_{in} is an unknown vector.

Let us write down the gradient and the Hessian matrix for the unfolding functional (2.25). (The formula for the smoothing functional (2.23) will follow after substitution $\chi_\varepsilon(x) = x$, $\chi'_\varepsilon(x) = 1$, $\chi''_\varepsilon(x) = 0$.) We will use the notation $\partial f / \partial \mathbf{a}$ for the gradient of some function f with respect to \mathbf{a} , i.e. a column vector, and $\partial f / \partial \mathbf{a}^T$ for the transposed gradient

vector, i.e. row vector. (For other notations recall the functional discretization in Section 2.3.) The following equalities hold

$$\begin{aligned} \nabla \mathcal{I}_{h,\varepsilon} &= \sum_{c=1}^{N_c} \sum_{q(c)=1}^{N_q} \sigma_{q(c)} \sum_{i=1}^n \frac{\partial \mathbf{a}_i^T}{\partial \mathbf{R}} \frac{\partial E_{\theta,\varepsilon}}{\partial \mathbf{a}_i} = \\ &= \sum_{c=1}^{N_c} \sum_{q(c)=1}^{N_q} \sigma_{q(c)} \begin{pmatrix} B\mathcal{R}_c^T \mathcal{Q}_{q(c)}^T & \cdots & 0 \\ \vdots & \ddots & \vdots \\ 0 & \cdots & B\mathcal{R}_c^T \mathcal{Q}_{q(c)}^T \end{pmatrix} \begin{pmatrix} \frac{\partial E_{\theta,\varepsilon}}{\partial \mathbf{a}_1} \\ \vdots \\ \frac{\partial E_{\theta,\varepsilon}}{\partial \mathbf{a}_n} \end{pmatrix} \end{aligned} \quad (4.1)$$

and

$$\begin{aligned} H &= \left(\frac{\partial^2 \mathcal{I}_{h,\varepsilon}}{\partial \mathbf{X}_i \partial \mathbf{X}_j} \right) = \begin{pmatrix} I - B & \cdots & 0 \\ \vdots & \ddots & \vdots \\ 0 & \cdots & I - B \end{pmatrix} + \\ &+ \sum_{c=1}^{N_c} \sum_{q(c)=1}^{N_q} \sigma_{q(c)} \begin{pmatrix} B\mathcal{R}_c^T \mathcal{Q}_{q(c)}^T & \cdots & 0 \\ \vdots & \ddots & \vdots \\ 0 & \cdots & B\mathcal{R}_c^T \mathcal{Q}_{q(c)}^T \end{pmatrix} P^\varepsilon \begin{pmatrix} \mathcal{Q}_{q(c)} \mathcal{R}_c B & \cdots & 0 \\ \vdots & \ddots & \vdots \\ 0 & \cdots & \mathcal{Q}_{q(c)} \mathcal{R}_c B \end{pmatrix}, \end{aligned} \quad (4.2)$$

where

$$P^\varepsilon = \begin{pmatrix} \frac{\partial^2 E_{\theta,\varepsilon}}{\partial \mathbf{a}_1^T \partial \mathbf{a}_1} & \cdots & \frac{\partial^2 E_{\theta,\varepsilon}}{\partial \mathbf{a}_1^T \partial \mathbf{a}_n} \\ \vdots & \vdots & \vdots \\ \frac{\partial^2 E_{\theta,\varepsilon}}{\partial \mathbf{a}_n^T \partial \mathbf{a}_1} & \cdots & \frac{\partial^2 E_{\theta,\varepsilon}}{\partial \mathbf{a}_n^T \partial \mathbf{a}_n} \end{pmatrix}.$$

For our implementation of Newton's method, instead of solving the full Newton's descent step, which is computationally expensive and time-consuming, we approximate the Hessian by a block-diagonal reduced Hessian matrix \mathcal{H} [34, 70], or even by diagonally reduced Hessian. The latter considerably facilitate implementation of the numerical minimization

algorithm, especially when dealing with large 3D meshes. The block-diagonal Hessian can be computed by the formula (4.2) using the following reduced block-diagonal form of P^ε :

$$\tilde{P}^\varepsilon = \begin{pmatrix} P_{11}^\varepsilon & \cdots & 0 \\ \vdots & \ddots & \vdots \\ 0 & \cdots & P_{nn}^\varepsilon \end{pmatrix},$$

where

$$P_{ii}^\varepsilon = \frac{\partial^2 E_{\theta,\varepsilon}}{\partial \mathbf{a}_i^T \partial \mathbf{a}_i} + \frac{\chi_\varepsilon''}{\chi_\varepsilon} \phi_\theta \mathbf{a}^i \mathbf{a}^{iT},$$

and vectors \mathbf{a}^i are defined by $\mathbf{a}^i \cdot \mathbf{a}_j = J \delta_{ij}$, and for diagonally reduced Hessian only the diagonal part of P^ε is used. This choice of reduced Hessian matrix \mathcal{H} allows reducing the numerical minimization problem to n minimization problems of lower dimension within the iterative step, which in terms of the original smoothing problem means that all coordinates are independent from each other. It also ensures that the associated reduced Hessian matrix \mathcal{H} is symmetric positive definite, as we will show in the following paragraph. This property allows employing fast and efficient symmetric iterative solvers for the numerical linear system (such as a conjugate gradient method) for our problem.

Properties of the reduced Hessian matrix. All n diagonal blocks of \mathcal{H} are independent and can be computed as follows

$$\mathcal{H}_{ii} = I - B + \sum_{c=1}^{N_c} \sum_{q(c)=1}^{N_q} \sigma_{q(c)} B \mathcal{R}_c^T \mathcal{Q}_{q(c)}^T P_{ii}^\varepsilon \mathcal{Q}_{q(c)} \mathcal{R}_c B. \quad (4.3)$$

Let us consider a standard finite element representation of the i^{th} coordinate function x_i on a grid of isoparametric elements: $x_i = \Phi \cdot \mathbf{X}_i$, where $\Phi \in \mathbb{R}^N$ and $\Phi(j)$ is a basis function for the node j . Then the corresponding row of the Jacobian matrix has the representation

$$\mathbf{a}_i = \nabla_{\vec{\xi}} x_i = \nabla_{\vec{\xi}} \Phi \mathbf{X}_i,$$

and

$$\mathbf{a}_i^T \mathbf{a}_i = \mathbf{X}_i^T (\nabla_{\vec{\xi}} \Phi)^T \nabla_{\vec{\xi}} \Phi \mathbf{X}_i.$$

On the other hand,

$$\mathbf{a}_i^T \mathbf{a}_i = \sum_{c=1}^{N_c} \sum_{q(c)=1}^{N_q} \sigma_{q(c)} \mathbf{a}_i^T|_{q(c)} \mathbf{a}_i|_{q(c)} = \mathbf{X}_i^T \left(\sum_{c=1}^{N_c} \sum_{q(c)=1}^{N_q} \sigma_{q(c)} \mathcal{R}_c^T \mathcal{Q}_{q(c)}^T \mathcal{Q}_{q(c)} \mathcal{R}_c \right) \mathbf{X}_i.$$

Thus we can write

$$M = \sum_{c=1}^{N_c} \sum_{q(c)=1}^{N_q} \sigma_{q(c)} \mathcal{R}_c^T \mathcal{Q}_{q(c)}^T \mathcal{Q}_{q(c)} \mathcal{R}_c = (\nabla_{\xi^-} \Phi)^T \nabla_{\xi^-} \Phi,$$

and $M = M^T \geq 0$. From the partition of unity property of the finite element basis $\sum_{j=1}^N \Phi(j) = 1$, it follows that $\sum_{j=1}^N \nabla_{\xi^-} \Phi(j) = 0$ and at least one row of $\nabla_{\xi^-} \Phi$ is a linear combination of other rows; e.g.

$$\nabla_{\xi^-} \Phi(N) = - \sum_{j=1}^{N-1} \nabla_{\xi^-} \Phi(j).$$

All other $N - 1$ rows of $\nabla_{\xi^-} \Phi$ are linearly independent (if $\nabla_{\xi^-} \Phi(k) = \sum_{j \in J} a_j \nabla_{\xi^-} \Phi(j)$, then $\Phi(k) = \sum_{j \in J} a_j \Phi(j) + \text{const}$ and $\Phi(k) = \sum_{j \in J} a_j \Phi(j) + \text{const} \cdot \sum_{j=1}^N \Phi(j)$; i.e. Φ is not a basis). Thus matrix M has rank $N - 1$, and $M(j, j) = - \sum_{k \neq j} M(k, j) > 0$. If at least one diagonal element in B is zero (at least one node is fixed in the grid), then matrix $I - B + BMB$ has a full rank, and since its Gershgorin disks are contained in those of M , $I - B + BMB$ is strictly positive definite. Now in order to prove $\mathcal{H} > 0$ it suffices to show that $P_{ii}^\varepsilon \geq wI$, $w > 0$.

Let us first write down expressions for derivatives that are necessary for the computation of the gradient and the Hessian matrix of the functional:

$$\begin{aligned} \frac{\partial E_{\theta, \varepsilon}}{\partial \mathbf{a}_i} &= \frac{1}{\chi_\varepsilon} \left(\frac{\partial \phi_\theta}{\partial \mathbf{a}_i} - \hat{\alpha} \phi_\theta \mathbf{a}^i \right) \\ \frac{\partial^2 E_{\theta, \varepsilon}}{\partial \mathbf{a}_i^T \partial \mathbf{a}_i} &= \frac{1}{\chi_\varepsilon} \left(\frac{\partial^2 \phi_\theta}{\partial \mathbf{a}_i^T \partial \mathbf{a}_i} - \hat{\alpha} \left(\frac{\partial \phi_\theta}{\partial \mathbf{a}_i} \mathbf{a}^{iT} + \mathbf{a}^i \frac{\partial \phi_\theta}{\partial \mathbf{a}_i^T} \right) \right. \\ &\quad \left. + \left(2\hat{\alpha}^2 - \frac{\chi_\varepsilon''}{\chi_\varepsilon} \right) \phi_\theta \mathbf{a}^i \mathbf{a}^{iT} \right), \end{aligned}$$

where $\hat{\alpha} = \frac{\chi_\varepsilon'}{\chi_\varepsilon}$, and $|\alpha| = |\hat{\alpha}J| < 1$.

In the **2D case**, for the *untangling* functional Hessian corresponding to (2.25) we have

$$\begin{aligned} \text{tr}P_{ii}^\varepsilon &= \frac{1}{\chi_\varepsilon} \left(2(1-\theta)(1-\alpha) + \frac{\theta}{v}(1-\alpha)^2|\mathbf{a}^i|^2 \right. \\ &\quad \left. + 2(1-\theta)\hat{\alpha}^2 \left(\frac{1}{2}\text{tr}(S^T S) \right) |\mathbf{a}^i|^2 + \theta v \hat{\alpha}^2 |\mathbf{a}^i|^2 \right) > 0, \end{aligned}$$

and since $|\alpha| < 1$,

$$\begin{aligned} \det P_{ii}^\varepsilon &= \frac{1}{\chi_\varepsilon^2} \left((1-\theta)^2((1-\alpha)^2 + \hat{\alpha}^2|\mathbf{a}^j|^2|\mathbf{a}^i|^2) \right. \\ &\quad \left. + \frac{(1-\theta)\theta}{v} ((1-\alpha)^2 + v\hat{\alpha}^2) |\mathbf{a}^i|^2 \right) > 0, \end{aligned}$$

For the *smoothing* functional Hessian ($\alpha = 1, J > 0$) we have

$$\begin{aligned} \text{tr}P_{ii} &= \frac{1}{J^3} \left(2(1-\theta) \left(\frac{1}{2}\text{tr}(S^T S) \right) |\mathbf{a}^i|^2 + \theta v |\mathbf{a}^i|^2 \right) > 0, \\ \det P_{ii} &= \frac{1}{J^4} \left((1-\theta)^2(|\mathbf{a}^j|^2|\mathbf{a}^i|^2) + (1-\theta)\theta v |\mathbf{a}^i|^2 \right) > 0. \end{aligned}$$

Thus, from the characteristic equation for the eigenvalues of P_{ii}^ε

$$\lambda^2 - \lambda \text{tr}P_{ii}^\varepsilon + \det P_{ii}^\varepsilon = 0$$

we get

$$\lambda_1 + \lambda_2 = \text{tr}P_{ii}^\varepsilon > 0, \quad \lambda_1 \lambda_2 = \det P_{ii}^\varepsilon > 0,$$

and, finally, $P_{ii}^\varepsilon > \min(\lambda_1, \lambda_2)I$, where $\min(\lambda_1, \lambda_2) > 0$, which yields the desired result.

In the **nD case**, $\mathbf{n} > \mathbf{2}$, diagonal entries of P^ε have the following form

$$\begin{aligned} P_{ii}^\varepsilon(k, k) &= \frac{(1-\theta) \left(\frac{1}{n}\text{tr}(S^T S) \right)^{n/2-2}}{\chi_\varepsilon} \left(\left(\frac{1}{\sqrt{2}} \mathbf{a}_i(k) - \sqrt{2}\hat{\alpha} \left(\frac{1}{n}\text{tr}(S^T S) \right) \mathbf{a}^i(k) \right)^2 + \right. \\ &\quad \left. + \frac{1}{n} \sum_{j=1}^n \sum_{l=1}^n \mathbf{a}_j(l) \mathbf{a}_j(l) + \frac{\frac{n}{2}-2}{n} \mathbf{a}_i^2(k) \right) + \frac{\theta(\mathbf{a}^i(k))^2}{\chi_\varepsilon} \left(\hat{\alpha}^2 v + \frac{1}{v}(\hat{\alpha}J - 1)^2 \right). \end{aligned}$$

The expression in parenthesis in the first term is nonnegative for any $n \geq 2$ and the expression in parenthesis in the second term is always positive. Thus, $P_{ii}^\varepsilon(k, k) \geq 0$ and the

equality is achieved only when $n > 2$ and all entries of the Jacobian matrix are zero (i.e. all element vertices have the same coordinates). In order to account for this rare situation, which will break down the numerical procedure, we make a small modification to the untangling metric (2.20) and define $\tilde{\phi}_\theta(S) = \phi_\theta(S) + \frac{(n-2)\epsilon}{2}\text{tr}(S^T S)$, $0 < \epsilon \ll 1$. This introduces a nonzero contribution to the Hessian $\tilde{P}_{ii}^\epsilon(k, k) = P_{ii}^\epsilon(k, k) + (n-2)\epsilon > 0$. Hence we have the desired result.

For the diagonal entries of matrix P_{ii} in case of the *smoothing* formulation (that is, applied to a valid grid) we get

$$P_{ii}(k, k) = \frac{(1-\theta) \left(\frac{1}{n}\text{tr}(S^T S)\right)^{n/2-2}}{J} \left(\left(\frac{1}{\sqrt{2}} \mathbf{a}_i(k) - \sqrt{2} \frac{\left(\frac{1}{n}\text{tr}(S^T S)\right)}{J} \mathbf{a}^i(k) \right)^2 + \frac{1}{n} \sum_{j=1}^n \sum_{l=1}^n \mathbf{a}_j(l) \mathbf{a}_j(l) + \frac{\frac{n}{2}-2}{n} \mathbf{a}_i^2(k) \right) + \frac{\theta v}{J^3} (\mathbf{a}^i(k))^2 > 0 \quad \forall n \geq 2.$$

The basic algorithms are summarized below.

Untangling algorithm. For the grid untangling minimization problem the following iterative solution scheme is used: choose the initial guess \mathbf{R}^0 ,

for $k = 0, 1, 2, \dots$

find minimization direction $\mathbf{P}^k = -\mathcal{H}^{-1} \nabla \mathcal{I}_{h,\epsilon}$,

solve approximately $\tau_k = \arg \min_{\tau} \mathcal{I}_{h,\epsilon}(\mathbf{R}^k + \tau \mathbf{P}^k)$;

$\mathbf{R}^{k+1} = \mathbf{R}^k + \tau_k \mathbf{P}^k$;

if $\min_{q(c)} \det S(\mathbf{R}^{k+1}) > 0$, stop.

Smoothing algorithm. For the grid smoothing minimization problem the following iterative solution scheme is used: choose the initial guess \mathbf{R}^0 ,

for $k = 0, 1, 2, \dots$

find minimization direction $\mathbf{P}^k = -\mathcal{H}^{-1} \nabla \mathcal{I}_h$,

solve approximately $\tau_k = \arg \min_{\tau} \mathcal{I}_h(\mathbf{R}^k + \tau \mathbf{P}^k)$;

$\mathbf{R}^{k+1} = \mathbf{R}^k + \tau_k \mathbf{P}^k$;

if $|\min_{q(c)} Q_\theta(\mathbf{R}^{k+1}) - \min_{q(c)} Q_\theta(\mathbf{R}^k)| < \epsilon$, stop.

After each iteration, the global minimum quality measure

$$(Q_\theta)|_{\min} = \min_{q(c)} \frac{1}{E_\theta(S_{q(c)})} \quad (4.4)$$

is computed in order to monitor the optimization process. Iterations cease when the difference between the minimum quality (4.4) of two subsequent grids is less than a given tolerance; (other criteria are possible). The linear system for determination of the minimization direction is solved using the conjugate gradient method.

Convergence of the iterative procedures. Let us assume that a mesh given by \mathbf{R}^* is the global minimizer for our functional

$$\mathbf{R}^* = \arg \min \mathcal{I}_{h,\varepsilon}(\mathbf{R}) \text{ and } S^* = Iv^{1/n}, \text{ so that } E_\theta(S^*) = 1 \text{ everywhere.}$$

Then $\nabla \mathcal{I}_{h,\varepsilon}(\mathbf{R}^*) = 0$, $P^\varepsilon(\mathbf{R}^*)$ is a constant diagonal matrix and at iteration $k+1$ the error satisfies

$$\|\mathbf{R}^{k+1} - \mathbf{R}^*\| = \|\mathbf{R}^k + \tau_k \mathbf{P}^k - \mathbf{R}^*\| = \|\mathbf{R}^k - \tau_k \mathcal{H}_k^{-1} \nabla \mathcal{I}(\mathbf{R}^k) - \mathbf{R}^*\| =$$

$$\|\mathbf{R}^k - \mathbf{R}^* - \tau_k \mathcal{H}_k^{-1} (\nabla \mathcal{I}(\mathbf{R}^k) - \nabla \mathcal{I}(\mathbf{R}^*))\| \leq \|\mathcal{H}_k^{-1}\| \cdot \|\mathcal{H}_k - \tau_k H(\mathbf{R}_c)\| \cdot \|\mathbf{R}^k - \mathbf{R}^*\|,$$

where $\mathbf{R}_c = \xi \mathbf{R}^k + (1 - \xi) \mathbf{R}^*$ for some $0 \leq \xi \leq 1$. Equivalently,

$$\|e^{k+1}\| \leq q_k \|e^k\|, \quad q_k = \frac{\|\mathcal{H}_k - \tau_k H(\mathbf{R}_c)\|}{w},$$

where w is the smallest eigenvalue of the modified Hessian \mathcal{H} proven above to be positive. As we have already seen, the maximum eigenvalue of the Hessian matrix of the functional $\|\mathcal{H}_k - \tau_k H(\mathbf{R}_c)\|$ is defined by the maximum eigenvalue of the Hessian matrix of the distortion measure $\|\tilde{P}^\varepsilon(\mathbf{R}^k) - \tau_k P^\varepsilon(\mathbf{R}_c)\|$. We get $\|\tilde{P}^\varepsilon(\mathbf{R}^k) - P^\varepsilon(\mathbf{R}^*)\| \rightarrow 0$ as $\mathbf{R}^k \rightarrow \mathbf{R}^*$ due to the continuity of the second derivatives of the distortion measure $\frac{\partial^2 E_{\theta,\varepsilon}}{\partial \mathbf{a}_i^T \partial \mathbf{a}_i}$. Thus, $q_k = \|\mathcal{H}_k - H(\mathbf{R}_c)\|/w \rightarrow 0$ as $k \rightarrow \infty$ (for $\tau_k = 1$) and we obtain a super-linear convergence for our iterative procedure. Note, that our iterative minimization procedure belongs to a class of quasi-Newton methods, since $\|\mathcal{H}_k - H(\mathbf{R}^*)\| \rightarrow 0$ as $\mathbf{R}^k \rightarrow \mathbf{R}^*$ and the approximation to the

Hessian is chosen to be symmetric positive definite in order to facilitate reliable computation of the solution. Numerical observations confirm almost quadratic convergence.

Remark: As noted earlier, local point relaxation is a popular strategy for optimization-based mesh smoothing. According to this strategy, a local optimization problem is solved for the optimal position of each node in the mesh depending on the positions of its neighbor nodes. (The computational complexity of such a problem is comparable to our algorithm.) Then, global sweeps through all nodes have to be repeated to account for possible influences that non-neighboring nodes may have on each other. Our global minimization accounts for all node interactions in each descent step. Also, local point relaxation algorithms rely on the patch-based mesh quality definitions. This can cause problems for smoothing of meshes with varying valence, as we will see later in Section 5.2. Our element-based approach to the mesh quality, on the other hand, overcomes those difficulties, since it provides us with the ability to control shape and size of each individual element in the mesh. This, in turn, makes our approach more suitable for adaptation (which will be discussed in Chapter 6).

4.1 Treatment of constraints

When the smoothing procedure is applied in conjunction with certain adaptive refinement schemes, it may have to deal with hanging nodes. Also the ability to move boundary nodes along a curved boundary of a manifold instead of fixing them is a basic practical requirement. In both cases the variational problem underlying the smoothing method becomes a constrained minimization problem. In the following section, we briefly describe a Lagrange multiplier approach which is suggested for use in the cases mentioned above as a postprocessing step. That is, this step is to be applied after the smoothing of the grid is done treating hanging nodes as interior and boundary nodes as fixed. Let us define the Lagrangian for constraints $g_i(\mathbf{R}) = 0$ as

$$\mathcal{L}_h = \mathcal{I}_h + \sum_{i=1}^{NC} \lambda_i g_i(\mathbf{R}), \quad (4.5)$$

where NC is the number of constraints, which is equal to n times the number of hanging nodes plus the number of “moving” boundary nodes. Here $\mathbf{\Lambda} = \{\lambda_i, i = 1, \dots, NC\}$ are

the discrete Lagrange multipliers. The minimization of the Lagrangian is done in a manner similar to the smoothing, i.e.

$$\text{First take initial guess } \begin{pmatrix} \mathbf{R} \\ \boldsymbol{\Lambda} \end{pmatrix} = \begin{pmatrix} \mathbf{R}^0 \\ \mathbf{0} \end{pmatrix}$$

for $k = 0, 1, 2, \dots$

find minimization direction \mathbf{P}^k from

$$\begin{pmatrix} \mathcal{H} & \mathcal{B} \\ \mathcal{B}^T & 0 \end{pmatrix} \begin{pmatrix} \mathbf{P}_R^k \\ \mathbf{P}_\Lambda^k \end{pmatrix} = \begin{pmatrix} -\nabla \mathcal{I}_h - \mathcal{B}\boldsymbol{\Lambda}^k \\ 0 \end{pmatrix}, \text{ where } \mathcal{B}(i, j) = \frac{\partial g_j}{\partial R_i};$$

$$\text{solve approximately } \tau_k = \arg \min_{\tau} \mathcal{L}_h \left(\begin{pmatrix} \mathbf{R}^k \\ \boldsymbol{\Lambda}^k \end{pmatrix} + \tau \mathbf{P}^k \right);$$

$$\mathbf{R}^{k+1} = \mathbf{R}^k + \tau_k \mathbf{P}_R^k;$$

$$\text{if } \left| \min_{q(c)} Q_\theta(\mathbf{R}^{k+1}) - \min_{q(c)} Q_\theta(\mathbf{R}^k) \right| < \epsilon, \text{ stop.}$$

The minimization direction may be computed efficiently using only the diagonal part of the Hessian \mathcal{H} from the system

$$\begin{aligned} \mathcal{B}^T \mathcal{H}^{-1} \mathcal{B} \mathbf{P}_\Lambda &= -\mathcal{B}^T \mathcal{H}^{-1} \nabla \mathcal{I}_h; \\ \mathcal{H} \mathbf{P}_R &= -\nabla \mathcal{I}_h - \mathcal{B} \mathbf{P}_\Lambda. \end{aligned} \tag{4.6}$$

For a ‘‘moving’’ boundary node j we first determine whether this node j and its neighbor boundary nodes b_1, \dots, b_{nb} lie on the same plane (line in 2D). In this case, the constraint forbids node movement in the normal direction

$$g_i = \sum_{k=1}^n (\mathbf{X}_k^{new}(j) - \mathbf{X}_k(j)) n_k.$$

For example, in 2D

$$n_1 = \frac{1}{\mathbf{X}(b_1) - \mathbf{X}(b_2)}, \quad n_2 = \frac{-1}{\mathbf{Y}(b_1) - \mathbf{Y}(b_2)}.$$

In the case of nonzero curvature boundary, the node is allowed to move along the sphere (circle), going through node j and its n boundary neighbors:

$$g_i = \sum_{k=1}^n (\mathbf{X}_k^{new}(j) - \mathbf{X}_k(center))^2 - r^2.$$

Computation of this quadratic approximation to a surface requires a minimal number of nodes, and in practice here is observed to provide an accurate fit in 2D, although other forms (than the sphere/circle) might be preferable in higher dimensions.

The constraints $g_i = 0$ for a hanging node j with adjacent edge nodes p_1 and p_2 defining the constraint for j are given by

$$g_i = \mathbf{X}_k(j) - \frac{\mathbf{X}_k(p_1) + \mathbf{X}_k(p_2)}{2}, \quad k = 1, \dots, n.$$

However, in situations with several levels of hanging nodes, e.g. when node p_1 or p_2 is also a hanging node and constraints become imbedded, it is preferable to use a penalty formulation to impose them. This is easily done by adding a penalty term to the functional:

$$\mathcal{I}_h \rightarrow \mathcal{I}_h + \sum_{i=1}^{NHN} \frac{1}{2\epsilon} g_i^2(\mathbf{R}), \quad (4.7)$$

where NHN is the number of hanging nodes and ϵ is the chosen tolerance. In the numerical algorithm we need to add linear terms (since g_i has a linear dependence on \mathbf{R}) to the right hand side and constant terms to the Hessian. That is,

$$-\nabla \mathcal{I}_h \rightarrow -\nabla \mathcal{I}_h - \sum_{i=1}^{NHN} \frac{g_i(\mathbf{R})}{\epsilon} \nabla g_i(\mathbf{R}); \quad \mathcal{H} \rightarrow \mathcal{H} + \sum_{i=1}^{NHN} \frac{\nabla g_i(\mathbf{R}) \nabla^T g_i(\mathbf{R})}{\epsilon}.$$

The above algorithms are implemented in software modules using the C programming language. Our methodology and software has been adopted by LANL and is being used in their applications simulators.

4.2 Parallel implementation

In this section we briefly describe how the above algorithms can be implemented on a parallel machine. Note, that due to our choice of the reduced Hessian matrix, the minimization

problems for each spatial direction are independent and can be solved in parallel, with communication between the processors only required to find an optimal step in the minimization direction.

Further, fine-grain parallelism can be achieved by the domain decomposition approach used for the finite element method which works for our smoothing method as well. The reduced Hessian matrix \mathcal{H} and the right hand side $-\nabla\mathcal{I}_h$ are assembled from the cell contributions in the usual FE fashion. After the mesh nodes are distributed between the processors, only the information from the cells divided by the interfaces needs to be transferred between the processors for the assembly of the numerical problem for subdomain mesh smoothing on each processor. After computing the linear system solution \mathbf{P} by parts over the processors, the 1D optimization problem for the optimal step τ is easily solved by computing all parts of the new functional values on each processor and then assembling the sums on one of the machines and performing a comparison there.

An alternative fine-grain parallel strategy relates to the two step smoothing with boundary node correction procedure described in the previous section. That is, after the mesh nodes are distributed between the processors, the interface (and boundary) nodes are marked as fixed and mesh smoothing in each subdomain is performed without any communication between the processors. Then, the interface node positions are corrected in a few iterations of global mesh smoothing (which requires some information transfer, as described in the previous paragraph). Since most of the global mesh is already smoothed, these correction steps will be inexpensive, thus providing a very effective and highly parallel strategy.

In the following chapters we illustrate the use of the new scheme and algorithm on several representative test problems and on relevant applications.

Chapter 5

Numerical examples

In this section we illustrate the performance of the new variational smoothing/unfolding algorithm on some representative examples that are challenging for other smoothing techniques. We also discuss the main issues presented by these examples. In particular, we perform mathematical and numerical investigations of effects of varying nodal valence on the smoothing, as well as impact of mesh distortion on the application problem solvability.

5.1 Smoothing and unfolding of meshes in nonconvex domains

It is well known [2] that the Laplace smoother may produce overlapping grids for nonconvex domains, so it is important to check the behavior of the present type of smoother for such domains. The improvement and untangling of folded meshes, e.g. including those with nodes outside of the domain, is also an important test.

Triangular grid in a nonconvex domain Consider the nonconvex (v-shaped) domain with triangular grid and fixed boundary nodes shown on the left in Figure 5.1. Clearly this is a valid high quality grid. Laplace smoothing will move points outside the domain and produce an invalid tangled mesh. Smoothing with our new additive functional using weight $\theta = 0.8$ produces the grid on the right in Figure 5.1. There is no overlap and the mesh lines are well behaved. Cells at the peak on the symmetry line are slightly dilated and those at the reentrant corner are slightly compressed, but the modified mesh remains of high quality. Note, that the “ideal” element in this example is the regular triangle, and most of the cells

modified during smoothing achieve a shape closer to ideal than the shape they had initially.

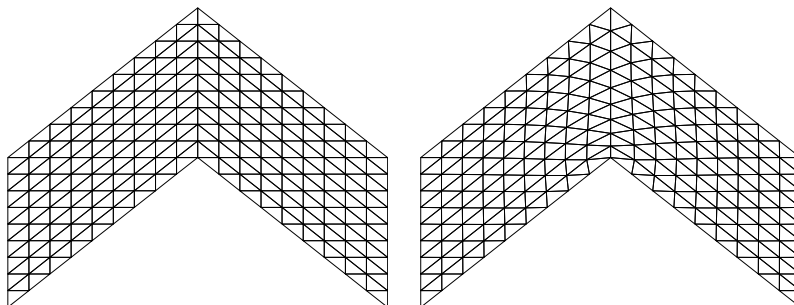


Figure 5.1: Triangular grid in nonconvex domain. Initial mesh (left) and smoothed mesh (right).

“Sliding” boundary nodes In the following example, the postprocessing Lagrange multiplier approach was used to improve the quality of a quadrilateral grid in a domain of complex shape. The initial grid, the grid after 5 smoother iterations, and the grid after 5 iterations with the constrained smoother are shown in Figure 5.2. The use of the lumped Hessian matrix in the constrained smoothing procedure does not degrade the grid quality when compared to results of the unconstrained smoothing. This is true only if the initial grid is “good enough”, which explains why we apply the constrained smoothing step as a postprocessing step. (Also, application of many iterations of constrained smoothing might change the boundary significantly). It can be observed that by allowing boundary nodes to “slide” we achieved near-orthogonality of grid lines to the boundary in the test problem, which is implied by the natural boundary conditions of the functional (recall Section 2.1.2).

Quadrilateral mesh unfolding in nonconvex domain As shown in Section 2.2, barrier formulations of variational smoothing algorithms facilitate mesh unfolding, as well as smoothing. As an example, let us consider the unfolding of a folded quadrilateral mesh for an annular cylindrical domain. For the initial grid, we relocate the nodes interior to a cylindrical polar mesh for a semicircular annulus and place them at the origin as indicated by

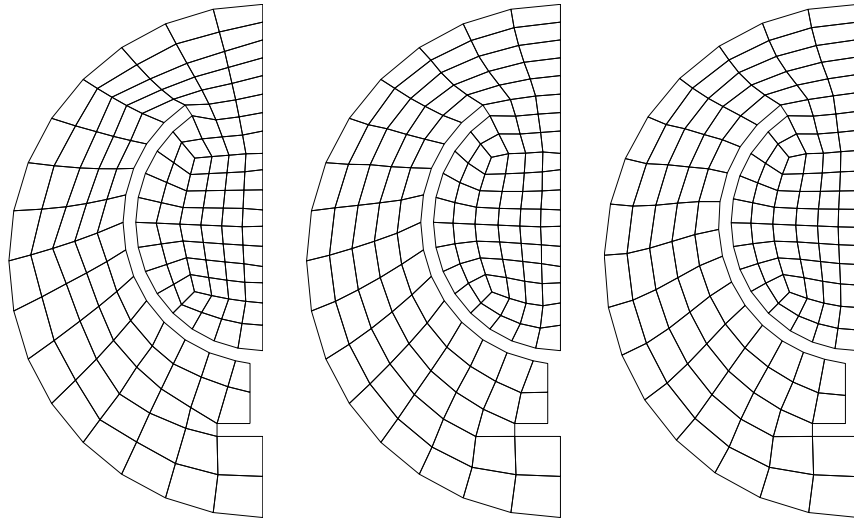


Figure 5.2: Initial grid (left), smoothed grid with fixed boundary nodes (middle) and smoothed grid with “sliding” boundary nodes (right) for the complex domain having two “cavities”.

the mesh on the left in Figure 5.3. After applying the smoothing algorithm for 5 iterations, the grid is close to equidistributed, as seen on the right in Figure 5.3.

The dynamics of minimal quality and minimal Jacobian determinant variation during unfolding is shown in Figure 5.4.

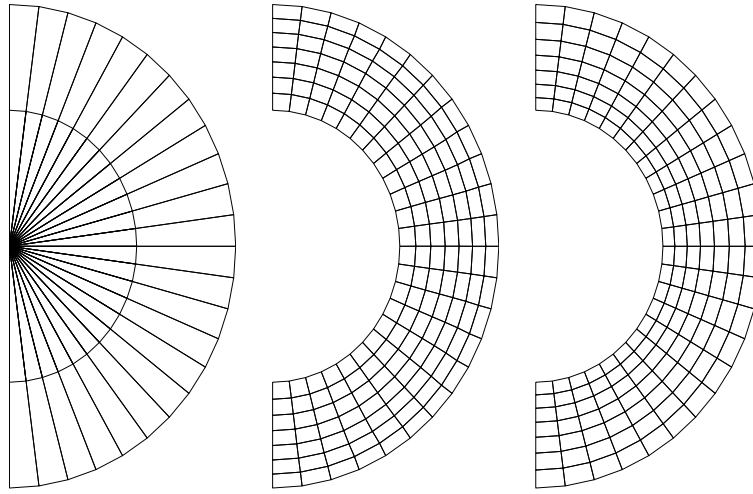


Figure 5.3: Unfolding. Initial mesh (left), smoothed mesh, $\theta = 0.8$ (middle) and smoothed mesh, $\theta = 0.2$ (right).

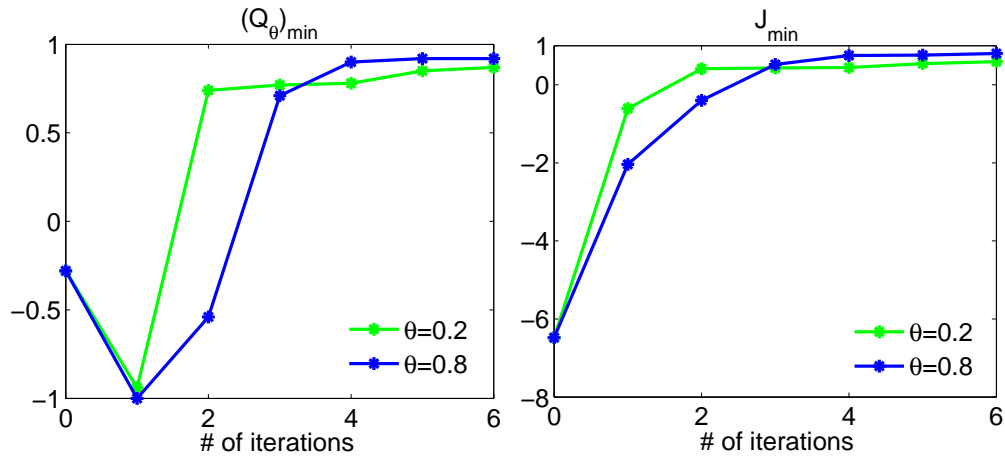


Figure 5.4: Unfolding. $(Q_\theta)_{\min}$ and J_{\min} vs number of iterations.

5.1.1 Large-scale tetrahedral mesh for basin modeling

In the following example we demonstrate the technique on a petroleum reservoir geomechanics application mesh for Reconcavo Baiano Basin [75]. Basin modeling is important in reservoir formation studies. Producing a viable mesh in this application is a challenging problem. In the present case, the initial tetrahedral mesh is for 8 geological horizontal material layers. It also contains faults, which makes the domain geometry very complex. In testing our smoothing algorithm, we treat the basin as a homogeneous medium and fix all nodes on external boundaries and fault boundaries.

Due to the complex geometry, the initial mesh has very poor quality. In particular, it contains a lot of “needle” tetrahedra with large height and negligibly small base area. Some of these “needle” tetrahedra have their base on one boundary and opposite vertex on another boundary, which implies that they cannot be improved during the smoothing in this test since we do not include boundary node motion. However, significant improvement is achieved in the quality of interior elements (with all vertices inside the domain). The general view of the mesh, consisting of interior elements only, before and after smoothing is shown in Figure 5.5. We can notice changes in this complex mesh, induced by the smoothing. In order to better illustrate these changes, the zoom-in on a patch of elements is shown in Figure 5.6, representing individual improvement in the interior cell quality. Initially, this patch had several “needle” tetrahedra. Their bases expanded during smoothing, thus improving their quality.

Each iteration of numerical optimization procedure took 7 seconds of CPU time on a PC with AMD 2.2GHz processor, and most of this time was spent on the Hessian matrix assembly over all 187,257 tetrahedra in the mesh. The initial quality evaluation and nondegeneracy check was performed under a second of CPU time.

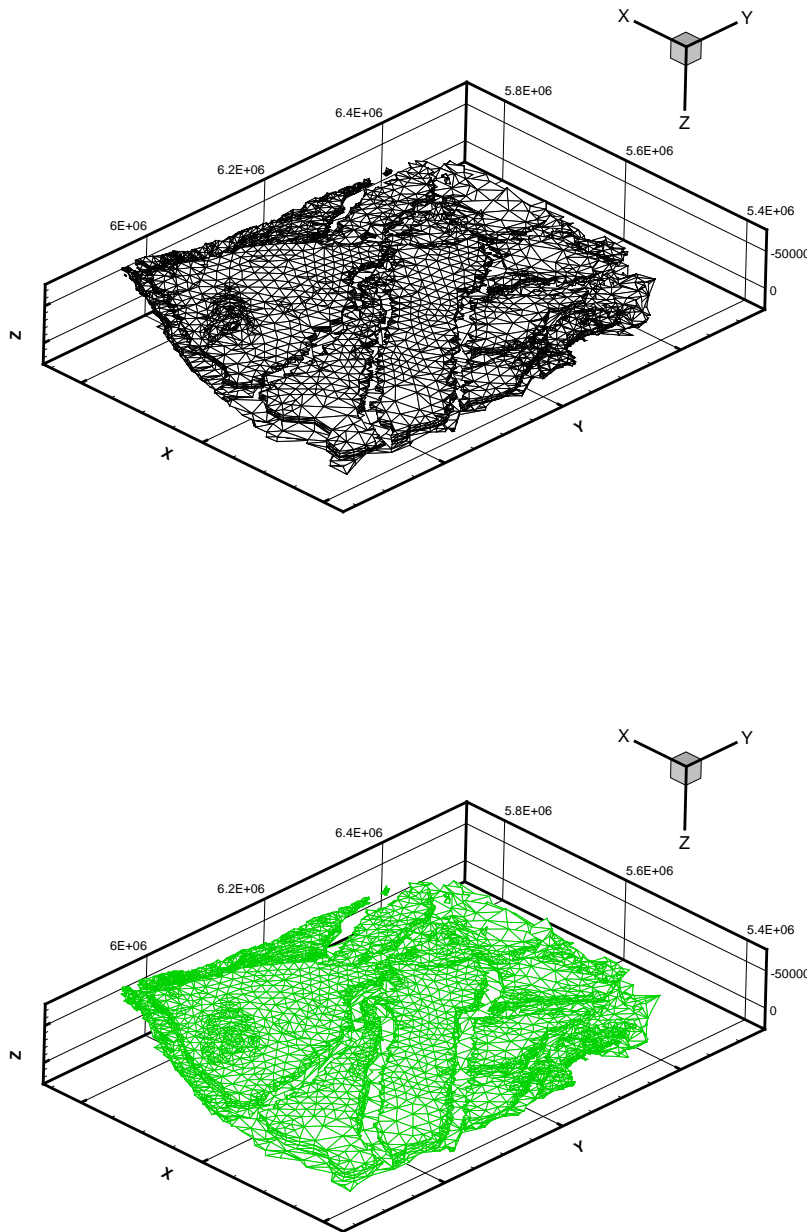


Figure 5.5: Interior of the basin mesh, 56,211 cells, initial (top) and smoothed (bottom).

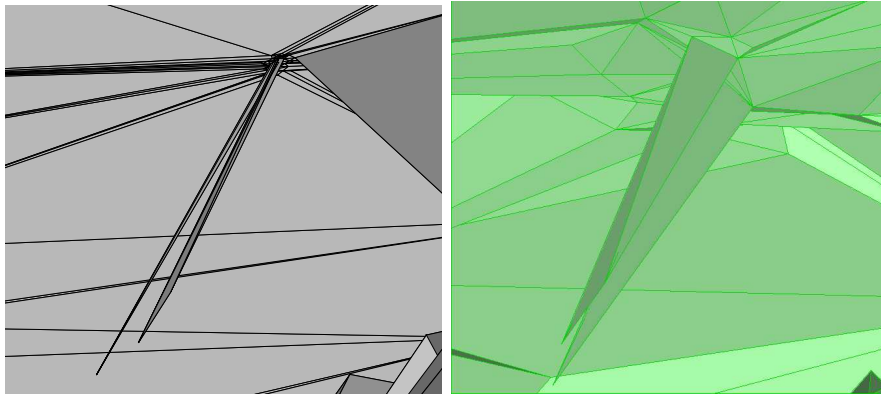


Figure 5.6: Fragment of the basin mesh, initial (left) and smoothed (right).

Histograms of cell distortion before and after smoothing are presented in Figure 5.7. From this Figure we observe that the number of cells with small distortion value (from 1 to 10) after smoothing increased almost 50% compared to the same number in the initial mesh. Also the maximum value of distortion in the smoothed mesh is three orders of magnitude smaller than initial maximum distortion. Remark: For better smoothing results, we would

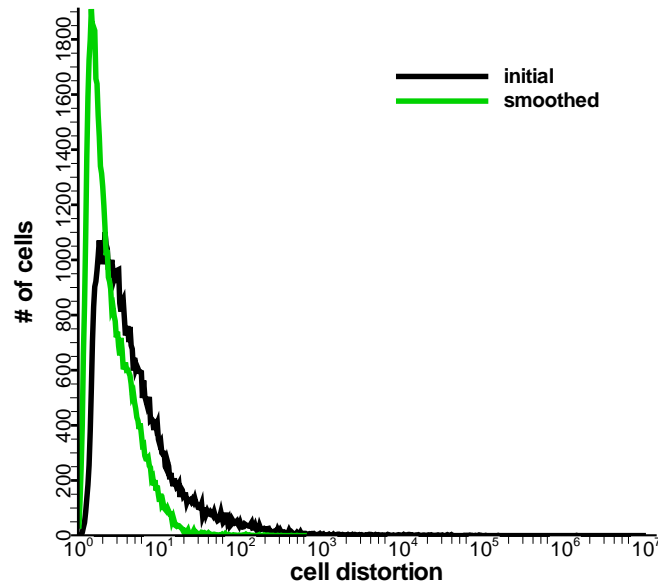


Figure 5.7: Interior of the basin mesh, cell distortion before and after smoothing.

enable node “sliding” along the domain boundaries (and interfaces between the layers, for

non-homogeneous material) in the algorithm. However, this would require an additional module for functional geometry description of these boundaries which was not provided with the data.

5.1.2 Hexahedral mesh of a brain

In this section we test our smoothing methodology on a hexahedral mesh of a human brain, that is being used in studies of brain motion occurring during brain surgery [76]. (A section of cranial bone is removed and the brain moves undergoing large displacement under the resulting change in pressure.) The initial hexahedral mesh consists of several subdomains of different material properties, representing brain and ventricles. This mesh was generated from a generic brain mesh mapped piecewise linearly to a patient-specific mesh that was “adjusted” manually to accommodate tumor, ventricle distortion and other pathologies. The general view of the initial surface mesh is shown in Figure 5.8. The initial mesh

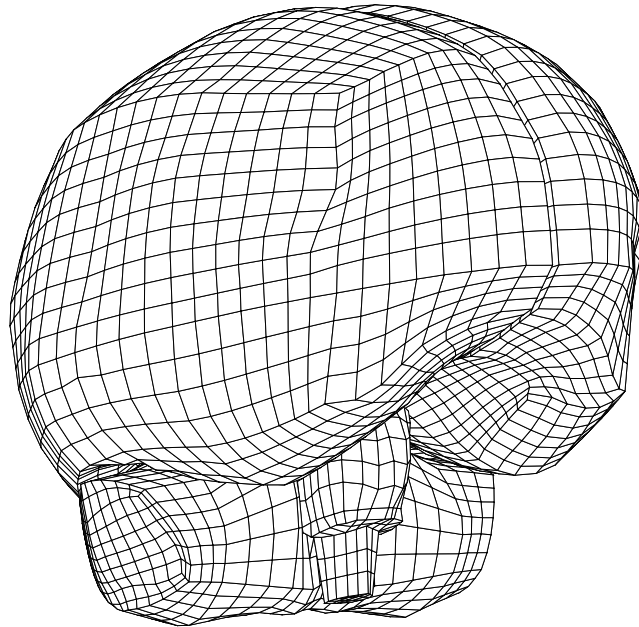


Figure 5.8: Hexahedral mesh of a brain, 15,036 cells.

provided to us [77] was assumed to be valid with no negative Jacobians. This reasoning was supported by the claim of the provider that “the commercial elasticity FE codes would fail if there was a negative Jacobian”. Our goal was: 1) to test this hypothesis using our metric and software; 2) to improve the mesh to permit more efficient, accurate nonlinear elasticity solution by the mesh provider. In step 1 our metric and scheme identified several “gap” areas (bounded by faces belonging to only one cell) inside the mesh, and the distortion metric located several severely-distorted elements with negative Jacobians. Most of these elements are adjacent to the boundaries of the domain (including “gap” boundaries), as can be seen in Figure 5.9. In this figure element coloring distinguishes between boundary (red) and interior (blue) nodes.

Smoothing of the initial mesh with $\theta = 0.8$ and fixed nodes on the boundaries and interfaces improves the quality of the mesh, as can be seen from three mesh cut-outs before and after smoothing, presented in Figure 5.10. The improvement in individual element quality is demonstrated in Figure 5.11. Here, the initial element is close to a degenerate hexahedron since its shape is almost prismatic. After smoothing, the element shape improves dramatically and it resembles a brick.

Each iteration of numerical optimization procedure took 23 seconds (on AMD 2.2GHz processor) for this example, where the Hessian matrix assembly required computing 64 contributions from each of 15,036 hexahedra in the mesh. The initial quality evaluation and nondegeneracy check was performed under a second of CPU time.

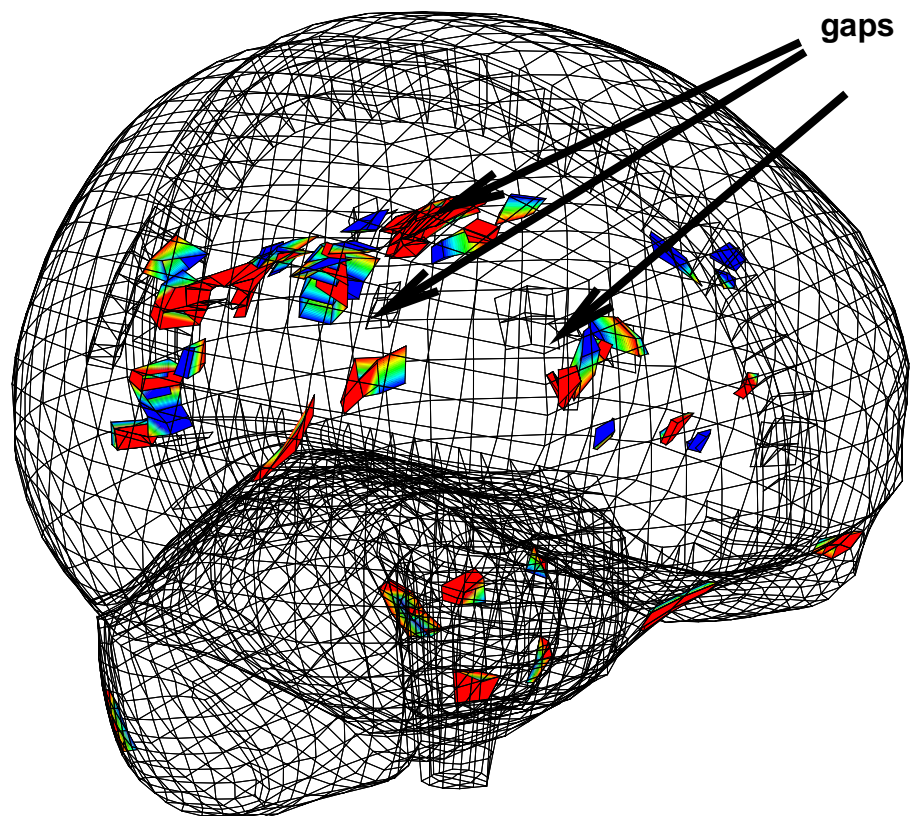


Figure 5.9: Hexahedral mesh of a brain: colored distorted elements and detected “gaps”.

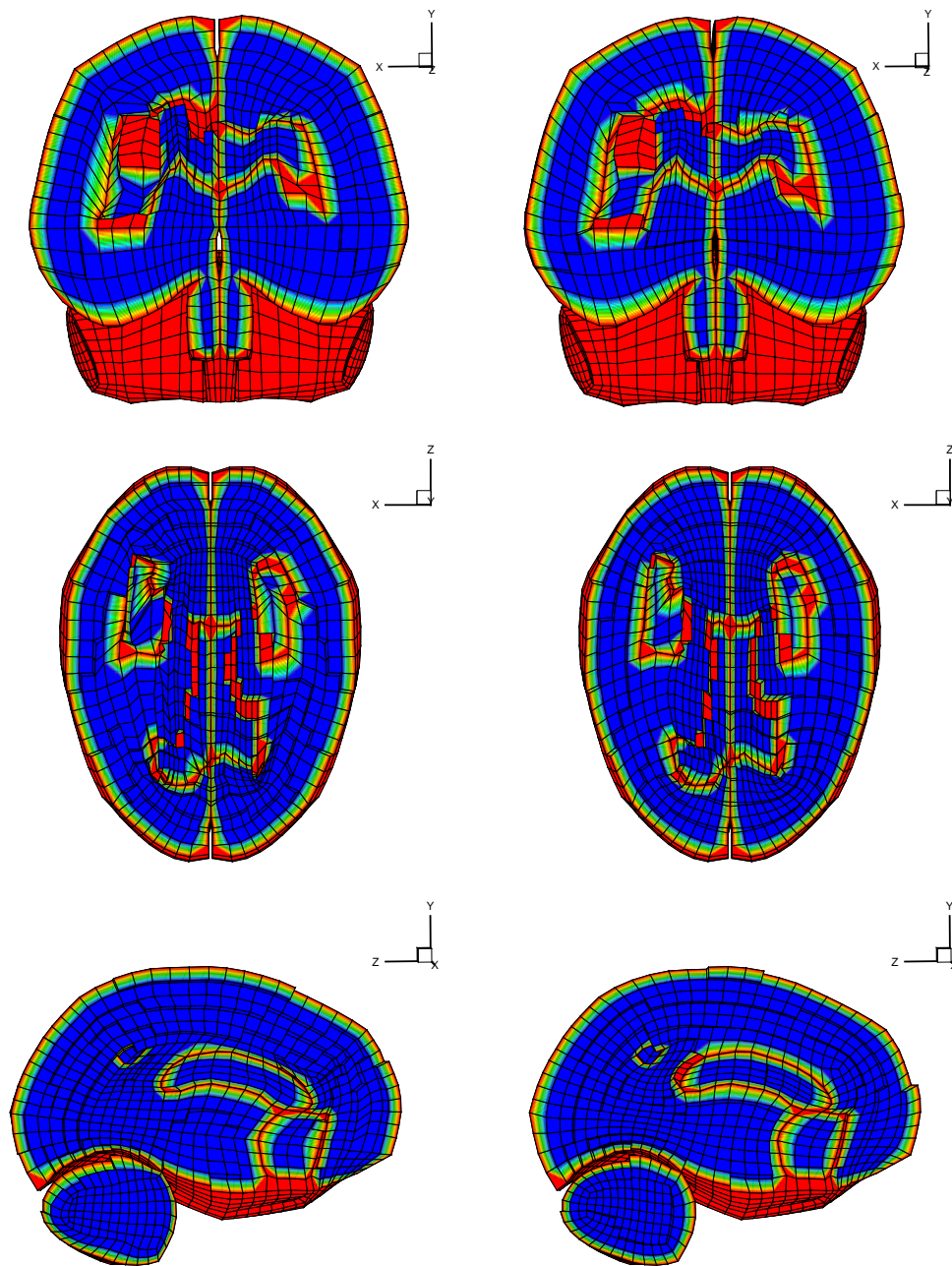


Figure 5.10: Hexahedral mesh of a brain: cut-outs before (left) and after smoothing (right).

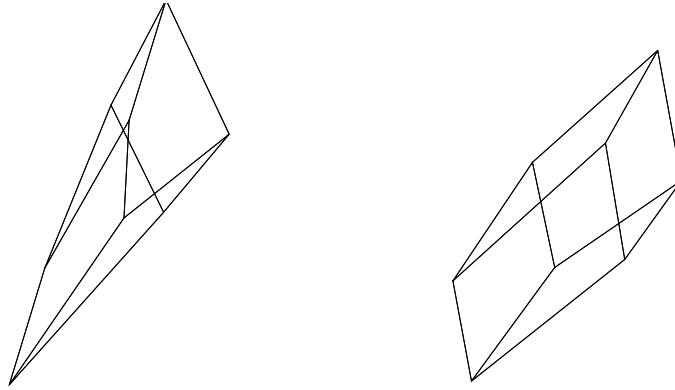


Figure 5.11: Hexahedral mesh of a brain: one element before (left) and after smoothing (right).

5.2 Valence treatment

The local valence of a vertex is defined here as the number of elements or cells that meet at that vertex. Most, if not all, current smoothing algorithms produce significant local dilation effects at vertices where valence differs from the mean [78]. The following numerical tests demonstrate the behavior of the smoothing algorithm when operating on a grid with varying valence. Since all unstructured grids have varying interior valence, we examine this case in detail.

5.2.1 Algorithm performance on meshes with points of changing valence.

In this subsection we will show the results of numerical tests for 4 cases of meshes with changing valence and then discuss these results at the end.

2D triangular meshes Figure 5.12 demonstrates the smoother behavior on triangular grids with changing valence. All boundary nodes are fixed in this example. There is some disparity in dilation effects but the behavior is satisfactory for smoothing with $\theta = 0.8$, whereas smoothing with $\theta = 0.2$ produces significant dilation.

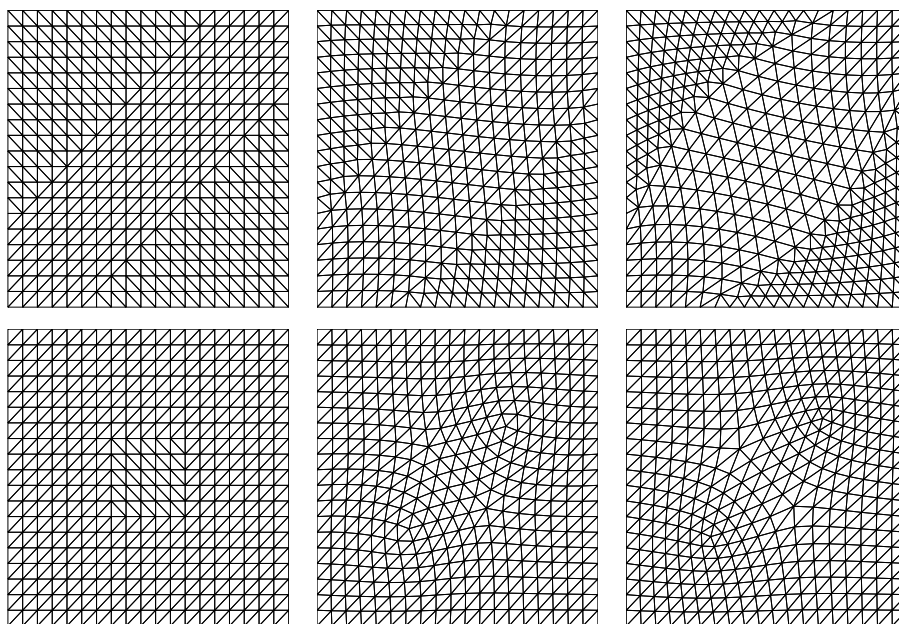


Figure 5.12: Triangular grids. Initial meshes (left), smoothed meshes, $\theta = 0.8$ (middle) and smoothed meshes $\theta = 0.2$ (right).

2D quadrilateral meshes The effect of smoothing on a mesh of quadrilateral cells is shown in Figure 5.13. The initial grid consists of two block-generated subgrids corresponding to a trapezoidal subdomain and its continuation to the annular region via an intermediate transition. Note the 2 interior points are valence 3 and other interior nodes are valence 4. Boundary nodes on the exterior circular boundary are fixed and nodes on the vertical diameter boundary of the semicircle are allowed to “slide” along this line. The initial mesh and the smoothed meshes for $\theta = 0.8$ and $\theta = 0.2$ respectively, after 3 iterations are shown. The minimal quality $(Q_\theta)_{\min}$, minimal value of the Jacobian determinant, and functional value \mathcal{I}_h for this test are graphed in Figure 5.14 as functions of the number of iterations.

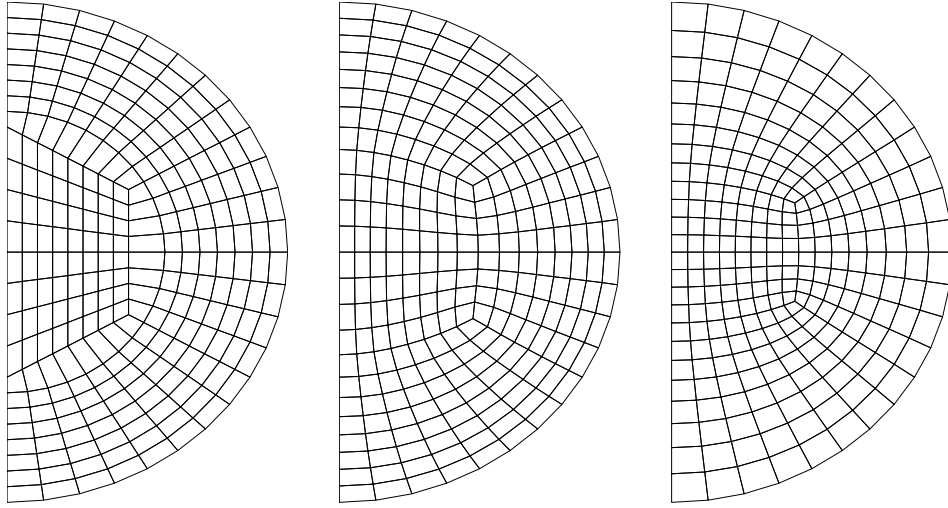


Figure 5.13: Quadrilateral grid smoothing. From left to right: initial grid, grid after 3 iterations of the smoother with $\theta = 0.8$, $\theta = 0.2$.

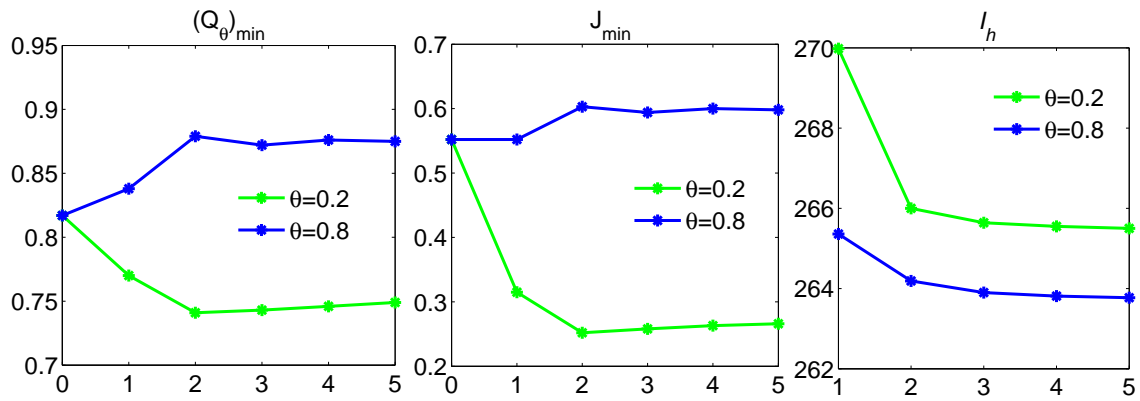


Figure 5.14: Smoothing. $(Q_\theta)_{\min}$, J_{\min} and I_h vs number of iterations.

3D meshes Let us now consider two 3D examples of grids with varying valence. First we examine a hexahedral grid with varying valence (Figure 5.15) that is generated by CUBIT [79]. The problem domain is composed of three tube segments that intersect as shown in Figure 5.15 and the main area of difficulty is the interior grid near the intersection. An expanded view of the 2D midplane slice near this area is shown on the extreme right of the figure. The interior grid on the section after 10 iterations of smoothing with $\theta = 0.8$ (size

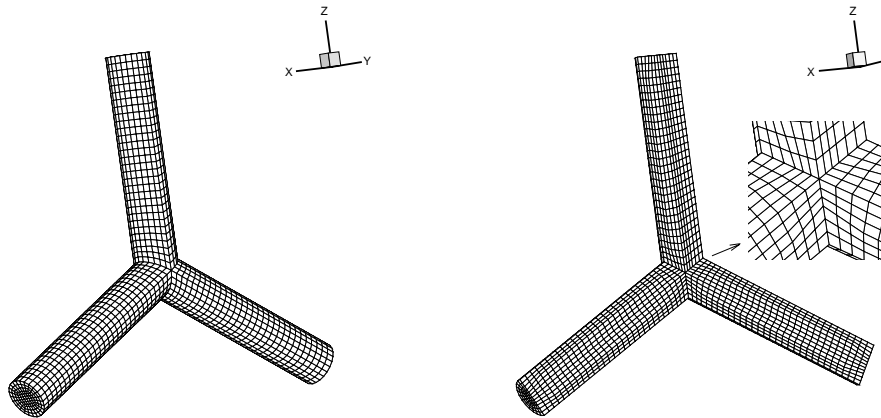


Figure 5.15: Initial 3D grid.

control) is shown on the left in Figure 5.16, and the result of smoothing with $\theta = 0.2$ (shape control) is shown on the right in the same Figure.

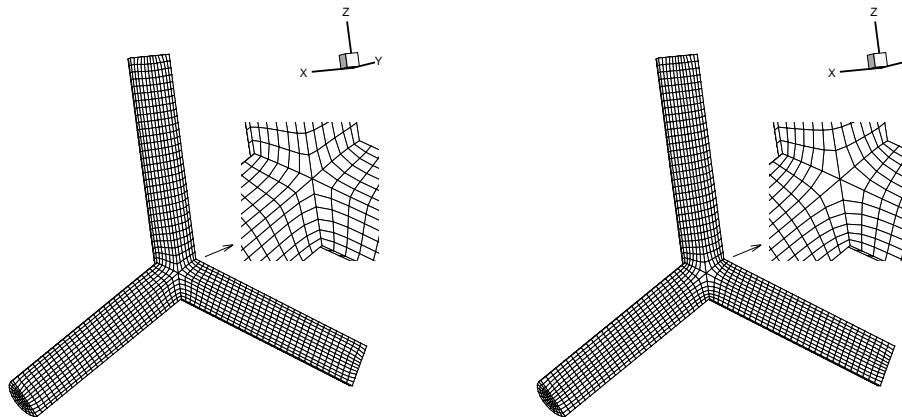


Figure 5.16: Grid slice after smoothing with $\theta = 0.8$ (left) and $\theta = 0.2$ (right).

Next, let us consider a 3D example of a hybrid mesh consisting of hexahedra and prisms. The mesh is constructed inside a sphere, and a 1/8 cut-away of the initial mesh is shown in Figure 5.17. This test problem was suggested by a DoE Lab since it exhibits problems for other mesh smoothing schemes and is important to their application class. The boundary nodes on the surface of the sphere are fixed during smoothing. Figure 5.18 demonstrates meshes obtained after smoothing with two values of θ . In this example the mesh includes hanging nodes and nodes with irregular valence (nodes belonging to cells of both types and valence 6 nodes of hexahedral cells - generalization of the previous 2D example).

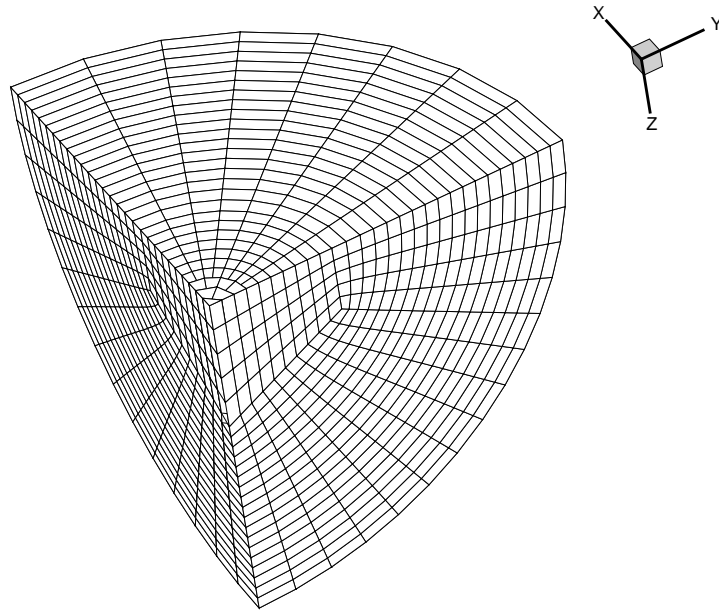


Figure 5.17: Cut-away showing 1/8 of a sphere for initial hybrid 3D grid.

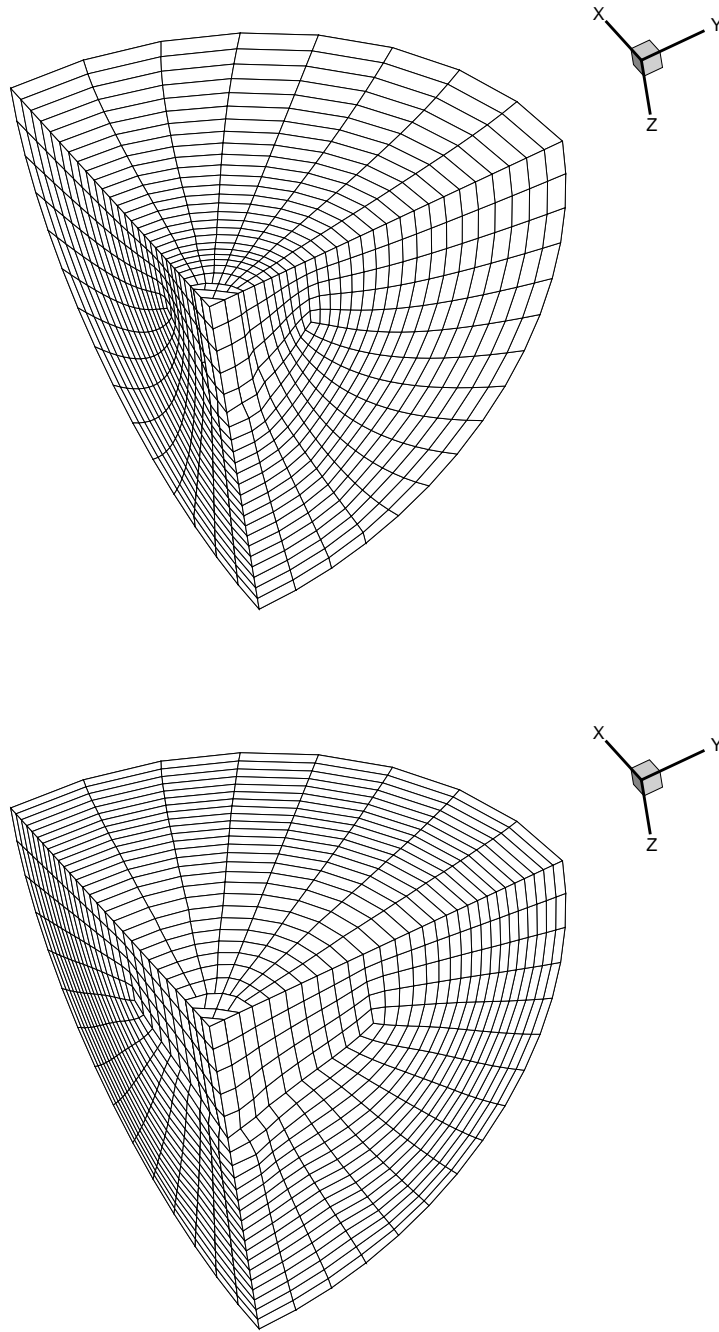


Figure 5.18: Cut-away showing 1/8 of a sphere for hybrid 3D grid smoothed with $\theta = 0.2$ (top) and $\theta = 0.8$ (bottom).

Results from these numerical tests demonstrate that significant dilation may occur in grids with varying valence when smoothing with θ near zero; that is, with the accent on the shape control metric (similar results are seen for Laplacian-type smoothers). Increasing the size control θ alleviates this problem. It can also be noticed (see Figure 5.14) that minimization of a global functional with more weight on shape control does not improve the minimal values of the quality metric and the Jacobian determinant compared to the initial state (although the global functional value decreases). That is, the value of such a functional depends more on the global mesh structure than on any individual cell contribution, as one might expect. On the other hand, when the weight is shifted towards the size control metric, all local quality metric values improve during smoothing. Thus, adding weight to the dilation metric makes our smoothing procedure less sensitive to the varying valence of the mesh. Nevertheless, we must always keep some nonzero weight on the shape control part of the metric in order to preserve the properties and validity of the smoothing algorithm. In the remainder of this section we will examine the effect of varying valence on both shape and size control parts of the functional.

5.2.2 Properties of the smoothing functional on meshes with changing valence

We first examine the local behavior of the discrete functional (2.23) on a patch of cells, then look at the global effect of smoothing on meshes with varying valence.

Patch of triangular elements Following [78], let us consider a patch of $val > 2$ equilateral triangular elements shown in Figure 5.19 for the case $val = 6$.

For each element in the initial patch configuration we have

$$\phi = \frac{2\pi}{val}, \quad \beta_0 = \frac{2 - \cos \phi}{\sqrt{3} \sin \phi}, \quad \mu_0 = \frac{v\sqrt{3}}{4 \sin \phi} + \frac{\sin \phi}{v\sqrt{3}}.$$

Now we move one vertex A_0 a distance δ to a position A . The functional for the new patch depends upon δ as

$$\mathcal{I}_h(\delta) = (val - 2)E_\theta(0) + 2E_\theta(\delta).$$

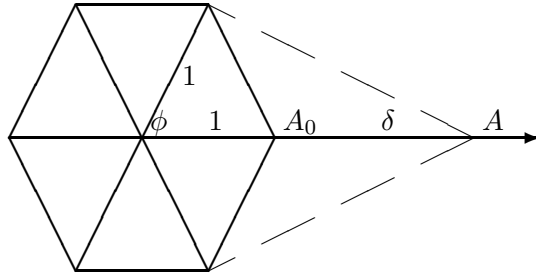


Figure 5.19: Patch of triangles.

Its derivative w.r.t. δ is equal to

$$\mathcal{I}'_h(\delta) = \frac{1}{\sqrt{3} \sin \phi} \left(2(1 - \theta) + \frac{2\theta \sin^2 \phi}{v} + \frac{4(\theta - 1) - 3\theta v}{2(1 + \delta)^2} \right).$$

The minimum of this functional is achieved when $\mathcal{I}'_h(\delta) = 0$, that is when

$$\delta = \sqrt{\frac{1 - (1 - 3v/4)\theta}{1 - \theta + \theta/v \sin^2 \phi}} - 1.$$

If $\theta = 0$ (only shape control is imposed), the minimum is at $\delta = 0$, independent of valence val . If $\theta = 1$ (only size control), the minimum is at $\delta = \sqrt{3}v/(2 \sin \frac{2\pi}{val}) - 1$ and is controlled by the value of desired element area v .

Patch of quadrilaterals The setting is similar to the previous case (see Figure 5.20) and

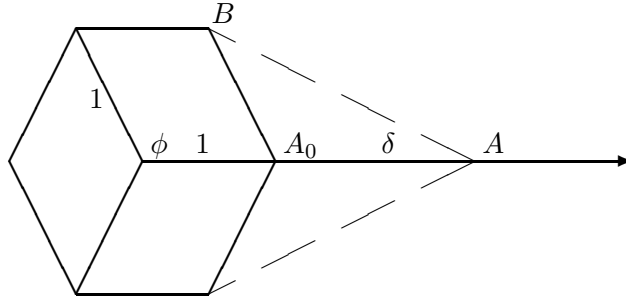


Figure 5.20: Patch of quadrilaterals.

the functional becomes

$$\mathcal{I}(\delta) = (val - 2)E_\theta(0) + \theta/2 \left(\frac{v}{(1 + \delta) \sin \phi} + \frac{(1 + \delta) \sin \phi}{v} \right) +$$

$$+(1-\theta)/2 \left(\frac{2 + 2(1+\delta)^2 + \delta^2 - 2\delta \cos \phi}{2(1+\delta) \sin \phi} + \frac{\delta^2 - 2\delta \cos \phi}{2 \sin \phi} \right),$$

with derivative

$$\begin{aligned} \mathcal{I}'_h(\delta) = & \frac{1-\theta}{2 \sin \phi} \left(3/2 + \delta - \cos \phi - \frac{3/2 + \cos \phi}{(1+\delta)^2} \right) + \\ & + \frac{\theta}{2 \sin \phi} \left(\frac{\sin^2 \phi}{v} - \frac{v}{(1+\delta)^2} \right). \end{aligned}$$

The contours $\mathcal{I}'_h(\delta) = 0$ as functions of valence val are shown in Figure 5.21 for different values of θ .

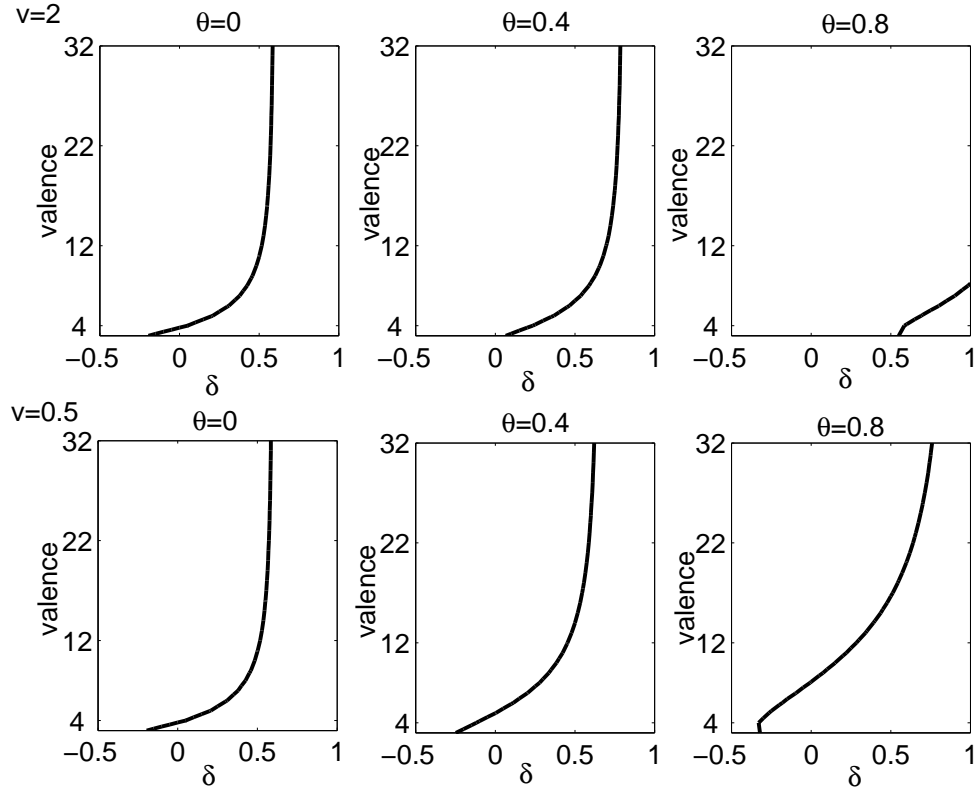


Figure 5.21: Optimal position δ as a function of valence and θ . On top: $v = 2$, on bottom: $v = 0.5$.

From Figure 5.21 we can conclude that smoothing of the quadrilateral grid with only shape control results in attraction of points to a node of valence smaller than regular and repulsion of points from a node of valence larger than regular. The same behavior

holds for any Laplace-type smoothing. Addition of size control to the functional introduces control over this attraction/repulsion force through the values of desired element area v and parameter θ . Figure 5.21 also demonstrates that, as expected, large values of target cell area v induce dilation, whereas small values of v promote attraction. The effect is more dramatic with the increase of θ (weight shifted towards the size control part of the functional).

Functional at a node Now, let us consider an interior node of a quadrilateral grid in a different setting, where all nodes on the patch boundary are fixed and only the interior node is allowed to move. Let us denote by l_1, \dots, l_{val} the lengths of all edges connected to this node. Let the angles between these edges be numbered in a counterclockwise manner as $\alpha_1, \dots, \alpha_{val}$ (see Figure 5.22). The angles satisfy an obvious restriction $\sum_{i=1}^{val} \alpha_i = 2\pi$.

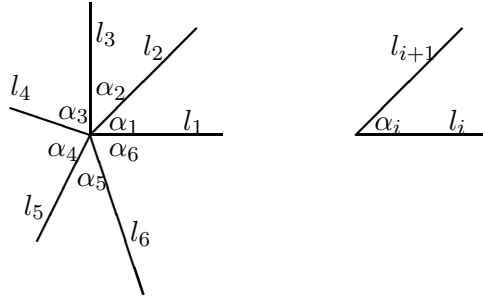


Figure 5.22: Interior node of valence $val = 6$.

The functional value at the node is equal to

$$\mathcal{I}_h(\text{node}) = (1 - \theta) \sum_{i=1}^{val} \frac{l_i + l_{i+1}}{2 \sin \alpha_i} + \frac{\theta}{2} \sum_{i=1}^{val} \left(\frac{l_i l_{i+1} \sin \alpha_i}{v} + \frac{v}{l_i l_{i+1} \sin \alpha_i} \right)$$

and achieves its minimum value

$$\mathcal{I}_h(\text{node})_{\min} = (1 - \theta) \frac{val}{\sin(\frac{2\pi}{val})} + \theta val$$

when $\alpha_1 = \dots = \alpha_{val} = \frac{2\pi}{val}$ (due to symmetry) and $l_1 = \dots = l_{val} = \sqrt{v/\sin(\frac{2\pi}{val})}$. Thus, such a symmetric configuration is preferable when it can be achieved under the given boundary and other constraints.

The position of any node influences the quality of the whole patch of cells surrounding the node. Suppose that in each cell of the patch the coordinates of three nodes (the interior node and two connected with it by edges) are determined by the conditions above. Let us consider the functional sensitivity to the position of the remaining vertices. It suffices to examine a typical cell. The level sets of the shape control metric β , as a function of coordinates of the fourth node (B in Figure 5.20) of a quadrilateral cell within the patch surrounding nodes with valence 3 and 5 are shown in Figure 5.23. In both cases the metric

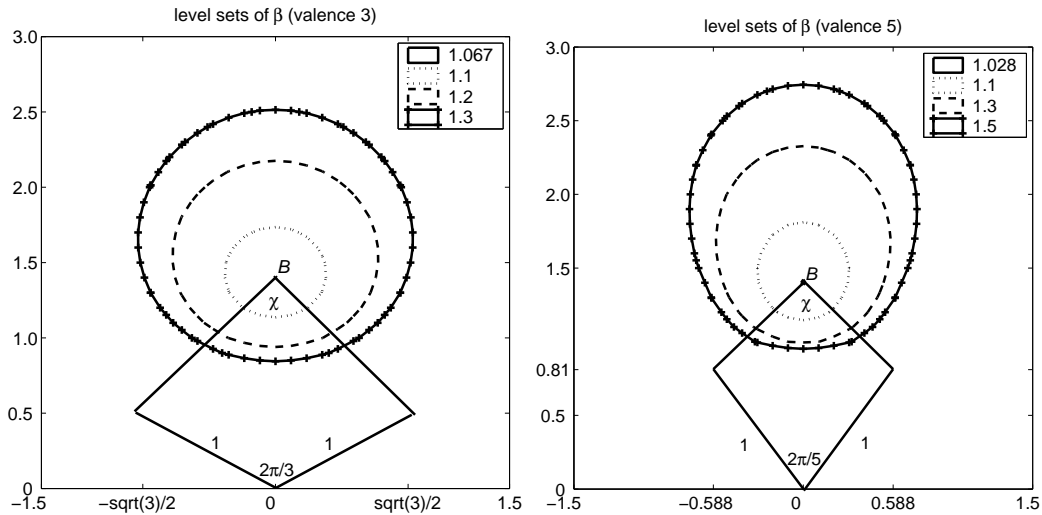


Figure 5.23: Level sets of β on a patch of valence 3 (top) and 5 (bottom).

β has its minimum when the angle χ at the free vertex is equal to $\pi/2$. Thus, the edges forming this angle are forced to be 25% longer (than 1) in the case of the valence 3 patch and 17% shorter in the case of the valence 5 patch. Thus, the local dilation or contraction effect near points of irregular valence is caused by the tendency of a Laplace-type smoother to (1) preserve symmetry, (2) keep edge lengths nearly equal and (3) attain a maximum possible (under these conditions) number of right angles in the mesh.

If we now suppose that all other vertices in the grid have valence 4 and consider the layer of cells surrounding the irregular valence patch, similar reasoning implies that node clustering or unclustering near the point of irregular valence is due to the restriction on the sum of angles imposed by the global mesh connectivity. In order to demonstrate that in this case clustering is independent of the central (irregular valence) node contribution (even of the patch contribution), we performed smoothing of the test grid with deleted patches of cells surrounding valence 3 nodes. That is, we deleted the cells and considered different configurations of the resulting inner boundary. Smoothing is performed with value $\theta = 0.2$, and boundary nodes are allowed to “slide” tangentially along the outer boundary. The results for a coarse grid are shown in Figure 5.24. Similar behavior is displayed on finer grids.

In other situations, irregular valence nodes tend to induce mainly local dilation or contraction of the surrounding cells, as in the following example. In this case we consider a mesh of regular triangles and a uniform mesh of square cells in a large enough domain. That is, a domain large enough that boundaries do not affect the behavior of the smoother on the interior patches of interest. For the initial grid configuration we removed one node in the center for each of the two meshes and reconnected the remaining vertices (see Figure 5.25). Thus, we obtained several vertices of varying valence inside each mesh, with the majority of the vertices being of regular valence. The results of the smoothing for these meshes with different values of θ are shown in Figure 5.26, and in all these cases smoothing affects only the patches of cells surrounding the irregular valence vertices. That is, the effect of valence change attenuates significantly under this smoother and weighting. This suggests that the effect of local valence irregularity can be addressed appropriately in this way. Hence, we anticipate the approach will improve element shape and not be impacted adversely by valence changes. This also suggests that local subgrid or patch optimization may be computationally efficient. However, in general, the exterior mesh will vary globally unlike the uniform meshes of Figures 5.25 and 5.26.

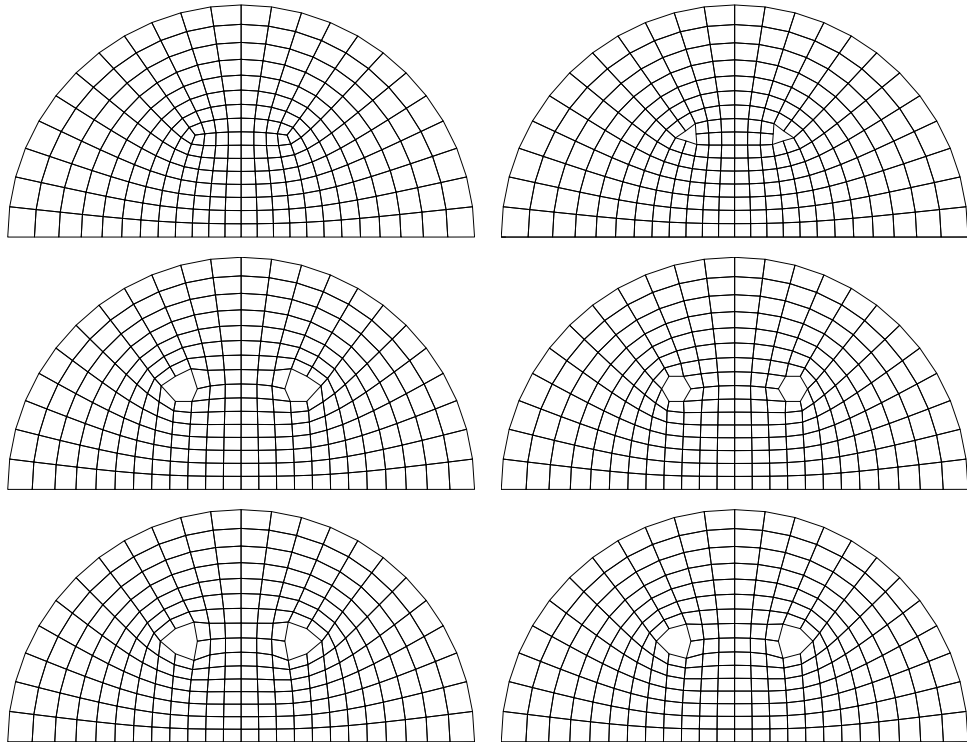


Figure 5.24: From top to bottom, left to right: whole smoothed grid, smoothed grid with free nodes on the boundaries of deleted patches, smoothed grid with patch boundaries fixed from initial grid, smoothed grids with vertex angle χ equal to 120, 80 and 90 degrees.

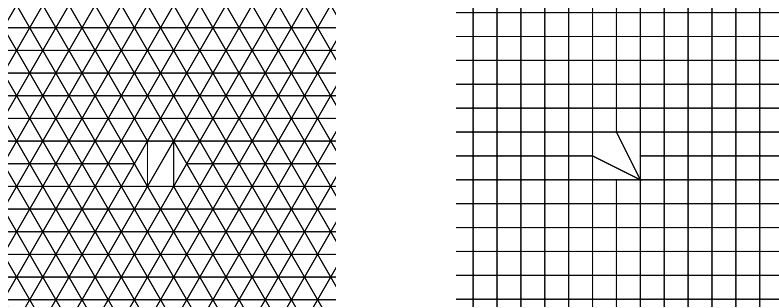


Figure 5.25: Zoom on the initial regular grids with one node removed.

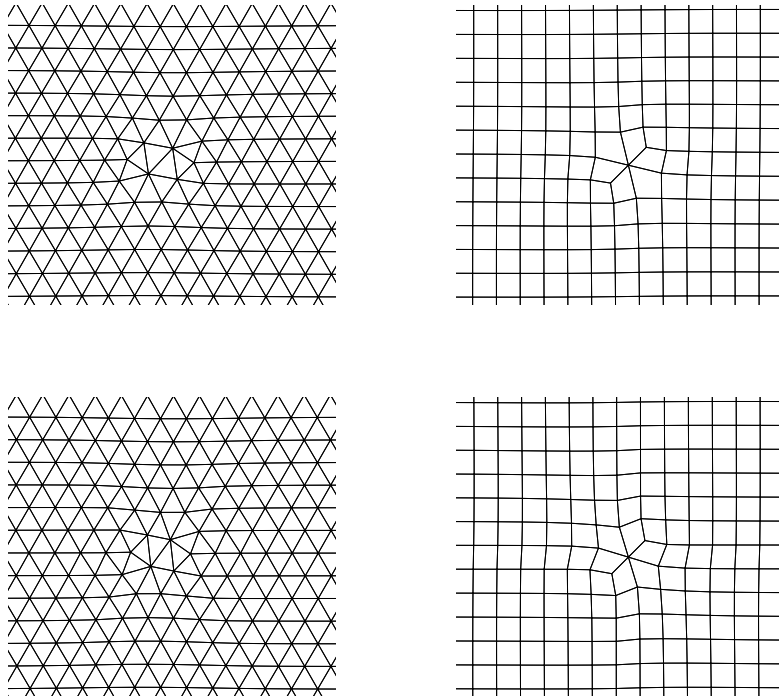


Figure 5.26: Zoom on the smoothed grids: on top $\theta = 0.2$, on bottom $\theta = 0.8$.

5.2.3 Bounds on angles

We conjecture that, in general, the maximum and minimum angles occur in the smoothed grid at the vertices with minimal (maximal) valence (excluding boundary influence). We do not have a proof of this yet, but we are able to obtain estimates on maximal and minimal angles in terms of distortion measure β for the case of triangular and tetrahedral grids, as described below. (Size distortion measure μ does not provide any control over cell angles.)

For the triangular element with area A and edges $l_1 \leq l_2 \leq l_3$, the shape distortion measure is reduced to

$$\beta = \frac{l_1^2 + l_2^2 + l_3^2}{4\sqrt{3}A}. \quad (5.1)$$

Let us denote the smallest angle by α_1 ; then we can rewrite the distortion measure as

$$\beta = \frac{l_2^2 + l_3^2 - l_2 l_3 \cos \alpha_1}{2\sqrt{3}A}.$$

For the sine of the smallest angle we, thus, have

$$\begin{aligned} \sin \alpha_1 &= \frac{2A}{l_2 l_3} = \frac{l_2^2 + l_3^2 - l_2 l_3 \cos \alpha_1}{\sqrt{3}\beta l_2 l_3} \geq \\ &\geq \frac{2 - \cos \alpha_1}{\sqrt{3}\beta}. \end{aligned} \quad (5.2)$$

From the last inequality and using the fact that $\alpha_1 \leq \pi/3$ it is easy to obtain the following estimate

$$\alpha_1 \geq \arcsin \left(\frac{2 - \sqrt{1 - \beta^{-2}}}{\sqrt{3}\beta + 1/(\sqrt{3}\beta)} \right). \quad (5.3)$$

For the largest angle α_3 in the triangle we can show (repeating (5.2)) the estimate

$$\sin \alpha_3 \geq \frac{2 - \cos \alpha_3}{\sqrt{3}\beta}.$$

If this angle is obtuse $\alpha_3 \geq \pi/2$ then

$$\sin(\pi - \alpha_3) \geq \frac{2 + \cos(\pi - \alpha_3)}{\sqrt{3}\beta}$$

and

$$\alpha_3 \leq \min \left(\pi - 2\alpha_1, \pi - \arcsin \left(\frac{2 + \sqrt{1 - \beta^{-2}}}{\sqrt{3}\beta + 1/(\sqrt{3}\beta)} \right) \right). \quad (5.4)$$

For the tetrahedron with volume V , solid angles $\gamma_1, \dots, \gamma_4$, and edges l_1, \dots, l_6 the shape distortion measure is

$$\beta = \frac{(\sum_{i=1}^6 l_i^2)^{3/2}}{72\sqrt{3}V}. \quad (5.5)$$

Using the estimates from [59], for the minimal solid angle γ_1 we get

$$1/(16\beta) \leq \sin(\gamma_1/2) \leq \sqrt[4]{8}/\sqrt{\beta}.$$

Thus,

$$\gamma_1 \leq 2 \arcsin \left(\frac{1}{16\beta} \right). \quad (5.6)$$

From [59] we also know that

$$\begin{aligned} \gamma_1 \leq \gamma_2 \leq \gamma_3 \leq \gamma_4 &\Rightarrow \\ \sin(\gamma_1/2) \leq \sin(\gamma_2/2) \leq \sin(\gamma_3/2) \leq \sin(\gamma_4/2). \end{aligned}$$

The tetrahedron is poorly shaped if γ_4 is close to 2π , i.e. when $2\pi - \gamma_4$ is small. However, since

$$\sin \left(\frac{2\pi - \gamma_4}{2} \right) \geq \sin(\gamma_1/2),$$

consequently

$$\gamma_4 \leq 2\pi - 2 \arcsin \left(\frac{1}{16\beta} \right), \quad (5.7)$$

which shows how the largest value of distortion measure for the grid can be used to estimate the bounds on the smallest and largest angles.

Figure 5.27 demonstrates the sensitivity of the angle bounds (5.3), (5.4) to the deformation of a triangular element. The type of deformation is schematically represented in the Figure: on the left, the base of the regular triangle is kept fixed, and the height varies from zero to twice the ideal height; on the right the base is fixed and the length of one adjacent edge varies from zero to twice the ideal, while keeping the angle between the base and this edge constant. The Figure shows that estimates are almost exact for the minimum angle and quite good for the maximum angle.

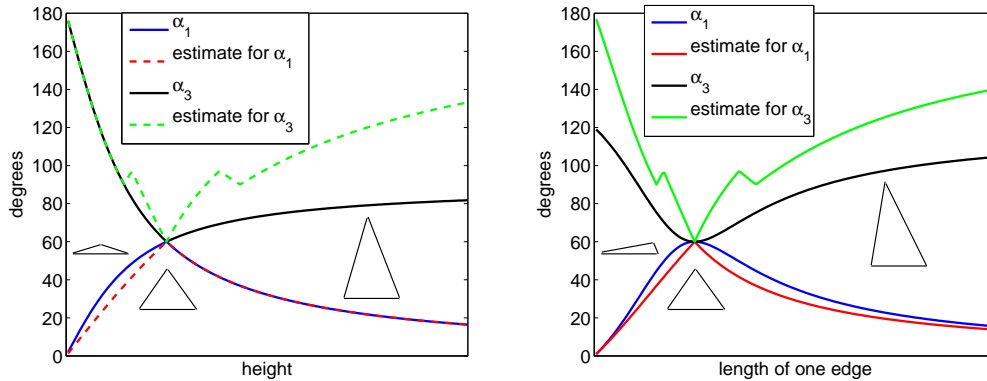


Figure 5.27: Sensitivity of angle bounds for triangles.

5.2.4 Algorithm with varying θ .

One approach to deal with the valence problem is to introduce an alternative target shape for the cells located near the irregular valence nodes. The drawback of this approach is that we do not know which shape should be considered ideal for these cells. (For example, what is the best configuration of the patch boundary in Figure 5.24?) A similar approach would be to enforce more size control near these irregular valence nodes and allow more shape control far from them. This can be achieved by varying parameter θ throughout the domain. Simply increasing or decreasing θ at a node with lower or higher valence is not enough. Our strategy is to identify the irregular valence nodes v_i , $i = 1, \dots, I$, for each such node compute a radius of its “domain of influence” $r_{v_i} = \min_j \{ \text{dist}(v_i, \partial\Omega), \frac{1}{2} \text{dist}(v_i, v_j) \}$, and define the piecewise-constant function θ on each cell by $\left\{ \theta(c) = 1 - \frac{\text{dist}(v_i, c)}{r_{v_i}}, \text{ if } \text{dist}(v_i, c) \leq r_{v_i} \right\}$. The implementation of this approach resulted in the central grid shown in Figure 5.28. The grid obtained with varying θ does not show much clustering near valence 3 points, and it still has nearly square elements close to the boundary of the domain.

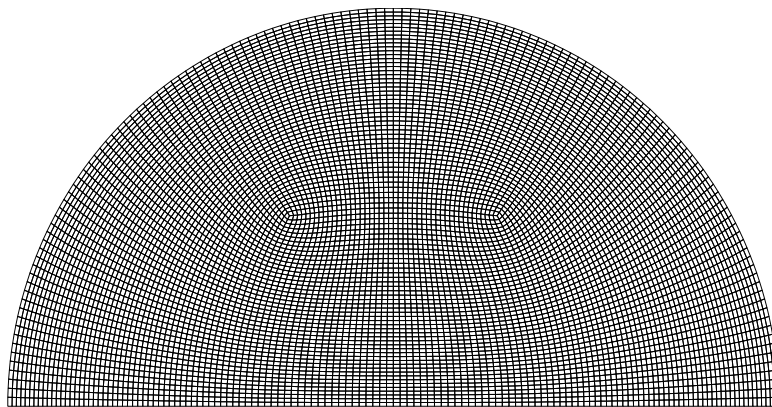
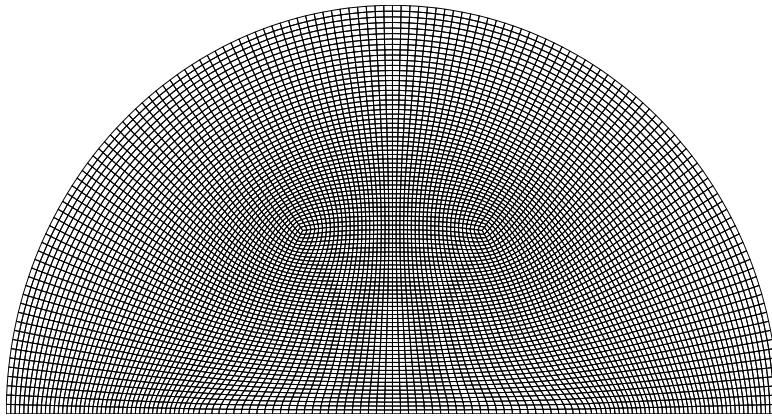
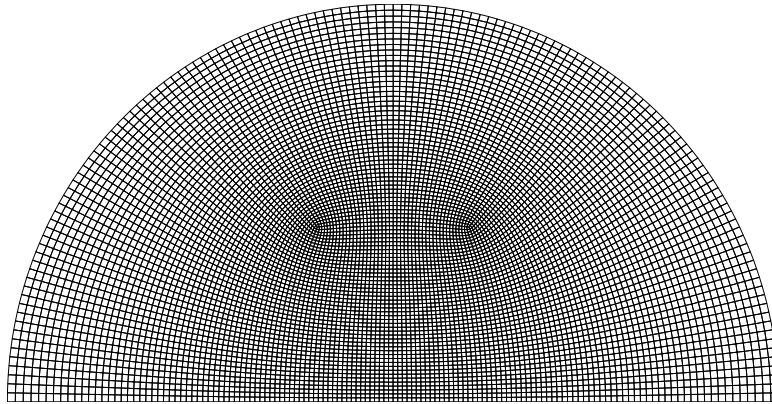


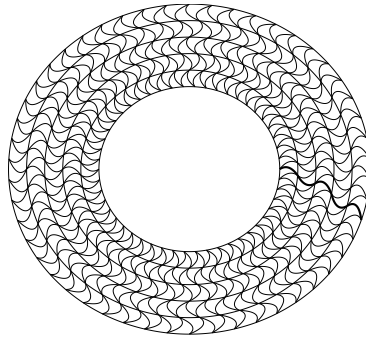
Figure 5.28: From top to bottom: grid smoothed with $\theta = 0.2$, varying θ , and $\theta = 0.8$.

5.3 Meshes with curvilinear elements

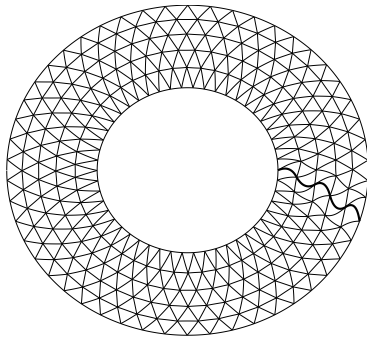
Curvilinear elements are most often used to provide better fit of domain boundaries and interfaces to improve the solution accuracy and are especially helpful for problems with moving boundaries/interfaces tracked by the mesh. Although quadratic FE bases are widely used, smoothing/improvement techniques for meshes of isoparametric quadratic elements have not been studied previously. In the following section we examine the performance of the present approach and algorithm on simple but representative 2D and 3D grids of quadratic simplices.

2D test case. First, we consider smoothing of 2D triangular grids generated inside a ring with a curvilinear cut or fracture. The domain boundaries are internal and external circles centered at the origin and a curved cut which is shown in bold in Figure 5.29 a). Boundary nodes are allowed to tangentially “slide” along the boundaries of the domain during smoothing; only the end nodes of the cut are fixed to preserve the geometry of the boundaries. Meshes obtained after 5 iterations of smoothing with $\theta = 0.8$ (Figure 5.29 b)) and $\theta = 0.2$ (Figure 5.29 c)) followed by 3 iterations of boundary node corrections contain only nondegenerate elements and preserve the curvature of the cut and the boundary. Note, however, that in order to keep valid elements, all edges of the quadratic triangles adjacent to the high curvature cut are forced to be curved. On the other hand, away from the high curvature boundaries the interior edges are close to straight line segments.

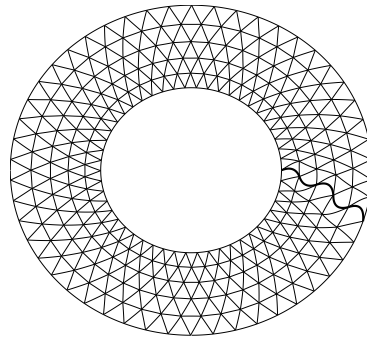
For the second example we keep the same domain geometry and mesh connectivity as in Figure 5.29 a), but place all interior nodes at the origin. Thus we obtain a folded mesh of curvilinear triangles as shown in Figure 5.30. Meshes after 15 iterations of untangling plus 5 iterations of smoothing with boundary node corrections are identical to several digits to the results of smoothing in Figure 5.29 b) and c). The evolution of an initially invalid mesh during the first 4 iterations of unfolding ($\theta = 0.2$) is presented in Figure 5.31. We can observe that the majority of the cells are untangled after 3 iterations, however it takes a dozen more iterations for the cells adjacent to the high-curvature cut to achieve a valid shape. The evolution of minimal quality and minimal Jacobian determinant variation during



a)



b)



c)

Figure 5.29: Grids of curved triangles: a) initial, b) smoothed with $\theta = 0.8$, and c) smoothed with $\theta = 0.2$.

smoothing and unfolding is shown in Figure 5.32.

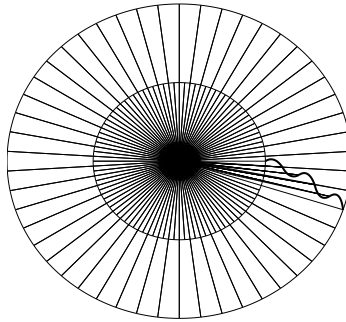
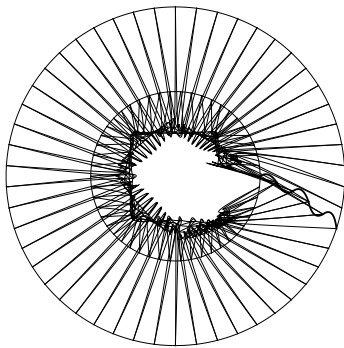
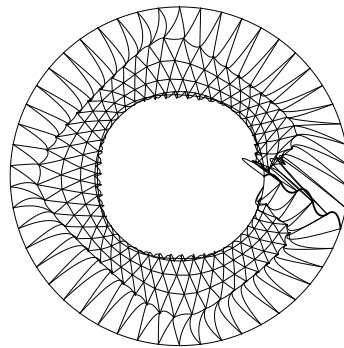


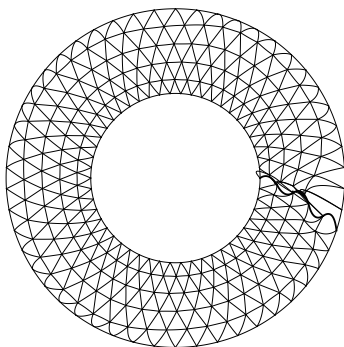
Figure 5.30: Folded grid of curved triangles.



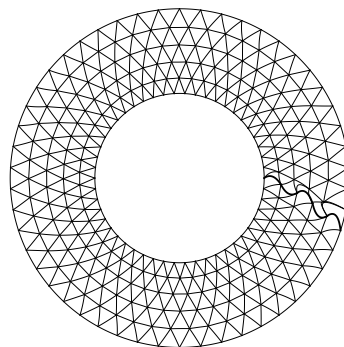
1 iter.



2 iter.



3 iter.



4 iter.

Figure 5.31: Evolution of grid of curvilinear triangles during unfolding.

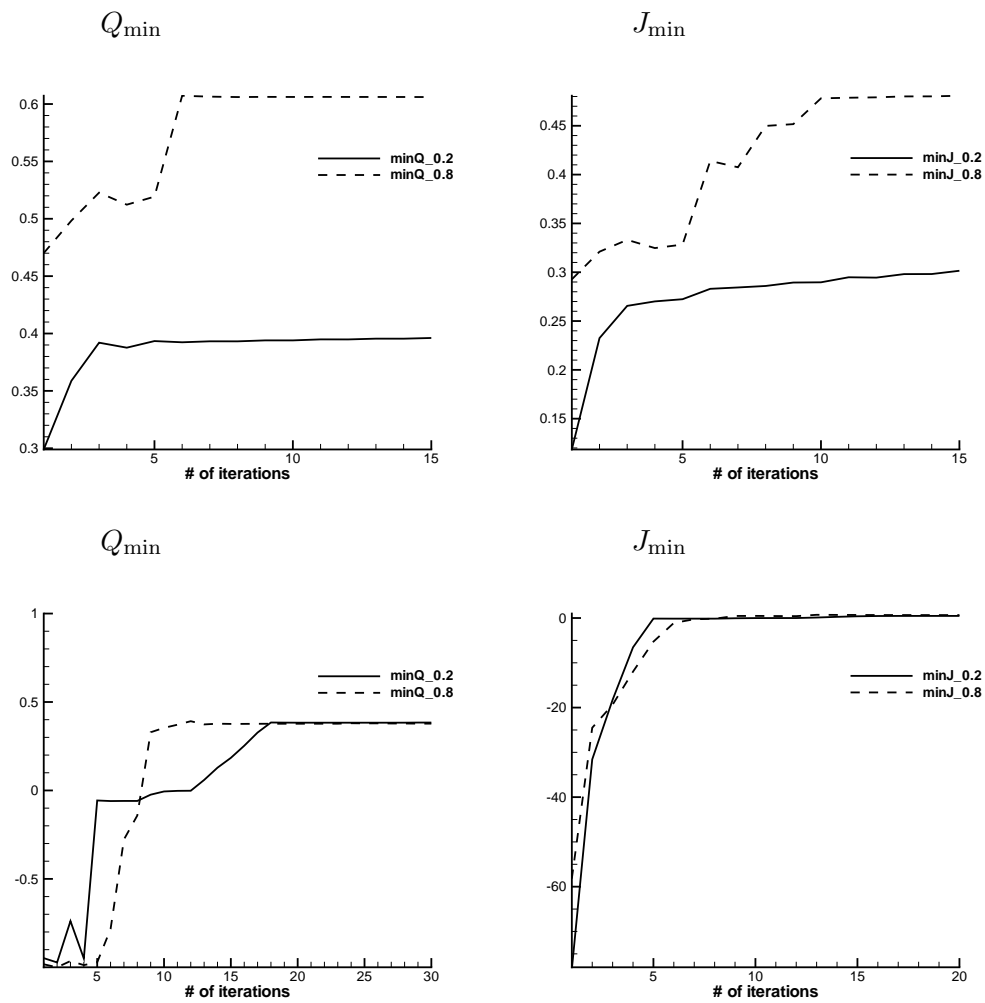


Figure 5.32: $(Q_{\theta})_{\min}$ and J_{\min} vs number of iterations. Upper figures: smoothing; lower figures: unfolding of the 2D curvilinear mesh.

3D test case. In this 3D numerical test example we start with a simple tetrahedral mesh inside a cylinder and “snap” the mid-edge nodes to lie on the curved cylindrical surface where appropriate (see Figure 5.33 a)). Hence, the mesh edges on the cylinder surface are approximated by a quadratic map. For clarity of presentation only the visible surface edges are shown. The discretization of the flat back surface is the same as for the front one except for a rotation through 30 degrees. There are no interior vertex nodes. Interior mid-edge nodes are free to move under the smoothing process. The mesh smoothed under

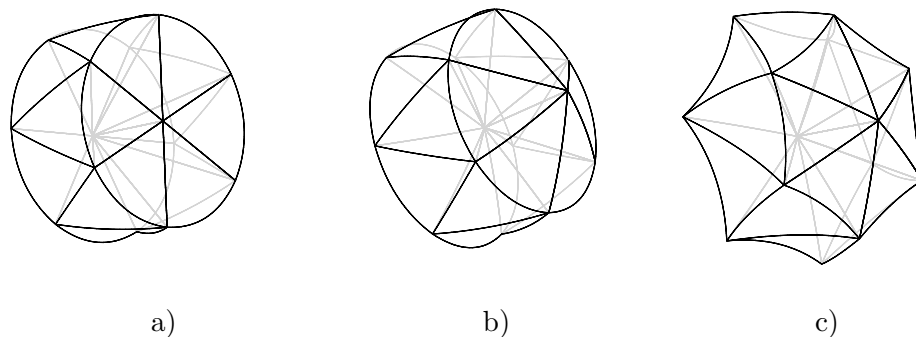


Figure 5.33: From left to right: a) curvilinear tetrahedral mesh inside a cylinder, b) smoothing result with fixed cylindrical boundary and c) with free boundary.

the condition of preserving the circular boundary of the cylinder but with the geometry constraint on the interior front and back faces of the cylinder relaxed is shown in Figure 5.33 b). In this resulting mesh the total volume is preserved, but the edge lying on the “cylindrical” symmetry axis of the domain moves so that the front circular surface (initially flat) becomes convex and the back surface - concave. In this way, the shape of all tetrahedra becomes closer to ideal. The mesh in Figure 5.33 c) is obtained by allowing all the nodes to move freely during smoothing. The volume of the domain is again preserved, but the areas of circular surfaces which were flat in the original mesh change. Also the front surface turns slightly to align radial edge directions more closely with those on the back surface. This configuration allows for even more improvement in element shape than in result b).

5.4 Effect of mesh distortion on the problem solvability

5.4.1 Condition number study

Since we want to have a practical understanding of the effect of mesh improvement on solvability after smoothing, we compute the condition numbers κ for a mass matrix M and a stiffness matrix K for the Laplace problem on several representative meshes, as well as derive theoretical predictions for their values. We assume here that Dirichlet boundary conditions apply and both mass and stiffness matrices are symmetric positive definite.

The series of numerical tests performed with 3D hexahedral meshes leads to the following observations:

1. Local distortion has almost no effect on $\kappa(M)$ and $\kappa(K)$, as well as on a solution to the Laplace problem;
2. Local tangling makes the stiffness matrix noninvertible, but does not affect mass matrix conditioning; severe local tangling results in negative masses for adjacent elements;
3. Small distortion of all elements leads to increase in both condition numbers;
4. $\kappa(K)$ worsens significantly when large elements are adjacent to small ones, but not in the case when transition between different sizes is gradual.

With regards to the smoothing procedure, as we already observed in Section 5.2, smoothing with shape control does not improve the individual worst values of the quality metric that occur near the irregular valence points. Whereas size control helps to improve all the values of quality. The conditioning of mass and stiffness matrices follows the behavior of the extremal values of quality and Jacobian determinant.

This last remark leads us to develop theoretical estimates, concerning the relation between the maximum value of mesh quality E_θ and the conditioning of mass and stiffness matrices for that mesh. Mass matrix elements are computed as follows:

$$M_{i,j} = \sum_{c=1}^{N_c} \int_{\Omega_c} \varphi_i \varphi_j d\mathbf{x} = \sum_{c=1}^{N_c} \int_{\hat{\Omega}_c} \varphi_i \varphi_j \det S d\vec{\xi} \quad (5.8)$$

$$\begin{aligned}
&= \sum_{c=1}^{N_c} \sum_{q(c)=1}^{N_q} \varphi_i(q) \varphi_j(q) \det S|_{q(c)} \sigma_{q(c)} = \\
&= \left(\sum_{c=1}^{N_c} \sum_{q(c)=1}^{N_q} a_{q(c)} \det S|_{q(c)} \right) M_{i,j}^{ideal},
\end{aligned}$$

where M^{ideal} is a mass matrix computed on a reference mesh, φ_i , $i = 1, \dots, N$ are the FE basis functions, and the constant coefficients $a_{q(c)} \geq 0$ satisfy $\sum_{c=1}^{N_c} \sum_{q(c)=1}^{N_q} a_{q(c)} = 1$. Thus, the i^{th} eigenvalue of the mass matrix satisfies

$$\max(\det S) \geq \frac{\lambda_i(M)}{\lambda_i(M^{ideal})} \geq \min(\det S), \quad (5.9)$$

and the condition number can be bounded as

$$\kappa(M) \leq \frac{\max(\det S)}{\min(\det S)} \kappa(M^{ideal}). \quad (5.10)$$

Similarly, the stiffness matrix elements can be written as:

$$\begin{aligned}
K_{i,j} &= \sum_{c=1}^{N_c} \int_{\Omega_c} (\nabla \varphi_i)^T \nabla \varphi_j d\mathbf{x} = \\
&= \sum_{c=1}^{N_c} \int_{\hat{\Omega}_c} (\nabla_{\xi} \varphi_i)^T S^{-1} S^{-T} \nabla_{\xi} \varphi_j \det S d\vec{\xi},
\end{aligned}$$

where by γ , Γ we denote the smallest and largest dimensionless singular values of the Jacobian matrix:

$$\gamma^2 v^{2/n} I \leq S^T S \leq \Gamma^2 v^{2/n} I. \quad (5.11)$$

From the definition of the singular values, we can write

$$S^{-1} S^{-T} = U^T \text{diag}(\gamma_k^{-2}) U v^{-2/n},$$

where U is an orthogonal matrix $U^T = U^{-1}$. The stiffness matrix above becomes

$$K_{i,j} = \sum_{c=1}^{N_c} \sum_{q(c)=1}^{N_q} (U_q \nabla_{\xi} \varphi_i(q))^T \text{diag}(\gamma_k^{-2})|_q (U_q \nabla_{\xi} \varphi_j(q)) v^{-2/n} \det S_q \sigma_q$$

and it follows that

$$\max_{q(c)} \left(\frac{\det S_q}{\gamma_q^2 v^{2/n}} \right) \geq \frac{K_{i,j}}{K_{i,j}^{ideal}} \geq \min_{q(c)} \left(\frac{\det S_q}{\Gamma_q^2 v^{2/n}} \right), \quad (5.12)$$

where $K_{i,j}^{ideal}$ is a stiffness matrix computed on a reference mesh. Thus, by continuity of the 2-norm, the estimates for the condition number of the stiffness matrices are related as follows

$$\kappa(K) \leq \frac{\max\left(\frac{\det S}{\gamma^2}\right)}{\min\left(\frac{\det S}{\Gamma^2}\right)} \kappa(K^{ideal}). \quad (5.13)$$

The singular values of the Jacobian matrix and its determinant can be estimated in terms of our local distortion measure $\beta(S)$ and dilation measure $\mu(S)$ (or, equivalently, in terms of the total metric E_θ). Thus, the condition number estimates (5.10) and (5.13) represent the dependence between the mesh quality and matrix conditioning, and they can be used to predict the difference in computational cost for iterative linear system solver on different meshes.

For the series of test grids presented in Figure 5.34, the condition numbers and their estimates are shown in Figure 5.35. In estimates for the stiffness matrix conditioning we assumed $\Gamma\gamma = O(1)$ and computed the proportionality coefficient in (5.13) as

$$n^2(\beta_{\max})^{4/n} \frac{(\max(\det S))^{1+2/n}}{(\min(\det S))^{1-2/n}}, \quad (5.14)$$

using the estimate

$$\Gamma^n \leq n^{n/2} \beta \det S$$

for the maximum singular value of the Jacobian matrix in terms of distortion metric. As we can observe from Figure 5.35, our theoretical predictions are in qualitative agreement with the computed values. The overestimation of the predictions is due to fact that we take extremum values of metrics over the whole computational mesh in (5.14). Thus, our estimate (5.14) assumes the worst case scenario: all cells in the mesh have the worst quality. However, the relative difference in condition numbers for different smoothing strategies is in agreement with the predictions. Another important observation we can draw from these estimates is that, for a highly distorted grid ($E_\theta \gg 1$), the condition number of the stiffness matrix is proportional to $(\max E_\theta)^{4/n}$.

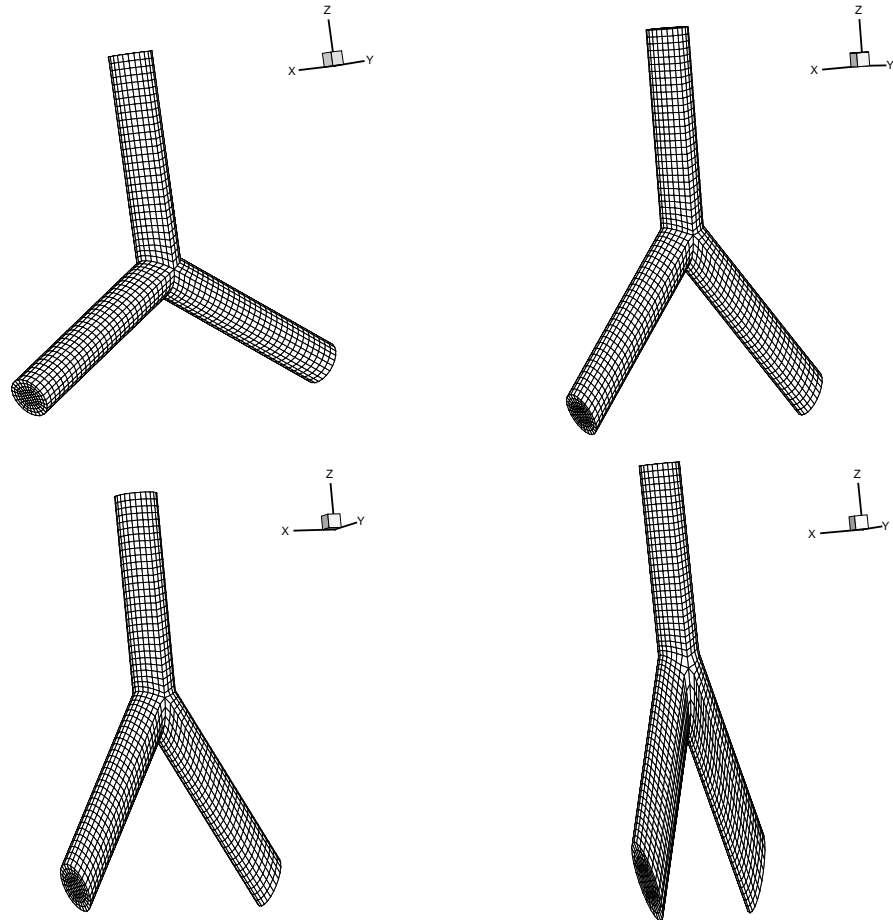


Figure 5.34: Test hexahedral grids with progressively decreasing angle between the lower tubes.

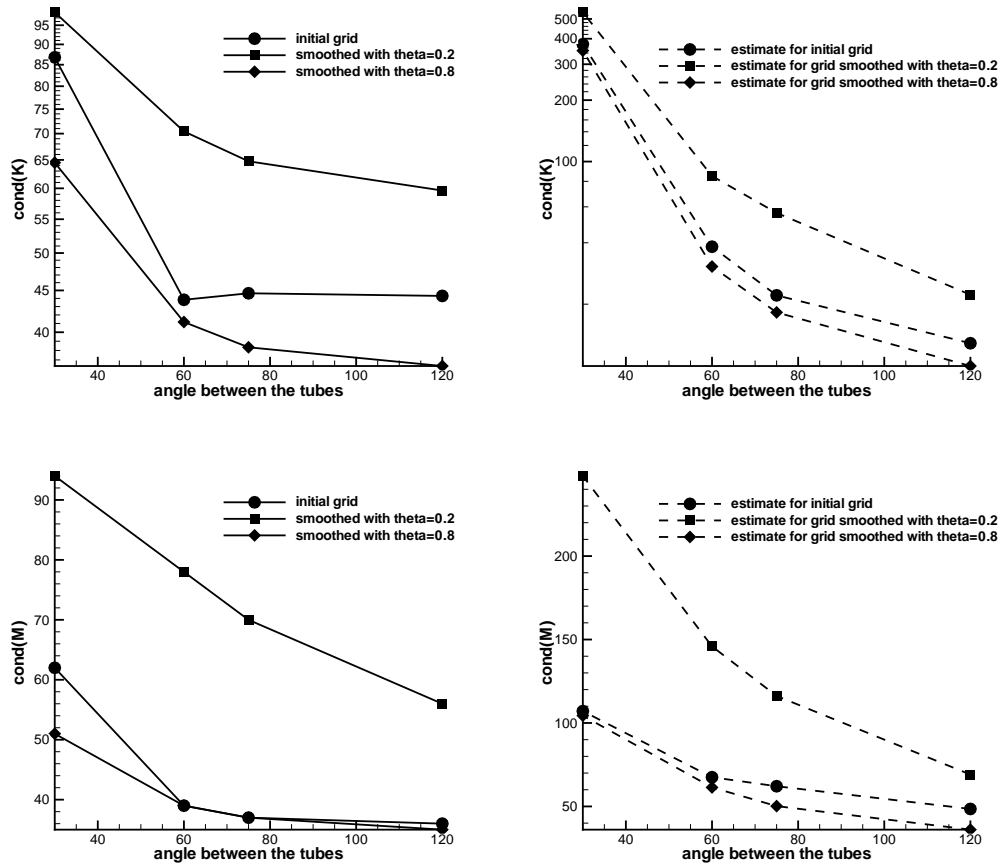


Figure 5.35: Condition numbers and their estimates for 3D test grids.

Figure 5.36 indicates the dependence of the condition number and minimum and maximum eigenvalues of the stiffness matrix for the Laplace operator on the cell distortion. The matrix is computed on one quadrilateral cell and distortion is caused by symmetric stretching of one edge, which remains parallel to the opposite fixed edge of the quadrilateral. The initial configuration corresponds to a unite square. Two cases with Dirichlet boundary conditions are considered that correspond respectively to fixing a node on the extending edge or on the opposite edge.

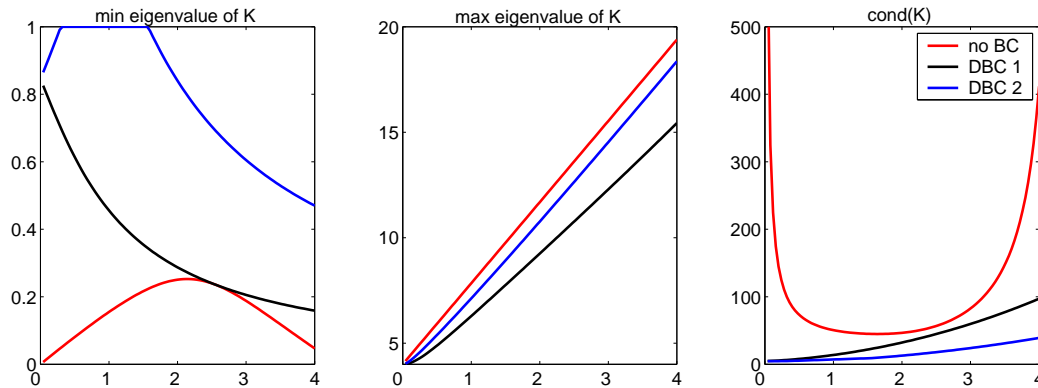


Figure 5.36: Dependence of $\kappa(K)$ on quadrilateral cell's distortion.

The main observation is that the stiffness matrix condition number is sensitive to the shape of the cells, whereas cell size does not have any effect on it. Thus, in the situation where a grid contains a pair of adjacent cells of very different sizes (for which $\kappa(K)$ is always large, e.g. in Figure 5.37 $\kappa(K) = 60$, $\frac{\max \det S}{\min \det S} = 7$), these two cells have to be highly distorted. However, when cell size varies gradually, which allows for almost “ideal” cell shape, the condition of the stiffness matrix is close to “ideal” as well (in Figure 5.38 $\kappa(K) = 44$, $\frac{\max \det S}{\min \det S} = 20$).

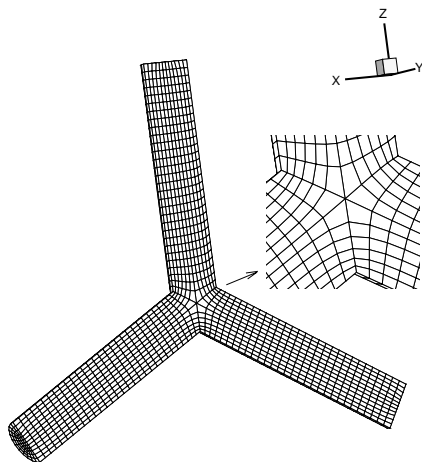


Figure 5.37: Grid with large $\kappa(K)$.

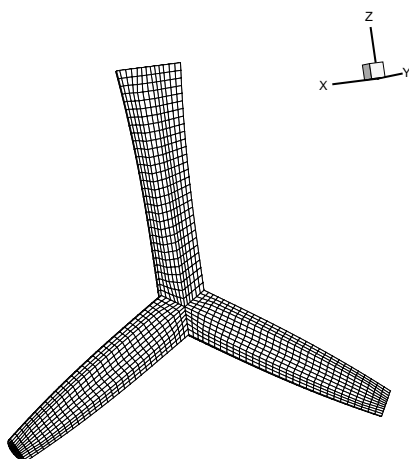


Figure 5.38: Grid with small $\kappa(K)$.

The estimate for condition number $\kappa(K)$ for the above case of a deformed quadrilateral cell

$$\kappa(K) \propto \max(\beta + \sqrt{\beta^2 - 1})^2$$

is presented in Figure 5.39 along with values of $\kappa(K)$ computed for different types of boundary conditions. This estimate is easy to obtain in 2D, since we can determine both singular values Γ, γ in terms of the distortion metric and Jacobian determinant

$$\Gamma^2 = \frac{\det S}{v} (\beta + \sqrt{\beta^2 - 1}) \tag{5.15}$$

$$\gamma^2 = \frac{\det S}{v} (\beta - \sqrt{\beta^2 - 1}) . \tag{5.16}$$

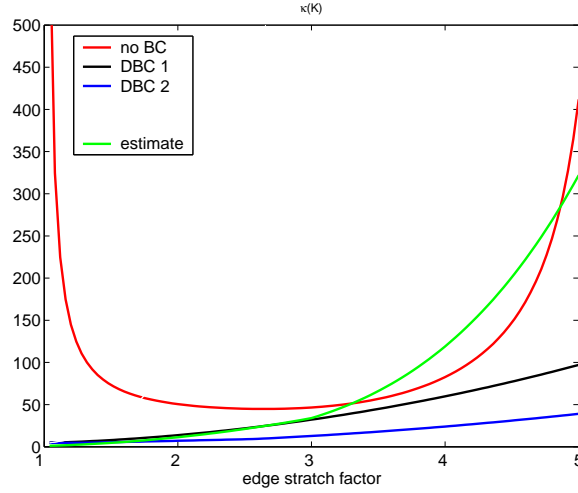


Figure 5.39: $\kappa(K)$ and its estimate on quadrilateral cell.

5.4.2 Solution error induced by local curvilinear mesh distortion.

In this section we consider the impact of local curvilinear mesh distortion on the solution accuracy.

In the numerical simulation we solve the following model diffusion problem

$$-\nabla \cdot (\alpha \nabla u) = f \text{ in } \Omega = [0, 1] \times [0, 1],$$

where

$$\alpha = \frac{1}{\nu} + \nu(x_1 + x_2 - 1)^2,$$

$$f(x_1, x_2) = 4\nu(x_1 + x_2 - 1)(\arctan \nu(x_1 + x_2 - 1) + \arctan \nu) + 4, \quad \nu = 100,$$

using a finite element technique on a mesh of isoparametric elements given by biquadratic maps. Dirichlet boundary data are specified on all boundaries from the analytic solution

$$u(x_1, x_2) = (2 - x_1 - x_2)(\arctan \nu(x_1 + x_2 - 1) + \arctan \nu).$$

The solution of this test problem has an interior layer (region of steep gradient) at large ν .

Following the results from our study of the quality measure dependence upon mid-edge node displacement in an element (recall Chapter 3, Section 3.5), a local displacement of only one interior mid-edge node is considered. Thus, only two elements sharing the curved edge are deformed, and all other cells in the mesh have “ideal” shape and size. The values for the node displacement $(\delta x, \delta y)$ are chosen from the following sets $\delta x \in \{0, 1/8, 1/4, 3/8, 1/2\}$, $\delta y \in \{0, 1/9, 2/9, 1/3\}$. Thus, some of the deformations involve zero or negative Jacobians. In some cases, the Jacobian is zero at one of the Gaussian quadrature points, so no numerical solution could be obtained (due to divide by zero). For all the other cases, we compute the error in L_2 norm, H^1 seminorm and L_∞ norm. The plots of error vs. mesh resolution are shown in Figure 5.40. We observe that the error in integral norms (i.e. averaged over the domain) does not noticeably change due to the local mesh distortion. However, error in the maximum norm differs significantly, and for some choices of distortion it does not decrease with mesh refinement. For example, on the finest undeformed mesh the relative maximum-norm error is $\|e\|_{L_\infty}/\|u\|_{L_\infty} = 2\%$ and can be compared to the $\|e\|_{L_\infty}/\|u\|_{L_\infty} = 21\%$ relative error on the mesh with local mid-edge node displacement $(1/4, 1/9)$ (yellow curve

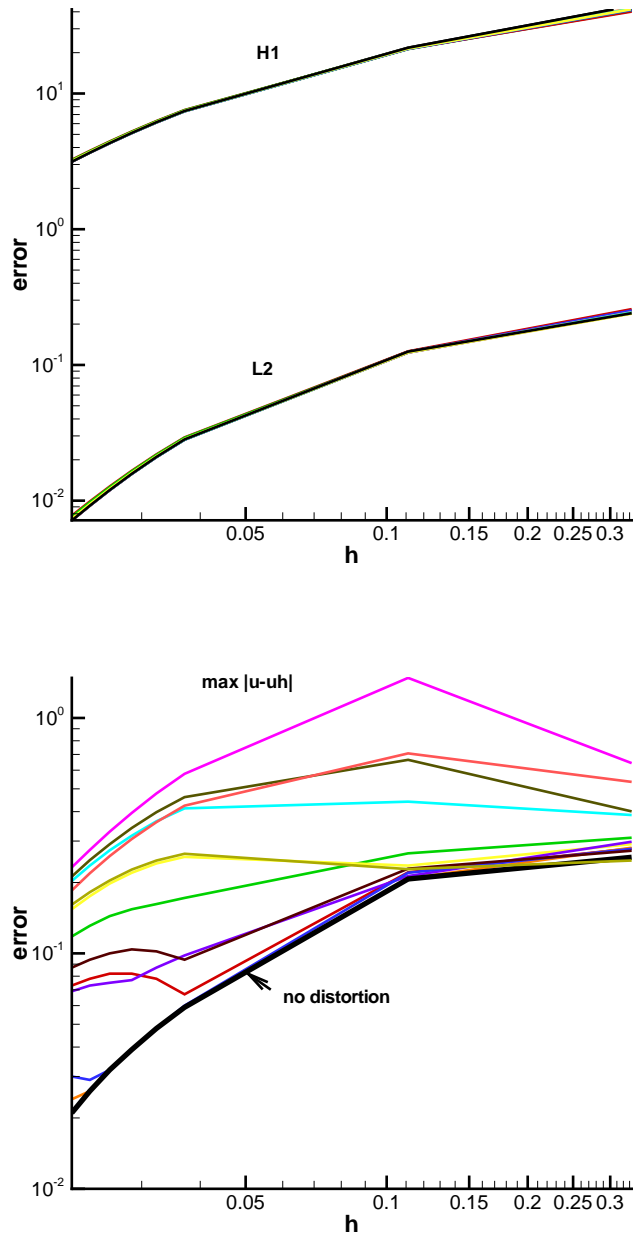


Figure 5.40: Solution error dependence on the local mesh deformation; L_2 and H^1 errors (top), and L_∞ error (bottom).

in Figure 5.40). This displacement results in two degenerate cells sharing a deformed edge. Thus, we see that the maximum-norm error might not improve during the mesh refinement, if degenerate cells are present.

Next, the numerical tests are repeated on meshes, consisting of 8-node “serendipity” elements. The FE basis functions for the solution approximation remain the same as before (biquadratic), but the geometric element now accepts more significant deformation (without losing its validity) due to the absence of the central node. The set of displacement for the mid-edge node is, therefore, extended to include $\delta y = 1/2, 3/4$, which caused negative Jacobians and failure of the numerical solution procedure on the previous mesh of isoparametric elements, but is acceptable now. On the other hand, the numerical solution procedure now fails for mesh deformations with $\delta x = 3/8$, which lead to negative Jacobians in both meshes, but was nevertheless solvable on isoparametric elements. The integral errors again do not display significant dependence upon the mesh deformation. Figure 5.41 compares the plots

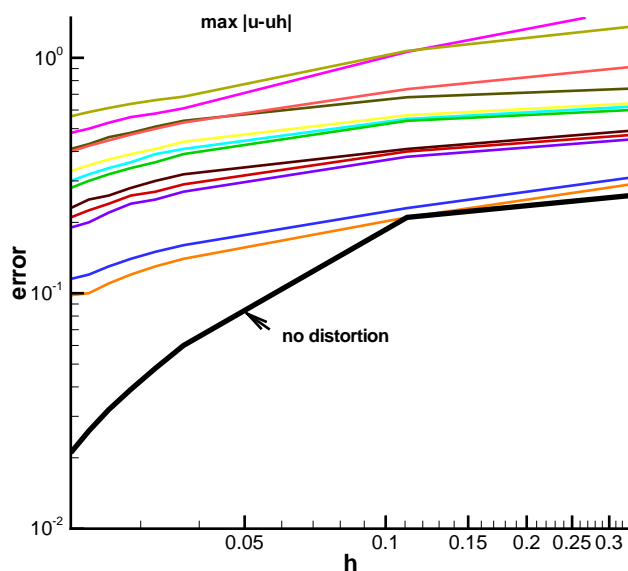


Figure 5.41: L_∞ solution error dependence on the local mesh deformation; mesh with 8-node “serendipity” elements.

of L_∞ error vs. mesh resolution. Here we observe that although in all cases error decreases with mesh refinement, the curve for error with a mesh having no distortion is the steepest. (Compare: in Figure 5.40 curves for small deformations $(1/8, 0)$ (blue) and $(0, 1/9)$ (orange) follow the “no distortion” error curve, whereas in Figure 5.41 they move away from this curve).

To conclude, isoparametric elements can better tolerate small distortions (in terms of the solution accuracy), but may lose asymptotic convergence in L_∞ -norm for distortions causing element degeneracy. (However, the asymptotic convergence rate in L_∞ -norm on meshes with “serendipity” elements is consistently smaller than the convergence rate on isoparametric meshes). Such loss of asymptotic convergence in L_∞ -norm may cause reduced rate of asymptotic convergence in L_2 -norm ($O(h^2)$ instead of $O(h^3)$ on biquadratic elements), since the error in L_2 -norm is proportional to the product of the maximum error and the area of local distortion $\|e\|_{L_2} \propto \|e\|_{L_\infty} h^2$. Thus, one must ensure high quality of the mesh in the regions of interest. In particular, high curvature of the element edges is not desirable and should be avoided in such regions.

Chapter 6

Adaptivity and mapping control

Adaptive dynamic mesh adjustment to the application problem and domain geometry is one of the major trends in mesh improvement strategies. In this chapter we demonstrate how our variational smoothing formulation can be extended to adaptive redistribution and mapping control. We compare adaptive redistribution and refinement strategies and investigate combining these strategies. Dependence of the solution error on the mesh quality is also analyzed both numerically and analytically. We also consider the problem of evolving mesh geometry.

The additive local distortion measure $E_\theta(S)$ in (2.7) provides control over both element shape and size, and it achieves its minimum on the “ideal” shaped reference element with the average cell volume v . This choice of “ideal” shape and size for the cell comes from geometric considerations. It is useful for recognizing inverted or degenerate elements in the mesh, but it clearly is not optimal for achieving the most accurate solution of an application problem. However, adaptivity can be easily incorporated into our smoothing framework through the choice of different “ideal” (or target) shapes and sizes for different cells in the mesh. Thus, by prescribing different target volumes v to different cells, one can define and control the desired cell size distribution via dilation measure $\mu(S)$. Similarly, one can define *a priori* the desired element shape by introducing a metric in reference coordinates. These metrics essentially use different reference elements for different cells in the grid. Minimization of the correspondingly modified functional will result in a grid with cells having their shape as close as possible (under given connectivity of the grid and imposed boundary conditions) to the target shapes due to the action of shape control distortion measure $\beta(S)$.

6.1 Preserving cell size distribution during smoothing

As an illustrative example, the smoothing procedure is applied to an elaborate grid generated to adaptively fit a multi-airfoil domain. This grid has many nodes with irregular valence and it initially had several folded cells. The most relevant part of this grid before and after smoothing is shown in Figure 6.1. This example indicates the importance of cell size control (via $\mu(S)$), since without it the smoothing procedure “undoes” desired clustering near the airfoils and tends to promote a uniform grid, which is undesirable because boundary layers need to be resolved. Initially, the volumetric factors v were computed for each cell, and then the smoothing algorithm was run enforcing these target values through μ . The improvement in the grid details can be seen in Figure 6.2. It can also be observed from Figure 6.2 that smoothing may not retain enough clustering in the boundary layers, even when weight in the distortion measure definition is shifted towards the size control metric (θ close to 1). This is explained by the fact that square is the “ideal” shape for all elements in this test (by the distortion metric definition). However, in the boundary layers, elongated cells with high aspect ratio define more desirable target shape. Although the size of the cells in the boundary layers of the smoothed mesh is close to the target, their shape is not, which causes node dilation from the boundary. Thus, in order to have a grid that retains the initial mesh density in the boundary layer, a block smoothing strategy may be desirable. In such a strategy blocks of boundary layer cells can be left unchanged during smoothing, or can be assigned a target shape different from square. In the next section we will introduce the framework which can be used in the implementation of the latter strategy.

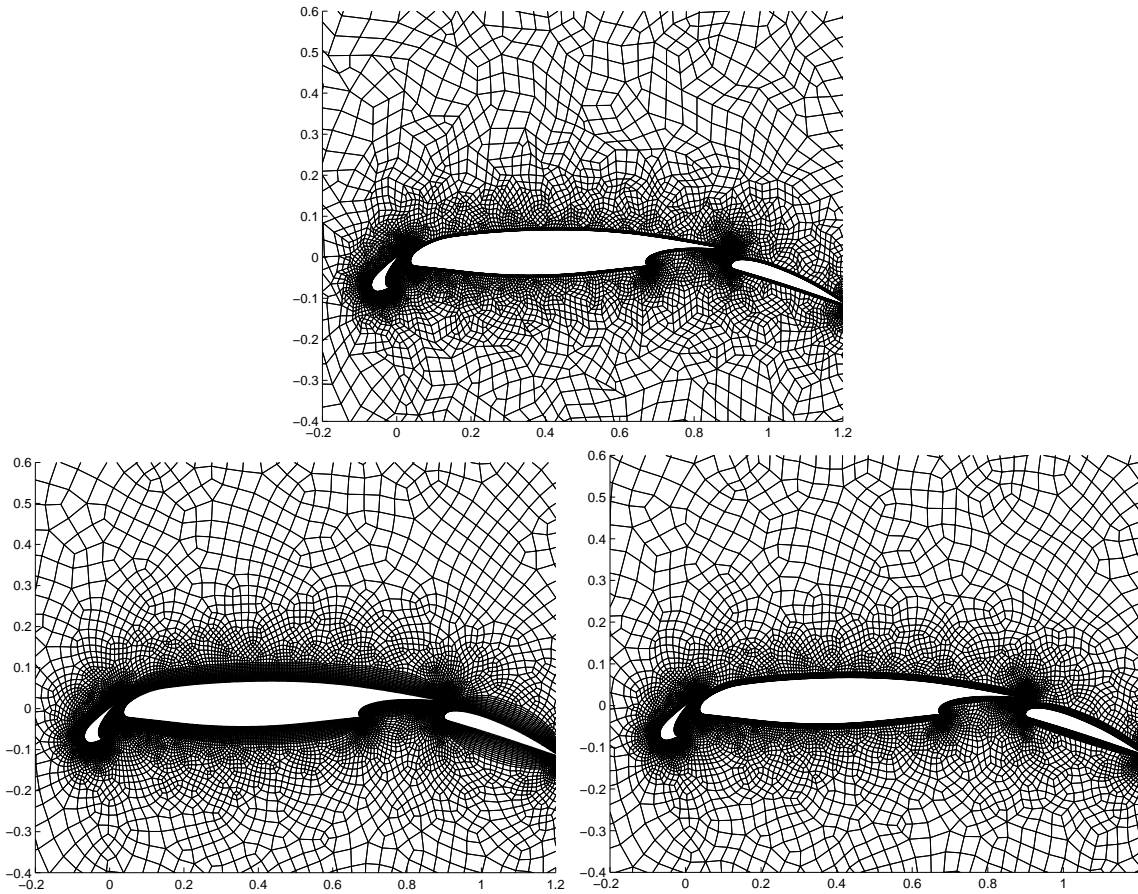


Figure 6.1: Subregion showing initial grid (top), smoothed with $\theta = 0.2$ grid (bottom left) and smoothed with $\theta = 0.8$ grid (bottom right).

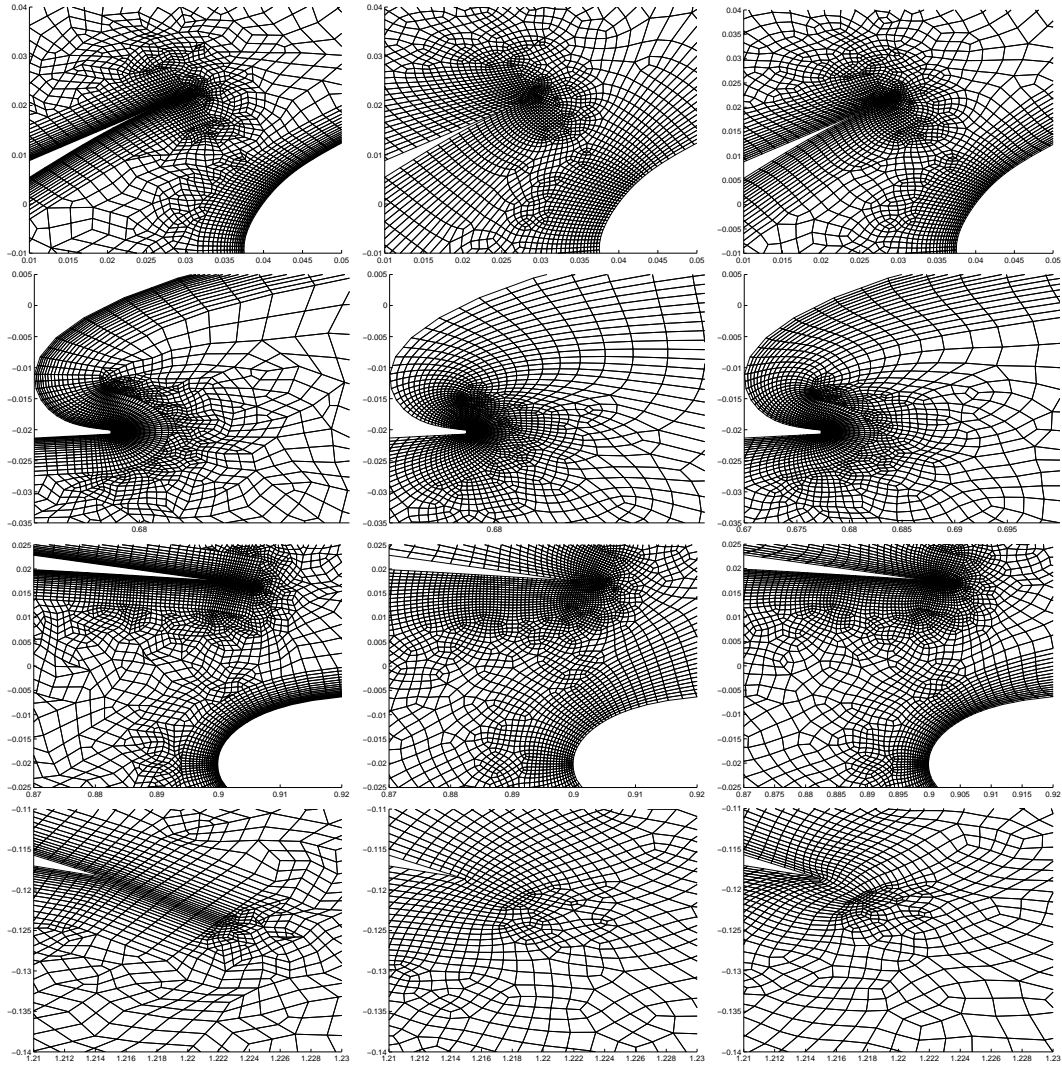


Figure 6.2: Fragments of initial grid (left), smoothed with $\theta = 0.2$ grid (middle) and smoothed with $\theta = 0.8$ grid (right).

6.2 Mapping control and domain shape recovery

6.2.1 Introducing mapping control in the metric and smoothing formulations

As we mentioned in the beginning of this chapter, the desired element shape and size can be defined *a priori* for each cell in the mesh by introducing a target metric $H(\vec{\xi})$ in reference coordinates and thus essentially providing different reference elements for different cells in the mesh. Figure 6.3 schematically demonstrates the idea: instead of the reference element representing the “ideal” target shape and size for the physical cell, we now define a new target element for each cell. Here, the target metric is given by the Jacobian matrix

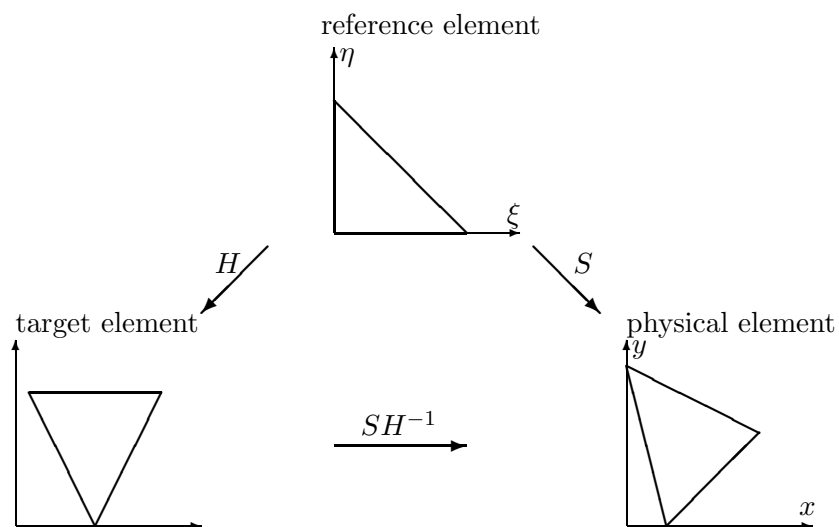


Figure 6.3: Target element definition.

$H(\vec{\xi})$ of the (nondegenerate) map between the reference and target elements. Note, that the Jacobian matrix of the map from target to physical cell, which can be defined as a superposition of two mappings, is SH^{-1} , as shown in Figure 6.3. In order to include the new target element definitions into the smoothing formulation, one needs to substitute this matrix SH^{-1} instead of S in the metric and functional definitions, yielding

$$E_{\theta}(SH^{-1}) = (1 - \theta) \frac{\left(\frac{1}{n} \text{tr}(H^{-T} S^T S H^{-1})\right)^{2/n}}{\det(SH^{-1})} + \frac{\theta}{2} \left(\frac{1}{\det(SH^{-1})} + \det(SH^{-1}) \right),$$

$$\mathcal{I} = \int_{\hat{\Omega}} E_{\theta}(SH^{-1})d\vec{\xi}. \quad (6.1)$$

(Since target size is already defined by the metric, the volumetric factor is set to be equal to one, $v = 1$.) Discretization of the functional is done using the same approximate integration rules as before, only now the matrix SH^{-1} is evaluated instead of S . Numerical optimization procedures are not affected by this modification. Thus, minimization of this modified functional is performed similar to the original smoothing procedure and it will result in a mesh with cells having the shape and size as close as possible (under given connectivity of the grid and imposed boundary conditions) to the target shapes and sizes. For example, if slender elements are desired in an anisotropic mesh, this can be achieved by using a slender target element in Figure 6.3. This, therefore, resolves the anisotropic grid issue.

6.2.2 Domain shape recovery

Many application problems include evolving domain geometry. As an example, let us consider flow of blood in the arteries. The walls of the arteries respond to the stresses induced by the viscous blood flow by stretching or contracting. The simulation algorithm for such a problem would incorporate continuous change of domain geometry (and, consequently, the mesh). Let us assume that at a certain moment in time t a nondegenerate deformation field defining the evolved geometry at time $t + \Delta t$ is known (from the viscous flow solution). Thus, we have a current mesh and a functional representation of a deformation field for the new geometry $H(\vec{\xi})$, and we are required to evolve the mesh. These provide the initial conditions for mesh smoothing with the target cell definition procedure, as described above. We now will illustrate the performance of this procedure on two examples for domain shape recovery.

In the first example, the 2D deformation field $H(\xi, \eta) = \left(\frac{\partial \mathbf{w}}{\partial \xi}, \frac{\partial \mathbf{w}}{\partial \eta} \right)$ is defined using the map

$$\mathbf{w}(\xi, \eta) = \begin{pmatrix} r + X - (r + X - \xi) \cos \frac{2\pi\eta}{Y} \\ (r + X - \xi) \sin \frac{2\pi\eta}{Y} \end{pmatrix}.$$

(Note, that in the algorithm we do not use the map $\mathbf{w}(\xi, \eta)$ itself, only the deformation field

derived from it. The formula for the map is listed here to give a better understanding of the desired domain shape.) The initial mesh is a uniform quadrilateral mesh inside a rectangular domain (see Figure 6.4 a)) with dimensions X and Y , which up to a scaling coincides with the reference domain $\hat{\Omega}$ for this problem. The above map describes deformation from this rectangular domain to a ring with inner radius r .

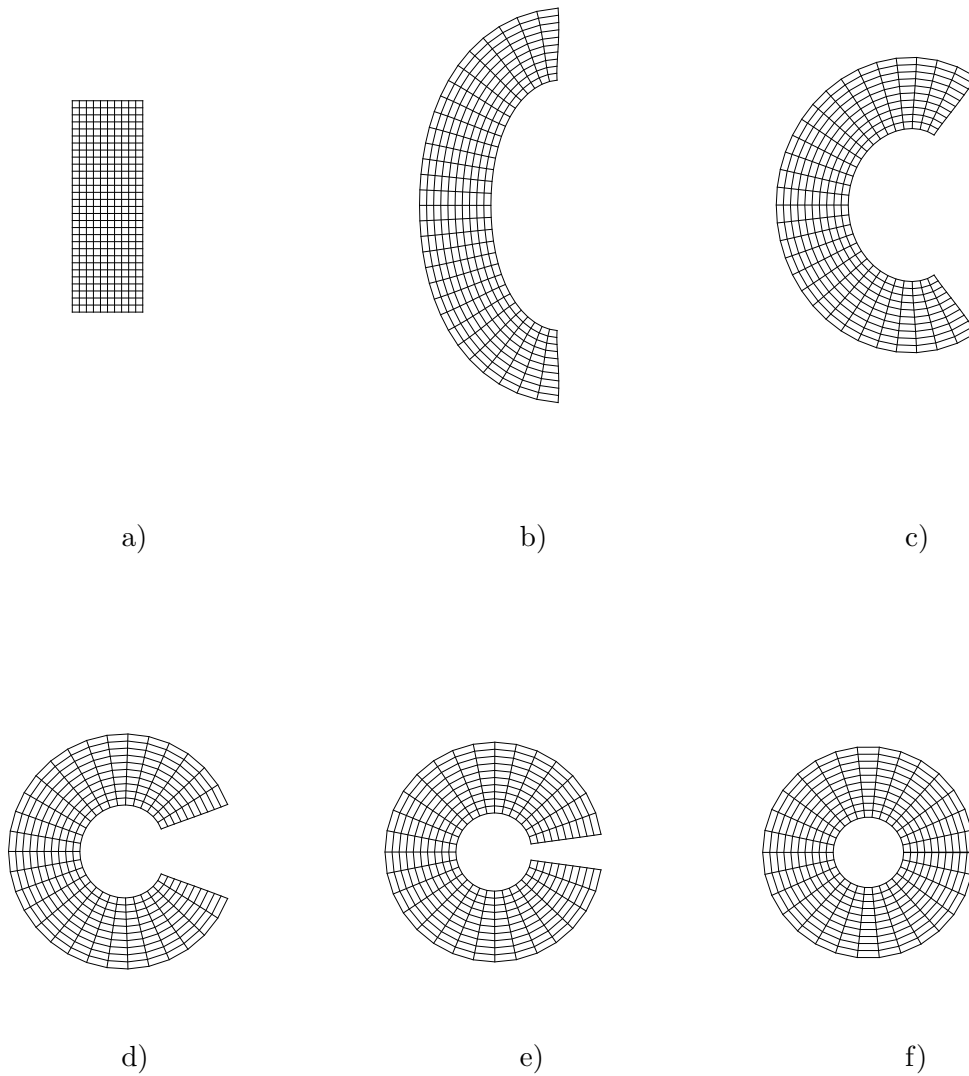


Figure 6.4: Target shape recovery of 2D quadrilateral mesh.

Smoothing of this mesh with $E_\theta(SH^{-1})$ results in a full recovery of the ring domain shape. During the smoothing all nodes are free to move, i.e. no Dirichlet-type boundary condition is involved. The mesh evolution during smoothing with $\theta = 0.5$ is shown in Figure 6.4. As expected, mesh changes dramatically within several first smoothing iterations (from a) to c)), but the deformation slows down when the domain shape becomes close to the target (approximately half of the total number of iterations is spent on the last transition from e) to f)).

In the second example, two different 3D geometries are chosen for the initial and target domain shapes. They are presented in Figure 6.5 (positioned according to the target element definition scheme in Figure 6.3). The initial domain (on the right in Figure 6.5) has a pipe shape given by the map

$$\mathbf{r}(\xi_1, \xi_2, \xi_3) = \begin{pmatrix} \xi_1 \\ (R + Z - \xi_3) \sin \frac{2\pi\xi_2}{Y} \\ R + Z - (R + Z - \xi_3) \cos \frac{2\pi\xi_2}{Y} \end{pmatrix}, \quad S = \left(\frac{\partial \mathbf{r}}{\partial \xi_1}, \frac{\partial \mathbf{r}}{\partial \xi_2}, \frac{\partial \mathbf{r}}{\partial \xi_3} \right),$$

and target domain (on the left in Figure 6.5) is a spiral with two full turns defined by

$$\mathbf{w}(\xi_1, \xi_2, \xi_3) = \begin{pmatrix} (R + \xi_3) \cos \left(\frac{X - \xi_1}{R} \sin \varphi \right) \\ \xi_2 + (X - \xi_1) \cos \varphi \\ (R + \xi_3) \sin \left(\frac{X - \xi_1}{R} \sin \varphi \right) \end{pmatrix}, \quad H = \left(\frac{\partial \mathbf{w}}{\partial \xi_1}, \frac{\partial \mathbf{w}}{\partial \xi_2}, \frac{\partial \mathbf{w}}{\partial \xi_3} \right),$$

where X, Y and Z are dimensions of the reference brick. (Again, the maps are given for clarification only, they are not used by the algorithm.)

The stages of domain shape recovery during smoothing of the hexahedral mesh with $\theta = 0.5$ and no fixed nodes are shown in Figure 6.6. As in the 2D case, the domain shape changes dramatically and becomes close to the target after the few first iterations, but “full” recovery of the target shape transition (from e) to f)) takes a significant number of iterations (about 300).

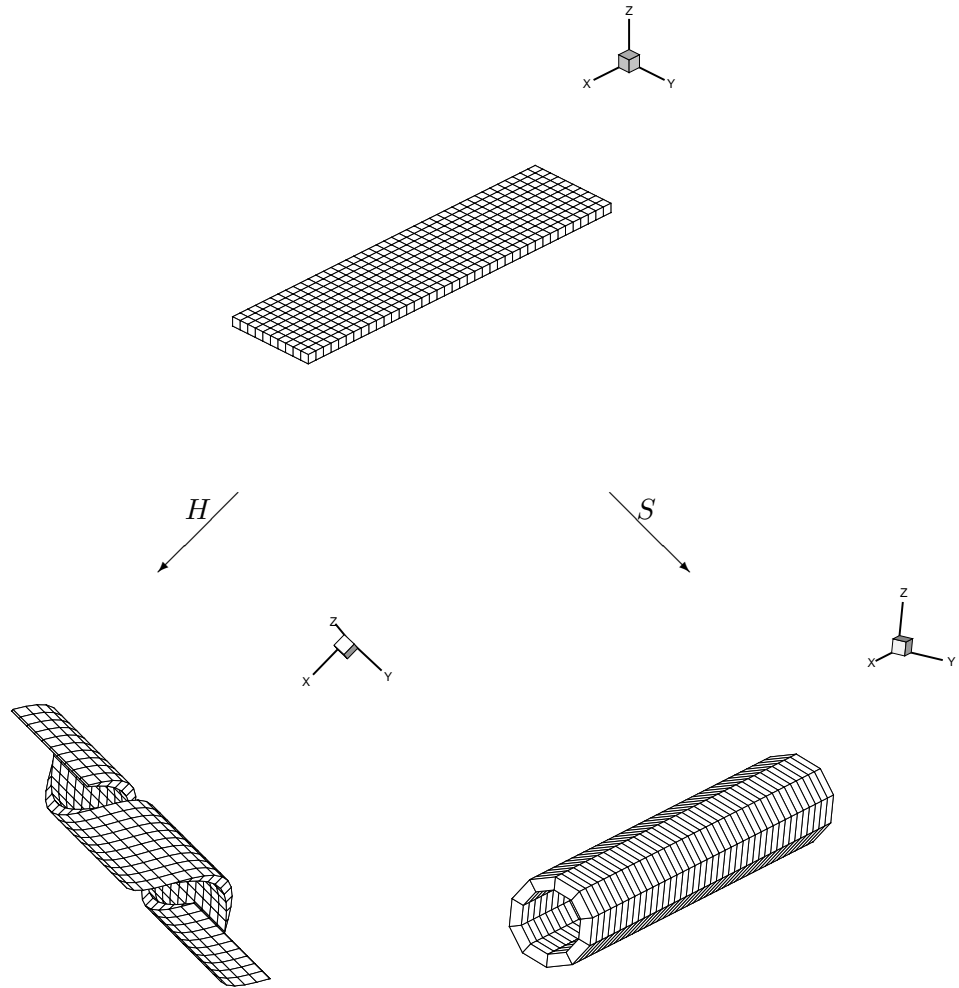


Figure 6.5: 3D domains: reference (top), target (bottom, left) and initial (bottom, right) shapes.

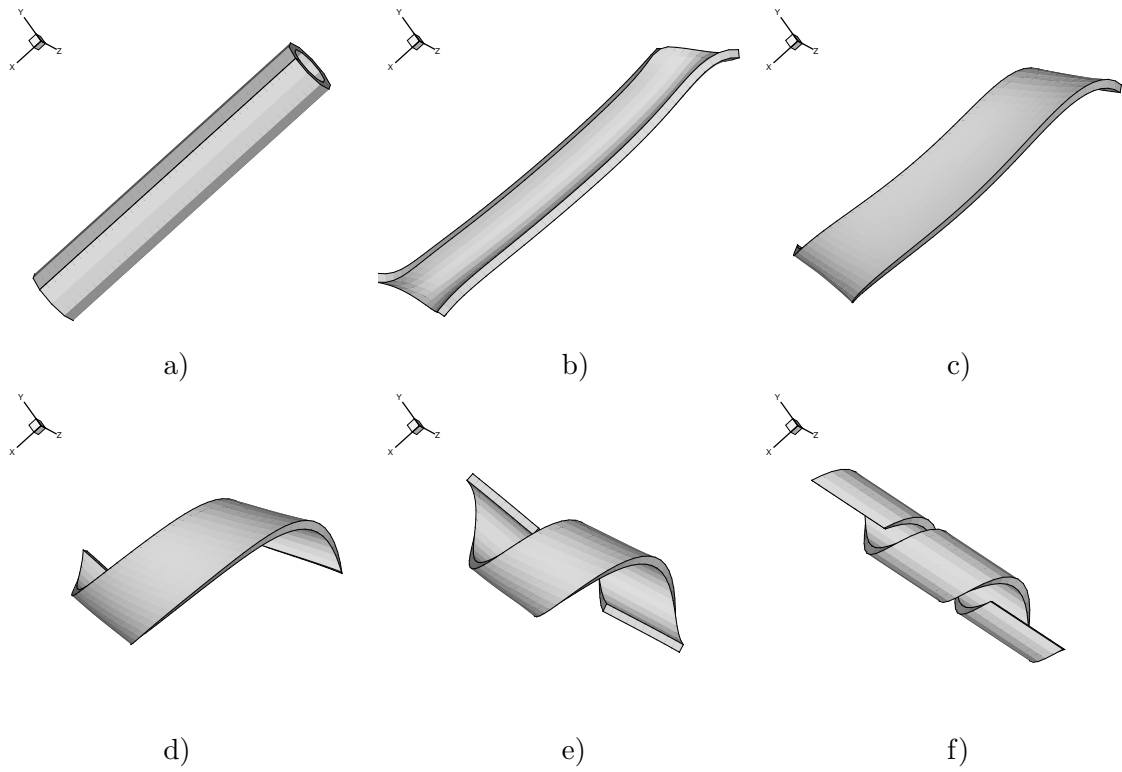


Figure 6.6: Shape recovery in 3D.

6.3 Introducing adaptivity in the smoothing formulation

In adaptive mesh redistribution techniques, mesh nodes are repositioned in order to improve solution accuracy. The solution or adaptive function u is known on the initial mesh. Mesh connectivity and total number of nodes do not change during redistribution, which gives this technique an advantage over uniform and adaptive refinement strategies (adaptive refinement often introduces “hanging nodes” into the mesh, which must be treated differently from usual nodes in the application simulation). However, some adaptive redistribution methods can distort mesh elements too much, thus affecting the efficiency of the numerical simulation and overall numerical problem solvability.

Most redistribution techniques aim to minimize the interpolation error for an adaptive function, which in turn controls the approximation error. The most widely used approach for adaptive mesh redistribution is to adaptively control the areas of the elements (through the map Jacobian determinant $J = \det S$) by introducing weights $w = w(u)$ as functions of the adaptive function and its gradient. The strategy then is to satisfy $Jw = \text{const}$ [1, 14], or to solve $w(J - 1)^2 \rightarrow \min$ [20] or $\int wJdV \rightarrow \min$ [10, 2]. The use of several metric coefficients (instead of the single weight) improves the technique, since it allows for directional adaptation. The metric coefficient matrix \mathcal{G} can be determined from the relation between the n D computational domain and the r D adaptive vector-function [80, 4, 13], and its elements will be dependent on the gradient of the adaptive function. Metrics based on the Hessian of the adaptive function are also used in unstructured mesh adaptation algorithms [26], and have been proved to be quasi-optimal for interpolation in the L_∞ -norm [44]. However, such meshes might be too “rough” for numerical simulations and require further adjustments.

In this work, the variational mesh smoothing problem (2.8) is generalized for adaptation by introducing the adaptive metric \mathcal{G} into the mesh distortion functional. We define this metric \mathcal{G} using different modifications of the covariant metric tensor for the surface of values of the scalar adaptive function u :

$$\mathcal{G} \propto (g_{ij}), \quad g_{ij} = \delta_i^j + \frac{\partial u}{\partial x_i} \frac{\partial u}{\partial x_j}, \quad i, j = 1, \dots, n.$$

Here, the metric represents the map between the physical domain $(x_1, \dots, x_n) \in \Omega$ and the surface of values of the adaptive function $u(x_1, \dots, x_n)$ ($\mathcal{G}^{1/2}$ is the Jacobian matrix of this map). The adaptive redistribution problem is then formulated as follows: minimize

$$\mathcal{I} = \int_{\hat{\Omega}} E_{\theta}(\mathcal{G}^{1/2}S)d\vec{\xi}. \quad (6.2)$$

This formulation is similar to smoothing with target element definitions (6.1), only now the metric \mathcal{G} is defined in the physical coordinates and represents the map of the physical cell onto the element on the surface of values of the adaptive function. Thus, the problem (6.2) is equivalent to the construction of a good quality mesh on the surface of values of u and the result is the projection of this mesh onto the computational domain Ω . This idea is illustrated in Figure 6.7. The functional discretization and numerical minimization

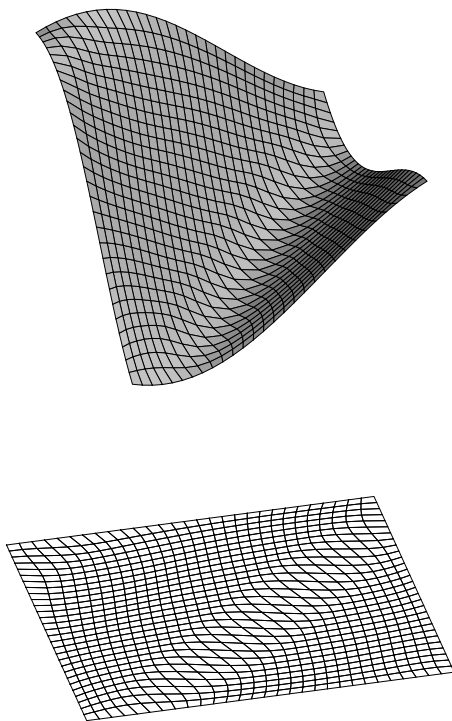


Figure 6.7: Adaptive mesh redistribution: smooth mesh on the surface $(x, y, u(x, y))$ projected onto the computational domain (x, y) .

procedures again are not affected by the introduction of the new metric into the smoothing formulation.

Remark: Both target shape definition metric and adaptive metric can be present in the functional, providing the capability of adjusting the mesh to target shape definition, smoothing and adaptivity at the same time. Also, since all metrics are nondegenerate ($\det H > 0$ and $\det \mathcal{G} > 0$), the cells in the resulting mesh will always be nondegenerate as a consequence of the barrier property of the functional.

We perform several numerical tests with different choices of adaptive metric. The first and the simplest choice we consider is a piecewise constant (on each cell) definition of the adaptive metric

$$\mathcal{G} = \sqrt{1 + |\nabla u|^2} I.$$

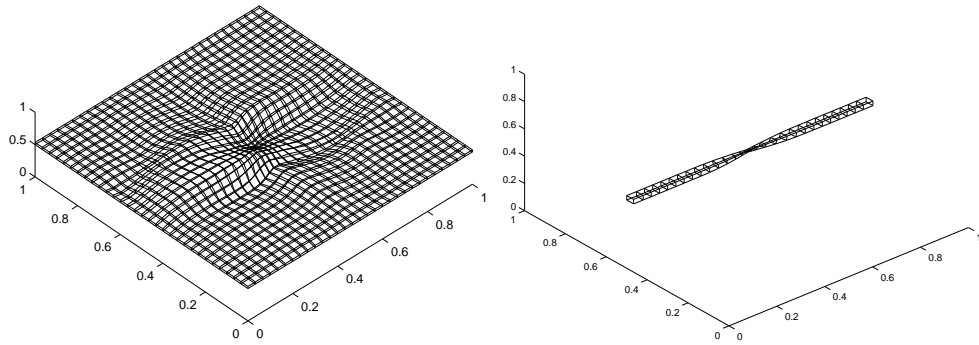
The shape control part β of the distortion measure is independent of this type of metric, so adaptivity is due only to area (volume) change. Thus, the technique is equivalent to those described in the beginning of the section, since only desired element volume $v = v_0/\sqrt{1 + |\nabla u|^2}$ is dependent upon the adaptive function. In the tests, the initial mesh is a uniform hexahedral mesh inside the unit cube. Figure 6.8 shows horizontal layers and strips of cells extracted from the middle of the domain for meshes, that have been redistributed with the adaptive functions:

$$\begin{aligned} \text{a) } u &= \exp\left(-\frac{|x-0.5|+|y-0.5|+|z-0.5|}{\epsilon}\right) \text{ (point source);} \\ \text{b) } u &= \begin{cases} 0 & \text{if } y \leq y_0 - \delta \\ \frac{1}{2} + \frac{1}{2}(1 + \sin(\pi(\frac{y-y_0}{2\delta}))) & \text{if } y_0 - \delta \leq y \leq y_0 + \delta \\ 1 & \text{if } y \geq y_0 + \delta \end{cases} \end{aligned}$$

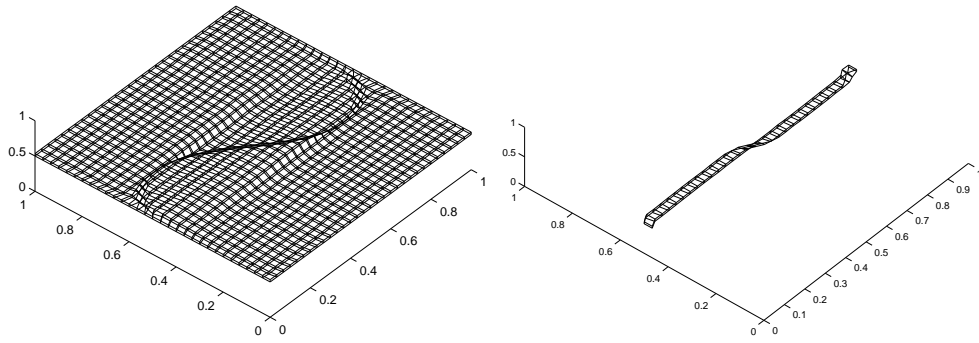
(steep front), where y_0 determines the location of the front and δ is the width of the front;

and

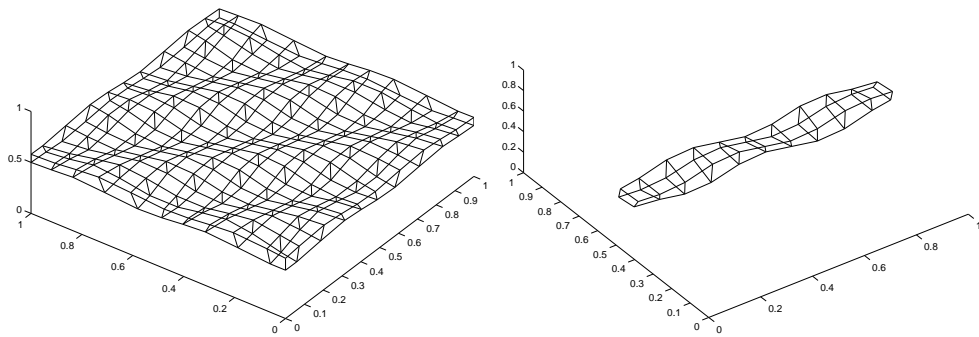
$$\text{c) } u = 4 \sin(2\pi(x + y + z)).$$



a)



b)



c)

Figure 6.8: Adaptation to a) point source, b) step front and c) sine function.

The choice of a piecewise constant on each cell metric for adaptive metric:

$$\mathcal{G} = \begin{pmatrix} 1 + u_x^2 & 0 & 0 \\ 0 & 1 + u_y^2 & 0 \\ 0 & 0 & 1 + u_z^2 \end{pmatrix}$$

allows for directional adaptation. In this case the shape control part of the functional depends on the metric in the following way: each row of the Jacobian matrix S is scaled with a metric factor $\mathbf{a}_i \rightarrow \mathbf{a}_i \sqrt{\mathcal{G}_{ii}}$. Thus, each direction has its own adaptive scaling factor, which is equal to the length of the tangent vector to the coordinate curve $(x_i, u(x_1, \dots, x_n))$. The results of directional adaptation to functions $u_1 = \exp\left(-\frac{|x-0.5|}{\epsilon_x} - \frac{|y-0.5|}{\epsilon_y} - \frac{|z-0.5|}{\epsilon_z}\right)$, where $\epsilon_z = 0.6 > \epsilon_y = 0.2 > \epsilon_x = 0.1$ and $u_2 = \sin(\pi(x + 2y + 3z))$ are shown in Figure 6.9. In this example, the initial mesh is again a uniform hexahedral mesh inside a unit cube. A 1/8 subcube cut-out and three of its projections are shown in the Figure. We observe that, for the first function, the clustering towards the center of the cube is different in each direction (the dimensions of the central element are $z > y > x$). For the second function, we can see different periods of the sine function in different directions.

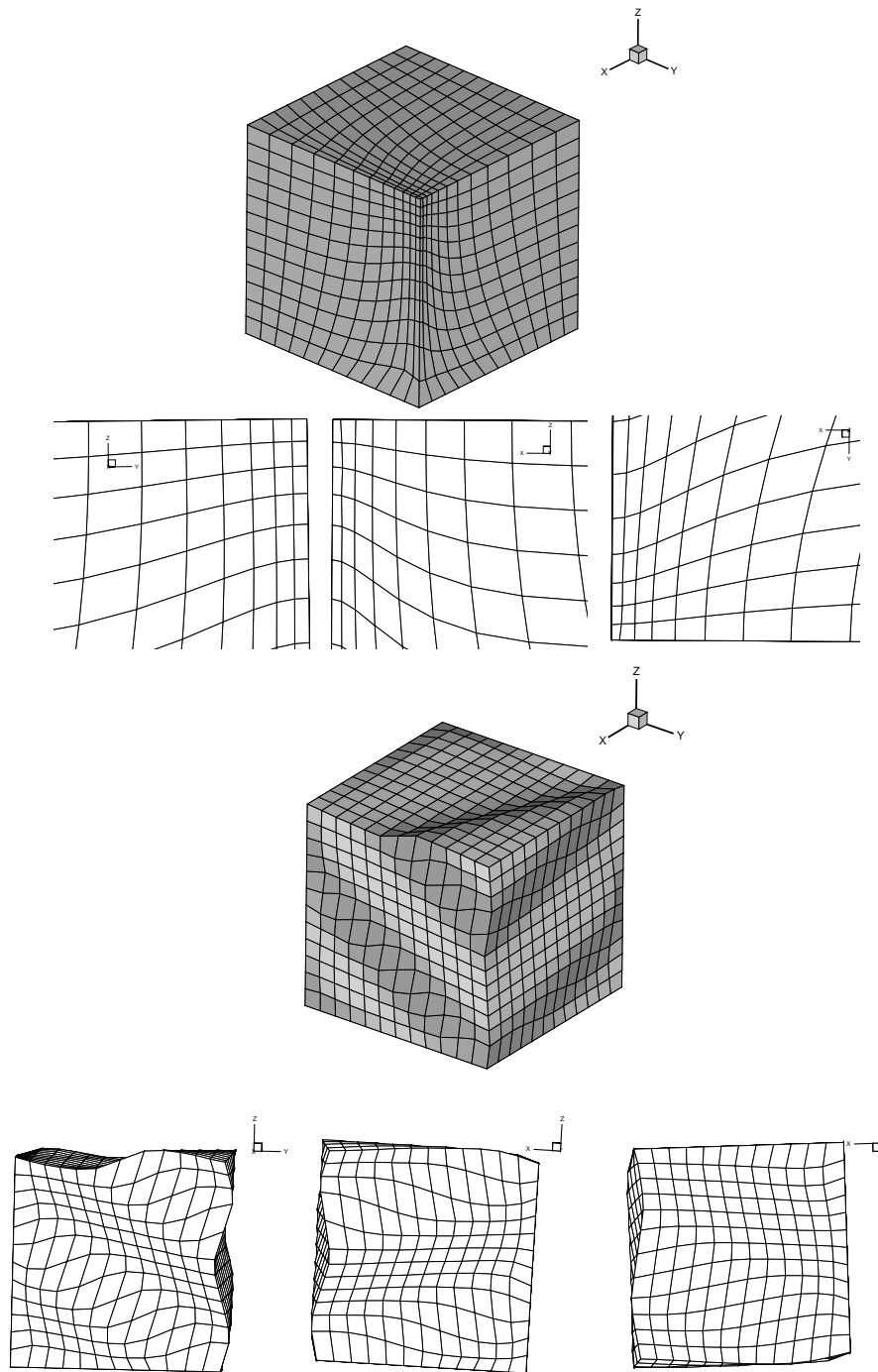


Figure 6.9: Directional adaptation to local exponential source (on top) and sine function (on bottom).

6.4 Combining adaptive refinement (h-) and redistribution (r-) strategies

One can expect that combination of r- and h-adaptivity will yield reduction in the number of degrees of freedom (number of nodes) in the optimal mesh compared to the results of pure adaptive refinement and may be useful in accommodating anisotropic effects. In order to investigate this topic, we perform a numerical comparison analysis for r- and h- adaptive strategies and their combination.

Let us consider an interpolation problem for the function

$$u(x, y) = \frac{\exp^{x/\varepsilon} - 1}{\exp^{1/\varepsilon} - 1} + \frac{\exp^{y/\varepsilon} - 1}{\exp^{1/\varepsilon} - 1}$$

on a quadrilateral mesh inside a unit square domain. This function is a solution to a convection-diffusion problem

$$-\varepsilon \Delta u + \nabla u = 0,$$

which has layers adjacent to the boundaries $x = 1$ and $y = 1$ and in the corner where these boundaries meet. The adaptive refinement criterion is to refine a quadrilateral cell “naturally” into four cells if the norm of the interpolation error on the cell is larger than a given tolerance. We consider two cases: the error is estimated in L_2 norm or in H^1 semi-norm, and the computations run while $\|e\|_{L_2} > \tau_{L_2} = 10^{-5}$, or $|e|_{H^1} > \tau_{H^1} = 10^{-3}$, respectively. The metric for adaptive redistribution (6.2) is taken to be a piece-wise constant function on each cell with the values $\mathcal{G}_{L_2}(c) = \|e\|_{L_2(c)}/\tau_{L_2}I$ and $\mathcal{G}_{H^1}(c) = \begin{pmatrix} \|u_x - (U_h)_x\|_{L_2(c)}/\tau_{H^1} & 0 \\ 0 & \|u_y - (U_h)_y\|_{L_2(c)}/\tau_{H^1} \end{pmatrix}$, correspondingly. These metrics cause mesh nodes to cluster in the regions of large error and spread everywhere else. (The lower limit for the metric is set to $1/N_c$).

Plots of global L_2 and H^1 interpolation errors vs the number of degrees of freedom (number of nodes in the mesh) for different strategies are shown in Figure 6.10. From this Figure we observe that the L_2 error decreases linearly with the increase in number of degrees of freedom during uniform refinement and quadratically during adaptive refinement. The

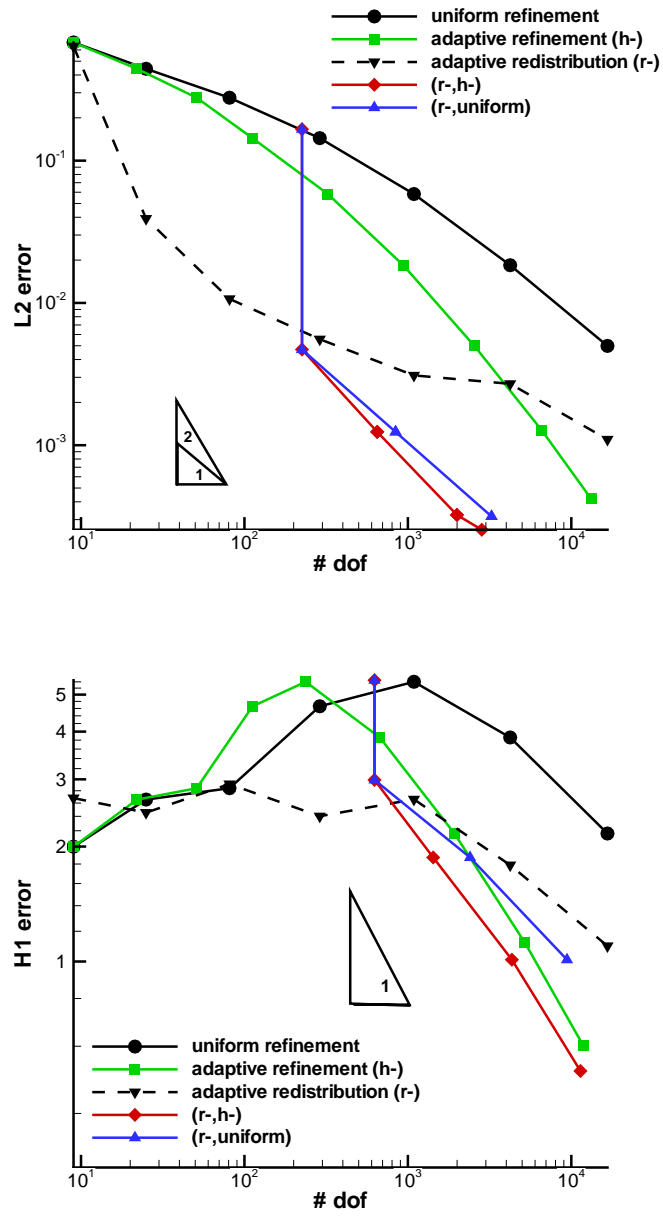


Figure 6.10: Interpolation error vs number of d.o.f. for different strategies.

adaptive redistribution curve was obtained by redistributing uniform meshes with different numbers of degrees of freedom. This r- strategy causes significant (an order of magnitude) decrease in the L_2 error compared to the error on the initial uniform meshes. However, the difference is less noticeable when the initial error (before redistribution) is small (and number of degrees of freedom is large). This can be explained by the fact that local errors on such meshes are already small (the order of τ), so the adaptive metric is close to unity and does not induce significant changes in the mesh.

Addition of the redistribution step before mesh refinement significantly reduces the final number of degrees of freedom. Also, one r- step is enough, since it already provides optimally shaped cells under the current metric. Their refinement does not change their distortion measure (as a consequence of the maximum principle), so additional r- steps between refinements do not affect the mesh. For example, in our case alternating r- and h- strategies give the same result as one r- step followed by h-steps. A similar trend is observed for the H^1 error case. From the plot we can see that up to $N = 10^3$ degrees of freedom the error grows, which is explained by the fact that initially boundary layers were not sufficiently resolved to pick up the true gradient value. Thus, the initial mesh for combination of r- and h- strategies was chosen fine enough.

The resulting meshes for the strategies from Figure 6.10 are demonstrated in Figure 6.11. The difference in global mesh appearance for L_2 and H^1 error adaptation cases is barely noticeable, but the differences in details near the corner $x = 1, y = 1$ are evident. Table 6.1 contains information about the minimum cell area in the final mesh for each strategy. The smallest cell occurs at the $x = 1, y = 1$ corner for every mesh, and its size provides better insight into the optimal mesh scaling.

Note: For smoothing and redistribution of highly adaptive meshes (with several levels of hanging nodes), as in the case of alternating adaptive redistribution and refinement in the above example, the treatment of hanging nodes constraints through penalty formulation (4.7) is preferable over the Lagrange multipliers.

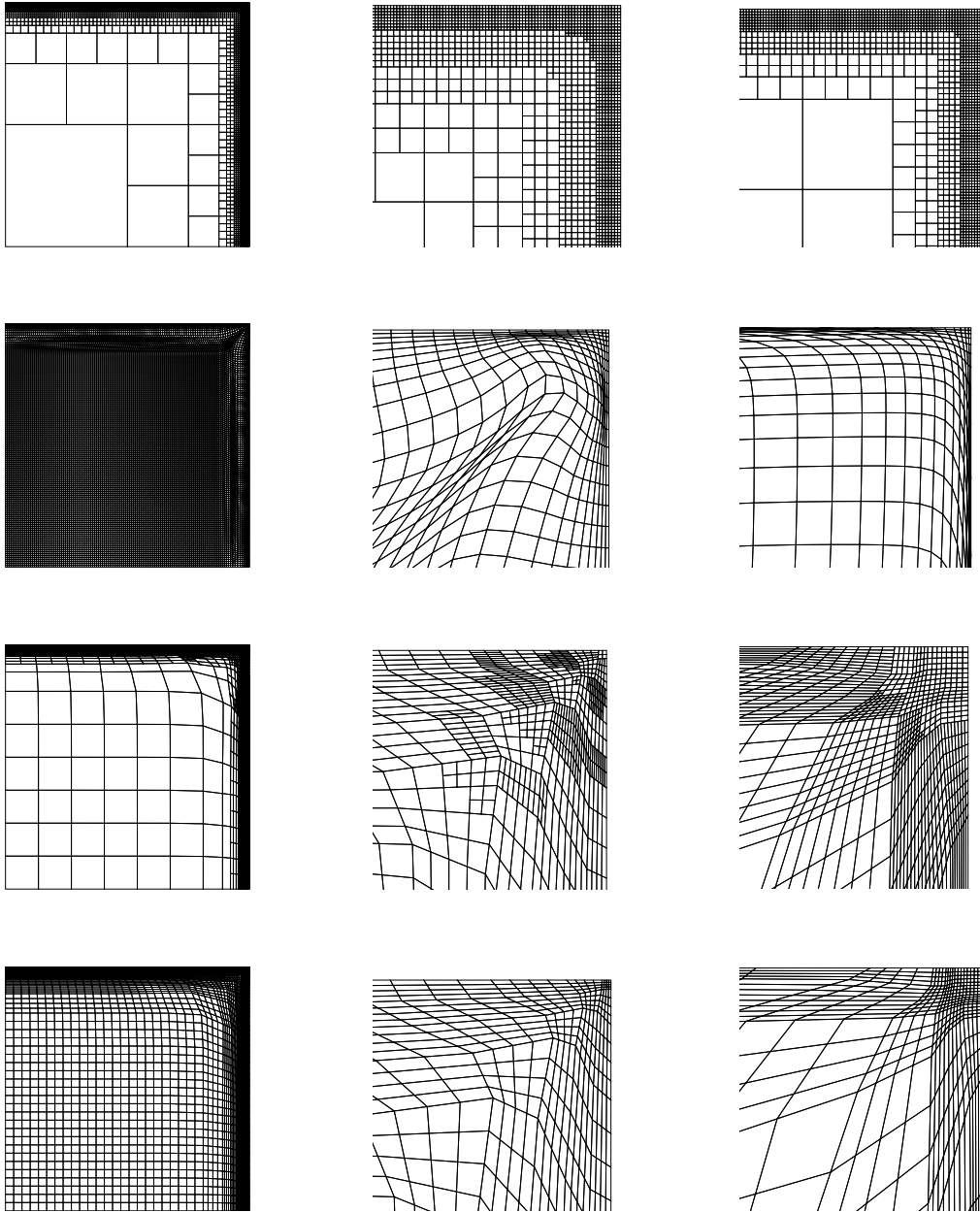


Figure 6.11: Resulting meshes (left) and their corner zoom for L_2 (middle) and H^1 error cases for different strategies, from top to bottom: adaptive refinement, adaptive redistribution, adaptive refinement following redistribution, uniform refinement following redistribution.

Strategy	minimum cell area in the final mesh	number of nodes in the final mesh
uniform refinement, L_2	$6.1 \cdot 10^{-5}$	16641
adaptive refinement (h-), L_2	$8.2 \cdot 10^{-5}$	13215
adaptive redistribution (r-), L_2	$4.4 \cdot 10^{-5}$	16641
(r-,h-), L_2	$2.9 \cdot 10^{-4}$	2832
(r-, uniform), L_2	$2.3 \cdot 10^{-4}$	3249
uniform refinement, H^1	$6.1 \cdot 10^{-5}$	16641
adaptive refinement (h-), H^1	$9.3 \cdot 10^{-5}$	11817
adaptive redistribution (r-), H^1	$5.4 \cdot 10^{-6}$	16641
(r-,h-), H^1	$8.21 \cdot 10^{-5}$	11374
(r-, uniform), H^1	$8.89 \cdot 10^{-5}$	9409

Table 6.1: Comparison of different adaptive strategies: minimum cell areas.

6.5 Error analysis

Error in the finite element solution is bounded above by the interpolation error on isoparametric elements. Several adaptive redistribution techniques are based on this fact, e.g. mesh is redistributed to better resolve the solution function where its gradients are high. On the other hand, mesh quality enters the interpolation error estimates predicting larger error on distorted elements. Thus, it is important for an adaptive mesh redistribution technique to keep the right balance between mesh clustering in the regions of interest and amount of cell distortion introduced by such a clustering. This motivates the following study of interpolation error for tensor product linear elements in the context of our adaptive redistribution methodology.

Lemma 4 *Suppose that sufficiently smooth function $u(x_1, \dots, x_n)$ has bounded second derivatives in the cell Ω_c , which is the image of a unit hypercube $\hat{\Omega}_c = D$ under nondegenerate tensor-product linear mapping, i.e. $|\frac{\partial^2 u(x_1, \dots, x_n)}{\partial x_i \partial x_j}| \leq K, \forall i, j \in \{1, \dots, n\}$ and $\Pi(u)$ denotes the polylinear interpolant of u , such that $\Pi(u) = u$ at the vertices of the cell. Then*

$$\|u - \Pi(u)\|_{H^1(\Omega_c)} \leq \sqrt{2}K \frac{\Gamma^2}{\gamma} \frac{v^{1/n}}{\sqrt[4]{1 + |\nabla u|^2}} \sqrt{\text{meas}(\Omega_c)}, \quad (6.3)$$

$$\|u - \Pi(u)\|_{L_2(\Omega_c)} \leq \sqrt{2}K\Gamma^2 \frac{v^{2/n}}{\sqrt{1 + |\nabla u|^2}} \sqrt{\text{meas}(\Omega_c)}, \quad (6.4)$$

where $v = h^n$ is the target cell volume, γ and Γ are the minimum and maximum singular values of the modified Jacobian matrix in (6.2), i.e. $v^{2/n}\gamma^2 \leq S^T \mathcal{G} S \leq v^{2/n}\Gamma^2$, $\mathcal{G} = \sqrt{1 + |\nabla u|^2}I$, and the following standard definition of the Sobolev norm is used

$$\|u\|_{H^1(\Omega_c)}^2 = \sum_{i=1}^n \left\| \frac{\partial u}{\partial x_i} \right\|_{L_2(\Omega_c)}^2 + \|u\|_{L_2(\Omega_c)}^2.$$

Proof:

Let $\phi = u - \Pi(u)$. Then

$$\begin{aligned} \|\phi\|_{H^1(\Omega_c)}^2 &= \int_{\Omega_c} (\nabla \phi)^T \nabla \phi d\mathbf{x} + \int_{\Omega_c} \phi^2 d\mathbf{x} = \\ &= \int_D J(\nabla_\xi \phi)^T S^{-1} S^{-T} \nabla_\xi \phi d\vec{\xi} + \int_D J\phi^2 d\vec{\xi}. \end{aligned} \quad (6.5)$$

We first consider the high-order term in (6.5), containing the derivatives of ϕ . Function $\Pi(u)$ is linear with respect to ξ_i , so the following estimate holds

$$(\phi_{\xi_i})^2 \leq \int_D (u_{\xi_i \xi_i})^2 d\vec{\xi}, \quad \forall i \in \{1, \dots, n\}. \quad (6.6)$$

We can write $u_{\xi_i \xi_i} = \mathbf{g}_i^T H \mathbf{g}_i$, where H is the Hessian of function u , and from the singular values definition in the Lemma's statement we get $S^{-1} S^{-T} \leq \frac{\sqrt{1+|\nabla u|^2}}{\gamma^2 v^{2/n}}$ and $(\mathbf{g}_i^T \mathbf{g}_i) \leq \frac{v^{2/n} \Gamma^2}{\sqrt{1+|\nabla u|^2}}$. Thus, for the high-order term in (6.5) we obtain

$$\begin{aligned} \int_D J(\nabla_{\xi} \phi)^T S^{-1} S^{-T} \nabla_{\xi} \phi d\vec{\xi} &\leq \frac{\sqrt{1+|\nabla u|^2}}{\gamma^2 v^{2/n}} \int_D J \sum_{i=1}^n (\mathbf{g}_i^T H \mathbf{g}_i)^2 d\vec{\xi} \leq \\ &\leq 2K^2 \frac{\Gamma^4}{\gamma^2} \frac{v^{2/n}}{\sqrt{1+|\nabla u|^2}} \text{meas}(\Omega_c). \end{aligned}$$

Using (6.6) twice we can obtain an estimate for the low-order term in (6.5)

$$\int_D J \phi^2 d\vec{\xi} \leq \int_D J(\nabla_{\xi} \phi)^T \nabla_{\xi} \phi d\vec{\xi} \leq \int_D J \sum_{i=1}^n (\mathbf{g}_i^T H \mathbf{g}_i)^2 d\vec{\xi} \leq 2K^2 \Gamma^4 \frac{v^{4/n}}{1+|\nabla u|^2} \text{meas}(\Omega_c),$$

which provides the L_2 -error estimate (6.4). We neglect this low-order term in the H^1 -error estimate (6.3). ■

Consequently, for the global estimates over the whole computational domain Ω , $\text{meas}(\Omega) = 1$, we get

$$\|u - \Pi(u)\|_{H^1(\Omega)} \leq \sqrt{2} K \frac{\Gamma^2}{\gamma} h, \quad (6.7)$$

$$\|u - \Pi(u)\|_{L_2(\Omega)} \leq \sqrt{2} K \Gamma^2 h^2, \quad (6.8)$$

where K, Γ, γ are global bounds over the whole domain.

Comparing the estimates in Lemma 4 with classical finite element local interpolation estimates

$$\|u - \Pi(u)\|_{H^1(\Omega_c)} \leq C \sigma_{\Omega_c}^4 h |u|_{H^2(\Omega_c)}, \quad (6.9)$$

$$\|u - \Pi(u)\|_{L_2(\Omega_c)} \leq C \sigma_{\Omega_c} h^2 |u|_{H^2(\Omega_c)},$$

we see that coefficients Γ^2 and Γ^2/γ in estimates (6.7)-(6.8) using the modified metric, enter in a similar manner as the element quality σ_{Ω_c} in the standard interpolation bounds of (6.9). As we have already established in Section 5.4, the singular values Γ and γ of the Jacobian

matrix can be evaluated in terms of distortion metric E_θ . Our local interpolation estimates (6.3), (6.4) also suggest better interpolation in the regions with high solution gradients, since as a result of minimizing the adaptation functional (6.2) we should have $\Gamma \rightarrow 1$ and $\gamma \rightarrow 1$. The above analysis leading to estimates (6.7)-(6.8) is illustrated on the following numerical test, where we compute the error in finite element solution and singular values of Jacobian matrices on different adapted meshes.

Numerical experiment. Let us consider the test problem

$$-\nabla \cdot (\alpha \nabla u) = f \text{ in } \Omega = [0, 1] \times [0, 1],$$

where

$$\alpha = \frac{1}{\nu} + \nu(x_1 + x_2 - 1)^2,$$

$$f(x_1, x_2) = 4\nu(x_1 + x_2 - 1)(\arctan \nu(x_1 + x_2 - 1) + \arctan \nu) + 4$$

and Dirichlet boundary data are specified from analytic solution

$$u(x_1, x_2) = (2 - x_1 - x_2)(\arctan \nu(x_1 + x_2 - 1) + \arctan \nu).$$

The solution of this test problem has an interior layer (region of steep gradient $O(\nu)$) for large ν .

Figures 6.12 and 6.13, respectively, are graphs of L_2 and H^1 errors and show rates of convergence in the finite element solutions, obtained on uniform and adapted grids. For each mesh size h two adapted grids were constructed using our adaptive redistribution approach, corresponding to values $\theta = 0.8$ and $\theta = 0.1$ in the functional (6.2). Our first observation is that for $\theta = 0.8$ and small ν , i.e. for solutions without steep gradients, errors on the adapted grid are independent of h and do not show the expected rate of convergence. This can be explained by the fact that at $\theta = 0.8$ the dominant part of the overall distortion measure E_θ is volumetric distortion measure μ . Since

$$\mu = \frac{1}{2} \left(x + \frac{1}{x} \right), \text{ where } x = \frac{\det S(\det \mathcal{G})^{1/2}}{v},$$

this distortion measure has a minimum at

$$x = 1, \text{ or } \det S = \frac{v}{(\det \mathcal{G})^{1/2}} = \frac{v}{\sqrt{1 + |\nabla u|^2}},$$

and, consequently, minimization of μ leads to cell clustering in zones where the function has a nonzero gradient. For functions with small gradient, this grid distortion is unnecessary and induces an error, which does not depend on the mesh spacing.

However, for $\theta = 0.1$ and small ν errors in the solutions on adapted and uniform grids agree. In this case shape distortion measure β , which is responsible for promoting an “ideal” square shape for the element, is dominant in the overall measure E_θ and does not allow severe mesh distortion, unless the function gradient is very high.

As expected, for solutions with sharp gradients, the error on adaptive grids is significantly less than on the uniform meshes. It achieves its asymptotic regime earlier and, consequently, is comparable to the error on a much finer uniform grid.

Graphs in Figures 6.14 and 6.15 verify the dependence expected from the above estimates (6.7), (6.8) on the interpolation error, i.e. $\|e\|_{L_2} \propto \Gamma^2 h^2$ (slope 2 on log-log scale) and $\|e\|_{H^1} \propto h \Gamma^2 / \gamma$ (slope 1). These plots were obtained again for adaptive redistribution with $\theta = 0.8$ and $\theta = 0.1$.

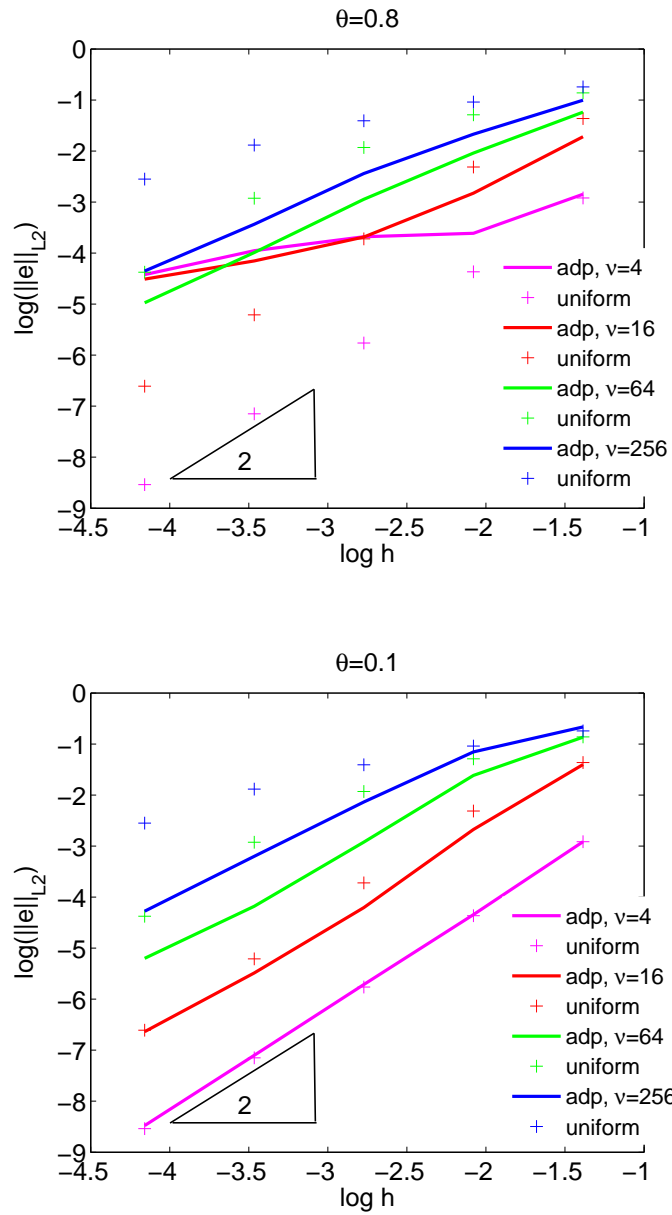


Figure 6.12: Comparison of the L_2 errors for solutions on uniform and adaptive meshes for $\theta = 0.8$ (top) and $\theta = 0.1$ (bottom).

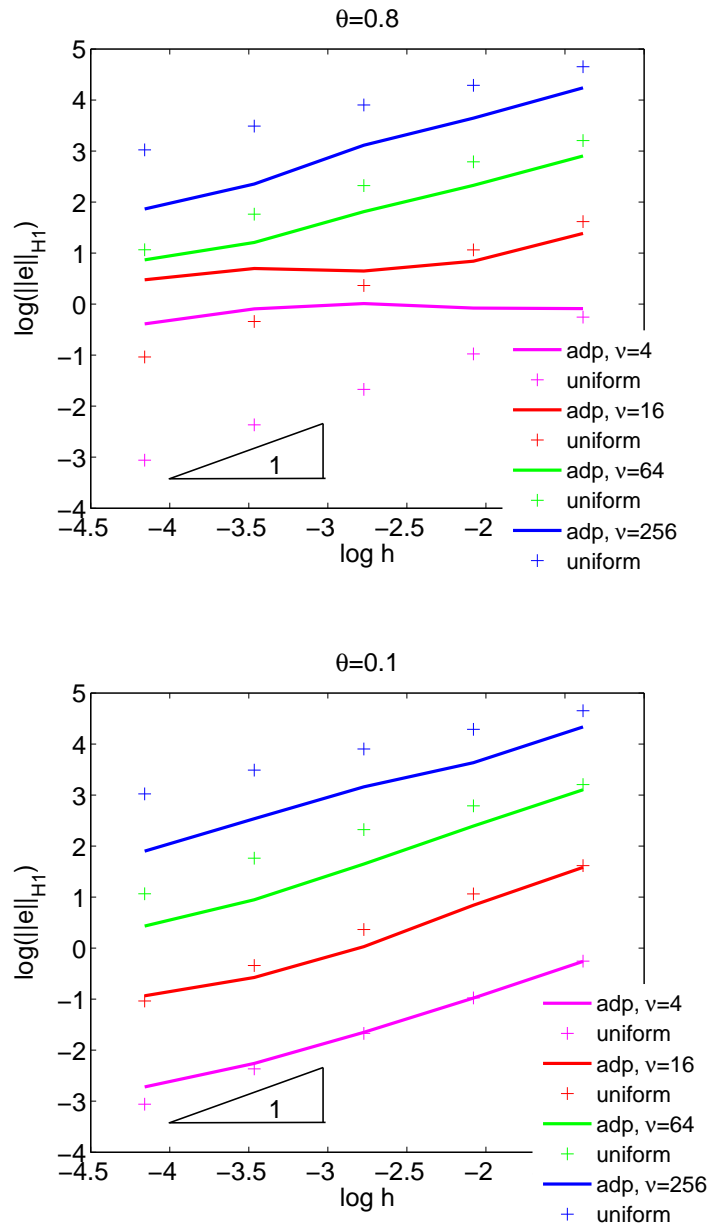


Figure 6.13: Comparison of the H^1 errors for solutions on uniform and adaptive meshes for $\theta = 0.8$ (top) and $\theta = 0.1$ (bottom).

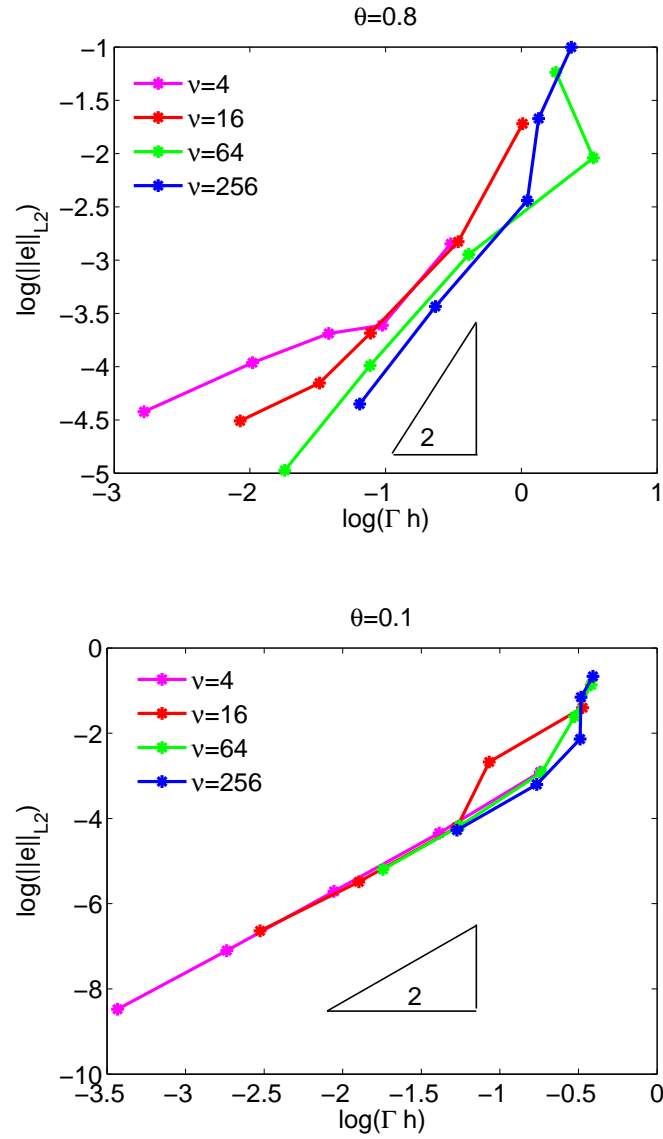


Figure 6.14: Plots of L_2 error vs estimate for solution on adaptive meshes for $\theta = 0.8$ (top) and $\theta = 0.1$ (bottom).

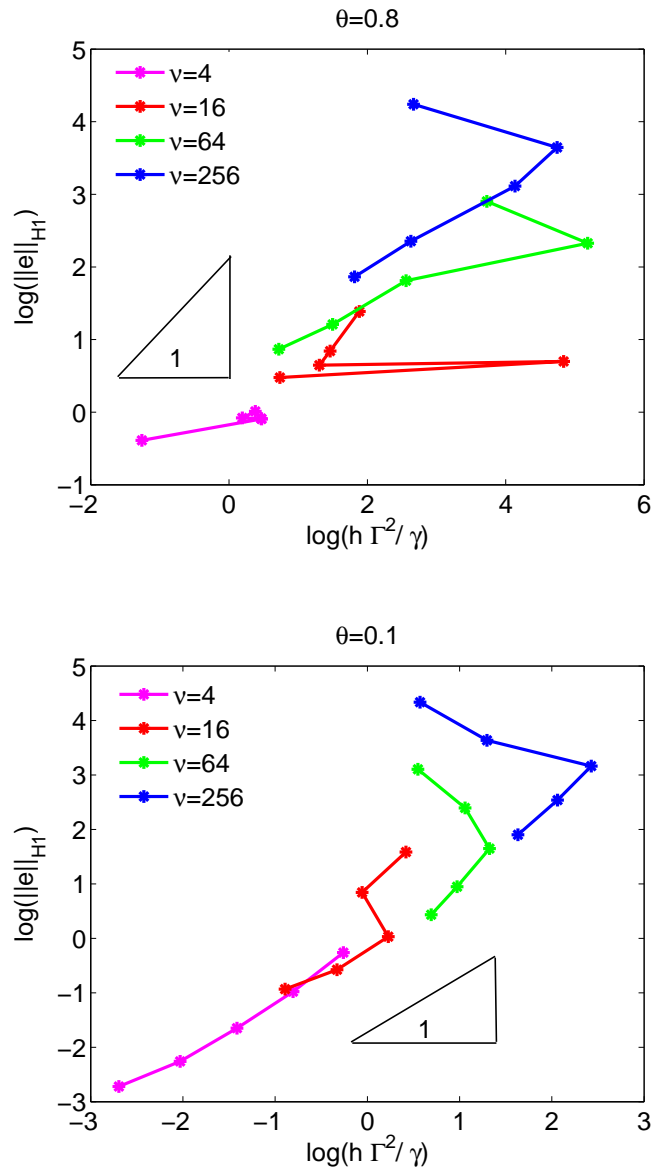


Figure 6.15: Plots of H^1 error vs estimate for solution on adaptive meshes for $\theta = 0.8$ (top) and $\theta = 0.1$ (bottom).

Chapter 7

Transport applications

In this chapter we present the results of simulations of several transport application problems and analyze the role of the smoothing technique in obtaining accurate solutions.

7.1 Moving interface problems: application to Lagrangian computations in fluid dynamics

An arbitrary Lagrangian-Eulerian (ALE) numerical technique for solving time-dependent fluid dynamics problems was introduced in [81]. The method uses a finite difference mesh with vertices that may be moved with the fluid (Lagrangian), be held fixed (Eulerian), or be moved in any other prescribed manner. The advantage over purely Lagrangian or Eulerian methods is that the mesh deformation can be controlled (avoiding folding), still keeping the mesh close to the Lagrangian mesh (for improved accuracy). However, following closely the Lagrangian mesh often results in a highly distorted mesh unsuitable for further computations. In rezoning formulations [82] - [84], a Lagrangian calculation runs until the mesh becomes unacceptably distorted, then a new good quality mesh is created, the solution is mapped onto it, and calculation continues. Our smoothing methodology can be used to detect unacceptable mesh distortions. A rezoning strategy, similar to that used in the ALE method, would be to smooth the Lagrangian mesh when it becomes highly distorted using our algorithm and map the solution onto the smoothed mesh. Thus, a new mesh will be close to Lagrangian and remapping will not introduce a significant error in the solution.

7.1.1 Rayleigh-Taylor instability problem.

In this example, we simulate the Rayleigh-Taylor instability problem for two ideal gases with nondimensional densities $\rho_h = 2$ and $\rho_l = 1$, and adiabatic constant $\gamma = 1.4$, following the problem formulation in [85]. Initially, the heavier gas is above the lighter gas in a rectangular vessel $[0 : 1/6] \times [0 : 1]$. A nondimensional gravitational acceleration $g = 0.1$ is directed downwards producing an unstable situation. The interface $y(x) = 1/2$ is deliberately perturbed as described by the formula $y(x) = 1/2 + \epsilon \cos(6\pi x)$, $\epsilon = 0.01$. Initially, velocity is zero everywhere; the pressure distribution is approximately hydrostatic.

The time evolution of this problem leads to a rollup of the interface and the generation of significant vorticity. Thus, this problem is generally regarded as poorly suited for Lagrangian methods; nevertheless, it is often used as a benchmark problem for comparison of robustness, accuracy and efficiency of different ALE techniques. Here we use it to test the limits of our smoothing algorithm in this context. Hence, we perform computations by a purely Lagrangian method, adding smoothing correction steps with remapping when the mesh becomes nearly folded. We use an explicit time-integration scheme, so the time step decreases when the mesh deforms. In the algorithm implemented here, the discretized conservation of mass and momentum equations in Lagrangian frame are [81]

$$\frac{d}{dt} \int_V \rho dV = 0, \quad (7.1)$$

$$\frac{d}{dt} \int_{V^*} \rho \vec{u} dV + \int_{V^*} \nabla p dV - \int_{V^*} \rho \vec{g} dV = 0, \quad (7.2)$$

where V is cell volume and V^* is the volume surrounding a grid point.

Solution algorithm Initializing the calculations: initial values are assigned to variables x, y, u, v, ρ, p and time step Δt .

At time t^k , $k = 0, 1, 2, \dots$

1. Solution is advanced one time step using an explicit Lagrangian calculation:
 - Velocity components are updated \tilde{u}^k, \tilde{v}^k using finite difference approximation [81] of the conservation of momentum equation (7.2).

- The time step Δt is adjusted so that the evolved mesh $x^k + \Delta t \tilde{u}^k, y^k + \Delta t \tilde{v}^k$ remains unfolded (our distortion functional is used to detect folding).
 - Using the adjusted time step Δt^k , the evolved velocity u^{k+1}, v^{k+1} , mesh x^{k+1}, y^{k+1} , density ρ^{k+1} and pressure p^{k+1} (from the equation of state) are computed.
2. If the time step $\Delta t^k < \epsilon$ is smaller than a given tolerance, the mesh x^{k+1}, y^{k+1} is smoothed using our algorithm yielding a new mesh $\tilde{x}^{k+1}, \tilde{y}^{k+1}$. During smoothing the grid points on the fluid interface, as well as on the domain boundaries, are allowed to tangentially slide along the interface/boundary.
 3. The solution is mapped onto the smoothed mesh: velocity components are interpolated from the piecewise-linear approximation on the old mesh; piecewise-constant density and pressure are remapped using either interpolation or conservative rezoning strategy described below (we compare results of computations using these two different remap strategies).

Rezoning Rezoning algorithms are usually defined by means of mapping algorithms operating between two arbitrary meshes. They are often required to be conservative, and to preserve the solution monotonicity, and they introduce a diffusive error into the solution. Hence, frequent remapping may be expensive. There are several basic rezoning approaches [86]. The cheapest, most diffusive and non-conservative method is interpolation; here, new values are evaluations of an interpolation function (to the new mesh) that is constructed from the solution on the old mesh. In the particle in cell method [82], the element of the old mesh is subdivided by a logically regular mesh, a particle is associated with each of the subelements. Then the values on a new mesh cell are computed as a sum of contributions from all the particles inside this new cell. In the completely conservative rezone strategies [83, 84], the integrals in the conservation statement are computed exactly on the intersections between the cells of new and old meshes.

In the simulation of the Rayleigh-Taylor instability problem undertaken here we use a modification of the latter rezoning approach, introduced in [87, 88]. This technique is specifically designed to work in cases where the new mesh is obtained by a small displace-

ment of the vertices of an old mesh. Then the signed flux integrals are evaluated for each cell (see Figure 7.1), yielding a conservative quadrature for computing new masses of the cells. The remap is exact for a global linear function.

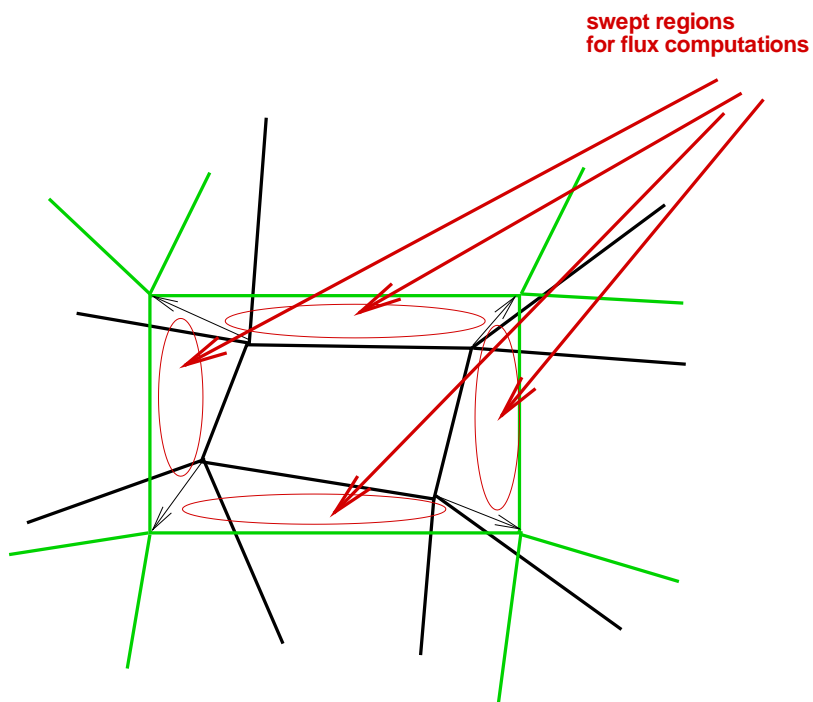


Figure 7.1: Conservative remap between the old (black) and the new (green) meshes; density fluxes are calculated over swept regions.

Results The explicit Lagrangian computations for the test problem without remap (step 1) only proceed to the time $t = 3.43$ (the timesteps become progressively smaller and after this time the mesh deformation requires $\Delta t \approx 0$). The solution ρ, p, u and v at this time is shown in Figure 7.2. With the addition of mesh smoothing (step 2) and the interpolation remapping in step 3 of the solution algorithm, we can run the explicit computations further, and the solution at time $t = 5.32$ is shown in Figure 7.3. However, from this Figure we

observe that too much distortion has been introduced in the density distribution by the interpolation remaps. Solution using the conservative remap strategy (in step 3) at a time $t = 5.58$ is presented in Figure 7.4. Here, a smooth density distribution is still observed, even though the interface distortion becomes quite large. Comparing the resulting meshes for solutions using the two remap strategies we can see that remap error in density introduces errors in other variables, and these errors increase with time giving an inaccurate solution field and interface position.

Next, the mesh correction results (at different times) are shown in Figure 7.5. Here, the interface between the two fluids is treated as a boundary in the smoothing procedure and interior points on the interface slide tangentially along this boundary.

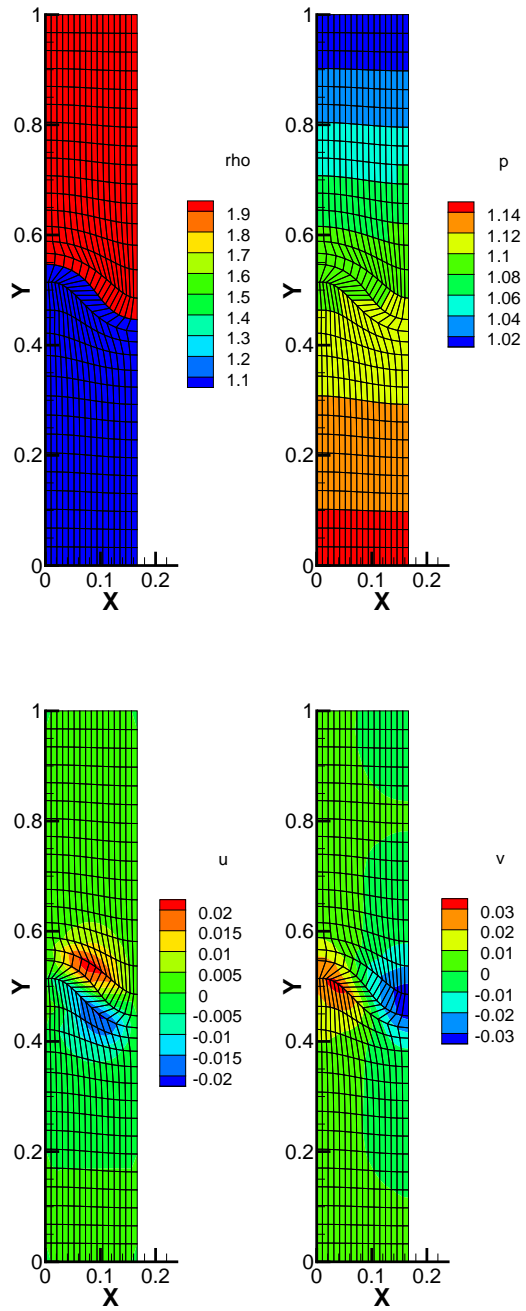


Figure 7.2: Solution to RT instability problem at $t=3.43$, no remap.

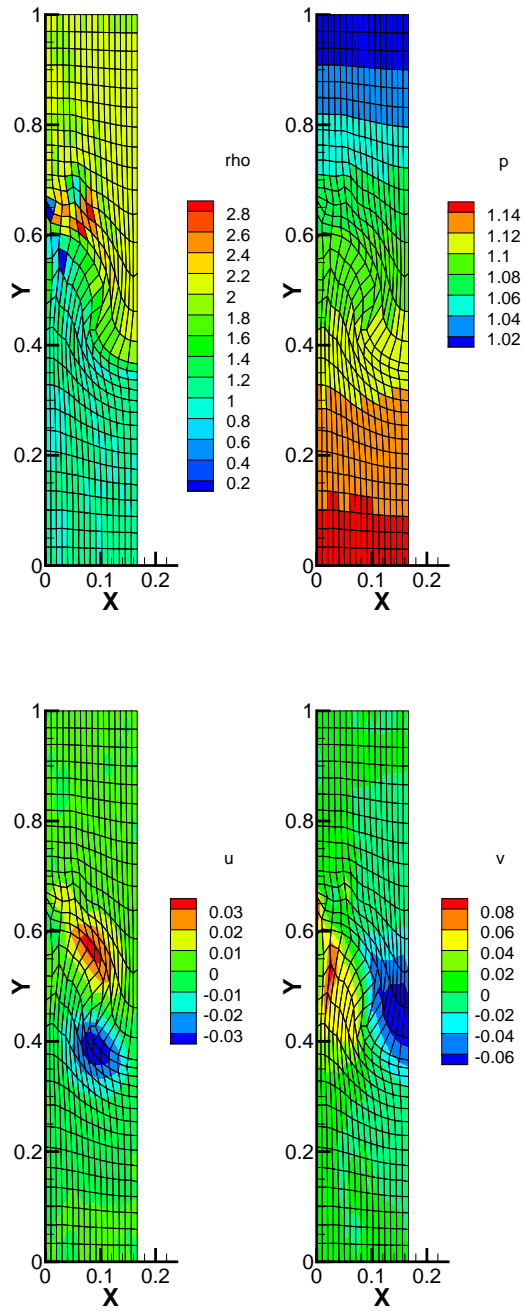


Figure 7.3: Solution to RT instability problem at $t=5.32$, interpolation remap.

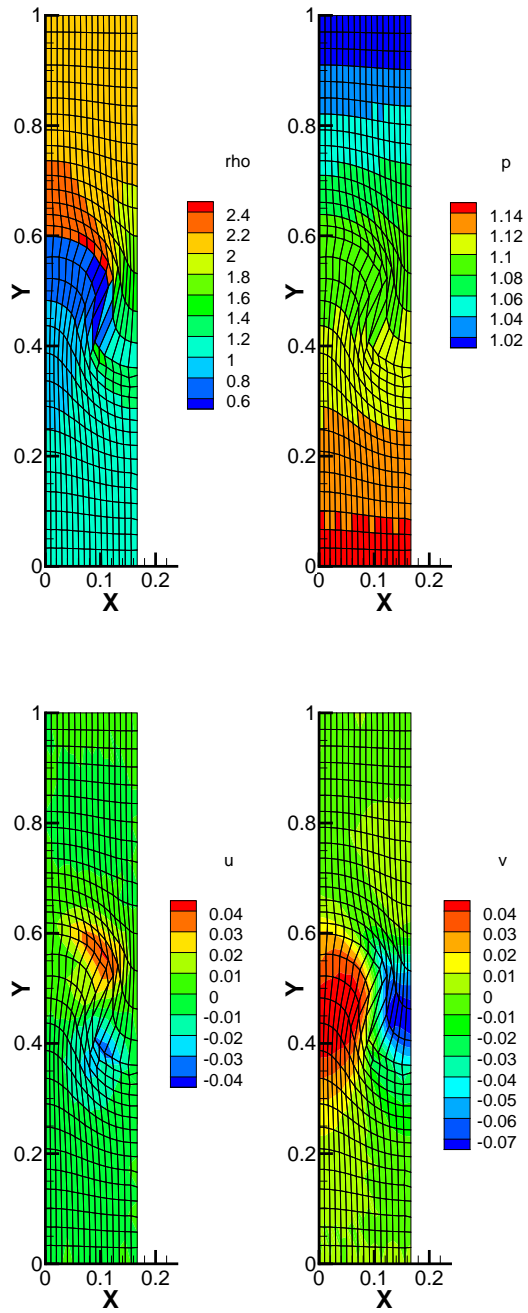


Figure 7.4: Solution to RT instability problem at $t=5.58$, conservative remap.

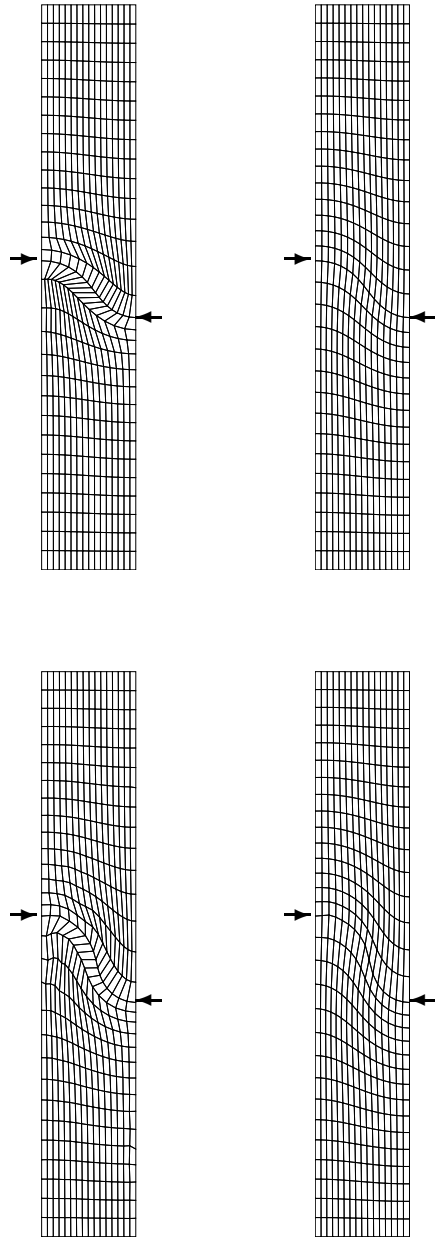


Figure 7.5: Grid corrections: before (left) and after smoothing (right); arrows indicate the interface.

7.2 Blood flow in arterial branches

In this section we consider a pressure-driven flow in a branched pipe. The pipe geometry is deformed to represent the branching arteries, and a Powell-Eyring viscosity model [89] - [91] is used for approximation of the blood flow. In this simulation we use CUBIT to generate the undeformed grid, new software to morph the domain and mesh, our smoothing software, and the flow code developed in [79].

The flow is modeled by the incompressible Navier-Stokes equations with a generalized viscous constitutive model. In the Powell-Eyring fluid model, the viscosity is a function of the strain rate in the fluid and is given by:

$$\mu(s) = \mu_\infty + (\mu_0 - \mu_\infty) \frac{\sinh^{-1} \lambda s}{\lambda s},$$

where μ_0 and μ_∞ are the limiting viscosities at zero strain rate $s = 0$ and infinite strain rate $s \rightarrow \infty$ respectively; λ is a characteristic time.

Two domain geometries, chosen to model arteries, are shown in Figure 7.6 together with the boundary conditions. The outer surface of the pipes is a no-slip and no-penetration boundary. The inflow section has a fixed normal component of the traction and no flow tangent to the section. The outflow sections have no flow tangent to the sections and zero normal component of the traction. In the first domain the pipe radii away from the branch region are fixed, and branch pipes are curved so that the medial axis of the two outflow pipes lie in a plane perpendicular to the medial axis of the inflow pipe. In the second domain the pipe geometry is the same, but the pipe radii vary throughout the domain to model constrictions and dilations of the arteries.

The pipe geometries in Figure 7.6 were obtained from a hexahedral mesh inside the straight branching pipe geometry (Chapter 5, Figure 5.15). For each pipe the deformation function was defined with the aim of modeling the actual arteries. Figure 7.7 shows two views of brain arteries which were used as a prototype for the domain geometry (pictures from <http://www.neuropat.dote.hu/table/angio.htm>).

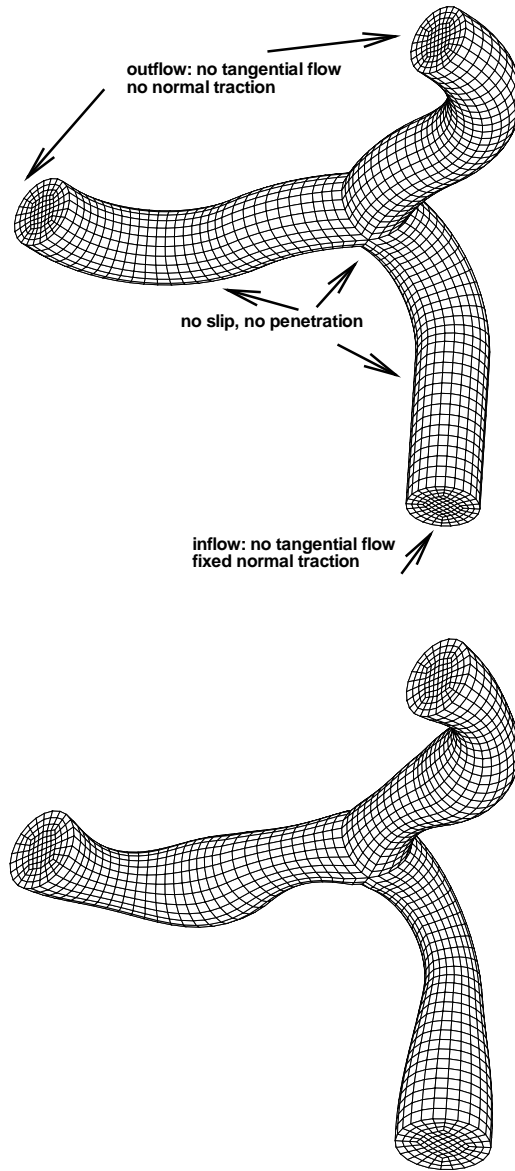


Figure 7.6: Domains and boundary conditions for the blood flow simulation: without constrictions (top) and with constrictions (bottom).

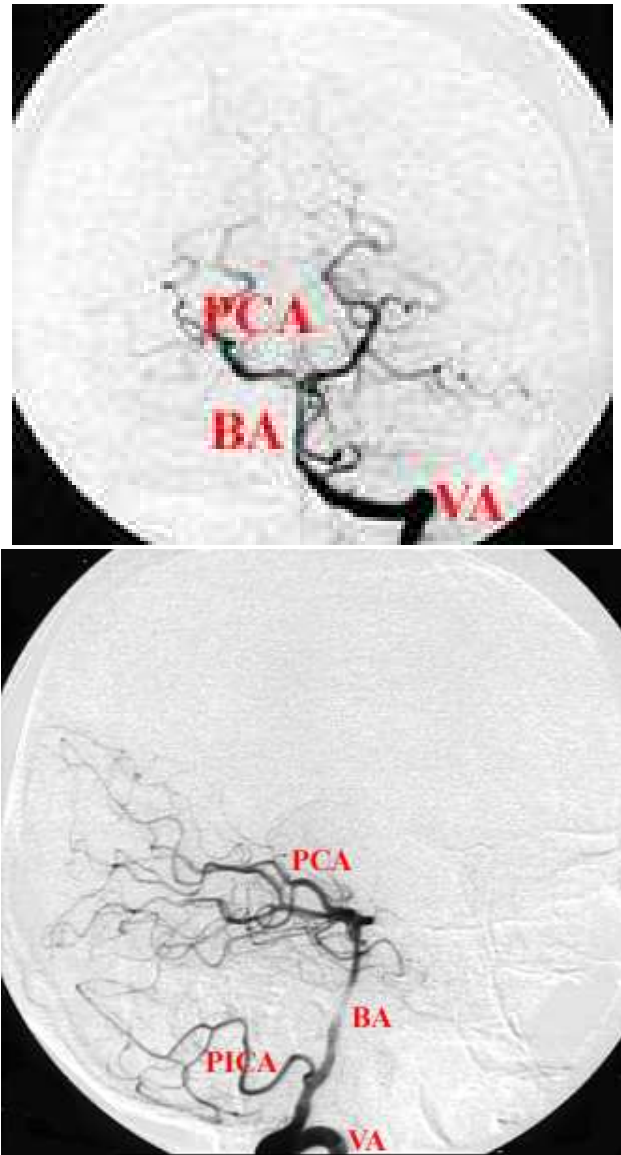


Figure 7.7: Two views of brain arteries.

The flow was computed at different values of $Re = 10, 20, 50$ (which is based on the given pressure difference and μ_0) and with $\mu_0/\mu_\infty = 1, 0.1, 0.03, 0.01$. Figures 7.8 - 7.11 show the plots of boundary viscous stress and flow streamlines, colored by pressure and velocity magnitude, for flow at $Re = 20$ in the pipes without constrictions with all stated choices of viscosity ratios. The color scale for each variable is defined from the maximum and minimum values of this variable through all four Figures in order to facilitate comparison between the Figures. The slow flow ($Re = 10$) does not exhibit significant changes with the change of μ_0/μ_∞ , and the fast flow ($Re = 50$) develop vortices even at μ_0/μ_∞ close to 1, i.e. the Newtonian case. From these Figures we can observe that:

- 1) The maximum boundary stress occurs at the non-smooth joints where the inflow pipe meets the two other pipes, as well as on the inside curve of the inflow pipe. The area near the joint for the two outflow pipes has very low stress in the case of Newtonian fluid, but the stress on this area grows significantly with reduction of μ_0/μ_∞ .
- 2) Pressure profiles are almost the same for all cases; however pressure at the joint of the two outflow pipes grows with reduction of μ_0/μ_∞ . That is, regions of higher pressure expand in the outflow direction.
- 3) The velocities of the fluid increase significantly with introduction of non-linearity, and the velocity profile displays sharper gradients. At $\mu_0/\mu_\infty = 0.03$ we can see a vortex starting to form near the joint for the outflow pipes, and the vortex formation becomes more evident at $\mu_0/\mu_\infty = 0.01$.

Figure 7.12 shows corresponding plots of boundary stress for different μ_0/μ_∞ for flow at $Re = 20$ with constrictions. The same trends in flow behavior with the change of μ_0/μ_∞ can be observed for this choice of geometry. However, we also see that the maximum boundary stress now occurs at the constriction in the inflow pipe for the Newtonian flow, but is reduced for the non-Newtonian fluid. Also the vortices do not form in this case. Figure 7.13 gives plots of stress, pressure and velocity for the flow at $Re = 20$, $\mu_0/\mu_\infty = 0.01$. The color scales here are the same as in the previous Figures. Comparing this result with that for flow under the same conditions in non-constricted pipes (Figure 7.11), we observe that constrictions reduce the non-linear effect of viscosity.

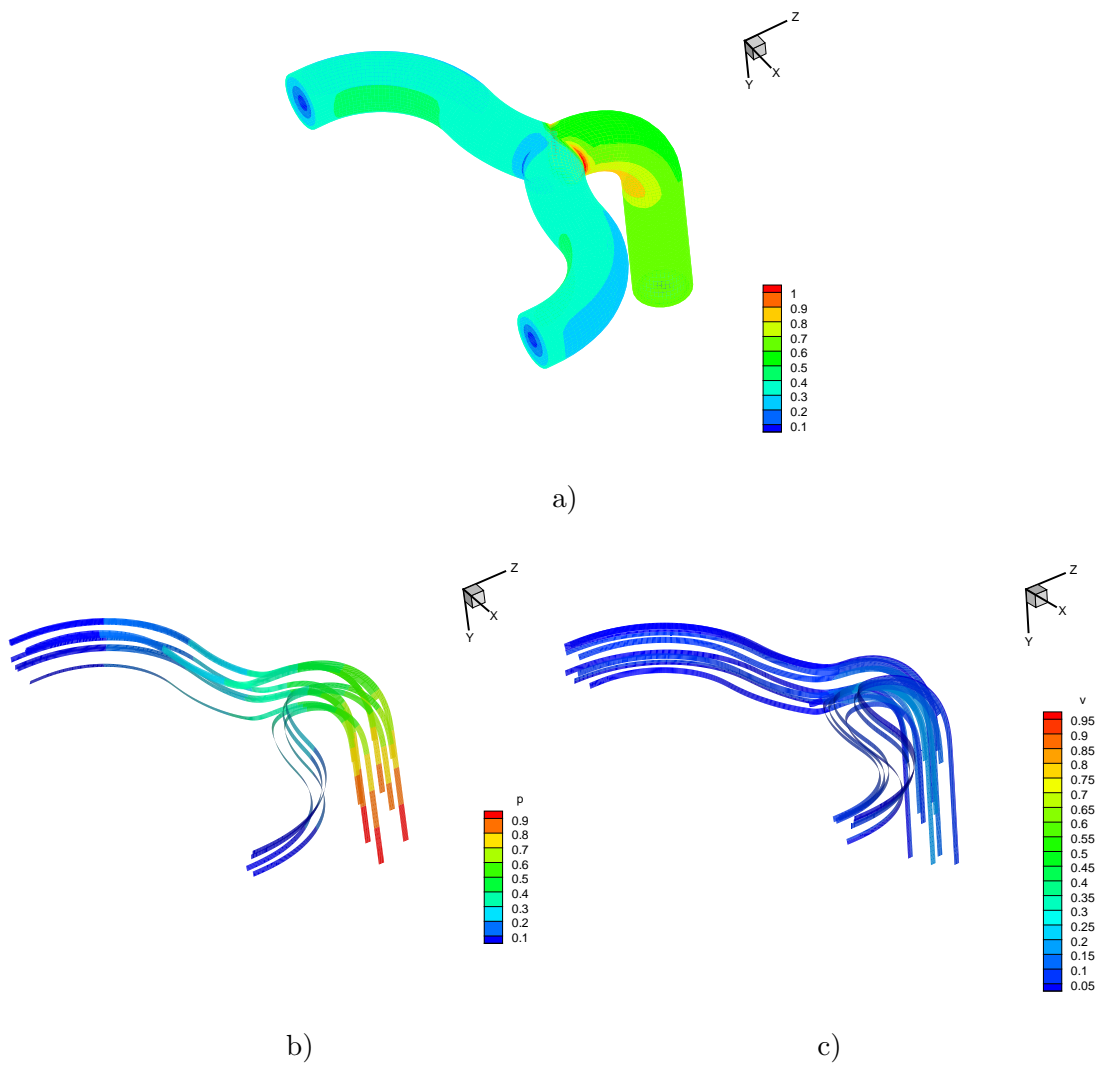


Figure 7.8: Flow at $Re = 20$, $\mu_0/\mu_\infty = 1$: a) boundary stress, b) pressure and c) velocity magnitude.

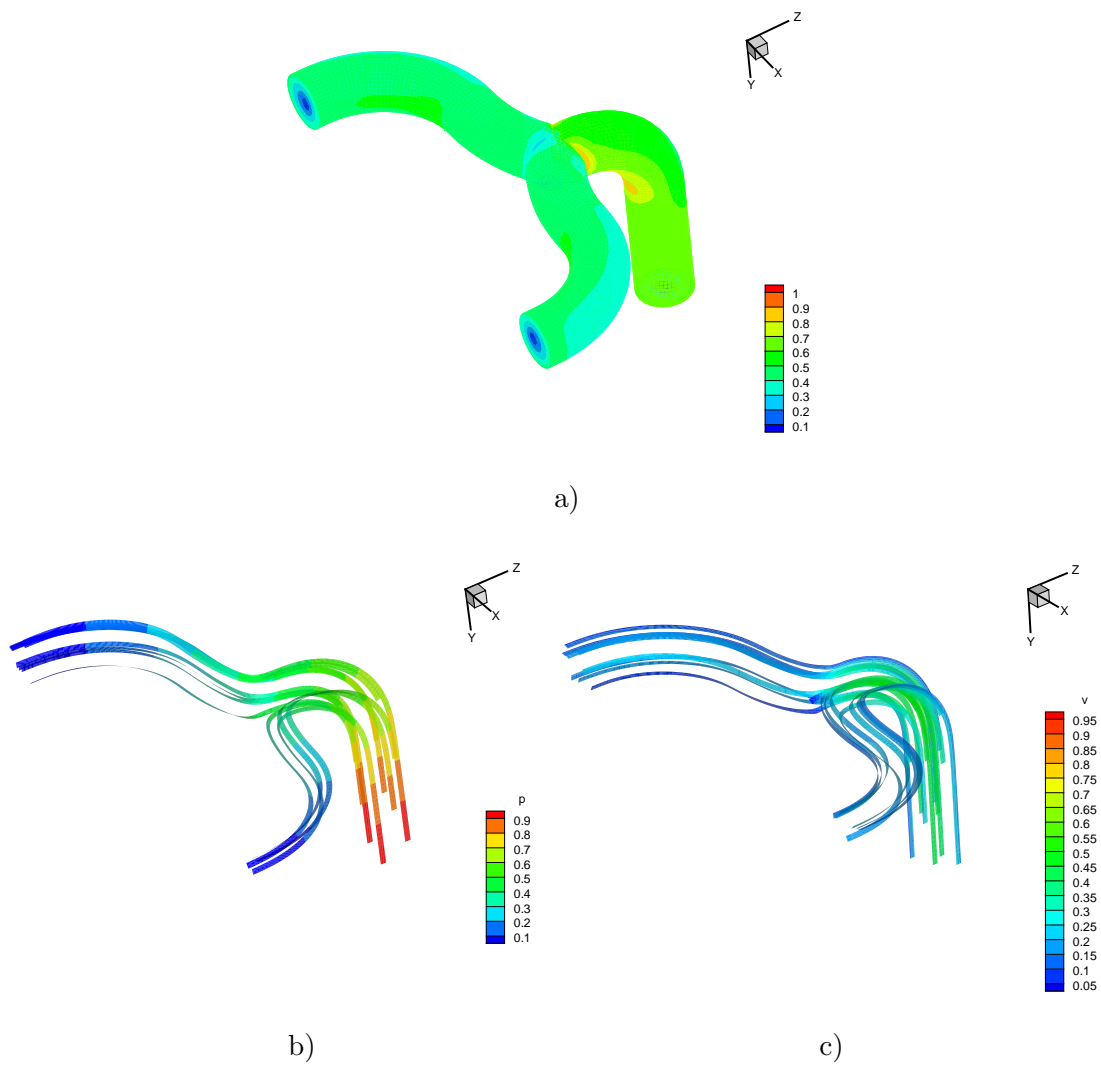


Figure 7.9: Flow at $Re = 20$, $\mu_0/\mu_\infty = 0.1$: a) boundary stress, b) pressure and c) velocity magnitude.

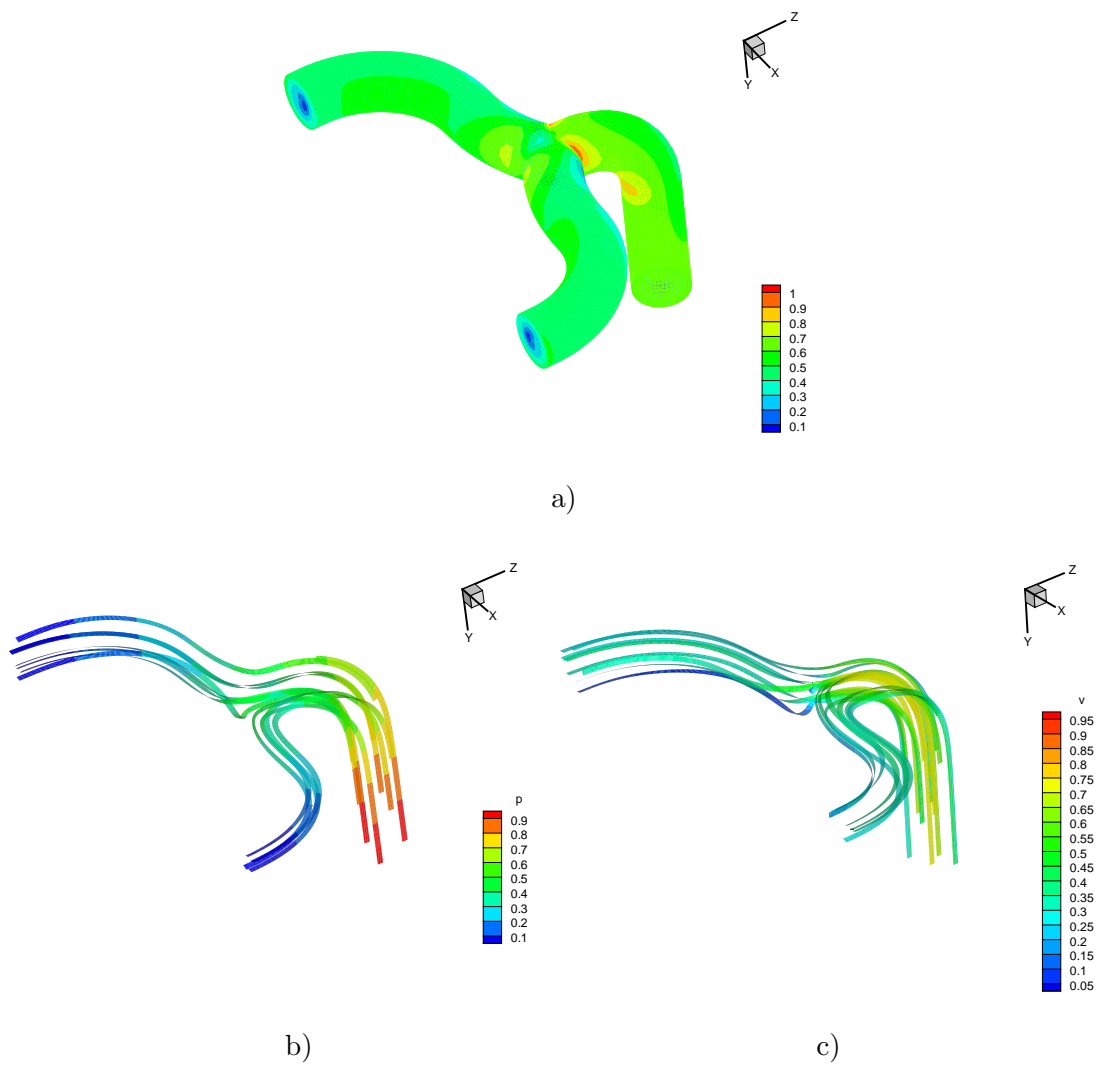


Figure 7.10: Flow at $Re = 20$, $\mu_0/\mu_\infty = 0.03$: a) boundary stress, b) pressure and c) velocity magnitude.

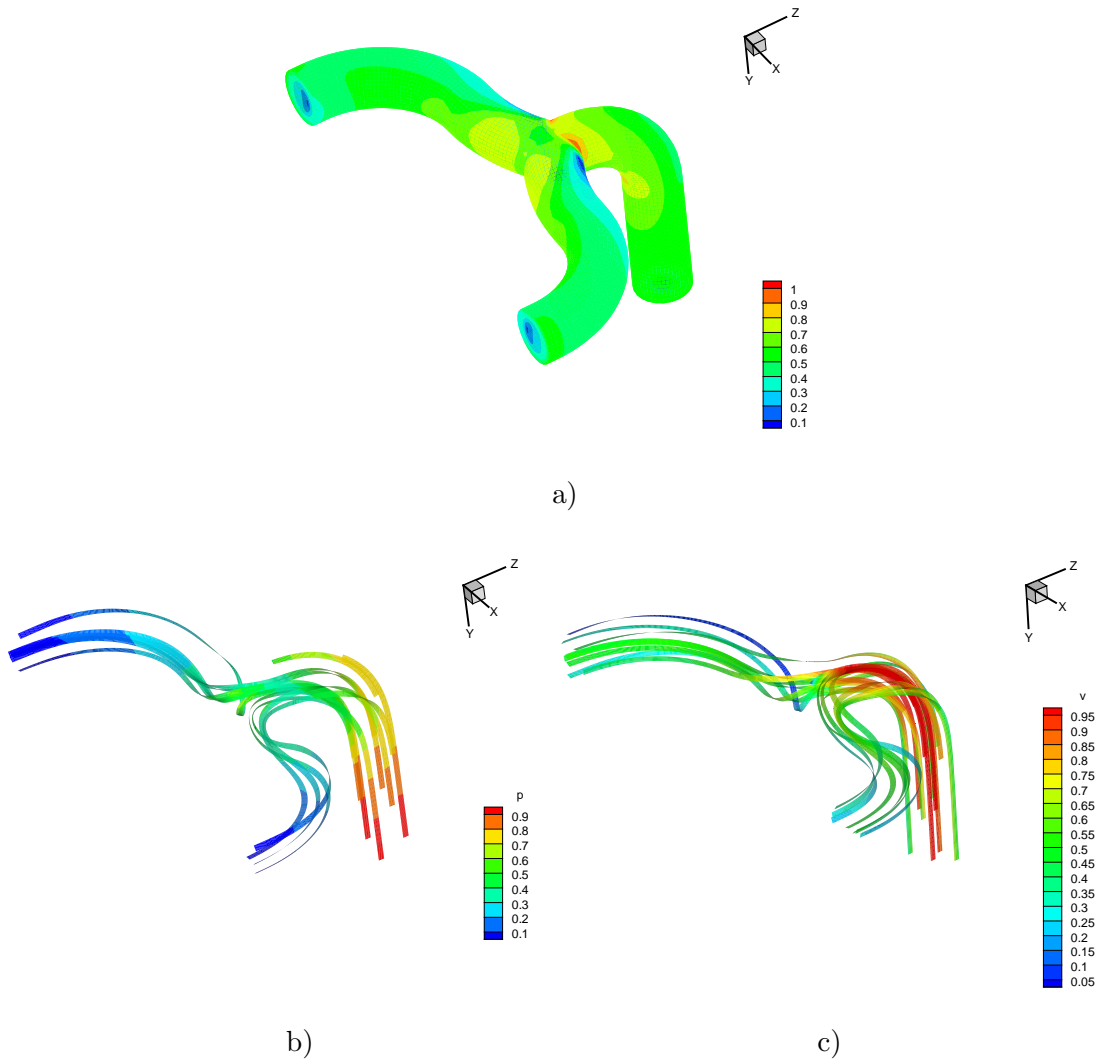


Figure 7.11: Flow at $Re = 20$, $\mu_0/\mu_\infty = 0.01$: a) boundary stress, b) pressure and c) velocity magnitude.

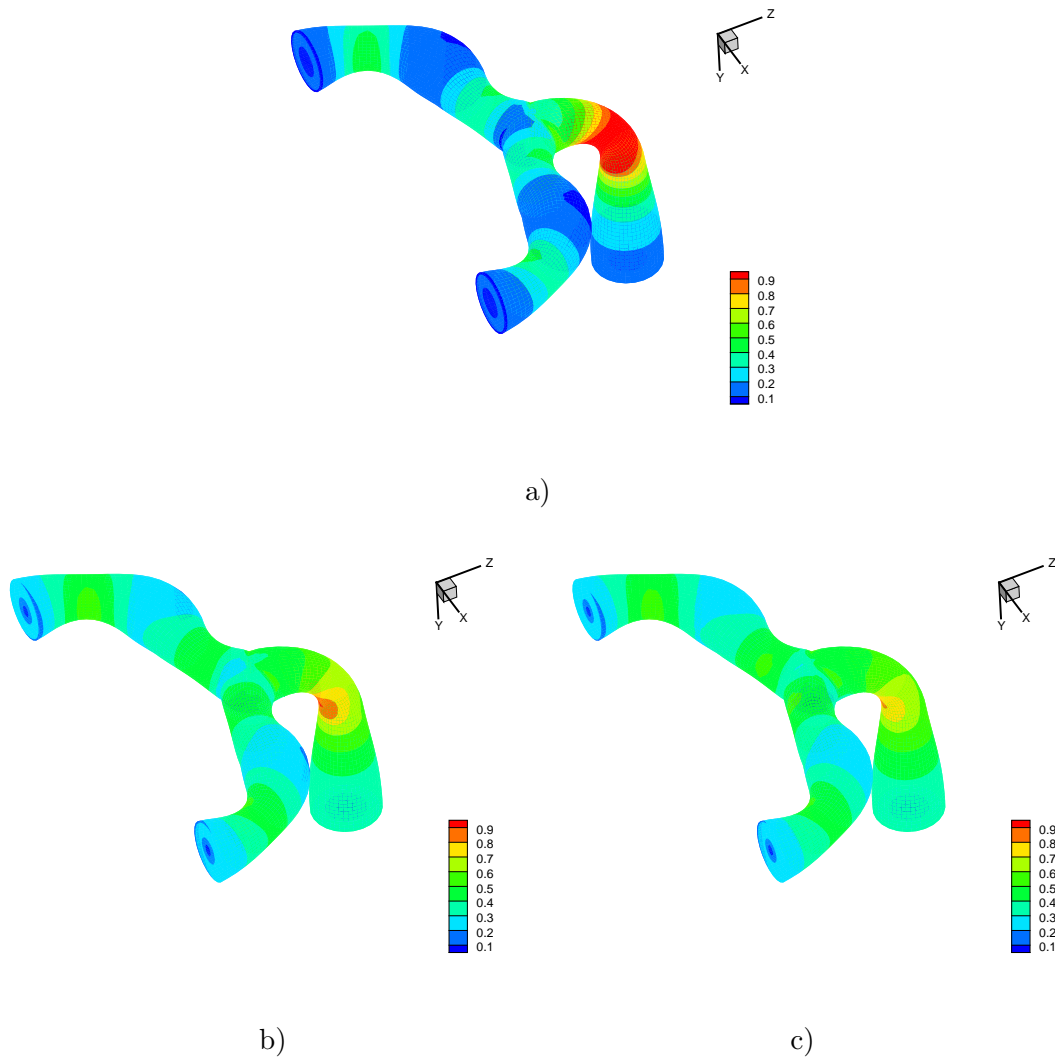


Figure 7.12: Boundary stress for flow in constricted pipes at $Re = 20$, a) $\mu_0/\mu_\infty = 1$, b) $\mu_0/\mu_\infty = 0.03$ and c) $\mu_0/\mu_\infty = 0.01$.

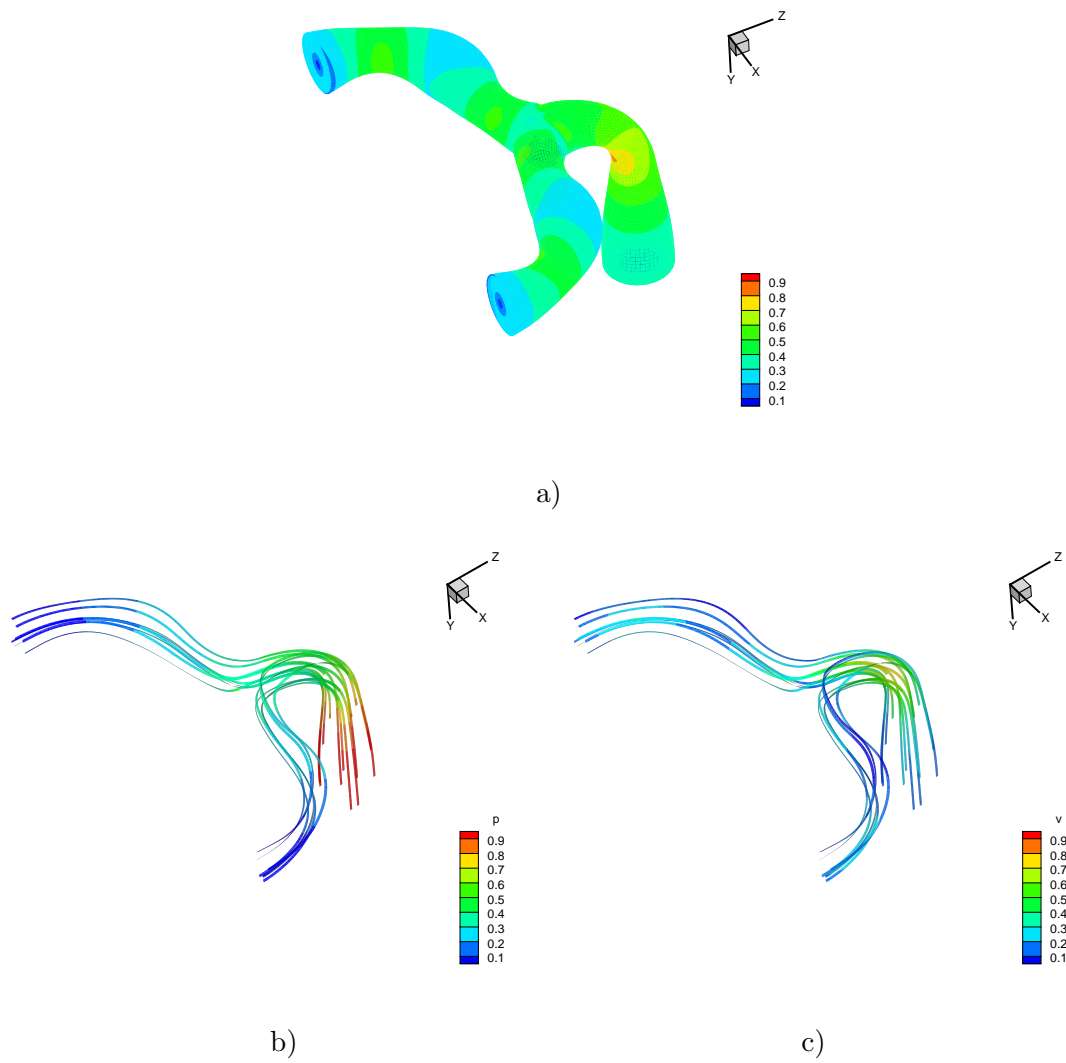


Figure 7.13: Flow in constricted pipes at $Re = 20$, $\mu_0/\mu_\infty = 0.01$: a) boundary stress, b) pressure and c) velocity magnitude.

In order to characterize the conditions of periodic blood flow in arteries better, transient “pumping” flow simulations were performed. In these computations, instead of a fixed pressure gradient between inflow and outflow boundaries $\nabla p = -1$ (i.e. fixed normal traction on the inflow boundary) we specify an oscillating function $\nabla p = -0.5(1 + \sin t)$. Simulations of the pumping flow at $Re = 20$ and with $\mu_0/\mu_\infty = 0.01$ yield similar results for both pipe geometries (i.e. with and without constrictions). The plots of velocity magnitude in the computed pumping flow in pipes without constrictions at different times are shown in Figure 7.14. Since the flow has no time to fully develop under this specified transient pressure gradient and the periodic average pressure gradient is smaller than the value in previous simulations, vortices do not form in this example (compare to Figure 7.11, where vortices form at the same flow conditions but fixed pressure gradient). Also, the maximum velocity magnitude, as well as the whole velocity profile, is similar to that of a Newtonian flow at $Re = 20$ and fixed pressure gradient. Thus, in this test of a pumping flow the effects of the nonlinear viscosity are not as significant.

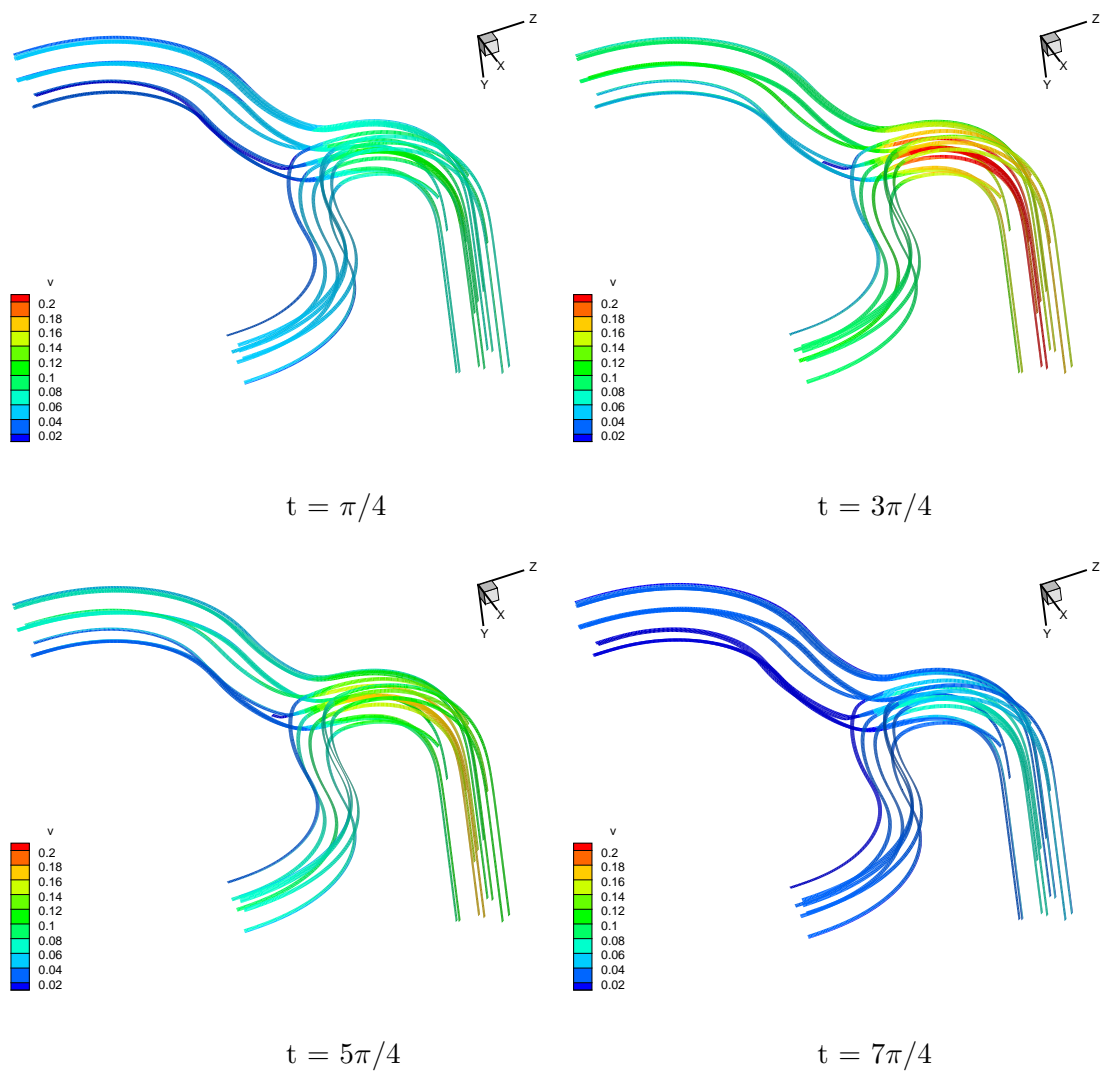


Figure 7.14: Pumping flow at $Re = 20$, $\mu_0/\mu_\infty = 0.01$: velocity magnitude at different times.

Next, in order to demonstrate the importance of using a high quality mesh for application simulations, we compare the results of the steady state non-Newtonian flow simulation with parameters $Re = 20$, $\mu_0/\mu_\infty = 0.01$ in the straight branched-pipe geometry (recall Figure 5.15) with three different meshes. All meshes are obtained by node redistribution of the same initial mesh. They include: 1) a mesh with randomly perturbed nodes (all elements remain valid, but the quality deteriorates), 2) a mesh smoothed with $\theta = 0.2$ (rapid cell size change due to valence effect, see Section 5.22) and 3) a mesh smoothed with $\theta = 0.8$ (high quality mesh). On these meshes the simulation runs till the times 1) $t = 54.8$, 2) $t = 61.1$ and 3) $t = 73.9$, respectively. After these times vortices form in the flow and no steady state can be achieved. The color plots of stress, pressure and velocity magnitude at the medial plane cut-out and streamlines of the flow computed on the third mesh at $t = 73.9$ are shown in Figure 7.15. We observe that the high pressure region forms at the joint of the lower pipes, and this information might be crucial in determining the conditions of break-down of the pipe walls. The calculations on the high quality mesh allow more reliable prediction of the flow.

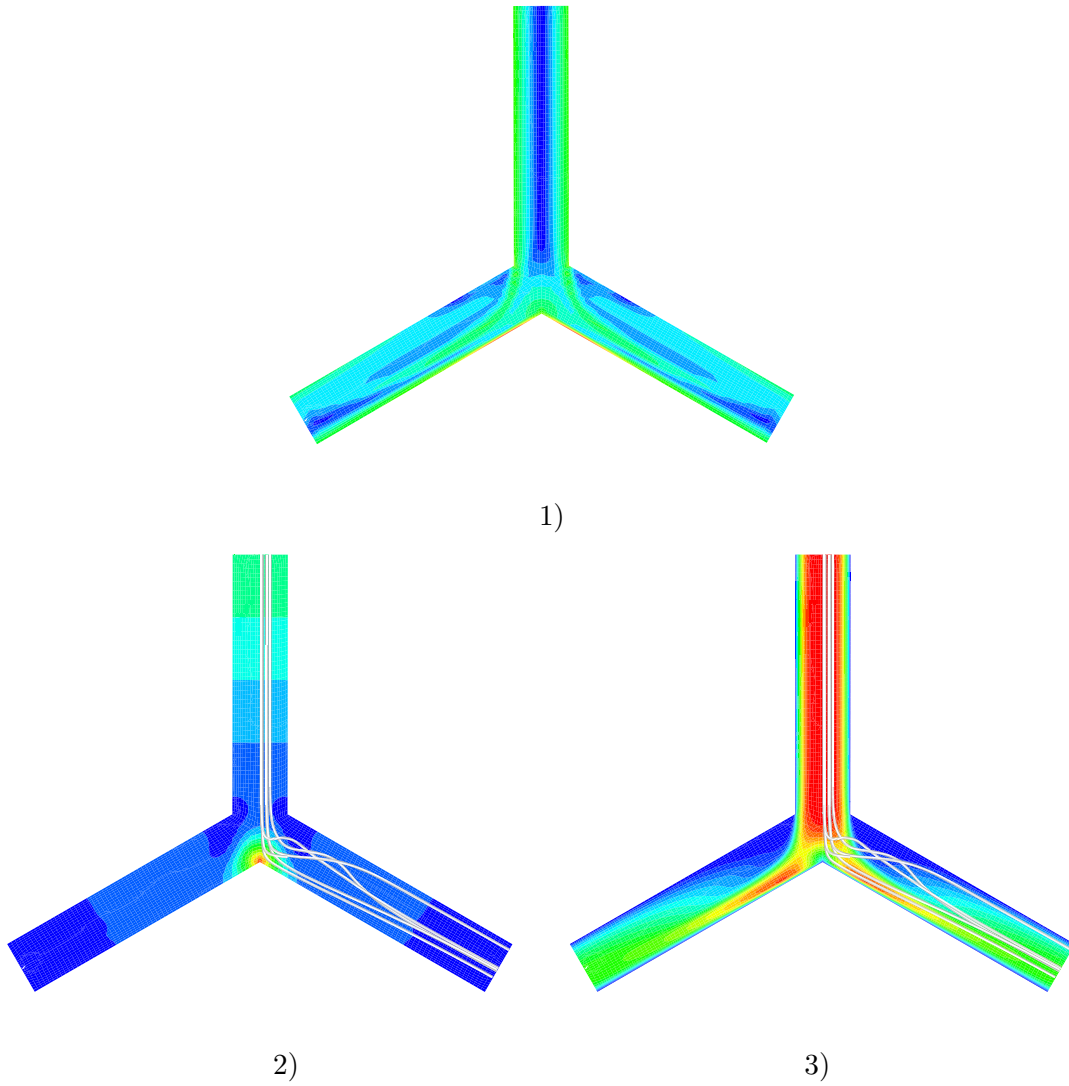


Figure 7.15: Flow in straight pipes at $Re = 20$, $\mu_0/\mu_\infty = 0.01$: 1) boundary stress, 2) pressure and 3) velocity magnitude.

Chapter 8

Concluding remarks

The variational smoothing algorithm developed here has been shown to be very versatile in its ability to treat many aspects of mesh improvement problems and several new theoretical results have been established. Furthermore, the scheme was implemented in C and its performance was tested for both 2D and 3D hybrid meshes for smoothing and unfolding, adaptive redistribution, improvement of meshes with hanging nodes and moving boundaries, and meshes containing curvilinear elements. The algorithm was tested on representative problems and yields good results in all these situations. It also overcomes several difficulties encountered by other popular smoothing techniques, such as effects of changing valence. The mathematical properties of the formulation were analyzed. In particular, a maximum principle for the local distortion metric was proved, providing a way for estimating quality and identifying degeneracy for a wide variety of element types. The importance of mesh smoothing was confirmed by numerical and analytical studies that investigate the relation between the application problem solvability, accuracy and mesh distortion. Application studies of problems describing various transport processes were conducted, and the impact of smoothing on their solution was investigated.

Our algorithm and software is now being used by the DoE National Laboratories and has been provided to the DoD Laboratories where its use is planned next year.

Future research directions include further extensions of the algorithm and its adaptation for an even wider range of problems. Further investigation of the analytical properties of the smoothing functional may lead to algorithm improvements. For example, implementation of the automatic selection for parameter θ depending on the particular problem would further facilitate the use of the algorithm. We have identified several open mathematical is-

sues, such as nondegeneracy and quality assessment for quadratic tensor-product elements, that are important and challenging. Our study of combined h-r schemes has important implications and in conjunction with solution feedback provides an elegant approach to the anisotropic grid need for boundary and interior layer problems. The present numerical studies suggest one r- step is very effective and this should be explored further numerically. We have described both coarse and fine grain parallel algorithms, but these have not yet been implemented, and it appears that no similar parallel strategy has yet been deployed. This will become an important issue for future large scale applications in industry and the US National Labs.

There are several other issues of similar significance that are identified during the course of this dissertation. The importance of these topics is evident from the studies in the annual International Meshing Roundtable meetings. Overall, there are several promising future research directions and improvement possibilities for the techniques and ideas presented in this work.

Bibliography

- [1] Thompson J.F., Warsi Z.U.A., Mastin C.W. *Numerical grid generation*. North-Holland, New-York, 1985
- [2] Carey G.F. *Computational Grids: Generation, Adaptation and Solution Strategies*. Taylor and Francis, 1997
- [3] Lohner R., Morgan K., Zienkiewicz O.C. “Adaptive Grid Refinement for the Compressible Euler Equations.” in *Accuracy Estimates and Adaptive Refinements in Finite Element Computations*, vol. Wiley, 281–297, 1986
- [4] Liseikin V.D. *Grid Generation Methods*. Springer-Verlag, Berlin, 1999
- [5] Branets L., Carey G.F. “A Local Cell Quality Metric and Variational Grid Smoothing Algorithm.” *Proceedings of the 12th International Meshing Roundtable, Santa Fe, NM*, pp. 371–378, 2003
- [6] Branets L., Carey G.F. “Smoothing and Adaptive Redistribution for Grids with Irregular Valence and Hanging Nodes.” *Proceedings of the 13th International Meshing Roundtable, Williamsburg, VA*, pp. 333–344, 2004
- [7] Branets L., Carey G.F. “A Local Cell Quality Metric and Variational Grid Smoothing Algorithm.” *to appear in Engineering with Computers*, 2005
- [8] Branets L., Carey G.F. “Extension of a Mesh Quality Metric for Elements with a Curved Boundary Edge or Surface.” *to appear in JCISE*, 2005
- [9] Winslow A.M. “Numerical Solution of the Quasilinear Poisson Equation in a Nonuniform Triangle Mesh.” *Journal of Computational Physics*, vol. 2, 149–172, 1967
- [10] Brackbill J.U., Saltzman J.S. “Adaptive Zoning for Singular Problems in Two Dimensions.” *Journal of Computational Physics*, vol. 46, 342–368, 1982
- [11] Godunov S.K., Prokopov G.P. “The Use of Moving Meshes in Gas-Dynamical Computations.” *USSR Computational Mathematics and Mathematical Physics*, vol. 12, 182, 1972
- [12] Thompson J.F., Thames F.C., Mastin C.W. “Automatic Numerical Generation of Body-Fitted Curvilinear Coordinate system for Field Containing Any Number of Arbitrary Two-Dimensional Bodies.” *Journal of Computational Physics*, vol. 15, 299, 1974

- [13] Charakhch'yan A.A., Ivanenko S.A. "A Variational Form of the Winslow Grid Generator." *Journal of Computational Physics*, vol. 136, 385–398, 1997
- [14] Anderson D.A. "Grid Cell Volume Control with an Adaptive Grid Generator." *Applied Mathematics and Computation*, vol. 35, 209–217, 1990
- [15] Pardhanani A., Carey G.F. "Optimization of Computational Grids." *Numerical Methods for Partial Differential Equations*, vol. 4, 95–117, 1988
- [16] Parthasarathy V.N., Kodiyalam S. "A Constrained Optimization Approach to Finite Element Mesh Smoothing." *Finite Elements in Analysis and Design*, vol. 9, 309–320, 1991
- [17] Canann S.A., Stephenson M.B., Blacker T. "Optismoothing: An Optimization-driven Approach to Mesh Smoothing." *Finite Elements in analysis and Design*, vol. 13, 185–190, 1993
- [18] Bank R.E., Smith R.K. "Mesh Smoothing Using A Posteriori Error Estimates." *SIAM Journal on Numerical Analysis*, vol. 34, 979–997, 1997
- [19] Yamada A., Shimada K., Itoh T. "Meshing Curved Wire-Frame Models Through Energy Minimization and Packing of Ellipses." *International Journal for Numerical Methods in Engineering*, vol. 46, 1221–1236, 1999
- [20] Jacquotte O.P. "A Mechanical Model for a New Grid Generation Method in Computational Fluid Dynamics." *Computer Methods in Applied Mechanics and Engineering*, vol. 66, 323–338, 1987
- [21] Shephard M.S., Georges M.K. "Automatic Tree-Dimensional Mesh Generation by the Finite Octree Technique." *International Journal for Numerical Methods in Engineering*, vol. 32, 709–749, 1991
- [22] Eiseman P. "Adaptive Grid Generation by Mean-Value Relaxation." *ASME Journal of Fluids Engineering*, vol. 107, 477–483, 1985
- [23] Joe B. "Construction of Three-Dimensional Improved-Quality Triangulations Using Local Transformations." *SIAM Journal on Scientific Computing*, vol. 16, 1292–1307, 1995
- [24] Amezua E., Hormaza M.V., Hernandez A., Ajuria M.B.G. "A Method of the Improvement of 3D Solid Finite Element Meshes." *Advances in Engineering Software*, vol. 22, 45–53, 1995
- [25] Zavattieri P.D., Dari E.A., Buscaglia G.C. "Optimization Strategies in Unstructured Mesh Generation." *International Journal for Numerical Methods in Engineering*, vol. 39, 2055–2071, 1996

- [26] Buscaglia G.C., Dari E.A. “Anisotropic Mesh Optimization and its Application in Adaptivity.” *International Journal for Numerical Methods in Engineering*, vol. 40, 4119–4136, 1997
- [27] Lo S.H. “Optimization of Tetrahedral Meshes Based on Element Shape Measures.” *Computers and Structures*, vol. 63, 951–961, 1997
- [28] Amenta N., Bern M., Eppstein D. “Optimal Point Placement for Mesh Smoothing.” *In 8th ACM-SIAM Symposium on Discrete Algorithms*, pp. 528–537, 1997
- [29] Freitag L. “On Combining Laplacian and Optimization-Based Mesh Smoothing Techniques.” *AMD Trends in Unstructured Mesh Generation, ASME*, vol. 220, 37–43, 1997
- [30] Canann S.A., Tristano J.R., Staten M.L. “An Approach to Combined Laplacian and Optimization-Based Smoothing for Triangular, Quadrilateral, and Quad-Dominant Meshes.” *Proceedings of the 7th International Meshing Roundtable*, Oct. 1998
- [31] Rassineux A. “Generation and Optimization of Tetrahedral Meshes by Advancing Front Technique.” *International Journal for Numerical Methods in Engineering*, vol. 41, 651–674, 1998
- [32] Zhou T., Shimada K. “An Angle-Based Approach to Two-Dimensional Mesh Smoothing.” *Proceedings of the 9th International Meshing Roundtable*, Oct. 2000
- [33] Garanzha V.A. “Barrier Variational Generation of Quasi-Isometric Grids.” *Computational Mathematics and Mathematical Physics*, vol. 40, 1617–1637, 2000
- [34] Branets L.V., Garanzha V.A. “Global Condition Number of Trilinear Mapping. Application to 3D Grid Generation.” *Proceedings of the minisymposium in the International conference “Optimization of finite-element approximations, splines and wavelets”, June 25-29, St.-Petersburg, Russia, 2001*
- [35] Chen Z., Tristano J.R., Kwok W. “Combined Laplacian and Optimization-Based Smoothing for Quadratic Mixed Surface Meshes.” *Proceedings of the 12th International Meshing Roundtable*, pp. 361–370, Sept. 2003
- [36] Mueller A.C., Carey G.F. “Continuously Deforming Finite Elements.” *International Journal for Numerical Methods in Engineering*, vol. 21, 2009–2126, 1985
- [37] Jacquotte O.P., Coussement G. “Structured Mesh Adaptation: Space Accuracy and Interpolation Methods.” *Computer Methods in Applied Mechanics and Engineering*, vol. 101, 397–432, 1992
- [38] Field D.A. “Laplacian Smoothing and Delaunay Triangulations.” *Communications in Applied Numerical Methods*, vol. 4, 709–712, 1988
- [39] Oddy A., Goldak J., McDill M., Bibby M. “A Distortion Metric for Isoparametric Finite Elements.” *Trans. Can. Soc. Mech. Eng.*, vol. No. 38-CSME-32, Accession No. 2161, 1988

- [40] Bank R.E., Xu J. “An algorithm for coarsening unstructured meshes.” *Numerische Mathematik*, vol. 73, 1–36, 1996
- [41] Freitag L.A., Ollivier-Gooch C. “Tetrahedral Mesh Improvement Using Swapping and Smoothing.” *International Journal for Numerical Methods in Engineering*, vol. 40, 3979–4002, 1997
- [42] Mezentsev A. “A Generalized Graph-Theoretic Mesh Optimization Model.” *Proceedings of the 13th International Meshing Roundtable, Williamsburg, VA*, pp. 255–264, 2004
- [43] Knobbe E. “Mesh Movement Governed by Entropy Production.” *Proceedings of the 13th International Meshing Roundtable, Williamsburg, VA*, pp. 265–276, 2004
- [44] Lipnikov K., Vassilevski Y. “Error Estimates for Hessian-Based Mesh Adaptation Algorithms with Control on Adaptivity.” *Proceedings of the 13th International Meshing Roundtable, Williamsburg, VA*, pp. 345–352, 2004
- [45] Li X., Remacle J., Chevaugeron N., Shephard M. “Anisotropic Mesh Gradation Control.” *Proceedings of the 13th International Meshing Roundtable, Williamsburg, VA*, pp. 401–412, 2004
- [46] Zlamal M. “On the Finite Element Method.” *Numerische Mathematik*, vol. 12, 394–409, 1968
- [47] Reshetnyak Y.G. “Mappings with bounded distortion as extremals of Dirichlet-type functionals.” *Siberian Mathematical Journal*, vol. 9, 652–666, 1968 (in Russian)
- [48] Babuska I., Aziz A.K. “On the angle condition in the finite element method.” *SIAM Journal on Numerical Analysis*, vol. 13, 214–226, 1976
- [49] Kerlic G.D., Klopfer G.H. “Assessing the Quality of Curvilinear Coordinate Meshes by Decomposing the Jacobian Matrix.” *Applied Mathematics and Computation*, vol. 11, 787–807, 1982
- [50] Cavendish J.C., Field D.A., Frey W.H. “An Approach to Automatic Three-Dimensional Finite Element Mesh Generation.” *International Journal for Numerical Methods in Engineering*, vol. 21, 329–347, 1985
- [51] Robinson J. “Some New Distortion Measures for Quadrilaterals.” *Finite Elements in Analysis and Design*, vol. 3, 183–197, 1987
- [52] Robinson J. “Quadrilateral and Hexahedron Shape Parameters.” *Finite Elements in Analysis and Design*, vol. 16, 43–52, 1994
- [53] Dannelongue H.H., Tanguy P.A. “Three-dimensional adaptive finite element computations and applications to non-newtonian flows.” *International Journal of Numerical Methods in Fluids*, vol. 13, 145–165, 1991

- [54] Girault V., Raviart P.A. *Finite Element Methods for Navier-Stokes Approximation, Series in Computational Mathematics, Vol. 5.* Springer, Berlin, 1980
- [55] Steinberg S., Roache P.J. “Variational Curve and Surface Grid Generation.” *Journal of Computational Physics*, vol. 100, 163–178, 1992
- [56] Parthasarathy V.N., Graichen C., Hathaway A.F. “A Comparison of Tetrahedron Quality Measures.” *Finite Elements in Analysis and Design*, vol. 15, 255–261, 1993
- [57] Lee C.K., Lo S.H. “A New Scheme for the Generation of a Graded Quadrilateral Mesh.” *Computers and Structures*, vol. 52, 847–857, 1994
- [58] Liu A., Joe B. “On the Shape of Tetrahedra from Bisection.” *Mathematics of Computation*, vol. 63, 141–15, 1994
- [59] Liu A., Joe B. “Relationship between Tetrahedron Shape Measures.” *BIT*, vol. 34, 268–287, 1994
- [60] Field D.A. “Qualitative Measures for Initial Meshes.” *International Journal for Numerical Methods in Engineering*, vol. 47, 887–906, 2000
- [61] Knupp P. “Algebraic Mesh Quality Metrics.” *SIAM Journal on Scientific Computing*, vol. 23, 193–218, 2001
- [62] Yuan K., Huang Y., Pian T. “Inverse Mapping and Distortion Measures for Quadrilaterals with Curved Boundaries.” *International Journal for Numerical Methods in Engineering*, vol. 37, 861–875, 1994
- [63] Baart M.L., McLeod R.J.Y. “Quadratic Transformations of Triangular Finite Element in Two Dimensions.” *IMA Journal of Numerical Analysis*, vol. 6, 475–487, 1986
- [64] Mitchell A.R., Phillips G., Wachspress E. “Forbidden Shapes in the Finite Element Method.” *Journal of the Institute of Mathematics and its Applications*, vol. 8, 260–269, 1971
- [65] Field D.A. “Algorithms for Determining Invertible Two- and Three-dimensional Quadratic Isoparametric Finite Element Transformations.” *International Journal for Numerical Methods in Engineering*, vol. 19, 789–802, 1983
- [66] Baart M.L., Mulder E.J. “A Note on Invertible Two-Dimensional Quadratic Finite Element Transformations.” *Communications in Applied Numerical Methods*, vol. 3, 535–539, 1987
- [67] Frey A.E., Hall C.A., Porsching T.A. “Some Results on the Global Inversion of Bilinear and Quadratic Isoparametric Finite Element Transformations.” *Mathematics and Computers*, vol. 32, 725–749, 1978
- [68] Ciarlet P.G. *Mathematical Elasticity, Vol. 1: Three Dimensional Elasticity.* Elsevier Science Publishers, North-Holland, 1988

- [69] Ball J.M. “Convexity Conditions and Existence Theorems in Nonlinear Elasticity.” *Archive for Rational Mechanics and Analysis*, vol. 63, 337–403, 1977
- [70] Garanzha V.A., Kaporin I.E. “Regularization of the Barrier Variational Grid Generation Method.” *Computational Mathematics and Mathematical Physics*, vol. 9, 1489–1503, 1999
- [71] Watabayshi G.Y., Galt J.A. “An Optimized Triangular Mesh System From Random Points.” *In Numerical Grid Generation in Computational Fluid Dynamics*, pp. 437–438, 1986
- [72] Suhara J., Fukuda J. “Automatic Mesh Generation for Finite Element Analysis.” *In Advances in Computational Methods in Structural Mechanics and Design*, pp. 607–624, 1972
- [73] Baker T.J. “Element Quality in Tetrahedral Meshes.” *In Proceedings of the 7th International Conference on Finite Element Methods in Flow Problems*, pp. 1018–1024, 1989
- [74] Strang G., Fix J. *Analysis of Finite Element Method*. Prentice-Hall, Englewood Cliffs, NJ, 1973
- [75] Coutinho A., Martins M. “<http://www.nacad.ufrj.br/marcos>.” *Personal communications*, January 2005
- [76] Miller K. *Biomechanics of Brain for Computer Integrated Surgery*. Warsaw University of Technology Publishing House, 2002
- [77] Miller K. *Personal communications*, April 2005
- [78] Brewer M. “Properties of the Element Condition Number Metric for Smoothing 2-D Meshes.” *MS Thesis*, 2001
- [79] Barth W. “Simulation of Non-Newtonian Fluids on Workstation Clusters.” *Ph.D. Thesis, The University of Texas at Austin*, 2004
- [80] Liseikin V.D. “On Construction of Uniform Grids on n-Dimensional Surfaces.” *Computational Mathematics and Mathematical Physics*, vol. 31, 1670–1683, 1991
- [81] Hirt C.W., Amsden A.A., Cook J.L. “An Arbitrary Lagrangian-Eulerian Computing Method for All Flow Speeds.” *Journal of Computational Physics*, vol. 14, 227–253, 1974
- [82] Horak H.G., Jones E.M., Kodis J.W., Sandford II M.T. “An Algorithm for the Discrete Rezoing of Lagrangian Meshes.” *Journal of Computational Physics*, vol. 26, 277–284, 1978
- [83] Dukowicz J.K. “Conservative Rezoing (Remapping) for General Quadrilateral Meshes.” *Journal of Computational Physics*, vol. 54, 411–424, 1984

- [84] Dukowicz J.K., Kodis J.W. “Accurate Conservative Remapping (Rezoning) for Arbitrary Lagrangian-Eulerian Computations.” *SIAM Journal on Scientific Computing*, vol. 8, 305–321, 1987
- [85] Knupp P., Margolin L.G., Shashkov M. “Reference Jacobian Optimization-Based Rezone Strategies for Arbitrary Lagrangian Eulerian Methods.” *Journal of Computational Physics*, vol. 176, 98–128, 2002
- [86] Benson D.J. “Computational Methods in Lagrangian and Eulerian Hydrocodes.” *Computer Methods in Applied Mechanics and Engineering*, vol. 99, 235–, 1992
- [87] Kucharik M., Shashkov M., Wendroff B. “An Efficient Linearity-and-bound-preserving Remapping Method.” *Journal of Computational Physics*, vol. 188, 462–471, 2003
- [88] Margolin L.G., Shashkov M. “Second-order Sign-preserving Conservative Interpolation (Remapping) on General Grids.” *Journal of Computational Physics*, vol. 184, 266–298, 2003
- [89] Eyring H. “Viscosity, plasticity, and diffusion as examples of absolute reaction rates.” *Journal of Chemical Physics*, vol. 4, 1936
- [90] Eyring H., Taikyue R. “Theory of non-Newtonian flow. I. Solid plastic system.” *Journal of Applied Physics*, vol. 26(7), 1955
- [91] Eyring H., Taikyue R. “Theory of non-Newtonian flow. II. Solution system of high polymers.” *Journal of Applied Physics*, vol. 26(7), 1955

Vita

Larisa Branets was born on August 30, 1978, in Moscow, Russia to Vladimir Branets and Tamara Ilina. She completed her primary and high school education in Korolev, Moscow region. After graduating from high school in 1995, she attended the Moscow University of Physics and Technology for 6 years, receiving a B.S. degree with honors in 1999 and a M.S. degree with honors in Applied Mathematics and Physics in 2001. She entered the graduate program at ICES, the University of Texas at Austin in August of 2001 and received a M.S. degree in Computational and Applied Mathematics in 2003.

Permanent address: Suvorova 20, kv. 31,
Korolev, Mosk. Obl.,
Russia, 141070

This dissertation was typeset with L^AT_EX by the author.